Università degli Studi di Cagliari

DOTTORATO DI RICERCA

IN FISICA

Ciclo XXIX

PERMEABILITY IN GRAM NEGATIVE BACTERIA

A microscopic journey

Settore/i scientifico disciplinari di afferenza

FIS/07

Presentata da: Silvia Acosta Gutiérrez

Coordinatore Dottorato Prof. Alessandro De Falco

Tutor Prof. Matteo Ceccarelli

Esame finale anno accademico 2015 – 2016

Tesi discussa nella sessione d'esame marzo – aprile 2017

PERMEABILITY IN GRAM-NEGATIVE BACTERIA.

A microscopic journey

SILVIA ACOSTA GUTIÉRREZ

Università degli Studi di Cagliari
Facoltà di Scienze
Dipartimento di Fisica

Relatore:
Prof. Matteo Ceccarelli

Coordinatore:
Prof. Alessandro De Falco

To my mother who gave me wings made of love and freedom, knowing that once she had finished I would go.

"Para mi madre que tejió mis alas con amor y libertad, aun sabiendo que cuando terminara yo me iría"

ACKNOWLEDGMENTS

"How strange is the lot of us mortals! Each of us is here for a brief sojourn; for what purpose he knows not, though he sometimes thinks he senses it. But without deeper reflection one knows from daily life that one exists for other people - first of all for those upon whose smiles and well-being our own happiness is wholly dependent, and then for the many, unknown to us, to whose destinies we are bound by the ties of sympathy. A hundred times every day I remind myself that my inner and outer life are based on the labors of other men, living and dead, and that I must exert myself in order to give in the same measure as I have received and am still receiving..."

—Albert Einstein

As part of the duty of putting together this three years of research, I must start by thanking all the people that has made it possible. Matteo thank you so much for giving me this amazing opportunity. This three years have been the most enriching and productive ones and I have to thank you for that. Thank you for your unreserved support, for your time and energy, thank you for sharing with me your passion for Science and thank you for motivating me in the bad times. I could not have had a better guide during these three years, you have taught me Physics, Biology, Chemistry, Microbiology... but most importantly human kindness. You are probably the most generous person I have ever encountered and without your support and of course scientific direction this work wouldn't have been possible. I also have to thank Igor, sometimes you've been the bad cop, pushing me against my limits, always asking for more accuracy, but for sure working with you have made me a better Physicist, a better scientist.

I also want to thank Prof. Bert de Groot and Prof. Francesco Luigi Gervasio for accepting the laborious work of reviewing this manuscript, and Prof. Alberto De Voto and Prof. Alessandro De Falco for their productive questions and comments during yearly seminars.

I have to thank all the people from the (influx-eflux) group, Tommaso, Susruta, Andrea, Alessandro, Debhia, Stefan, Pierpaolo, Giuliano, Paolo, Attilio, Alessio and Ivana, each of you have a special place in the pages of this journey. You adopted me from the very beginning and your help, friendship and support have been very important as these three years have been a very corrugated landscape to deal with.

Thanks Andrea Bosin and Giovanni for all the technical support. I also have to thank all the people I have met at the department from different groups, specially those who have become friends outside, Claudia, Giuliana, Cristina and Francesca.

I have travelled a lot, I do not remember how many planes I have took and in every destination I have met wonderful people. From my visit to external labs I have to thank Prof. Fabio Sterpone for hosting me in Paris but specially for sending me to Cagliari in the first place. Also I want to thank Maria Kalimeri who taught me everything about water polygons even tough those were her final days before defending her thesis. I have to thank Alessia and Elisa for the Hamburg experience. Thank you for gifting me with your time and teaching me the virtual screening mysteries. Special thanks goes to Prof. Michele Parrinello for hosting me for three months in Lugano, thank you for having your office door always open for discussion. I want to thank also all the great people in the lab, starting from Daniela Wirz that makes everything happen, to all the guys in the lab. Thank you for being always willing to work, help and discuss. I must admit I was really impressed with all of you, you really made me feel home.

During these three years of PhD I have been part of an amazing training network, that took eleven young researchers and (gently) squeeze them until they eventually become doctors. Eleven people (Alessia, Luana, Pauline, Monisha, Satya, Fabio, Vincent, JJ, Sushovan and Venkata) with very different backgrounds and cultures that have made this journey really enriching. I'll always have beautiful memories, specially from the Marseille meeting. This training bound me to my efflux-colleague Venkata, my quiet office mate that has become one of the person I most admire for his hard work, patience and peaceful mind. Thank you for being always there. I would also like to thank our coordinator Prof. Mathias Winterhalter who keeps everything spinning-round in the middle of the chaos and all the professors involved in this training network.

This PhD has been to this date the most enriching experience of my entire life, and it has been possible thanks to the support and love of all the people I love and made me feel loved, even though they are far away in a tiny island in the middle of the Atlantic Ocean or sparse around the world. This is to my colleagues and professors from Physics and the supervisors of my masters thesis, specially Prof. Breton that encourage me to leave the comfort zone. This is specially to my colleague Luis, who never let me gave up even when I wasn't able to remember two lines I had read 20 times. This is to my friends, Sandra, Goretti, Laura y Cristy, that were always there, even when I didn't find the time to call or visit. Thank you for making me feel that nothing has changed. This

to my grandmothers who died and to whom I couldn't say goodbye. Two women that did not have an easy life but were able to build with lots of love and hard work my big family. This is to my fan, my father, that is always proud of any tiny thing I do and puts up with all my angry answers when I'm stressed and keeps writing, calling and asking questions about everything I do. This is to my sister, my beloved sister, my English dictionary, my partner in crime.

This is to my mother, my first teacher, whose life is devoted to me and my sister. Thank you for teaching us all you knew and for encourage us to go further, to know more, to learn more, to work harder and to give always nothing but the best we can.

Further away, across the same ocean but a continent apart, there is you Alberto. The busy guy in the office next door who brought the needed peace and love that made possible the journey.

FINANCIAL SUPPORT AND COMPUTING RESOURCES

The research leading to the results herein has been funded by EU FP7-PEOPLE-2013-ITN Translocation network N.607694.

PUBLICATIONS

The results of this thesis have been published as follows:

CHOREOGRAPHY ALONG THE DIFFUSION PATHWAY INSIDE PORINS

Silvia Acosta-Gutiérrez, Andrea Mariano Scorciapino, Igor Bodrenko and Matteo Ceccarelli, Filtering with Electric Field: The Case of *E. Coli* Porins, *The Journal of Physical Chemistry Letters* **6**, 1807-1812 (2015)

M.A. Scorciapino, **S. Acosta-Gutiérrez**, T. D'Agostino, I. Bodrenko, M. Ceccarelli,Internal electric field of Gram-unspecific porins and the translocation of beta-lactam antibiotics (Proceeding) *EUROPEAN BIOPHYSICS JOURNAL WITH BIOPHYSICS LETTERS, Springer*,**4**, S218-S218 (2015)

M.A. Scorciapino, T. D'Agostino, **S. Acosta-Gutiérrez**, I. Bodrenko, M. Ceccarelli, Internal Electric Field of GRAM- Unspecific Porins Directs the Choreography of Antibiotic Translocation (Proceeding), *Biophysical Journal*, **DOI: 10.1016/j.bpj.2015.11.674** (2016)

M.A. Scorciapino, T. D'Agostino, **S. Acosta-Gutiérrez**, G. Malloci, I. Bodrenko, M. Ceccarelli, Exploiting the porin pathway for polar compounds delivery into Gram-negative bacteria, *Future Medicinal Chemistry* ,**8**,1047-1062 (2016)

QUANTIFYING THE MACROSCOPIC INTRINSIC ELECTRIC FIELD

Silvia Acosta Gutiérrez, Igor Bodrenko, Mariano Andrea Scorciapino and M. Ceccarelli, Macroscopic electric field inside water-filled biological nanopores, *Phys. Chem. Chem. Phys*, **18** ,8855-8864 (2016)

Silvia Acosta-Gutiérrez, Andrea Mariano Scorciapino, Igor Bodrenko and Matteo Ceccarelli, Water-Based screening of Antibiotics Permeability (Proceeding),*Biophysical Journal*, **DOI: 10.1016/j.bpj.2015.11.675** (2016)

Luana G M Ferrara, Gregor D Wallat, Lucile Moynié, Naresh Niranjan Dhanasekar, Mathias Winterhalter, Jean-Michel Bolla, Soumeya Aliouane, Jean-Marie Pagès, **Silvia Acosta-Gutiérrez**, Matteo Ceccarelli, James H Naismith, Crystal Structures of MOMP from Campylobacter jejuni,*Journal of Molecular Biology*,**428**,4528-4543 (2016)

ULTRA-COARSE-GRAINED MODEL FOR PERMEABILITY THROUGH PORINS

M.A. Scorciapino, **S. Acosta-Gutiérrez**, D. Benkerrou, T. D'Agostino, G. Malloci, S. Samanta, I. Bodrenko, and M. Ceccarelli, Rationalizing permeation of polar antibiotics in Gram-negative bacteria,*Journal of Physics: Condensed Matter*,**29**,113001 (2017)

CONFERENCES

The results presented in this thesis have been discussed in the following national and international conferences:

1 (July 2014) Contributed talk@ "ITN-Translocation Meeting" Jacobs University (Germany)

2 (July 2014) Contributed Poster@ "DFG Translocation Meeting: "Molecular basis of antibiotic permeability in Gram-negative bacteria." Jacobs University (Germany)

3 (March 2015) Contributed talk and poster@ "Maria Slodowska-Curie Initial Training Netwrok: Translocation, Mid-term Meeting" Cagliari University (Italy)

4 (July 2015) Contributed talk@ "Translocation Meeting: Molecular basis of antibiotic permeability in Gram-negative bacteria." Jacobs University (Germany)

5 (August 2015) Contributed talk@ " 259^{th} American Chemical Society Meeting" Boston (USA)

6 (November 2015) Contributed poster@ "Understanding function of proteins in membrane by atomistic and multiscale simulations" CECAM USI-Lugano (Switzerland)

7 (November 2015) Contributed poster@ "2nd workshop on High-Throughput Molecular Dynamics 2015" Barcelona Biomedical Research Park (Spain)

8 (Feb-Mar. 2016) Contributed poster@ "60^{th} Biophysical Society Annual Meeting" Los Angeles,California (USA)

9 (July 2016) Contributed talk and poster@ "Novel Approaches to fight bacteria" Jacobs University (Germany)

10 (Sept. 2016) Contributed poster@ " 21st EuroQsar" Verona (Italy)

ABSTRACT

Bacteria multi-drug resistance is a challenging problem of contemporary medicine and a new molecular framework for antibiotics is needed. General bacterial porins are recognized as the main pathway for polar antibiotics, but the permeability rules are still under debate. Recent works in literature pointed the electrostatics of the channel to be responsible for its filtering mechanism, and some theoretical investigations are already reported in the literature aimed at characterizing the electrostatics inside water-filled channels.

Using Molecular dynamics simulations we revealed the electrostatic filtering mechanism for porins, using water as sensing tool. We further quantify from water polarization density inside the channel the macroscopic internal electric field inside porins. This method allowed us to put forward an ultra-coarse-grained model in which the channel is described by its cross-section area, internal electric field and electrostatic potential along the axis of diffusion. Once these three descriptors are defined, it is possible to estimate the whole free energy along the channel axis of diffusion for a molecule represented by its size, charge and electric dipole moment in a few seconds.

This model would allow to virtually screen libraries of molecules searching for hits with enhanced permeability. These results may have important implications for the formulation of a general model for antibiotics translocation, and can be taken into account for rational drug design.

CONTENTS

i INTRODUCTION, SCOPE OF THE RESEARCH, STATE OF THE ART AND METHODS 1

1 INTRODUCTION 3

2 RESISTANCE IN GRAM-NEGATIVE BACTERIA 9
- 2.1 Antimicrobial Resistance . . . 9
- 2.2 Antibiotic Resistance . . . 10
- 2.3 Antibacterial drug discovery . . . 11
- 2.4 Gram-negative bacteria . . . 16

3 STATE OF THE ART: IN VIVO, IN VITRO AND IN SILICO 21
- 3.1 In vitro and in vivo techniques . . . 21
- 3.2 In silico studies . . . 24

4 METHODS 27
- 4.1 Molecular Dynamics . . . 28
  - 4.1.1 Force Fields . . . 32
- 4.2 Enhanced Molecular Dynamics . . . 37
  - 4.2.1 Metadynamics . . . 38
  - 4.2.2 Variationally Approach to Enhanced Sampling . 43
- 4.3 Docking . . . 46

ii RESULTS, DISCUSSION AND CONCLUSIONS 49

5 CHOREOGRAPHY ALONG THE DIFFUSION PATHWAY INSIDE PORINS 51
- 5.1 Summary . . . 51
- 5.2 Water choreography . . . 51
- 5.3 Antibiotics choreography . . . 61

6 QUANTIFYING THE MACROSCOPIC INTRINSIC ELECTRIC FIELD 67
- 6.1 Summary . . . 67
- 6.2 Electrostatic problem . . . 68
- 6.3 Response Function . . . 72
- 6.4 The method . . . 73
- 6.5 Electrostatic Characterization of porins . . . 75
- 6.6 Changes in the Macroscopic electric field due to pH, media osmolarity . . . 77

7 ULTRA-COARSE-GRAINED MODEL FOR THE FREE-ENERGY OF POLAR COMPOUNDS TRANSLOCATION THROUGH PORINS. 85
- 7.1 Summary . . . 85

7.2 Diffusion model 86
7.3 Docking of penicillins 89
7.4 Metadynamics: Translocation of penicillins 90
7.5 The free-energy model 94
8 CONCLUSIONS 97

iii COMPENDIUM 99
Filtering with the Electric Field: The case of *E. Coli porins* 102
Exploiting the porin pathway for polar compound delivery into Gram-negative bacteria 110
Macroscopic Electric Field inside water-filled biological nanopores 128
MOMP from *Campylobacter jejuni* is a trimer of 18-stranded β-barrel monomers with a Ca^{2+} ion bound at the constriction zone 140

iv APPENDIX 157
A COMPUTATIONAL METHODS 159
A.1 Filtering with the Electric Field: The case of *E. Coli porins* 159
A.2 Model 161

BIBLIOGRAPHY 163

Part I

INTRODUCTION, SCOPE OF THE RESEARCH, STATE OF THE ART AND METHODS

1 INTRODUCTION

This thesis dissertation covers the topic of permeability of antibiotics in Gram-negative bacteria. The evolution and widespread of resistant bacterial pathogens along with the failure in antibacterial drug discovery has led to the resistance era[22] in which simple treatable infections had become deadly again. In this adverse scenario, a new molecular framework for identifying and developing new antibiotics is absolutely needed[126,133].

The situation is particularly critical for Gram-negative bacteria where the presence of the additional outer membrane (OM) represents an extra barrier for any antibiotic to access its internal targets[122]. In the OM, general diffusion porins are expressed to facilitate the entry of polar molecules as ions, vitamins and nutrients. Today we know that porins are the main pathway for polar antibiotics to overcome the OM barrier[71,98]. Hence, Gram-negative bacteria have an additional strategy to react to antibiotic stress, reducing the OM permeability, either (i) by modulating the expression of porins, or (ii) by selecting key residue mutations that alter the permeability of porins themselves[94]. Porins differently to 'Efflux systems' are an intrinsic resistance mechanism and the reaction time under antibiotic stress is very slow compared to the latter. However, porin mutation can alter the its filtering mechanism, ultimately modifying the rules for permeability, and hence, compromising polar drugs ability to reach their targets.

Unfortunately, to date no direct and robust experimental methods are available for measuring drug permeation or accumulation into bacteria[170], neither in vitro nor in vivo. This technological gap has reduced enormously the research and investment in the field[126,160], leaving the pipeline empty. Understanding at molecular level the filtering mechanism that controls membrane permeability through porins will fill one of the current knowledge gaps for seeking new effective antibiotics.

Membrane channels like porins with large aqueous pores are traditionally regarded as 'molecular sieves' that allow the diffusion of polar molecules. Since the x-ray resolution of the Outer membrane porin F (OmpF), one of the most expressed porins in *Escherichia Coli*[36], much attention has been paid to its striking architecture: (i) a constricted central region, and (ii) a strong charge segregation along its walls. The constricted central region, giving rise to its hourglass shape as depicted in figure 1, is the real bottleneck for permeation: free diffu-

sion is avoided and molecules are filtered out by size and electrostatic properties. Till now the attention has been focus in understanding the molecule-pore interaction in the constriction region[90,113,138], but recent studies have pointed out that the permeation process might be also modulated by the whole pore electrostatics[45,84]. The OmpF porin can be simply modelled as an hourglass shaped nano-pore decorated with charged motifs, as depicted in figure 1 on the right panel. Within this ultra-coarse-grained model, the diffusion problem of a small molecule is governed by the interplay between the entropic barrier due to the size-exclusion criteria and the enthalpic compensation arising from the electrostatic interaction of the molecule with the electrostatic motifs of the pore.

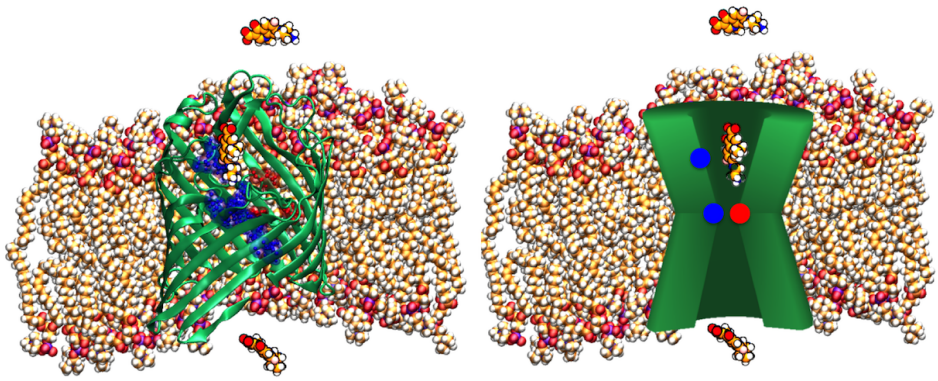

Figure 1: Cartoon representation of the microscopic journey through porins. On the left panel, one OmpF monomer is depicted in new-cartoon representation in green, embedded in a symmetric 2-oleoyl-1-pamlitoyl-sn-glyecro-3-phosphocholine (POPC) in van der waals representation. Inside OmpF the most important charged residues are highlighted as licorice with its van der waals surface in transparent material, coloured according to its charge. A norfloxacin molecule in van der waals representation is placed in three random steps along the diffusion path. On the right panel the OmpF model has been replaced for a toy model representation of its architecture: a green hourglass toroid (cut along the longitudinal plane) decorated with a few charged motifs represented as accordingly coloured circles.

The analysis of ion transport through membrane channels based on the reaction rate theory provides different models for translocation[34,88,91], depending on the number of energy barriers that the ion has to overcome inside the channel. The simplest, two-barriers-one-binding-site model was extended for the first time in 1987 to analyse sugar transport through the sugar-specific channel (LamB) from *Es-*

cherichia coli in[14], assuming single occupancy of the internal binding site.

The general diffusion model can be compared with the two-barrier-one-binding-site[15] model, both schematised in figure 2. The flux formula, for the two models, is respectively:

$$J = \frac{D}{L}c \ , \tag{1}$$

$$J = \begin{cases} k_{on}c & \text{low concentration} \\ k_{off} & \text{high concentration} \end{cases} \tag{2}$$

where D is the molecule diffusion constant, L the length of the channel, and k_{on}, k_{off} the association and dissociation rates.

The main differences between the two models is the description of the particle dynamics inside the channel, simple diffusion for the former, diffusion with binding for the latter. In the general diffusion model eq.1, the flux is linear with the solute molecule concentration while in the case of the two-barrier-one-binding-site model eq.2 the linear regime holds only at low concentration, while it tends to saturate at high concentrations due to binding. In this case, the molecule residence time distribution inside the channel is a single-exponential, being the average residence time $\tau = \frac{1}{k_{off}}$

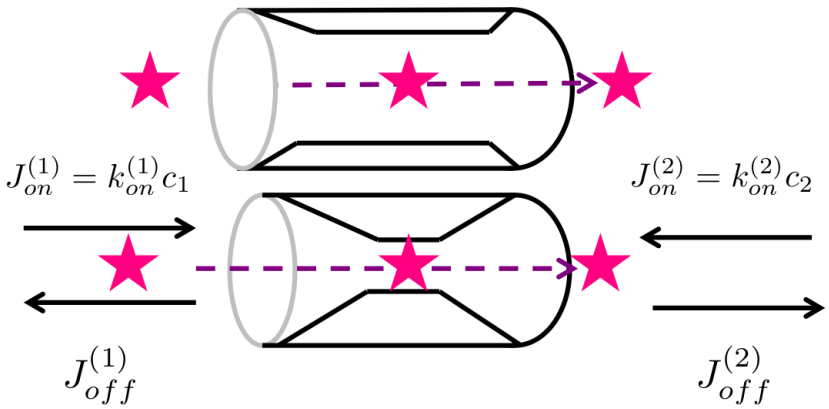

Figure 2: On the top the free diffusion model is schematize, in the absence of a binding site inside the channel the solute (magenta star) is free to diffuse through the channel (cylinder), while in the case of the two-barriers-one-binding-site model in the bottom, there exist a binding site in the middle of the channel changing the diffusion kinetics.

Hence, the stronger the channel-molecule interaction is the longer its residence time, consequently decreasing the flux with respect to the

general diffusion model. It is counter-intuitive that a channel naturally engineered for transporting a certain type of molecule, exhibits a binding site that reduces the flux. But, it is also interesting to note that, the maximum flux at physiological concentrations (low concentration of solute molecule) is higher for the two-barrier-one-binding-site model than for simple diffusion[15]. This observation lead the authors to conclude that a binding site inside the channel leads to faster transport when compared with general diffusion, establishing the current paradigm.

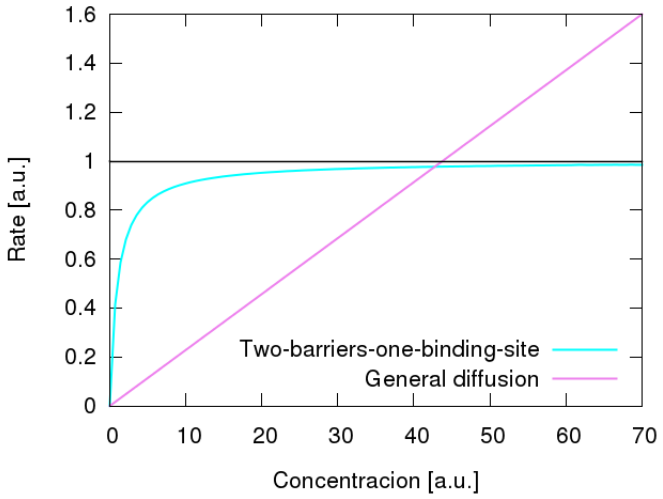

Figure 3: Molecule rate comparison as a function of concentration for the two models: Two-barrier-one-binding-site (cyan), general diffusion model (magenta).

In order to determine the importance of the interaction of the molecule with the channel, electrophysiology experiments[113] at single-molecule single-channel showed that changing the pH of the solution dramatically changes the frequency of the binding events. pH affects the protonation state of both the channel and the molecule, changing the electrostatic picture. This modulated "on rate" reflects once more the importance of the channel-molecule interactions, and in particular of the electrostatic interaction of the molecule with the channel unique electrostatic motifs. However, x-ray co-complex experiments did not find any evidence for a unique binding site[175]. In particular different antibiotics seem to find favourable interactions far from the constriction region, though these experiments are performed under very unrealistic conditions. Today it is not yet clear if, as in the enzyme problem, this affinity sites are biologically relevant in terms of flux control, like in the two-barrier-one-binding-site model. A rationale analysis should focus on the role of the whole pore properties modulating the flux: (i) How does the entropic barrier of the constriction region modulate the

flux? (ii) how does the electrostatics of the channel affect its filtering mechanism?

The aim of this thesis is to put forward an ultra-coarse-grained model for calculating the energy of small polar molecules interacting with membrane channels during diffusion, using the OmpF porin from *E. coli* as prototype. We trained the model to reproduce the free-energy obtained from all-atom simulation of the translocation of well-known drugs, selected in order to cover different physico-chemical properties (size, charge, dipole, shape), through OmpF using metadynamics to enhance the conformational space sampling. This ultra-coarse-grained model will help to generate molecular descriptors for enhanced permeation[69]. Further, the energetic decomposition of the problem will help to understand which are the most important energetic terms in determining the flux.

In chapter 2 a further discussion about the "Antibiotic resistance" problem in bacteria is given as well as a briefly historical overview of the antibiotic discovery. We review in chapter 3 the state of the art of antibiotic permeability in gram-negative bacteria obtained with in silico techniques, and we describe briefly the main in vitro and in vivo techniques available for measuring permeability.

In the methods chapter 4 we introduce the computational techniques employed in this thesis as well as a new enhanced sampling technique which is being set up in the last period of the research.

In chapter 5 the electrostatic pattern along the axis of diffusion of porins is described using water as a molecular probe. Both the choreography of water and antibiotics while diffusing through the pore helped us to show qualitatively the role of the internal electrostatics of porins in its filter mechanism.

In chapter 6 we provide a method based on water polarization for the exact quantification of the macroscopic intrinsic electric field felt by the molecule while permeating through the channel. Moreover we discuss the ability of this macroscopic observable to account for environmental differences, like ion concentration or the presence of metallic ions, and pin-point mutations, as well as the main differences in electrostatics among general porins.

Finally, in chapter 7 we introduce an ultra-coarse-grained model for the free energy of polar molecules permeation through porins based on the calculation of the entropic barrier due to the size-exclusion problem along the pore and the enthalpic contribution of the electrostatic interaction of the molecule with the internal wall of the channel.

2

RESISTANCE IN GRAM-NEGATIVE BACTERIA

Contents

2.1 Antimicrobial Resistance 9
2.2 Antibiotic Resistance 10
2.3 Antibacterial drug discovery 11
2.4 Gram-negative bacteria 16

2.1 ANTIMICROBIAL RESISTANCE

With few replacement products in the pipeline, the world is heading towards a post-antibiotic era in which common infections will once again kill. This will be the end of modern medicine as we know it. If current trends continue, sophisticated interventions, like organ transplantation, joint replacements, cancer chemotherapy, and care of pre-term infants, will become more difficult or even too dangerous to undertake.

— Dr. Margaret Chan, World Health Organization general director speech at G7 meeting on antimicrobial resistance, October 2015

Antimicrobial resistance (AMR) is a broad term, that encloses resistance to drugs to treat infections caused by all types of microbes, as bacteria, parasites, viruses and fungi. Resistant microorganisms threaten the effective prevention and treatment of an ever-increasing range of infections. Its ability to survive attack by antimicrobial drugs such as, antibacterial drugs (e.g. antibiotics), antifungals, antivirals and antimalarials renders standard treatments ineffective and infection persist, increasing the risk of spread to others.

The evolution of resistant strains is a natural phenomenon that occurs when microorganisms replicate themselves erroneously or when resistant traits are exchanged between them. The use, abuse and misuse of antimicrobial drugs accelerates the emergence of drug-resistant strains. Poor infection control practices, inadequate sanitary conditions and inappropriate food-handling encourage the further spread of antimicrobial resistance.

In the past, resistant infections were associated predominantly with hospitals and care settings, but over the last decade resistant infections have been seen in the wider community too. With resistance on

the rise, we stand to lose the immense ground we have gained in the last century. This includes: 1) our fight against life threatening infectious diseases such as pneumonia, tuberculosis (TB), Human Immunodeficiency Virus (HIV) and malaria; 2) our battle against conditions such as cancer, where antibiotics are crucial in helping chemotherapy patients avoid and fight infection; and 3) huge advances in surgical procedures like organ transplants and caesarean sections, which have now become routine and relatively low risk, thanks to our ability to effectively stave off or treat acute infections with antibiotics.

2.2 ANTIBIOTIC RESISTANCE

This study is focused in antibiotic resistance. Antibiotic resistance refers specifically to the resistance to antibiotics that occurs in common bacteria that cause infections[119]. The evolution and widespread distribution of antibiotic-resistance elements in bacterial pathogens has made diseases that were once easily treatable deadly again.

The discovery of penicillin in 1929, streptomycin in 1943 and cephalosporins in 1948 by Giuseppe Brotzu, give rise to the golden era of antibiotic discovery. With infections under control, clinicians started to transform and revolutionize medicine. Invasive surgery became routinely, immune-system destroying chemotherapy was introduced to fight cancer, organs transplantation became a reality for extending lives and multiple replacement surgeries improved the quality of life of humanity.

In his Nobel Lecture on penicillin, Sir Alexander Fleming stated: *" It is not difficult to make microbes resistant to penicillin in the laboratory by exposing them to concentrations not sufficient to kill them, and the same thing has occasionally happened in the body"*. Nevertheless, antibiotics has been used as magic weapons to cure all infections, regardless their use was really appropriate for the infection. Unfortunately, due to the existence of antibacterial resistance, the control of bacterial infection through the use of non-toxic, cheap and plentiful antibiotics cannot be taken for granted any more and it is a real challenge for contemporary medicine.[22]

The rise and spread of antibiotic resistance presents a unique challenge to both science and medicine. The spread of multidrug-resistant "ESKAPE" organisms (*Enterococcus spp., Staphylococcus aureus, Klebsiella spp., Acinetobacter baumanii, Pseudomona aeruginosa adn Enterobacter spp.*) represent a real crisis, indeed, in the case of some Gram-negative bacteria, such as some strains of *A. baumanii* that are resistant to all currently available antibiotic[60,160].

The microbial world has always had the molecular tools to drive resistance. The antibiotic resistome - the global collection of all microbial resistance genes - is genetically diverse, widespread across all environmental niches and pre-dates the modern antibiotic era by millennia. Resistance is a natural process related to the evolution of bacteria, which is accelerated by the pressure exerted by antibiotic exposure, as predicted by Fleming. This natural evolution is unavoidable and we will always need new antibiotics to fight bacteria.

The use of large quantities of antibiotics to control infection in human and animal diseases and in agriculture has created unprecedented conditions for the mobilization of resistance elements in bacterial populations and their capture by previously antibiotic-sensitive pathogens.

Antibiotics shut down essential cellular functions, and resistance mechanisms appear to exploit every possible strategy of preventing a drug from hitting its target. The major types of clinically relevant resistance have been long studied and are generally well understood[47,126].

In the resistance era, in order to come up with new antibiotics for treating resistant infections, we need a better understanding of the cell biology of these microorganisms. We need to understand better the mechanisms of action of the existing antibiotics and to learn from the history of antibiotic discovery.

2.3 ANTIBACTERIAL DRUG DISCOVERY

The number of new antimicrobial classes discovered or patented has decreased over the years triggered by many different reasons[145] as it can be seen in Figure 4. Finding new drugs as efficient as the "historical" antibiotic classes has proven to be extremely challenging and moreover, antibiotics have a poor projected return on investment[22,160] for pharma companies.

In the golden era of antibiotic discovery, natural scaffolds and alternative versions of these pioneering drugs were uncovered by mining the specialized metabolism of bacteria and fungi or by chemical modification of existing scaffolds5. Nevertheless, there are many fundamental gaps in our knowledge about antibiotics, from the exact target of many of them, to the penetration pathway that the molecule undertakes to reach its target inside the cell and the mechanisms adopted by the pathogens to actively pump out the noxious molecules.

Antibiotics perturb important biochemical processes, which results in the inhibition of cell growth and division and, in the case of bactericidal agents, cell death. The first antimicrobial agents were synthetic molecules that were discovered by screening libraries of chemicals, in particular dyes. This screening was superseded by the realization that

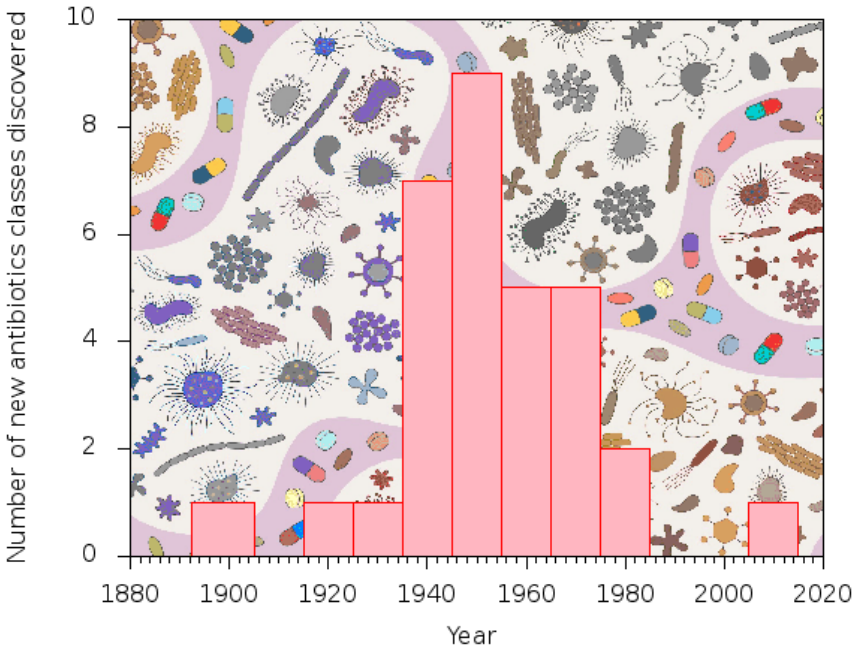

Figure 4: Source: Readapted from Lynn L. Silver "Challenges of Antibacterial Discovery," Clinical Microbiology Review (2011)[145]

bacteria and fungi in the environment produce metabolites that could treat bacterial infections in humans with remarkable efficacy and minimal toxic side effects. The strategy adopted by Selman Waksman, a co-discoverer of streptomycin, involved screening soil-dwelling bacteria, and in particular spore-forming Actinomycetes, for the production of metabolites that block the growth of pathogens — a process that was later termed the Waksman platform.[77,78]. The simplicity and effectiveness of the platform lead to the golden era of antibiotic discovery, the period in which most of the antimicrobial natural scaffolds that serve as our antibiotic arsenal were discovered 5. The platform also imposed measures of success that following drug-discovery efforts would need to use, in particular the use of the inhibition cell growth *in vitro*, which is assessed on rich media, as the way to determine the minimal inhibitory concentration (MIC) of a compound.

By the middle of the 1960s, new and effective antibiotic scaffolds were becoming harder to identify using the Waksman platform. Due to fact that these specialized metabolites are product of microbial evolution within specific environment and were not designed as drugs, hence, most of them have considerable pharmacological and toxicological drawbacks. Furthermore, the resistance to these early antibiotics started to become a problem. These issues opened the door to the medicinal chemistry era 5, the next period in antibiotic discovery. The development of

antibiotics was dominated in this period by cycles of innovation that focused essentially on creating synthetic versions of the natural scaffolds discovered in the previous era. These derivatives led to exceptional improvements in the application of antibiotics, which included lower doses, an expanded antimicrobial spectrum against various pathogens, and the avoidance of resistance.

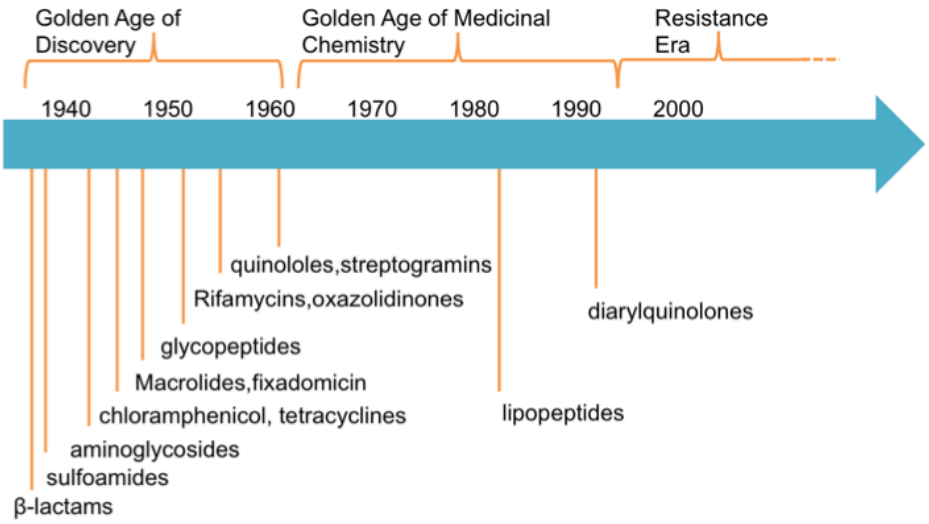

Figure 5: Antibiotic classes discovery time-line.

Most existing antibiotics are therefore derived from natural products and tend to target the bacterial cell wall, DNA or ribosomes. With a few exceptions these compounds have complex effects on bacterial cell and often have more than one molecular target. Moreover, there is an increasing appreciation that bacterial cell death is complex and probably requires the involvement of several cellular pathways. Many natural-product antibiotics are the product of selection for these complex traits over millions of years of evolution. Therefore is perhaps unsurprising that modern methods in drug discovery have yet to deliver compounds with efficacy comparable to that of the first generation of natural antibiotics and semisynthetic derivatives.

The golden era was followed by a considerable innovation gap in the identification of new scaffolds that began in the middle 60s and lasted until the early 90s, where a fresh wave of resistance precipitated a renaissance of discovery efforts. Coinciding with the emergence of innovative drug-discovery approaches in all therapeutic areas. These new methods were strengthened by remarkable advances in technology, such as breakthroughs in the manipulation of recombinant DNA to produce desired proteins at high yields and high−throughput synthesis to

create large chemical libraries. Improvements in protein−structure determination enabled rational drug design, and robotic liquid handling facilitated high-throughput screens of biochemical assays. Furthermore, a computing revolution made it possible to handle much larger data sets. When coupled with emergent genomic technologies, these advances enabled a "gens-to-drugs" model that has been applied with success to many therapeutic areas and become convention.

Antibacterial drug discovery has been especially influenced by genomic data, technology and innovation. The first free-living organism to be sequenced was the pathogen *Haemophilus influenzae* and, since then, thousands of bacterial genomes have been sequenced. High-throughput techniques that can create precise deletions at the genome scale have been used to explore methodically the dispensability of each gene in both the model Gram-positive bacterium *Bacillus subtilis* and in the model Gram-negative bacterium *Escherichia coli*. Pathogens such as *Staphylococcus aereus* and *Pseudomonas aeruginosa* have also been the subject of systematic approaches to mutagenesis, due to the prevalence of *M. tuberculosis*. The goal of these large-scale surveys has been to identify new targets for a generation of antibiotics that will not be susceptible to existing mechanism of resistance.

Large-scale gene dispensability studies generated numerous targets and many were tested *in vitro* screening campaigns. However, this high-throughput biochemical screens of large collections of synthetic chemicals often were unable to find promising compounds with the necessary physical and chemical properties. Gram-negative bacteria have proved especially discouraging owing to a poor understanding of drug penetration and efflux systems that are pervasive in this group of pathogens.

Modern antibacterial drug discovery has also employed large chemical screens of whole cells for growth inhibition. However, such screens produce huge numbers of active compounds that are difficult to follow up because of a lack of tools for prioritization. Indeed, there has been a resurgence in cell-based approaches that includes innovative strategies for focusing in promising leads that target different aspects of bacterial survival. Ultimately, these approaches will focus on specific targets to facilitate the lead-optimization strategies that are inherent to modern drug discovery.

Approximately 7 percent of the *E. coli* genome, some 303 genes, has been shown to be essential for growth in rich media, which represents typical Waksman-screen conditions. Nevertheless, systematic studies of stress conditions such as nutrient deprivation and chemical perturbation have demonstrated that a further 285 genes are conditionally essential. These conditionally essential genes largely encode enzymes that are important for the utilization of carbon sources or biosynthe-

sis of the outer membrane as well as in the synthesis of amino acids, vitamins and nucleobases. Yet these processes have been ignored by antibacterial drug discovery.

In vivo essential genes represent a set of emerging targets that remain untested in modern antibacterial drug discovery. However, they hold great promise for expanding the pool of targets for new drugs. Inhibitors of this class of targets often fail to show standard phenotype of cell-growth inhibition, which is used to calculate the MIC. The MIC is an important driver of compound optimization in preclinical antibiotic development and a gold standard for efficacy.

Although, historically, natural-product have shown great efficacy against bacteria, they have many drawbacks. Natural-product antibiotics are often chemically complex with challenging and intractable routes to synthesis in the laboratory that make it difficult to prepare derivatives. The pharmacology of most first-generation is also not ideal, which reflects the origins of these drugs as specialized microbial metabolites not medicines. Furthermore, because these ancient metabolites are important components of microbial chemical ecology, genetic elements that provide resistance against them have been retained by and are often widely dispersed in communities of microorganism in the environment.

Libraries of chemical of synthetic chemicals can exceed several million compounds and, in principle, provide access to a vast spectrum of chemical space. Although, these collections have been explored as source of new antibiotics using modern drug-discovery platforms for more than three decades. Driven by metrics such as the Lipinski rule of five for orally available drugs, the synthetic libraries of most pharmaceutical companies tend to be dominated by compounds that are optimized for human biology. But most antibiotics in clinical use do not conform to these parameters because they are natural products or their derivatives. The Achilles' heel of synthetic compounds as new antibiotic drugs seems to be their general inability to penetrate readily the cell envelope of bacteria, which comprises inner and outer membrane, porins and complex carbohydrate polymers, couples with their susceptibility to active efflux by membrane associated pumps. Because they are products of evolution, antibiotic natural products have evolved to overcome these challenges.

A proposed solution to this problem is the development of synthetic libraries that capture the chemical diversity and physiochemical properties of natural products. Another proposed solution is to capitalize on the ability of synthetic compounds to inhibit essential bacterial targets by developing delivery systems that solve the cell-envelope penetration and efflux challenges. One example of the second strategy are

siderophores also known as "Trojan horse" approach that has been explored but not yet proved to be clinically efficacious. A further solution is to combine these compounds with molecules that enhance their transport or otherwise help to breach the permeability barrier of the bacterial cell.

2.4 GRAM-NEGATIVE BACTERIA

Broadly speaking there are two big types of bacteria: gram-negative and gram-positive, according to the reaction of the cells to Gram stain, a long-standing test for the classification of bacterial species.

The main difference among gram-positive and gram-negative bacteria arise from the cell envelope type: gram-positive bacteria have a thick envelope made of several layers of peptidoglycan and teichoic acids, while gram-negative bacteria posses a thinner one, but more complex.

The gram-negative bacteria cell wall is made of fewer layers of peptidoglycan with respect to gram-positive but this layers are surrounded by a second lipid membrane 6, the outer membrane (OM).

The OM itself is highly asymmetric. Its inner leaflet, which faces the periplasmic space, is composed of phospholipids, similar in composition to the inner membrane. By contrast, the outer leaflet contains large lipopolysaccharide (LPS) molecules, which contain multiple saturated fatty acid tails and heterogeneous, charged polysaccharides that are cross-linked by divalent cations.

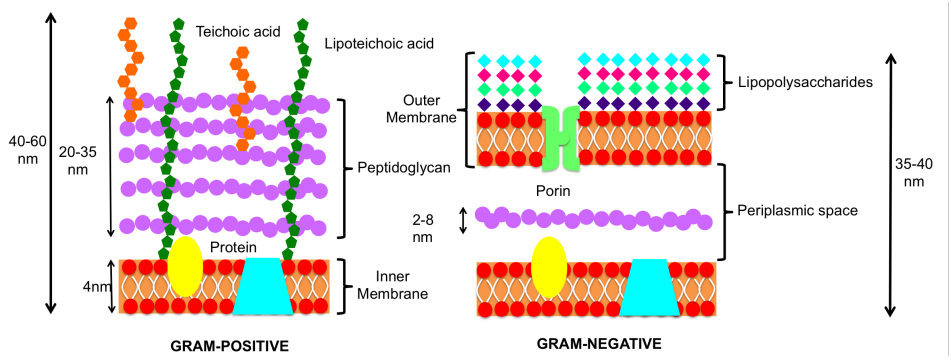

Figure 6: Schematic representation of Gram-positive and Gram-negative cell envelops.

The OM in gram-negative bacteria acts as a first line of defence against toxic compounds[115]. The combination of a highly charged sugar region and tightly ordered, gel-like hydrocarbon chains results in low permeability. Clinical Gram negative-bacteria strains such as *Escherichia coli*, *Salmonella spp.*,*Klebsiella spp.*,*Enterobacter spp.*, *Campylobacter spp.*, *Acinetobacter spp.* and *Pseudomonas aeruginosa*

are frequently reported as multidrug resistant (MDR). For this type of pathogen the pipeline is virtually empty, limiting the therapeutical options and in the worst cases leading to death.

Gram negative-pathogens use three major strategies for drug resistance[122]:

1. the membrane barrier hinders the access to the intracellular region;
2. the enzymatic barrier produces enzymes able to degrade or modify antibiotics;
3. the target protection barrier that diminish target recognition and hence antimicrobial activity.

In this thesis dissertation we will focus the attention in the first strategy: the access to the intracellular region in gram-negative pathogens.

Permeation through the OM is largely controlled by membrane proteins and protein complexes that regulate the influx and efflux of nutrients and nocive species[43,115,143]. The majority of hydrophilic antibiotics exploit membrane protein pores or porins to penetrate the outer membrane and reach their targets in periplasmic space[13]. Thus, the OM provides this type of bacteria with a very effective intrinsic resistance mechanism against antimicrobial compounds, and many resistant strains present porin mutations[51,122]. This passive resistance mechanism is additional to the acquired and adapted resistance, that are due to the incorporation of new genetic material or mutation, ultimately resulting in modified proteins and protein expression level[51].

Porins Protein pores or porins are typically closed barrels, monomeric or homotrimeric proteins, consisting of transmembrane anti-parallel β-strands that are strongly tilted with respect to the barrel axis. Each strand is connected by short turns on the inner side of the membrane and by long, mobile loops on the extracellular side as it is shown in Figure 7. Matching the lipid bilayer environment, the outer surface of the barrel is strongly hydrophobic, whilst at the membrane-solvent interface, amphipatic aromatic groups (i.e. Trp, Tyr) are generally observed[143]. These β-barrel channels form transmembrane water-filled channels allowing the passive diffusion of hydrophilic molecules, up to 600 Da, acting as molecular filters in the OM of gram-negative bacteria.

Different types of porins have been characterized in Gram-negative bacteria and classified according to their activity: non-specific or specific channel or selective pore; their functional structure: monomeric or trimeric; and their regulation and expression[43,81,115,123,143].

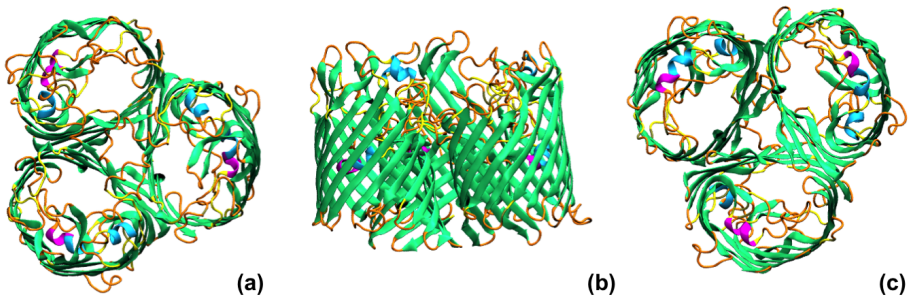

Figure 7: Cartoon representation of general channel, OmpF from *E. coli* (a) extracellular view of the homotrimer, (b) front view, (c) periplasmic view. Colour scheme: extended beta-strands in green, alpha-helix in cyan, 3-10 helix in magenta, coils in orange ad turns in orange.

The pioneering studies of the three major outer membrane porins of *E. coli* - OmpF[36], OmpC[11] and PhoE[36] - constitute the foundation of our current knowledge of outer membrane channels[43,115]. OmpF, OmpC and PhoE are classified as general or non-specific channels and together with their homologue's in other Gram-negative bacteria are termed as classical porins[115].

(Classical) General Porins Classical porins are characterized for presenting an open conformation in the absence of any specific substrate[43,115]. Despite its "non-specificity", they can be subclassified according to several physico-chemical properties of the solutes that can translocate trough them: size, charge, electrical dipole moment... But also in terms of its own physico-chemical parameters, such as conductance, selectivity and voltage gating. The two major porins of *E. coli*: OmpF and OmpC have been widely studied[68,81,86,127,147,158]. This family of porins allow the passage of ions and metabolites up to 600 Da. They are slightly cation-selective, whereas PhoE selects inorganic phosphate and anions[43,81,115,141,143]. Growth conditions alter the level of expression of these two porins[104], in particular, rich media like the mammal intestine, favours the expression of OmpC over OmpF. Despite the pore size, constricted halfway down the pore by the so-called loop L3, was pointed out as the most important feature behind channel permeability[86,104], later computational and experimental studies[84,135] have pointed out the channel electrostatics as playing a major role in the filtering mechanism, due to charge segregation along the channel. In Figure 8a-b. we provide a cartoon of OmpF, in panel (a) the constriction loop L3 is highlighted in orange as well as the charged residues in the narrower region, while in (b) the lumen pore is schematize using

a surface representation, highlighting the accessible area with a dashed magenta ellipse.

Although, most of the porins involved in polar antibiotics translocation belong to the classical porins family, there are exceptions, such as OprD from *Pseudomonas Aeruginosa* and other porins from *Acinetobacter baumanii* and *Neisseria spp*, for which their specific nature suggest more specific rules for permeation.

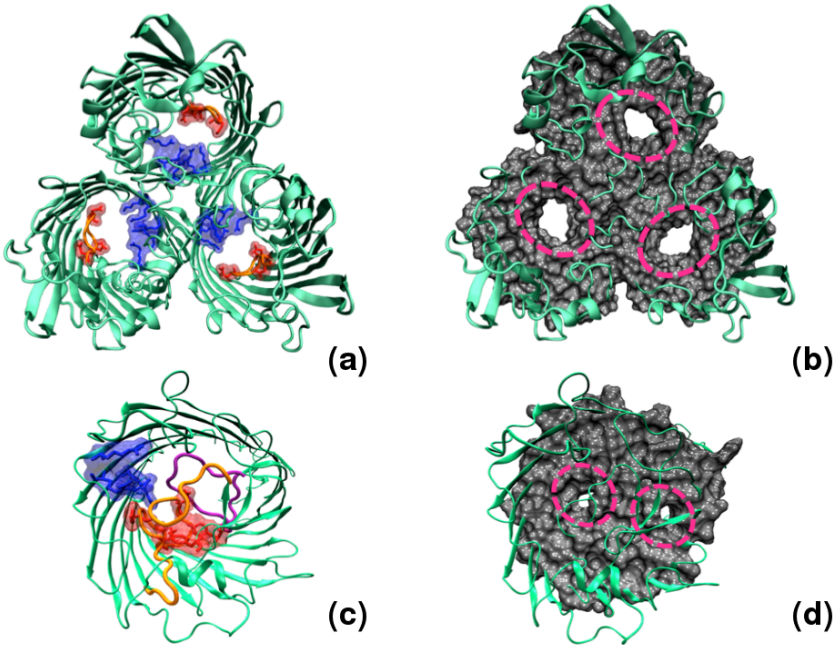

Figure 8: Cartoon representation of a general porin, OmpF from E. coli, and a specific channel, OprD from P. aeruginosa. (a) Top view of the trimeric OmpF, where loop L3 has been highlighted in orange. Charge segregation is highlighted in the constricted region in red (negative) and blue (positive). (b) Same as panel a, where atoms Van der Waals surface was added in order to highlight the solvent accessible area inside each monomer. (c) Top view of the monomeric OprD, where the loops that folds back into the pore and generate the constriction region are highlighted in purple and orange. The oppositely charged residues that characterized the constriction region have been also highlighted in red (negative) and blue (positive). (e) Same as panel d, where atoms Van der Waals surface was added in order to highlight the solvent accessible area inside the channel.

Specific-Porins Certain species like *P. aeruginosa* and *A. baumanii* exhibit lower permeability than *E. coli*. These species instead of expressing relatively large 'non-specific' channels, show a variety of specialized

porins for the uptake of nutrients[57]. Such as the outer membrane carboxylate channel (Occ) family of transporters also known as OprD family[48,157]. Specific porins are smaller than general porins but the exclusion size of other solutes is only about half the value determined for general porins. This porins are normally closed in the absence of the substrate. The presence of a binding site for the substrate within the channel, as found by means of electrophysiology for Maltoporin (LamB), a sugar-channel of *E.coli*[15], is the key feature driving translocation. In the case of sugar channels the 'greasy slide'[142], a smooth hydrophobic path, which extends from the floor of the vestibule, through the constriction to the periplasmic exit, guides sugar through the channel by engagement in nonspecific hydrophobic interactions with the pyranose rings. In Figure 8c-d, the OprD channel from *P. aeruginosa* is depicted, in this case as previously mentioned the accessible area is smaller than in the case of general porins, as in can be appreciated in panel(d) and the loops involved in the channel constriction or gating is more complex as it can be seen in panel (a) where also the most important charged residues have been highlighted.

In order to analyse this physico-chemical properties porins have been purified and reconstituted in different experimental setups like liposomes and planar bilayers[43]. This techniques will be briefly reviewed in the next chapter 3

3

STATE OF THE ART: IN VIVO, IN VITRO AND IN SILICO

Contents

3.1 In vitro and in vivo techniques 21
3.2 In silico studies 24

3.1 IN VITRO AND IN VIVO TECHNIQUES

To date there is neither a direct nor a robust experimental method to quantify antibiotic permeation in vivo or in vitro.[170]. The quantification of the flux of small molecules across the OM is highly influenced by kinetics as only a few thousand molecules per cell enter within few minutes to hours[153]. Typical devices have a detection limit of 10^{12} molecules, so antibiotic flux is substantially below that limit, thus requiring signal amplification. Nevertheless, there exist different assays to try to measure antibiotics' flux into bacteria.

In vivo One of the methods available to measure flux in vivo is the antibiotic accumulation assay. Bacteria is incubated with antibiotics for a fixed time period and then washed in order to remove all the antibiotic from the media. There are several techniques, that mainly differ in the separation/washing method[111]. Then different biophysical techniques can be applied to quantify the intracellular antibiotics, like counting radioactive labelled compounds or in the case of the naturally fluorescent quinolones with a plate reader.

Another approach is based on enzymatic assays[176] in which bacteria is engineered to express β-lactamase enzymes. This enzymes hydrolyse the β-lactam group from β-lactam antibiotics, like penicillins, cephalosporins or carbapenems. The signal is collected from beta-lactamase cleavage of the antibiotic, using for example 'Fluorescence Resonance Energy Transfer' (FRET)-based methods in the most modern set-ups[112,169,176].

More recently strong light sources enabled uptake quantification of fluorescent molecules using the increasing fluorescent intensity inside a single cell[80]. Bacteria are soaked in fleroxacin, a natural fluorescent antibiotic, and separated. Using the light source at the synchrotron

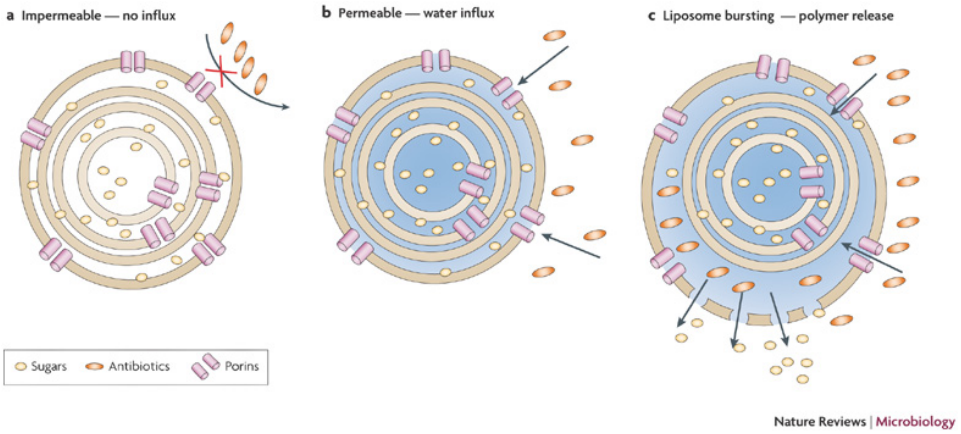

Figure 9: Liposome swelling assay scheme. Reprinted from[122]

Soleil (Paris) the authors were able to image single bacteria at the emission wavelength of fleroxacin. Accounting for smart background elimination this approach allows to follow the kinetic of single bacteria influx and efflux mechanism.

A promising tool is to use mass spectrometry in order to measure the uptake of antibiotics by quantifying the change of extracellular drug concentration, as it have been recently shown[26,40,174].

In vitro To understand the molecular origin of the rate limiting steps in permeability less macroscopic information is needed. Different in vitro biophysical assays have been developed for this purpose.

Liposome swelling assay provides information on a model system[96]. Porins are reconstituted in a multilayer liposome preparation as it is shown in Figure 9. The substrate is added under iso-osmotic addition and diffuses inside causing a change in light scattering. Briefly caged fluorescent dyes are encapsulated into single wall liposomes. Antibiotics able to displace the fluorescent dye from the cage in a competitive manner will create an increasing fluorescence. In case of uncharged molecules the change in light scattering signal correlates well with the relative permeability, but disadvantages are: (i) the need of large quantity of material to achieve enough signal and (ii) counter ion flow effects in case of charged molecules. Also multichannel based assays provide an average value and do often not allow conclusion on rates.

Another technique consist in using reconstitution of a single porin into planar artificial lipid bilayer, apply a transmembrane voltage and record the ion current flow across the channel. Antibiotic is added to one of the sides (cis or trans) of the chamber and it will passively diffuse into the channel. The interaction between the antibiotic and

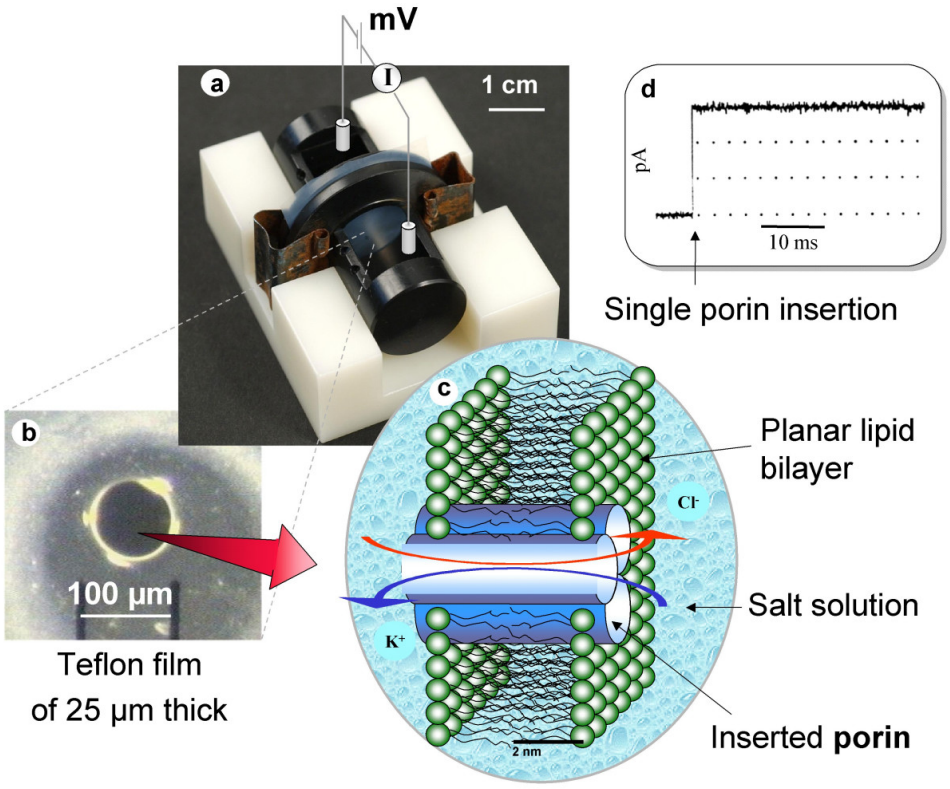

Figure 10: Schematic representation of a typical planar bilayer set-up for ion current recording. 1.a) Two half cells made of Delrine separated by a 25 Îijm Teflon foil with a hole in the center, clamped together 1.b) Microscope picture of the teflon hole.c) Schema of a lipid bilayer with a reconstituted trimeric porin. d) The insertion of a single channel will give raise to a jump in conductance. Reprinted from[16]

the channel will block the ion current, as the antibiotic atoms will compete with ions, blocking diffusion inside the channel 10.

As mentioned before this analysis provides data on interaction but not directly on translocation as the molecule may exit from the entry side after blockage[101]. In case of charged molecules we may directly conclude on translocation: increasing voltage will reduce the residence time of the molecules inside the channel in case of transport[146]. However most of the molecules do not carry a net charge and are thus invisible. Furthermore the finite time resolution of electrophysiology requires a sufficient strong occlusion of the channel to be visible. Although recent analysis techniques allow to better discriminate between reflected and translocated molecules to beat the resolution time below microseconds[17].

3.2 IN SILICO STUDIES

As it was mentioned in the introduction, porins are believed to be the main pathway for polar antibiotics to overcome the outer membrane permeability barrier.

Since the crystallization of the first porins X-ray structure (OmpF and PhoE from *E. coli*)[36], its peculiar architecture has dragged much attention, in particular, its decorated eyelet depicted in Fig.11. Starting from these X-ray structures , the authors calculated the internal electrostatic potential and electric field of OmpF and PhoE using a macroscopic multi-dielectric model, revealing that in the case of OmpF the highest field intensity was located in the constriction region in[79].

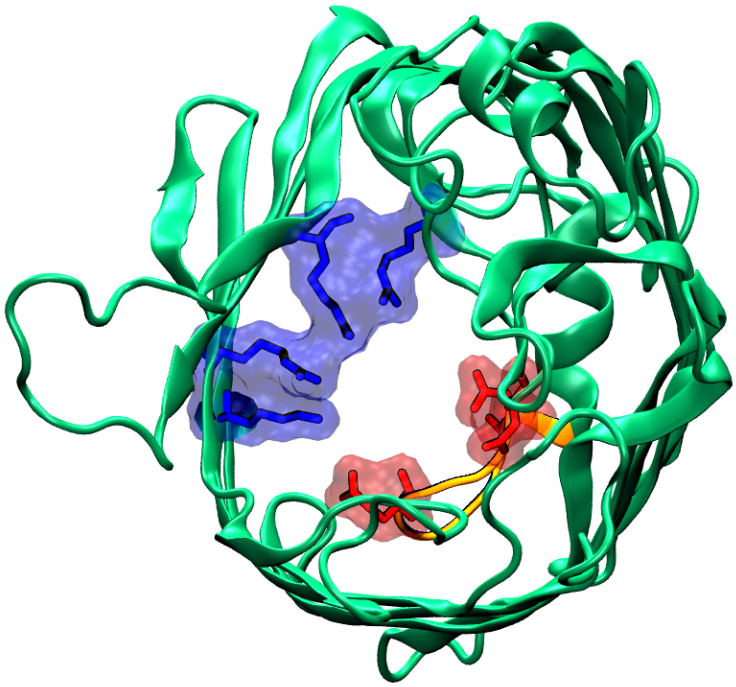

Figure 11: Cartoon representation of the eyelet region of the OmpF porin. The constriction loop L3 is highlighted in orange and the oppositely charged residues decorating the eyelet are depicted in licorice representation with its van der waals surface in transparent material, coloured according to its charge.

The early simulation of the OmpF porin in a fully hydrated symmetric bilayer shed some light in its dimension, ionic conductance and water properties inside the pore[158]. Simulations revealed the existence of structured water in the constriction region, caused by the intense transversal electric field calculated[79], though simulations were limited to a few nanoseconds. Previous studies[140] had revealed that the dynamical properties of water inside model pores is different from bulk,

and water dynamics is influenced by confinement and channel electrostatics. Later, by using molecular dynamics, Brownian dynamics and continuum electrodiffusion theory[67,68] the authors showed two different pathways for cations and ions inside OmpF, due to charge segregation inside the pore, and addressed the importance of the formation of ion-pairs for its diffusion trough the channel. Also the authors reported small fluctuations of the constriction loop L3, hence, non gating was reported.

In the case of the transport of small molecules through general porins by using non-equilibrium molecular dynamics, it was shown for alanine and methyglucose diffusing trough OmpF. The structural perturbation of the protein is minimal and during the permeation process, both alanine and methylglucose are strongly aligned to the electric field in the eyelet region, but no binding was observed[138].

In the case of antibiotics, it has been reported[23] that the activity of many well-known antibiotics like β-lactams and fluoroquinolones is highly influenced by their ability to overcome the OM[23,82], being their target the synthesis of the peptidoglycan, in the periplasmic space. Different experimental/computational studies have been performed in order to determine the main diffusion pathway for different classes of antibiotics.

Traditionally *E. coli* classic porins OmpF and OmpC have been taken as prototypes for enteric Gram-negative bacteria general diffusion channels. OmpF and OmpC are expressed under different growth media conditions[104],low media the former and rich media like the mammal intestine the latter . Even though, they have similar structure and high sequence similarity (77 %), these two channels have different filtering properties. OmpF has higher conductance than OmpC and a lower voltage threshold for channel closure. The diffusion of solutes has been experimentally proven to be very different[13,83,84,101,114,116] . Moreover OmpC has shown lower permeability to different classes of antibiotics than OmpF, and mutants lacking OmpF and expressing OmpC accordingly showed decreased antibiotic susceptibility[94,104]. This facts lead to the conclusion that the pore size was the primary determinant for drug permeability, but, still no evident strong correlation between the rates of permeation and antibiotics' physic-chemical properties has been found so far[22,38,56,83,84,86,94,101,120,135,163,175].

In order to investigate the limiting steps for permeation rates, in[29] using the number of H-Bonds (and salt bridges) between the antibiotic and the channel residues, and the antibiotic position along the axis of diffusion as metadynamics collective variables, the authors identified the breakage of H-bonds and salt bridges in the constriction region (CR) as rate-limiting step for translocation. They also showed the importance

of the charged residues outside the CR for the exit path of the drug, as it has been previously shown by means of experiments and simulation in[21,128] .

In the case of ampicillin it had been shown experimentally that it strongly interacts with the pore in the CR, and it was hypothesized to sit transversally in the CR with its dipole moment matching the oppositely charged residues of the eyelet[90,113]. By using metadynamics[38] the authors identify for the zwitterionic molecules ampicillin and amoxicillin a binding region near the CR, whereas for axlocillin and piperacillin they stated that they were to big to cross the CR. In the case of carbenicillin it was found that it makes favourable interactions in the extracellular vestibule. This work suggested the hypothesis that a set of high-affinity sites at the narrowest part of the OmpF channel enhances drug's ability to cross the membrane via the pore.

Further investigations[56,85] started to question the two-barriers-one-binding-site model for antibiotics in general diffusion channels. By using liposome swelling assays to complement electrophysiology experiments and simulations, the mentioned studies support the idea that for translocation a balance between the antibiotic confinement (entropic contribution) and the favourable specific interactions inside the channel (enthalpy compensation) are rather more limiting than the existence of a binding site. In addition, desolvation upon binding of both antibiotic and residues involved in binding were suggested to provide a favourable entropic increase, calculated using WaterMap for OmpC[163]. It was also shown, for enorfloxacin[100] that electrophysiology blockages, not always indicate translocation, as the molecule after binding and blocking the current might be reflected back, debilitating the binding hypothesis.

Using a Monte-Carlo scheme[30] the authors predicted that a concentrations comparable to in vivo ones, the only important parameter for flux is the barrier created by the size reduction of the channel pore, while at lower concentrations an affinity site located near the CR might increase the flux. At high concentrations the accumulation in the mouth of the channel leads to saturation.

Later, the OmpF channel was co-crystallize with different β-lactam antibiotics[175]. In this case all the binding sites were found to be outside the CR, and the mutation of the residues involved in binding decreased the translocation barrier in MD simulation, bolstering the idea there is no need of a binding-site for translocation through general channels.

4

METHODS

Contents

4.1 Molecular Dynamics **28**
4.1.1 Force Fields 32
4.2 Enhanced Molecular Dynamics **37**
4.2.1 Metadynamics 38
4.2.2 Variationally Approach to Enhanced Sampling 43
4.3 Docking **46**

The fundamental laws necessary for the mathematical treatment of a large part of physics and the whole of chemistry are thus completely known, and the difficulty lies only in the fact that application of these laws leads to equations that are too complex to be solved.

— Paul Dirac, P. A. M. Dirac, Proc. Royal Soc. of London, Series A 123, 714-733 (1929).

Theoretically, all details of molecular structures and interactions can be predicted from first principles using quantum mechanics. Unfortunately, many of the problems we are interested in cannot be tackled with quantum mechanical techniques due to its extremely high computational cost.

Computer simulations have become an ubiquitous tool for the study of many-body systems. The basic idea is that one can follow explicitly the trajectory of a system involving many degrees of freedom. If the system is constructed appropriately, meaning that it is physically meaningful and boundary conditions and interparticle interactions are considered, the trajectory can be used to simulate the behaviour of a real assembly of N-bodies, and the statistical analysis of the trajectory will determine meaningful predictions for properties of the system . There are two general classes of molecular simulations: Molecular dynamics (MD) method and Monte Carlo (MC) methods.

In MD, as it will be further discussed in section 4.1, one considers a classical dynamical model for atoms and molecules, and the trajectory is collected from the integration of the Newton equations of motion. This procedure provides dynamical information as well as equilibrium statistical properties. Monte Carlo methods is more generally applicable than MD and it can be used to study quantum systems and lattice

models as well as molecular assemblies. However, MC method doest not provide a straightforward method for obtaining time-dependent dynamical information.

In the interface between "Quantum mechanics" and "Molecular mechanics", hybrid multi-scale quantum mechanics/molecular mechanics (QM/MM) simulations have become a popular tool for investigating chemical reactions in condensed phases. In QM/MM methods, the region of the system in which the chemical process takes place is treated at an appropriate level of quantum chemistry theory, while the remainder is described by a molecular mechanics force field. Within this approach, chemical reactivity can be studied in large systems, such as enzymes.

The results shown in this thesis dissertation have been obtained using molecular dynamics and enhanced molecular dynamics techniques. Therefore this two techniques will be further discussed while MC methods and QM/MM methods are out of scope.

4.1 MOLECULAR DYNAMICS

As anticipated, molecular dynamics is a simulation technique that allows to compute equilibrium and transport properties of a classical many-body systems. It is an approximation in which, the nuclear motions of the N-particles of the system obey the classical mechanics laws[52,136]. After its early beginning in the late 1950's, MD has become a standard tool used in many branches of science, ranging from physics to biology, chemistry or material science. Thanks to the incredible improvements in computing science, MD is nowadays a precious tool to understand the mechanisms underlying complex processes, interpreting experimental results and making novel predictions

Starting from an initial configuration of the system one integrates the Newton equation of motion for each particle of the latter,

$$\vec{F} = m_i \ddot{\vec{r}}_i \tag{3}$$

$$m_i \frac{\partial^2 \vec{r}_i}{\partial t^2} = -\frac{\partial V(r)}{\partial r_i} \tag{4}$$

where m_i is the mass of the i-th particle and $\vec{r}_i$ its position $V(r)$ the atomic potential energy and $\vec{F}$ the resulting force, until the properties of the system do not change in time (equilibration). Once the system is equilibrated, it is possible to measure any observable that can be expressed in terms of the position and momenta of the N-particles that constitute the system, if the trajectory(chronological sequence of configurations of the system) is ergodic. Ergodicity means that the the Boltzmann distribution law is in agreement with the relatives frequen-

cies with which different configurations are visited and hence, time averages correspond to microcanonical ensemble averages.

$$\langle G \rangle = \lim_{T \to \infty} \langle G \rangle_T \tag{5}$$

The equations of motion can only be solved numerically, because of the nature of the interatomic interaction. Several numerical approaches are available for the integration of 3, ranging from the simplest leapfrog and Verlet algorithms to higher order methods like predictor-corrector[132].

As expressed in 4 to obtain the system time evolution we need to consider the atomic potential energy function that describes the interactions among particles. The potential energy function is the core of a molecular dynamics simulation and the accuracy of our potential function or "Force-Field" (further discussed in section 4.1.1) will determine our accuracy to predict many phenomena.

When we want to simulate complex systems like biological systems, the number of particles used to simulate bulk properties of a macroscopic system plays an essential role. The behaviour of finite systems is very different from that of infinite (massive) systems. In macroscopic systems, only a small negligible fraction of the atoms are located in the vicinity of the boundaries (walls of the container in which the system resides). Current simulations, especially of biological systems, involved hundreds of thousands of particles and in this case the fraction of atoms located in the surface is non negligible leading to strong surface effects or artefacts[3]. The most convenient solution to overcome both the problem of the "finite" size of the system and to minimize the surface effects is to use periodic boundary conditions. Using periodic boundary conditions implies that particles are enclosed in a box, which is replicated to infinity by rigid translation in all the three Cartesian directions, completely filling the space. The system interacts with it "images" in every dimension, so that when a particle enters or leaves the simulation region, an image particle leaves or enters this region, such that the number of particles from the simulation region is always conserved. One can easily see that the surface effects are thus virtually eliminated and the position of the box boundaries plays no role.

According to the Newton's equations of motion, energy is constant. The definition of periodic boundary conditions implies that the system has a volume, which is also constant. Hence a system under periodic boundary conditions is under constant volume and constant energy conditions, NVE ensemble. Nevertheless, in order to be able to compare our results with the experimental data, we need constant temperature and constant volume (NVT), which corresponds to Gibbs free energy, so

we have to allow the system to exchange energy with the surroundings through heat and pressure.

Unlike Monte Carlo simulations, which generate constant pressure and constant temperature ensembles by the application of temperature as parameter in the definition of the method and changes in the volume in the Monte Carlo trial moves[5]. Molecular dynamics requires non trivial changes in the equations of motion to generate proper constant-temperature/constant-pressure ensembles under the constraint of continuous dynamics. Several methods have been developed to allow for the continuous transfer of heat and pressure between the system and additional degrees of freedom[5,62,117,124]. These methods are rigorous from a theoretical perspective, they not only assure that the average temperature and pressure of the system remain constant, but also that the fluctuations in energy and volume are consistent with those in real system, reproducing Boltzmann statistics. In contrast, 'weak-coupling' or 'Berendsen' algorithm, which also reproduce constant average temperature and pressure with continuous dynamics, does not reproduce proper energy or volume fluctuations and therefore, does not correspond to the Gibbs thermodynamic ensemble.

Another problem related to the size of the system is the treatment of the long-range nonbonded interactions. The simplest solution in a periodic system is the minimum image condition, in which a particle interacts with the closest images of the other particles in the system[3]. However, this can become computationally very costly as the system size increases, because the number of pairwise interactions goes as N^2 where N is the number of particles. To lessen the computational burden, various truncation schemes have been developed in which, nonbonded interactions beyond a cutoff distance are ignored, and a smoothing function is typically applied to ensure continuity in the forces[152]. Such procedures can be a particularly severe approximation in the case of electrostatic interactions, whose energy goes as $\frac{1}{r_{ij}}$. As a result, not only do the sums of these interactions continue to make a substantial contribution to the total system energy beyond the typical cutoff length of approximately 10 Å, but pairwise forces are also non-negligible beyond the cutoff.

The introduction of Ewald sum[50] into biomolecular simulations under periodic boundary conditions has essentially solved the problem of long-range electrostatic truncation. The system is treated as being infinitely periodic, and interaction energies and forces beyond the cutoff length are calculated using the Ewald algorithm, which works in reciprocal space, instead of being calculated directly using Coulomb's law. Although the original Ewald formalism is computationally expensive, recent developments based on grid-based treatments of reciprocal

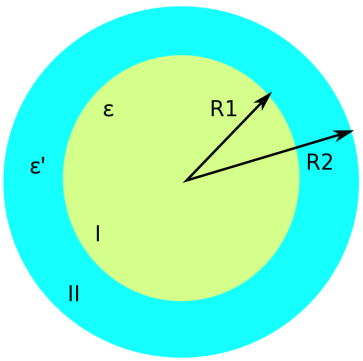

Figure 12: Spherical dielectric surrounded by a sphere.

space, including particle-mesh Ewald (PME) methods, allow for the rigorous treatment of long-range electrostatics in a computationally efficient manner[49,61,131,139,172,173].

PME are standard in biological simulations, nevertheless when dealing with electrostatic properties of the system, much attention has to be paid to the chosen boundary condition for the Ewald summation method. The Ewald potential is a solution of the Poisson equation under (toroidal) periodic boundary conditions; however it gives also rise to an implicit contribution analogous to a reaction field. This term is directly related to the dielectric boundary conditions employed in the simulation.

Our system is made of charges and dipoles, and the potential energy of such an infinite periodic system will depend on the the nature of the boundary conditions at infinity. The fluctuating dipole moment of the unit cell $\mathbf{D}$ creates a charge surface at the boundary of the sphere I in 12, generating an homogeneous depolarizing field:

$$\mathbf{E} = -\frac{4\pi\mathbf{P}}{2\epsilon' + 1} \tag{6}$$

where $\mathbf{P} = \mathbf{D}/V$ is the polarization density of the unit cell. If we consider the reversible work per unit volume that must be performed against the depolarizing field to create a net polarization $\mathbf{P}$

$$dW = -\mathbf{E}d\mathbf{P} = \frac{4\pi}{2\epsilon' + 1}\mathbf{P}d\mathbf{P} \tag{7}$$

so that the total work to polarize the system I with volume V,

$$U_{Pol} = \frac{2\pi}{2\epsilon' + 1} P^2 V = \frac{2\pi}{2\epsilon' + 1} \frac{D^2}{V} = \frac{2\pi}{(2\epsilon' + 1)V} \Big| \sum_{i=1}^{N} r_i q_i \Big|^2 \quad (8)$$

Standard implementation of PME in MD use "tin-foil" boundary conditions: the Ewald sphere is immersed in a perfectly conducting medium and hence the dipole term on the surface of the Ewald sphere is zero[42], meaning that the dielectric constant, $\epsilon' \to \infty$, conducting boundary or tin-foil boundary. Tin-foil boundary conditions are essential for ionic systems and advantageous for polar systems.

4.1.1 *Force Fields*

Classical molecular dynamics (MD) simulations are founded on the idea of using a differentiable function of the atomic coordinates to represent the energy of the system. The fundamental assumption underlying all molecular mechanics or force fields methods is the Born-Oppenheimer approximation, which allows the separation of nuclear and electronic motions (which happen in very different time scales) and therefore one can write the energy of a system as a function of the nuclear coordinates only.

Force fields also have to fulfil the assumptions of additivity and transferability, meaning that the potential energy of any system can be written as a sum of different terms with a simple physical interpretation as bond deformations, electrostatics, dispersion forces, etc ... In the case of transferability, any potential energy function written for a small set of molecules can be applied to a much wider range of molecules with similar chemical groups. The correctness of a force field depends on the validity of these assumptions

Most classical force fields rely on five terms with a simple physical interpretation: there are potential energy terms associated with deformation of bond and angle geometry (stretching/compression of bonds, bending of angles), terms associated with the rotation about certain dihedral angles (torsions), and the so-called nonbonded terms, describing the electrostatic interactions and terms describing the dispersion interactions and repulsion when atoms overlap (van der Waals forces). More complex force fields include additional terms accounting for atomic polarizability and more complex coupling terms such as cross coupling between bonds and angle.

A force field consists of the equations chosen to model the potential energy and their associated parameters. It is important to keep in mind that molecular mechanics force fields are empirical: the separation of the potential energy in terms with a simple physical interpretation is

not strictly correct, as there is no unique way to "translate" quantum mechanical effects into classical mechanics equations. As a consequence, there is no unique solution for the optimal set of functions and parameters. In other words, a force field is supposed to reproduce a certain potential energy surface (PES) derived from quantum mechanics, but different force fields might reproduce the same PES by summing up contributions that are different. For this reason, it is in general not correct to mix energy functions and parameters from different force fields to represent a certain molecule.

As above mentioned current potential models are based on three different components: non-bonded interactions, bonded interactions and restraints. The non-bonded interactions term encloses all the interactions between atoms that are not directly linked via chemical bonds, as it is schemetized in Fig.13, therefore repulsion, dispersion and electrostatics. Lennard-Jones functions Eq.9 Buckingham term, describe repulsion and dispersion. The Buckingham term is more realistic for repulsion but it is computationally more expensive. The Lennard-Jones potential between the atoms i and j, at distance r_{ij} :

$$V_{LJ} = 4\epsilon_{ij}\left[(\frac{\sigma_{ij}}{r_{ij}})^{12} - (\frac{\sigma_{ij}}{r_{ij}})^{6}\right] \tag{9}$$

where ϵ_{ij} and σ_{ij} its an empirical parameter that depends on the pair of atoms considered. In all the currently used Force-Fields the atoms

Figure 13: Cartoon of atoms involved in non-bonded interactions: lennard jones and electrostatics

electrostatic distributions are represented by point charges fixed on the nuclei. Thus the electrostatic interactions between a pair of charges can be treated using the Coulomb's law:

$$V_{Coulomb} = \frac{1}{4\pi\epsilon_0}\frac{q_i q_j}{\epsilon_r r_{ij}} \tag{10}$$

where ϵ_0 is the vacuum dielectric permittivity, q_i and q_j are respectively the charge of the i-th and j-the atoms, ϵ_r their dielectric constant and r_{ij} the distance between the two atoms.

In the case of bonded interactions Fig.14, such as covalent-bond stretching, angle-bending and improper and proper dihedral angles, are commonly modelled with harmonic potential functions

$$V_{Bond} = \frac{1}{2} k_{ij} (r_{ij} - r_{ij}^0)^2 \tag{11}$$

$$V_{angle} = \frac{1}{2} k_{ijk}^{\theta} (\theta_{ijk} - \theta_{ijk}^0)^2 \tag{12}$$

where r_{ij}^0 is the equilibrium distance, θ_{ijk}^0 is he equilibrium angle, and k_{ij} and k_{ijk} are the harmonic constants.

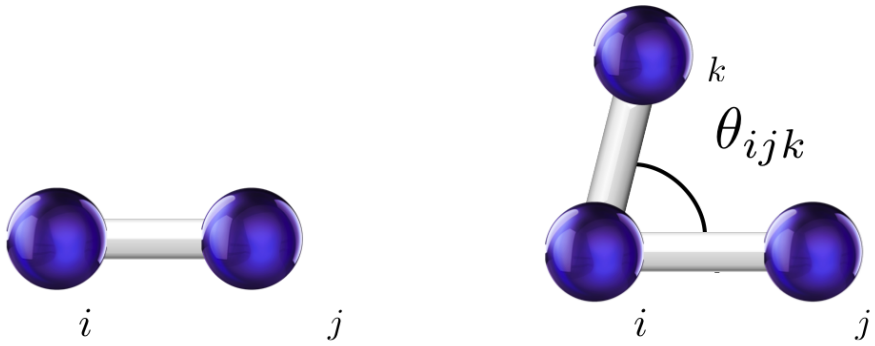

Figure 14: Cartoon of atoms involved in bonded interactions

It is a common practice to use the improper dihedral angle term to keep some groups with specific geometries (e.g. planar). Also this interaction can be described by an harmonic potential between four atoms (i,j,k and l) as reported in Eq.13 and illustrated in Fig.15

$$V_{improper} = \frac{1}{2} k_{\xi} (\xi_{ijkl} - \xi_{ijkl}^0)^2 \tag{13}$$

where k_{ξ} is the harmonic constant and ξ_{ijkl}^0 is the equilibrium improper angle.

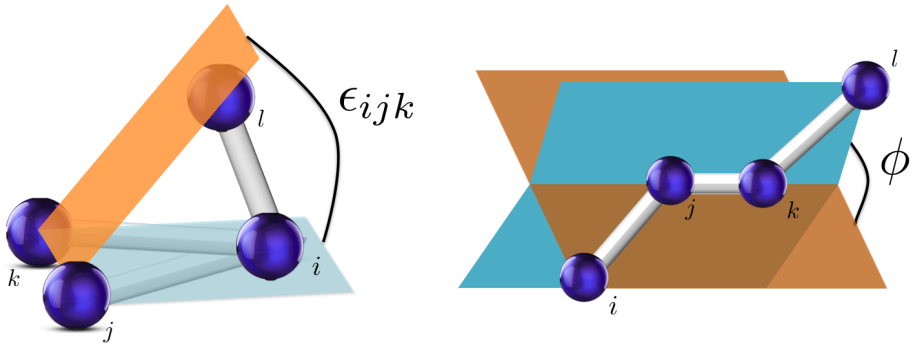

Figure 15: Cartoon of atoms involved in bonded interactions

The proper dihedral angles interactions are instead used to describe the rotation of four atoms around a specific bond. Each force field use in general different function for this term, depending whether they include or not a special Lennard-Jones and Coulomb interaction between the first and the fourth atom involved in the dihedral angle definition, the so called 1-4 interaction. The most employed expression is based on a cosine function:

$$V_{dihedral} = \frac{k_\phi}{2}(1 + cos(n\phi - \phi^0)) \tag{14}$$

in which k_ϕ is the force constant, ϕ^0 is the equilibrium angle and n is the multiplicity. For convention ϕ is the angle between the ijk and jkl plane as shown in Fig.15.

The last contribution to the potential energy is the restraint term. In some simulations peculiar potentials are used to impose restraints on the time evolution of the system.

Therefore, the most frequently used expression for the potential energy of molecular systems, like simple organic molecules and biological macromolecules is the following:

$$\begin{aligned} V(r) = & \sum_{Bonds} \frac{k_{ij}}{2}(r_{ij} - r_{ij}^0)^2 + \sum_{Angles} \frac{k_{ijk}^\theta}{2}(\theta_{ijk} - \theta_{ijk}^0)^2 + \\ & \sum_{Dihedrals} \frac{k_\phi}{2}(1 + cos(n\phi - \phi^0)) + \sum_{Impropers} \frac{k_\xi}{2}(\xi_{ijkl} - \xi_{ijkl}^0)^2 \\ & + \sum_{\substack{Non-bonded \\ pairs(i,j)}} 4\epsilon_{ij}\left[(\frac{\sigma_{ij}}{r_{ij}})^{12} - (\frac{\sigma_{ij}}{r_{ij}})^6\right] + \sum_{\substack{Non-bonded \\ pairs(i,j)}} \frac{1}{4\pi\epsilon_0}\frac{q_i q_j}{\epsilon_r r_{ij}} \end{aligned} \tag{15}$$

The most popular force-fields for molecular dynamics simulations of proteins are AMBER[35], GROMOS[32,148,168],CHARMM[99] and OPLS-AA[55,76]. All share the energy terms described in Eq.15.

It is worthy to note that nonbonded interactions involve only pairs of atoms. Early simulations of noble gases[3] and liquid water[105,121] proof that in reality multi-body terms involving three or more atoms simultaneously contribute to the total energy in multiparticle systems, whereas the non-bonded contribution in Eq.15 is limited to the a sum over pairs of atoms for computational tractability. Hence, current biomolecular force fields use *effective* pairwise-nonbonded potentials, also known as additive or non-polarizable models, in which the parameters involved in the non-bonded interactions are developed with the constraint of accurately modelling condensed-phase properties. Moreover, one should note that there is not explicit term for hydrogen bonding. In all most

common force fields, biologically important hydrogen bonds are handled by the combination of the LJ and the Coulomb terms. Amber, CHARMM, GROMOS and OPLS-AA only include interaction sites for bonded and nonbonded interactions at the location of the atomic nuclei. This model is generally very good with respect to being able to reproduce hydrogen bond energies and geometries, although it can lead to deviations from QM results with respect to the angular dependence of hydrogen bonding energy[110].

One of the primary differences among the most popular force fields for biological systems exist in the bonded portion of the force fields. The first is the variable use of 'improper' dihedrals. In Amber and OPLS-AA , improper dihedral angles contribute to the total energy via the dihedral term Eq.14, and are applied to planar groups with periodicity n=2. CHARMM and GROMOS add a separate term for improper dihedral energy that has a quadratic dependence on the value of the improper dihedral Eq.13. There are also difference in the selection of the rules for calculating the Lennard-Jones parameters between pairs of atomtypes. Atoms with the same atomic number are assigned different atom types for parametrization purpose, depending on the chemical context. OPLS-AA and GROMOS use geometric combining rules for both ϵ_{ij} and σ_{ij}; $\epsilon_{ij} = (\epsilon_i \epsilon_j)^{1/2}$ and $\sigma_{ij} = (\sigma_i \sigma_j)^{1/2}$. CHARMM and Amber also use the geometric mean for calculating ϵ_{ij} but an arithmetic mean, $\sigma_{ij} = \frac{1}{2}(\sigma_i + \sigma_j)$, for σ_{ij}.

There are also differences among the four force fields in the scaling constants to the LJ and Coulomb interactions between the atom pairs involved in 1,4-nonbonded interactions. The special treatment of 1,4-nonbonded interactions was needed for an accurate reproduction of the dihedral rotation energetics, due to the fact that the pairwise-additive nature of the nonbonded interactions prevents the lowering of the rotational barriers caused by electronic polarization.

The optimization of force fields parameters involves adjusting parameter values until the force field is able to reproduce a set of experimental spectroscopic, thermodynamic, and crystallographic data as well as data computed using QM methods. The Amber, CHARMM, GROMOS and OPLS-AA force fields for proteins target a different subset of experimental and QM data, although there is substantial overlap. The Coulomb partial atomic charges in the case of OPLS-AA are empirically adjusted along with LJ parameters during the fitting of the experimental heat of vaporization and densities. In contrast, Amber uses computed QM electrostatic potential surfaces as the target data for partial charge determination. Thus, Amber partial charges aim to reproduce molecules' gas-phase electrostatic potentials. In CHARMM, the QM computed dimerization energies and minimum-energy inter-

action distance for small molecule-water dimers are used, aiming to balance water-protein, water-water and protein-protein interaction energies in the condensed phase. Finally GROMOS and OPLS-AA target thermodynamic data in the refinement of partial atomic charges to properly capture the partitioning of protein moieties between aqueous and non-aqueous environments.

4.2 ENHANCED MOLECULAR DYNAMICS

As mentioned in the MD section 4.1, once the system is equilibrated, in order to measure any physical observable, our system must be ergodic in the time-scale of simulation or in other words, we should have run long enough so that the system have had time to visit all the energetically relevant conformations. Taking into account that the time step for integration is of the order of femtoseconds, in order to resolve the fastest motions of the system, ergodicity for many cases is an incredibly computational chimera, specially for biological process. The energy landscapes of most of systems under study are very corrugated, with many metastable states separated in most of cases with really high energy barriers. Overcome and sample such a landscape with plain MD is computationally unaffordable in most cases due to the fact that in many cases thermal fluctuations are not enough to overcome such energetic barriers and that many systems diffuse really slowly in the phase space. Moreover, even if we were able to do it, probably the phenomena under study is a rare event, meaning it happens not very often and we will not be able to gather enough statistics.

As above mentioned, the knowledge of the free energy surface (FES) of the system allows the calculation of the ensemble average of the system observables. For a canonical ensemble (NVT), the probability distribution fuction of such ensemble is given by the Boltzmann's distribution:

$$P(\mathbf{R}) = \frac{e^{-\beta U(\mathbf{R})}}{Z} \tag{16}$$

where $U(\mathbf{R})$ is the energy of the state that depends on the system configuration R, β is equivalent to $1/k_B T$ where k_B is the Boltzmann constant. Z is the partition function, that can be written as:

$$Z = \int d\mathbf{R} e^{-\beta U(\mathbf{R})} \tag{17}$$

We can estimate the Helmotz Free-Energy ($\tilde{F}$) by evaluating the histogram of the visited configurations $N(s)$, along any generic coordinate of the system, as:

$$\tilde{F}(s) = -\frac{1}{\beta} log(N(s)) + c \tag{18}$$

where c is a constant.

Unfortunately the free-energy estimation provided by this method is greatly affected by the simulation length. A long MD trajectory is needed in order to visit all the relevant system conformations and in the case of rare-events, where these configurations are separated by high free-energy barriers, greater than k_BT, it becomes computationally unaffordable with common computer architectures[72,151]. Ergodicity makes MD expensive in terms of computational time, but in any case affordable when compare to *ab initio*. In order to overcome the time-scale problem, a series of enhanced sampling techniques have been developed to tackle this issue[65,161,166].

Most of the results in this thesis were performed using as enhanced technique, Metadynamics[87], for this reason this method will be discussed deeper in the next section.

4.2.1 *Metadynamics*

"Let every valley be lifted up, And every mountain and hill be made low; And let the rough ground become a plain, And the rugged terrain a broad valley

— Isaiah 40:4, Extracted from Prof. Michele Parrinello conference lecture at EuroQsar2016, Verona Italy

Metadynamics belongs to a class of methods in which sampling is facilitated by the introduction of an additional bias potential (or force) that acts on a selected number of degrees of freedom, often referred as collective variables (CVs). A number of methods can be thought as belonging to this class such as umbrella sampling, local elevation, conformational flooding, adaptative force bias, steered MD, and self-healing umbrella sampling.

Metadynamics is both able to enhance the sampling and reconstruct the underlying free energy surface (FES) as a function of the chosen CVs. An external history-dependent bias potential which is a function of the CVs is added to the Hamiltonian of the system. This potential can be written as a sum of Gaussians deposited along the system trajectory in the CVs space to discourage the system from revisiting previously sampled configurations[87].

The reduction of the number of degrees of freedom affects the complexity of the FES, making it smoother and with less local minima, and to some extent it helps the interpretation of the results.

If S is set of d functions of the microscopic coordinates R of the system:

$$S(R) = (S_1(R), ..., S_d(R)) \tag{19}$$

At time t, the metadynamics bias potential can be written as

$$V_G(S,t) = \int_0^t dt' \omega \, exp(-\sum_{i=1}^{d} \frac{(S_i(R) - S_i(R(t')))^2}{2\sigma_i^2}) \tag{20}$$

where ω is the energy rate and σ_i is the width of the Gaussian for the *ith* CV. The energy rate is constant and usually expressed in terms of a Gaussian height W and a deposition stride τ_G:

$$\omega = \frac{W}{\tau_G} \tag{21}$$

To understand the effect of the bias potential, V_G, one can consider a simple one-dimensional potential with three local minima A, B, C present as depicted in 16. The system is prepared in the local minimum A. In standard MD the system will be stuck in this minimum because barriers are larger than thermal fluctuations. On the contrary, with a metadynamics simulation, as time goes by, Gaussians are deposited causing the underlying bias potential to grow, until the system is pushed out the basin A into a new local minimum, naturally falling in the left basin (due to the form of the selected potential).

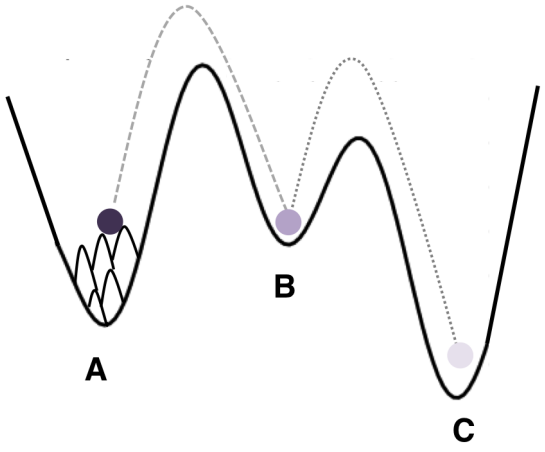

Figure 16: Metadynamics scheme

Then the system will be trapped in B till the underlying potential allows the system to diffuse to the third basin. Eventually when the last basin is also compensated the system evolution resembles a random walk on the flattened FES.

Metadynamics accelerates the sampling of rare events by pushing the system away from local free-energy minima. It allows exploring new reaction pathways as the system tend to escape from local minima passing through the lowest free-energy saddle point. Metadynamics

inherently explores the low free-energy regions first. Finally, the bias potential provides an unbiased estimate of the underlying free energy

$$V_G(S, t \longrightarrow \infty) = -F(S) + C, \tag{22}$$

where C is an additive constant and the free energy $F(S)$ is defined as

$$F(S) = -\frac{1}{\beta} ln(\int dR\, \delta(S - S(R)) e^{-\beta U(R)}) \tag{23}$$

where $\beta = (k_B T)^{-1}$,k_B is the Boltzmann constant, T the temperature of the system, and $U(R)$ the potential energy function.

Metadynamics simulations are intrinsically parallelizable. Indeed multiple interacting metadynamics simulations can be performed for exploring and reconstructing the same FES. Each simulation contributes to the overall history-dependent potential. This implementation, called multiple-walkers metadynamics[134], leads to a fully linear scaling algorithm that does not need fast and expensive connections between CPUs.

In this formulation of metadynamics, in a single run, V_G does not converge modulo a constant to the free energy, but oscillates around it, eventually overfilling the underlying FES.

Well-tempered metadynamics[10] was formulated to solve this problem by decreasing the deposition rate over simulation time. In practice the Gaussian rate ω_0 is decreased along simulation by rescaling the Gaussian height as follows:

$$W = \omega \tau_G e^{-\frac{V_G(S,t)}{k_B \Delta T}} \tag{24}$$

where ΔT is an input parameter with the dimension of a temperature, that is controlled via the bias factor $\gamma = \frac{T+\Delta T}{T}$. The bias potential for Well-Tempered Metadynamics then reads:

$$V(s,t) = \int dt' \omega e^{V(s(\mathbf{R}(t'),t')/\Delta T} exp\left(-\sum_{i=1}^{d} (\frac{s_i(\mathbf{R}) - s_i(\mathbf{R}(t'))^2}{2\sigma_i^2}\right) \tag{25}$$

The bias potential does not fully compensate the FES, but it converges to

$$V_G(S, t \longrightarrow \infty) = -\frac{\Delta T}{T + \Delta T} F(S) + C \tag{26}$$

where C is an immaterial constant. And the FES can be estimated as:

$$\tilde{F}(s,t) = -\gamma V(s,t) \tag{27}$$

Therefore, for $\Delta T \longrightarrow 0$, ordinary MD is recovered, whereas $\Delta T \longrightarrow \infty$) limit corresponds to standard metadynamics. In between one can

regulate the extent of FES exploration by tuning ΔT. This avoids overfilling and might save computational time when a large number of CV's are used[10,37].

The introduction of a history-dependent potential alters the probability distribution. Although the probability distribution for the bias CV's can be easily reconstructed, the probability distribution for the non-bias degrees of freedom is distorted in a non trivial way. Different techniques have been proposed to reweight a metadynamics run and recover the unbiased distribution from variables other than the CV's[18,54,103,159] assuming an adiabatic evolution for the bias potential. Using a two step algorithm one can compute on the fly expectation values of any variable. Therefore, one does not need to use CV's directly related to measurable quantities to make quantitatively contact with experiments[9].

One of the key points of most of the current enhanced sampling methods is the employment of a bias potential along a a system of collective variables, CVs. The number of CV's must be small enough so that we will be able to obtain a converged FES of the system. A big number of biased descriptors will lead to a highly dimensional space, so that the FES is less easily comprehensible and of course increasing the computational cost to arrive to convergence. The selection of the collective variables is crucial. The selected CV's must take into account the slowest degrees of freedom and must distinguish the initial and final state, but also the relevant intermediate configurations of the system . When we project the potential energy function on a FES we operate a dimensional reduction. Then if the CV's does not discriminate between the relevant configurations of the processes this transformation it is not appropriate[44]. If one neglects a slow degree of freedom, the system will remain trapped in the basin and the barrier to pass to the next basin will be overestimated. The real barrier is hidden in the non-considered slow variable. The overall result is a situation in which the free energy grows evenly and the diffusion between the two basins is never reached.

A large variety of CVs have been used and their choice usually depends on the nature of the specific process under study. Frequently used CVs in literature are: interatomic distances, angles,dihedrals, coordination numbers, radius of gyration, dipole moment, number of hydrogen bonds, and Steihardt parameters, etc.

A very general choice is to use the potential energy of the system as metadynamics CV[46,107,108]. It has been shown[19] that using the potential energy as CV within well-tempered metadynamics results in the sampling of a well-defined distribution called well-tempered-ensemble (WTE). In this ensemble, the average energy is very close to its canon-

ical value but the fluctuations are enhanced in a tunable way, thus improving the sampling.

In many cases to find a small set of CVs is a cumbersome process. Processes like protein folding take place in a large and complex conformational space and often involves many alternatives pathways. In order to study such processes, it is instrumental to enhanced sampling along a great number of degrees of freedom besides those than can be targeted by metadynamics. A successful strategy is to combine metadynamics with a replica exchange method (REM) such as the popular parallel tempering algorithm (PT)[58,154].

In PT, multiple copies of the same system at different temperatures are independently simulated. At fixed intervals, an exchange of configurations between two adjacent replicas is attempted while respecting detailed balance. By exchanging with higher temperatures, colder replicas are prevented from being trapped in local minima.

If one considers M independent replicas of the system at different temperatures $T_1, T_2, T_3, ..., T_M$. In order to satisfy detailed balance, we use the following acceptance probability for the exchange between configuration R_j at temperature T_j and configuration R_k at temperature T_k:

$$p(j \to k) = min1, e^{\Delta_{jk}} \tag{28}$$

where

$$\Delta_{jk} = (\beta_j - \beta_k)(U(R_j) - U(R_k)) \tag{29}$$

When combining PT with metadynamics[25], each replica performs at a different temperature a metadynamics that uses the same set of CVs. Thus indicating with $V_G^{(i)}$ the bias potential acting on the ith replica, the acceptance probability is determined by

$$\Delta_{jk} = (\beta_j - \beta_k)(U(R_j) - U(R_k)) + \beta_j[V_G^{(j)}(S(R_j), t) - V_G^{(j)}(S(R_k), t) + \beta_k[V_G^{(k)}(S(R_k), t) - V_G^{(k)}(S(R_j), t) \tag{30}$$

The combination of PT and metadynamics (PT-MetaD) is particularly effective because it compensates for some of the weaknesses of each method individually taken. PT allows the system to overcome moderately high free-energy barriers on all degrees of freedom, so that in PT-MetaD, the effect of neglecting a slow degree of freedom in the choice of the CVs is less harmful that in metadynamics. Because the metadynamics bias potential allows overcoming higher barriers on selected CVs, PTMetaD enhances significantly the sampling efficiency of PT.

One limitation of PTMetD approach is the poor scaling with system size. In fact, a sufficient overlap between the potential energy distributions of neighbouring replicas is required in order to obtain a significant

diffusion in temperature space. Thus, as in standard PT, the number of replicas needed to cover the same temperature range scales as the square root of the number of degrees of freedom, making this approach prohibitive expensive for large systems.

Different solutions have been proposed to overcome this latter difficulty. One has to combine metadynamics with other type of REM, leading to a combination of solute tempering and metadynamics[27]. In solute tempering[93] the parts of the Hamiltonian that describe the solute-solvent and solvent-solvent interactions are rescaled across the replicas in such a way that the number of replicas need scales as the square root of the number of solute degrees of freedom.

The combination of PT with WTE (PT-WTE) has been proven to be particularly effective[19]. In PT-WTE, the energy fluctuations can be enhanced in order to always guarantee an effective overlap of the energy distributions between neighbouring replicas. Moreover, the quantity Δ_{jk} that in standard PT governs the swapping probability 28 is reduced by a tunable parameter. These two properties lead to an effective diffusion in temperature space, regardless of the number of degrees of freedom of the system.

An alternative approach is bias exchange[130], wherein a replica exchange scheme is implemented among multiple metadynamics simulations that bias different set of CVs. In this case, swap exchange probabilities are derived assuming instantaneous equilibrium from each metadynamics simulation.

4.2.2 *Variationally Approach to Enhanced Sampling*

One of the last developments in enhanced sampling techniques and free energy calculations is the 'Variational Approach to Enhanced Sampling and Free Energy calculation' introduce in[164]. It is based on the introduction of the bias potential which is a function of a small set of collective variables as metadynamics. But in this case, the main idea is to construct a functional of the bias potential and apply a variational principle, so that the bias minimizing the functional relates in a simple way to the free energy surface.

Considering a N-particle system described by its microscopic coordinates $\mathbf{R} \in \mathbb{R}^{3N}$ whose dynamics at temperature T is governed by the potential energy function $U(\mathbf{R})$ that leads to the canonical probability distribution $P(\mathbf{R}) = e^{\beta U(\mathbf{R})}/Z$ where $\beta = (k_B T)^{-1}$ and $Z = \int d\mathbf{R} e^{-\beta U(\mathbf{R})}$ is the partition function of the system. A dimension reduction of $\mathbf{R}$ is then performed by introducing a set of collective variables $s(\mathbf{R}) = (s_1(\mathbf{R}), s_2(\mathbf{R}), ..., s_p(\mathbf{R}))$ as it was described for metady-

namics in the previous section 4.2.1. The free energy surface associated to the collective variable set $\mathbf{s}$ is defined up to a constant as

$$F(\mathbf{s}) = -(1/\beta) log \int d\mathbf{R} \delta(\mathbf{s} - \mathbf{s}(\mathbf{R})) e^{-\beta U(\mathbf{R})} \tag{31}$$

By introducing the following functional of the bias potential $V(\mathbf{s})$:

$$\Omega[V] = \frac{1}{\beta} log \frac{\int d\mathbf{s} e^{-\beta[F(\mathbf{s})+V(\mathbf{s})]}}{\int d\mathbf{s} e^{-\beta F(\mathbf{s})}} + \int d\mathbf{s} p(\mathbf{s}) V(\mathbf{s}) \tag{32}$$

where $p(\mathbf{s})$ is a normalized arbitrary probability distribution, hence, the second term can be interpreted as the expectation value of $V(\mathbf{s})$ over the distribution $p(\mathbf{s})$. The potential that renders $\Omega[V]$ stationary, but a constant

$$V(\mathbf{s}) = -F(\mathbf{s}) - \frac{1}{\beta} log p(\mathbf{s}) \tag{33}$$

for $p(\mathbf{s}) \neq 0$. This stationary point is also the global minima as the functional is convex. The $\mathbf{s}$ values sampled will be only the ones with $p(\mathbf{s}) \neq 0$, and hence, $p(\mathbf{s})$ is their resulting distribution. This mean that one has the possibility to choose the region in the CV space that wants to explore by appropriately choosing $p(\mathbf{s})$ giving a high degree of flexibility to the method.

Assuming the CV set defines a compact space of volume Ω_s, a natural choice for $p(\mathbf{s})$ might be $p(\mathbf{s}) = 1/\Omega_s$, this choice would lead to an uniform sampling of the CV space as traditionally done in other enhanced sampling algorithms, like standard metadynamics. This $p(\mathbf{s})$ leads to $V(s) = -F(s)$ modulo a constant. Another possibility is to choose

$$p(\mathbf{s}) = \frac{e^{\beta' F(\mathbf{s})}}{(\int d\mathbf{s} e^{-\beta' F(\mathbf{s})})} \tag{34}$$

where $\beta' = [k_B(T + \Delta T)]^{-1}$ and $F(\mathbf{s})$ is the targeted free energy surface at inverse temperature β. This is the distribution sampled in well-tempered metadynamics, being the bias factor $\gamma = \beta/\beta'$ as described in section 4.2.1 and $V(\mathbf{s}) = -[1 - (1/\gamma)]F(\mathbf{s})$.

Lets write the bias potential as a function of a set of variational parameters $\boldsymbol{\alpha} = (\alpha_1, \alpha_2, ..., \alpha_d)$, so that, $V(\mathbf{s}; \boldsymbol{\alpha})$, then applying the variational principle we will minimize the function $\Omega(\boldsymbol{\alpha}) = \Omega[V(\boldsymbol{\alpha})]$ with respect to $\boldsymbol{\alpha}$, the converged $V(\mathbf{s}; \boldsymbol{\alpha})$ leads to $F(\mathbf{s})$ as described in Eq.33. Otherwise the free energy surface can be obtained from the standard umbrella sampling relation

$$P(\mathbf{R}) \propto e^{\beta V(s(\mathbf{R}))} P_V(\mathbf{R}) \tag{35}$$

where $P_V(\mathbf{R})$ is the distribution biased by $V(\mathbf{s}(\mathbf{R}))$. It is also important that one can reweight then non-biased degrees of freedom after

convergence or even on the fly if the bias potential converges quickly to a quasistationary state during the optimization process.

In the optimization procedure the gradient $\Omega'(\boldsymbol{\alpha})$ and Hessian $\Omega''(\boldsymbol{\alpha})$ must be calculated,

$$\frac{\partial\Omega(\boldsymbol{\alpha})}{\partial\alpha_i} = -\Big\langle\frac{\partial V(\mathbf{s};\boldsymbol{\alpha})}{\partial\alpha_i}\Big\rangle_{V(\boldsymbol{\alpha}))} + \Big\langle\frac{\partial V(\mathbf{s};\boldsymbol{\alpha})}{\partial\alpha_i}\Big\rangle_p \tag{36}$$

$$\frac{\partial^2\Omega(\boldsymbol{\alpha})}{\partial\alpha_j\partial\alpha_i} = \beta Cov\Big[\frac{\partial V(\mathbf{s};\boldsymbol{\alpha})}{\partial\alpha_j}, \frac{\partial V(\mathbf{s};\boldsymbol{\alpha})}{\partial\alpha_i}\Big]_{V(\boldsymbol{\alpha})} - \Big\langle\frac{\partial^2 V(\mathbf{s}}{\partial\alpha_j\partial\alpha_i}\Big\rangle_{V(\mathbf{s};\boldsymbol{\alpha})} + \Big\langle\frac{\partial^2 V(\mathbf{s};\boldsymbol{\alpha})}{\partial\alpha_j\partial\alpha_i}\Big\rangle_p \tag{37}$$

where $\langle ...\rangle_{V(\boldsymbol{\alpha})}$ and $Cov[...]_{V(\boldsymbol{\alpha})}$ are the expectation value and the covariance, respectively, obtained in a biased simulation employing the potential $V(\mathbf{s};\boldsymbol{\alpha})$ and $\langle ...\rangle_p$ is the expectation value in the distribution $p(\mathbf{s})$. A straightforward approach is to expand $V(\mathbf{s};\boldsymbol{\alpha})$ in a linear basis set and use the coefficients of the expansion as variational parameters,

$$V(\mathbf{s};\boldsymbol{\alpha}) = \sum_{\mathbf{k}} \alpha_{\mathbf{k}} G_{\mathbf{k}}(\mathbf{s}) \tag{38}$$

In this case the free energy surface will be a smooth function of the collective variables and a few expansion terms will be normally enough. In contrast, when using metadynamics, a large number of Gaussians are needed to represent $V(\mathbf{s})$. By expanding the potential, the gradient and Hessian simplify,

$$\frac{\partial\Omega(\boldsymbol{\alpha})}{\partial\alpha_i} = -\langle G_{\mathbf{i}}(\mathbf{s})\rangle_{V(\boldsymbol{\alpha})} + \langle G_{\mathbf{i}}(\mathbf{s})\rangle_p \tag{39}$$

$$\frac{\partial^2\Omega(\boldsymbol{\alpha})}{\partial\alpha_j\partial\alpha_i} = \beta Cov[G_{\mathbf{j}}(\mathbf{s}), G_{\mathbf{i}}(\mathbf{s})]_{V(\boldsymbol{\alpha})} \tag{40}$$

For the constant term $\alpha_{\mathbf{0}}$ the gradient and the Hessian are zero for any $p(\mathbf{s})$, so it can be drop it from the linear expansion. The gradient and the Hessian are computed statically, and depending on the chosen optimization algorithm it would require long sampling time. The current version of the Variational Enhanced Sampling method uses a recent stochastic gradient descendent-based algorithm[7]. In this algorithm at iteration n both the instantaneous iterate $\boldsymbol{\alpha}^{(n)}$ and the average iterates $\bar{\boldsymbol{\alpha}}^{(n)} = (n+1)^{-1}\sum_{k=0}^{n}\boldsymbol{\alpha}^{(k)}$. The instantaneous iterate is then updated using,

$$\boldsymbol{\alpha}^{(n+1)} = \boldsymbol{\alpha}^{(n)} - \mu[\Omega'(\bar{\boldsymbol{\alpha}}^{(n)}) + \Omega''(\bar{\boldsymbol{\alpha}}^{(n)})[\boldsymbol{\alpha}^{(n)} - \bar{\boldsymbol{\alpha}}^{(n)}]] \tag{41}$$

where μ is the step size and the gradient and Hessian are always obtained from the averaged iterates $\bar{\boldsymbol{\alpha}}^{(n)}$, which amounts to taking a first-order Taylor expansion of the gradient $\Omega'(\boldsymbol{\alpha}^{(n)})$ around $\bar{\boldsymbol{\alpha}}^{(n)}$. As it can

be seen in Figure ? for the case of tri-alanine, the instantaneous iterates $\boldsymbol{\alpha}^{(n)}$ fluctuate considerably while their averages $\bar{\boldsymbol{\alpha}}^{(n)}$ vary smoothly, leading to a good behaving biasing potential $V(\mathbf{s}; \bar{\boldsymbol{\alpha}}^{(n)})$ and converges smoothly to the $F(\mathbf{s})$ estimation.

4.3 DOCKING

Molecular docking is a largely used molecular modelling method to predict the preferred conformation between to molecules to form a bound complex and the binding affinity of such a complex by using scoring functions. Although, this computational technique is not the main technique used in research project discussed in this thesis dissertation, it will be used to discussed the binding of some small molecules, and hence, we will only discussed here the docking techniques for small molecules (ligand) interactions with larger molecules (receptor), in this case porins.

This technique is particularly relevant in medicinal chemistry, in computer-aided-drug discovery in order to virtually screen chemical libraries of compounds for the identification of hits and lead optimization[74,150]. The original problem in molecular docking id the 'lock-key' problem: find the optimal conformation of the 'key' (in our case, small molecule) to perfectly fit and "open-up" the 'lock' (in our case, the protein or porin). So, molecular docking can be defined as an optimization problem, which will predict the relative conformation for optimizing the 'key-lock' interaction, in other words it searches to minimize the complex free energy.

The original 'key-lock' concept evolve to 'induced-fit', in which one or both components are considered flexible and changes it conformation in order to minimize the free energy of the complex. Many different software are available that take into account flexibility[31] of both components (full-flexible docking), but it is not very common due to its high computational cost. Semi-flexible docking is more popular, in this case the protein is fixed and only some flexibility is allowed in the binding pocket and on the contrary, the ligand is fully flexible and many conformations are generated on the docking run for the latter[162]. Another approach consists in generating a conformational ensemble for each of the constituents and rigidly dock conformations from both ensembles[63].

After the conformational exploration 'scoring-functions' are used to rank the 'docking-poses' or ligand-receptor conformation obtained. In this case the ideal scoring must rank the experimental co-complex as highest score, and before docking virtual screening campaigns, the score function is selected in by training with experimental co-complex for

the desired receptor. A second important job is to calculate the binding affinity of the complex in order to perform lead optimization or improve binding tightness of a new compound. There are four classes of scoring functions: force-field based, empirical,knowledge-based and consensus scoring. The Force-field based scoring function evaluate the typical force-field energetic terms discussed in 4.1.1. Empirical scoring functions estimate the binding affinity based on a set of weighted energy terms, $\Delta G = \sum_i \omega_i \Delta G_i$, such as van der waals energy, electrostatics, hydrogen bonds, desolvation entropy, hydrophobicity, etc. The corresponding weights are determined by fitting binding affinities data of co-complex for which the crystal structure is known. Knowledge-base scoring functions employ energy potentials derived from structural information embedded in experimentally determined atomic structures. Pairwise potentials are obtained from the occurrence frequency of atom pairs in database using the inverse Boltzmann relation, in the case protein-ligand $w(r) = -k_B T ln[g(r)], g(r) = \rho(r)/\rho^*(r)$ where k_B is the Boltzmann constant, T is the absolute temperature of the system, $\rho(r)$ is the density number of the protein-ligand atom pair at distance r, and $\rho^*(r)$ is the pair density in the reference state where the interatomic interactions are zero. Finally the consensus scoring technique was introduced to take the advantages and balance the deficiencies of different scoring functions and improve the accuracy of the prediction combining multiple scoring functions.[64]

Part II

RESULTS, DISCUSSION AND CONCLUSIONS

5

CHOREOGRAPHY ALONG THE DIFFUSION PATHWAY INSIDE PORINS

Contents

5.1 Summary 51
5.2 Water choreography 51
5.3 Antibiotics choreography 61

Water is the driving force of all nature.

— Leonardo Da Vinci

5.1 SUMMARY

Although the role of general bacterial porins is well established as main pathway for polar antibiotics, its molecular filtering mechanism is still under debate. Using molecular dynamics simulations and water as a probe, we show in this chapter how water is differently ordered along the channel axis of diffusion. The qualitatively study of water local ordering in different regions along the channel axis helped us to depict the intrinsic electrostatic pattern for a series of porins. Moreover, the analysis of the electric dipole moment of the antibiotic in the minima conformations obtained from metadynamics experiments of translocation through different channels allowed us to start to unveil the filtering mechanism of porins, and to put forward a general model for filtering, as well as, to identify key molecular properties of antibiotics that might enhance its permeability.

5.2 WATER CHOREOGRAPHY

In order to investigate the filtering mechanism inside outer membrane (OM) channels of Gram-negative bacteria, we started studying the ordering of water inside porins. As it was anticipated in the introduction section 1, since the first X-ray structure was solved for two main porins of *E.coli*, OmpF and Phoe,[36] its striking architecture, specially its decorated eyelet (depicted in 17.b), has attracted much attention.

As it is represented in Fig. 17.a, porins are classified as hourglass-shaped water-filled channels. Karshikoff *et.al* calculated the internal

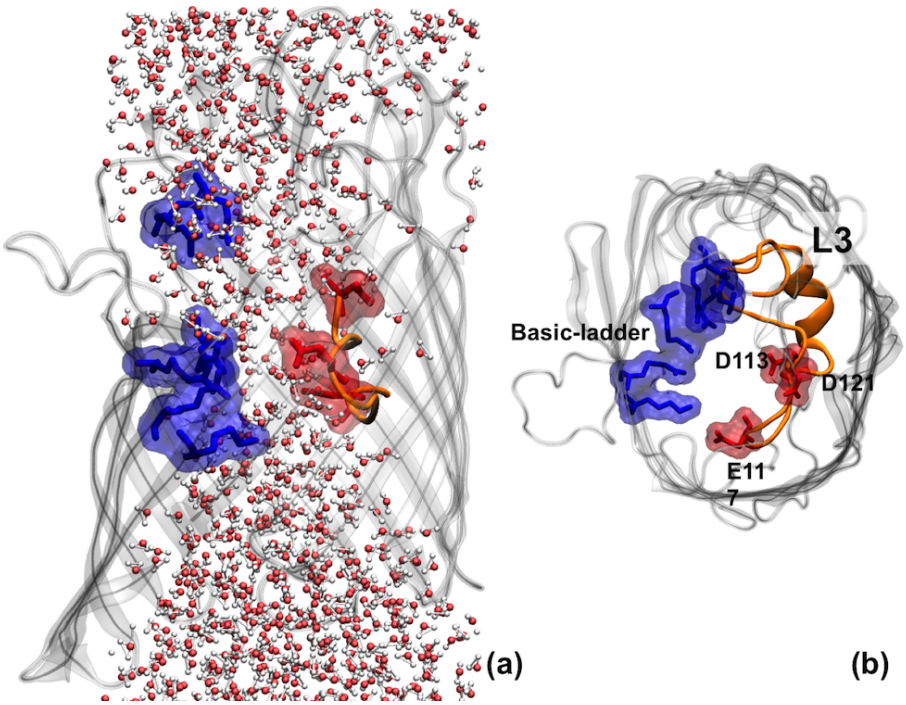

Figure 17: One monomer of OmpF (pdb code 2OMF) is depicted. Panel (a) shows the hourglass shaped of the water filled channel, with the most relevant charged residues highlighted in licorice with its van der waals surface and the constricting loop (L_3) highlighted in orange. Explicit water, in CPK representation, in a cylinder of 17 radius centered in the monomer center of mass is also represented. Panel (b) is a top view of the monomer without the explicit water.

electric field from the pdb X-ray structure by using a multi-dielectric model, revealing a screw-like pattern along the diffusion axis with a strong transversal component in the CR. In the early work of Tielman *et.al*[158], they showed well structured water in the constriction region (CR) of OmpF, ordered by a strong transversal electric field. Later, the works of Im *et. al*[67,68] showed the two distinct pathways for anions and cations inside the OmpF lumen, mapping the electrostatic potential with ions. Moreover, when this calculations were repeated using a more realistic outer membrane composition[125], it was shown that the intrinsic selectivity of the channel, and the ions pathway inside, was not affected by the presence of the lipopolysaccharides in the outer leaflet.

In this work we used water as a probe for mapping the electrostatics of the channel along the putative diffusion pattern of polar molecules aiming to decipher the filtering mechanism of porins. We selected the two classical porins from *E. coli*, OmpF and OmpC. This two porins have been deeply investigated in the past three decades and plenty of experimental and computational data is available. As it was mentioned in the revision of the *in silico* state of the art 3, OmpF and OmpC share the same architecture and they have a 77% of sequence similarity. Nevertheless, they have different filtering mechanisms, as well as conductance and voltage threshold. Its permeability to different solutes is rather different[13,83,84,101,114,116] and OmpC has shown lower susceptibility to different classes of antibiotics than OmpF[94,104]. Moreover, we also investigated the changes in the filtering mechanism along a mutation series in successive *E. coli* resistant clinical strains. In particular, seven strains isolated during the treatment of a patient suffering from Caroli syndrome over two years with cephalosporins and carbapenems but also fluoroquinolones[95]. The isolation of these strains offered the rare opportunity to investigate the evolution of bacteria within the same patient with progressively greater antibiotic resistance along the series. The high resolution crystal structures were published for four OmpC mutants of these series, namely OmpC20, from the first clinical isolate, OmpC26 and OmpC28 and the final OmpC33. We selected the first (OmpC20) and the last (OmpC33) of the series for this study.

Because water completely fills these channels and possesses a large dipole moment though its small size, it represents the natural probe for the channel internal electrostatics along the diffusion pathway. In both human aquaporin-1 AQP1 and the E. coli aquaglyceroporin GlpF,[41,156] the internal electric field of the transmembrane pore was found to be absolutely essential for both channel specificity and functionality. Water molecules and not protons permeate the channel by following a specifically designed "choreography" referred to as "global orientational tuning"[41,156] by aligning their dipole moment to the

porin's electric field that changes orientation from the extracellular to intracellular side.

The main goal of this work, presented as part of this thesis dissertation, is to use water as a probe for mapping the electrostatics of the entire lumen without restricting the attention to the constriction region (CR). By doing so, we revealed a remarkable water "choreography" across the channel, with striking differences among the four porins investigated, particularly at the interface between the extracellular vestibule (EV), $10\text{Å} < z < 5\text{Å}$ and the CR, $5\text{Å} < z < -5\text{Å}$.

The sequence alignment of the four porins is displayed in Fig.18. We found insertions only in the extracellular loops, the constriction region basic ladder and the constricting loop L3 are highly conserved along the series, meaning that the decorated eyelet (Fig.17.b) is conserved even after mutation due to antibiotic stress, in OmpC33[94]. Furthermore, despite the expression level of the classic OmpF/OmpC depends on the growth media osmolarity[104], the electrostatic of the CR is also conserved and hence, must play crucial role in the filtering mechanism.

All the investigated porins have a net negative charge (Fig.19) which increases from OmpF to OmpC and from OmpC20 to OmpC33. As already mentioned, the charge in the CR region was found to be conserved. The largest differences were found in the extracellular vestibule ($z > 10\text{Å}$), which is more negative in OmpC than in OmpF, and whose net negative charge is further increased in OmpC20 and OmpC33, Fig. 19. The same trend was found for the periplasmic vestibule (PV), despite the differences being less pronounced. It is also interesting to note that in the two wild-type porins the periplasmic vestibule is more negatively charged than the extracellular one, while in the two clinical mutants, residues mutations led to the same increased negative charge for both the vestibules.

In order to characterize such an altered electrostatics inside the lumen and to examine the effect of the porin's intrinsic electric field, we analyse water ordering using the transversal component of its electric dipole moment $\vec{\mu}_t$ as order parameter along the whole diffusion pathway. After equilibrating[1] each trimer (PDB Ids: 2OMF; 2J1N; 2XE2; 2XE3) embedded in a fully hydrated POPC (1-palmitoyl-2-oleoyl-sn-glycero-3-phosphocholine) bilayer, we run 300ns of plain molecular dynamics for each system. We extracted the coordinates of the water molecules solvating the lumen of the channel, and we divided the pore in 12 adja-

1 equilibration protocol is detailed in the Appendix

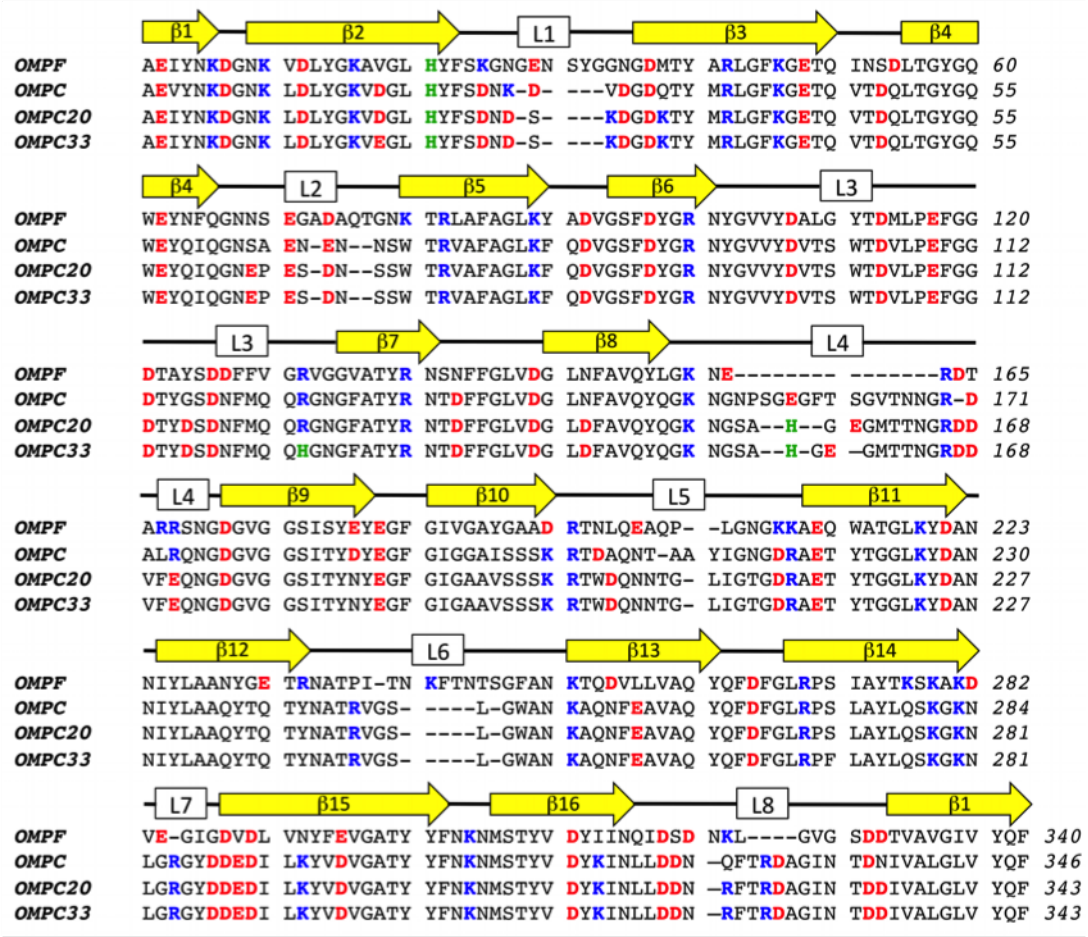

Figure 18: Multiple-structure alignment of the first monomer of OmpF, OmpC, OmpC20 and OmpC33 from E. coli. Positively charged residues are highlighted in blue, negatively charged in red, histidine residues in green. The secondary structure is also reported to easily identify different β-strands and loops.

cent regions along the axis of diffusion. For each region, we calculated the total averaged transversal dipole moment of water,

$$\langle \vec{\mu}_t \rangle = \langle \frac{1}{N_w} \sum_{i=1}^{N_w} \vec{\mu}_t^i \rangle \tag{42}$$

Bulk waters are characterized by a rather short correlation-time for reorientation, such that the corresponding autocorrelation function decays to zero rapidly. We found that in this case that the ordering of water molecules inside the porin resulted to be time-correlated. The autocorrelation function of μ_t / N_w did not decay to zero but asymptotically tended to a constant value Fig.20, which depended upon the specific z region considered, indicating the presence of an external elec-

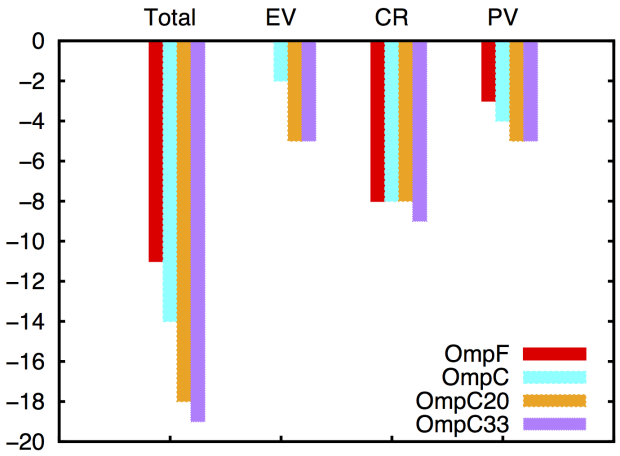

Figure 19: Net charge histogram of the first monomer of OmpF, OmpC, OmpC20 and OmpC33 from E. coli. The net charge is shown for different protein sections: total, extracellular vestibule (EV) ($z > +10$Å), constriction region (CR) ($+10$Å$z - 10$Å) and periplasmic vestibule (PV) ($z < -10$Å).

tric field, in this case created by the charge segregation along the porin walls, as previously pointed out[158].

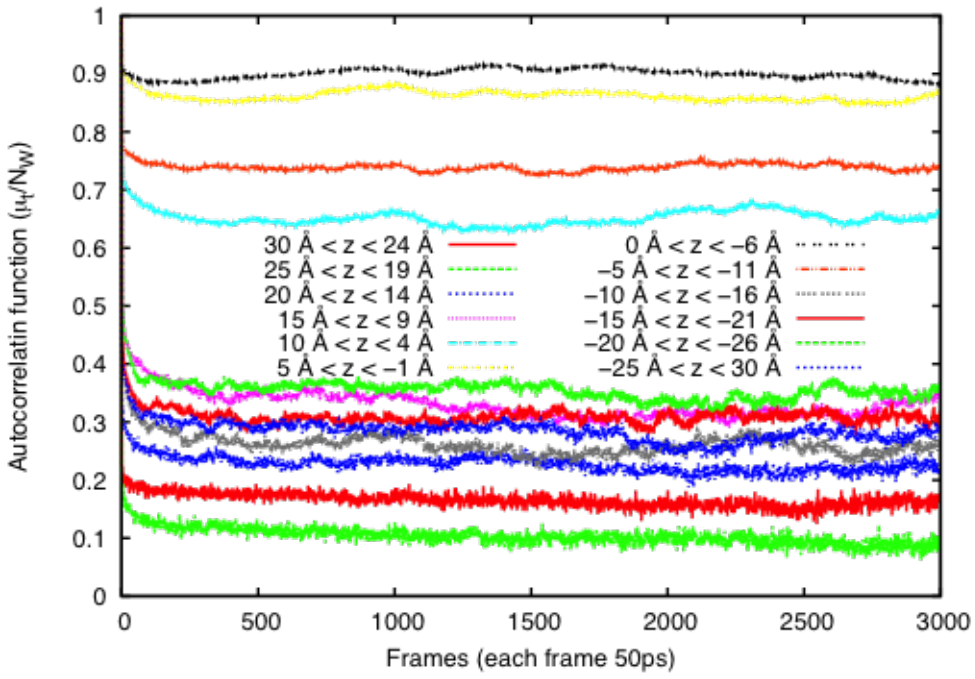

Figure 20: Autocorrelation function for the total averaged dipole moment for each of the 12 regions along the diffusion pathway, inside OmpF.

In Fig.21a it can be observed that the total averaged dipole moment of water, μ_t/N_w, increases while going down the diffusion path (from positive to negative z), it reaches its maximum in the CR ($5\text{Å} < z < -5\text{Å}$) and then decreases almost symmetrically. Interestingly this behaviour is conserved for all the analysed systems but for OmpC33, in which two peaks are observed (Fig.21.a). Furthermore, the highest intensity peak decreases along the series as it can be observed in Fig.21(a). In Fig.21(b) we show how also along the series the polar angle in the transversal plane changes. This means that a reorientation is induced in the plane perpendicular to the diffusion axis from plane to plane, and this reorientation is different for each porin. It is worth to note that the polar angle in the transversal plane is conserved in the CR and its exit, the periplasmic vestibule, but not in the entrance to the CR. In the case of OmpC20 and resistant OmpC33 prior to enter the CR the orientation is opposite to that in OmpF and OmpC. In OmpC20 is opposite but not very intense while in OmpC33 it corresponds to a peak almost as intense as the CR.

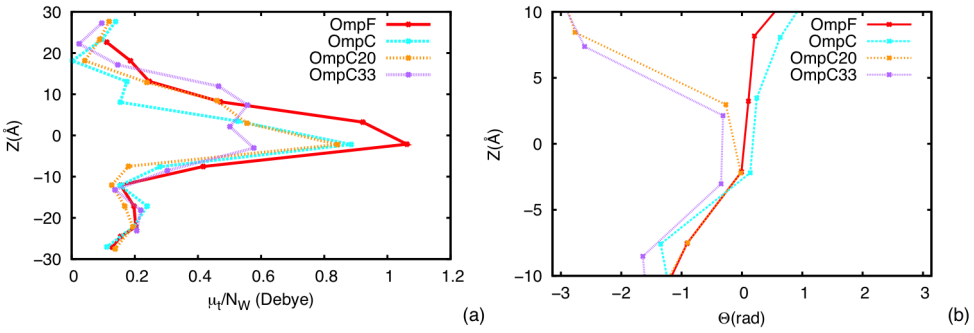

Figure 21: In panel (a) the μ_t/N_w module profile is shown along the channel axis for the four porins studied. Panel (b) shows the polar angle of μ_t/N_w for each porin, zoomed to the central part of the channel ($10\text{Å} < z < -10\text{Å}$)where the transversal dipole moment of water is more intense.

The ordering of water dipoles in each channel is determined by the specific distribution of the positively and negatively charged residues inside the lumen. The analysis of the xy-distribution of charged residues in the different regions along the diffusion path from the coordinates recorded along the MD trajectories was performed and the results are shown in Fig.22. The parameter $\Delta\rho_{xy}$ was calculated as the difference between the xy-distribution of the positively and the negatively charged residues for each channel section or z-region.

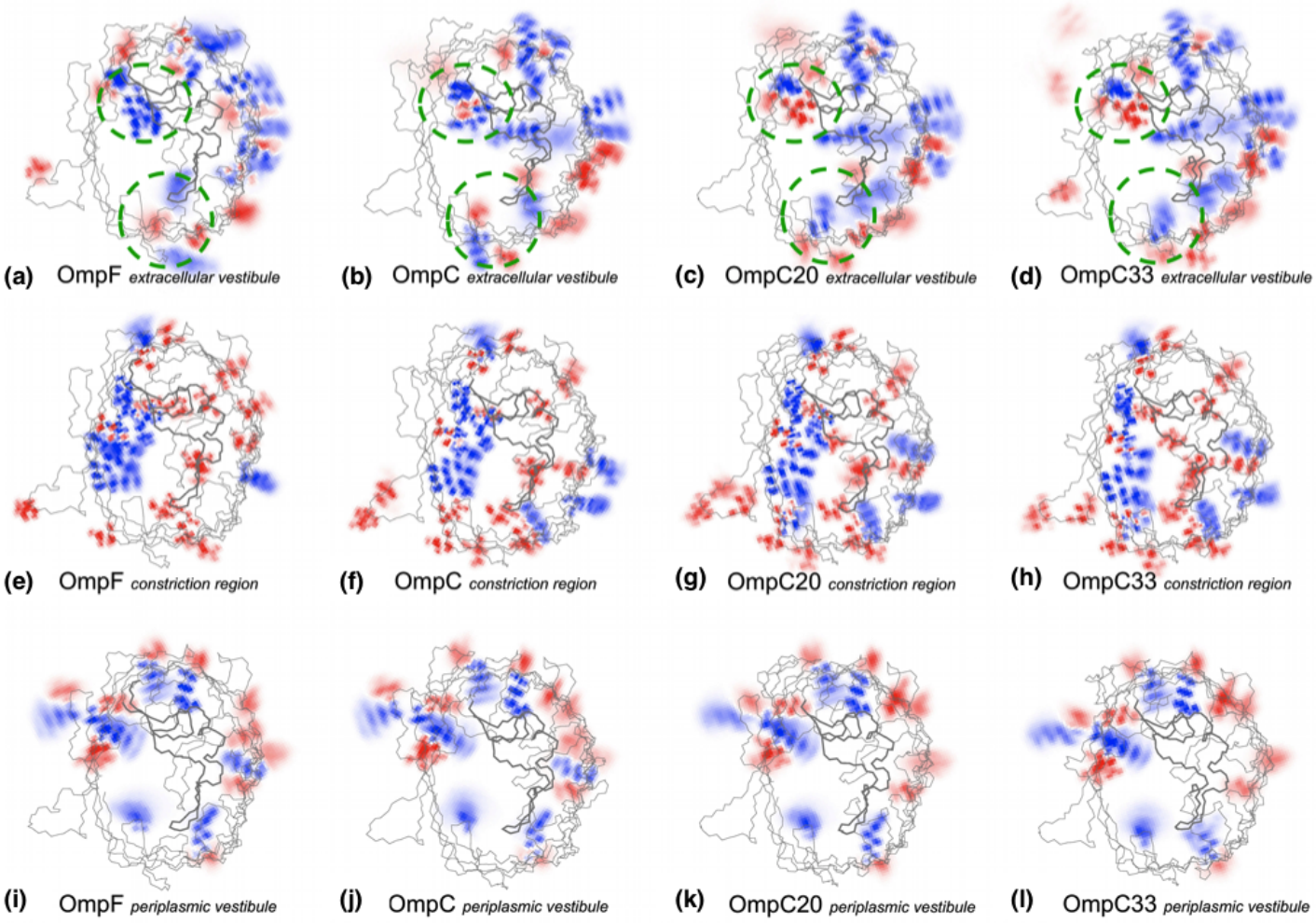

Figure 22: The difference $\Delta\rho_{xy}$ between the distribution of positively (blue) and negatively (red) charged residues on the xy-plane is shown for OmpF, OmpC, OmpC20 and OmpC33 from *E. coli*. In(a-d) results of the extracellular vestibule ($z > +10$Å) are reported, where two green ovals are used to highlight the most significant differences found between the four porins. In (e-h) the constriction region results ($+10$Å$z - 10$Å) are reported, in (i-l) those pertaining to the periplasmic vestibule ($z < -10$Å)

Looking specifically at the residues facing the lumen, the most dramatic differences were found in the extracellular vestibule (Fig. 22. a-d, green ovals) whereas the constriction region and the periplasmic vestibule (Fig. 22. f-l) resulted to be comparable in the four porins. The upper green ovals in Fig. 22. a-d highlight the region where amino acid mutations appear to be the main responsible for the different orientation of the electric field before the entrance to the constriction region. A closer inspection led to the precise identification of the responsible mutations. Figure 23 shows the position of such residues in the three-dimensional structure of OmpF, for instance. They form a cluster around the R167 and R168 (of OmpF) located at the mouth of the constriction region. In Figure 23b the mutations along the series OmpF, OmpC, OmpC20 and OmpC33 are schematically reported. The formal net charge of this residues cluster is +1, 0, -3 and -3, respectively. It is interesting to note that the R167 and R168 are key motifs in the co-crystallization of the zwitterionic antibiotic ampicillin in OmpF[?] and have been defined as the positively charged selectivity filter in OmpF for ionic current rectification purposes[109].

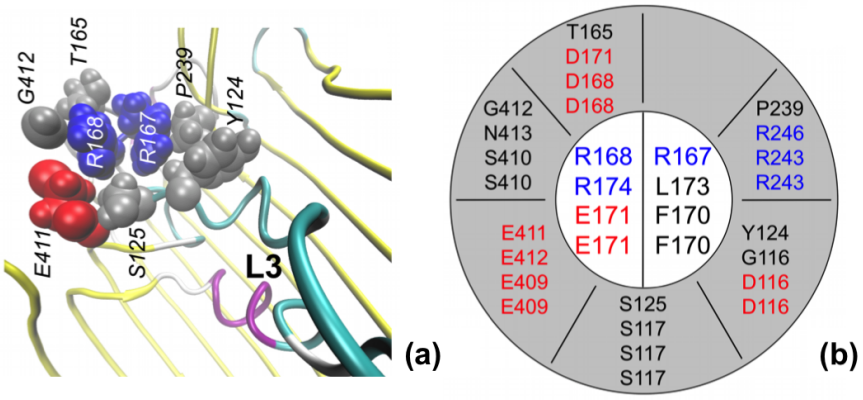

Figure 23: (a) The position of residues whose mutation is responsible for the different orientation of the electric field before the entrance in the CR observed in the four porins under investigation is shown. OmpF has been selected as template and the loop L3 is labelled as reference. (b) The chart schematically reports the relative position of such residues and their mutations. A series of four residues is reported in each space, corresponding to OmpF, OmpC, OmpC20 and OmpC33, respectively. Positively charged residues are highlighted in blue, negatively charged in red.

The overall emerging picture is that specific mutations have been introduced to tune the transversal electric field right at the entrance of the CR ($+10\text{Å} < z < +5\text{Å}$) while leaving the CR almost unaffected. When compared to the case of AQP1 and GlpF, in which the direction

of the water dipole mostly changes along the channel axis[41,156], in the case of general porins the transverse reorientation appears to be predominant and represents the most striking difference among the examined channels, especially in the two porins extracted from clinical series.

The entrance to the CR is a key point due to the fact that the translocating molecule experiences a remarkable decrease of the conformational entropy due to the significant pore size reduction. This is the most significant term controlling permeation. The resulting increase of the free energy would be compensated by a favourable preorientation of the molecular electric dipole with respect to the channel transverse electric field, as already claimed for the transport of urea in a specific urea channel.[106]. Thus, the effect of a weak field just above the CR (e.g., in OmpC) or, even worse, of an electric field pointing in the opposite direction (e.g., in the two OmpC mutants) is expected to impose an adverse "preorientation" to the translocating molecule, exactly where steric hindrance to molecular reorientations starts to be severe. The same can be applied to the conserved water's order deviation observed upon emerging from the CR to the PV. From a general point of view, it is absolutely plausible that the internal electric field of the channel forces a dipolar molecule to align its moment accordingly while translocating. A higher free energy barrier for escaping the CR, thus, is expected for those molecules that cannot reorient easily inside.

5.3 ANTIBIOTICS CHOREOGRAPHY

Known antibiotics have different physico-chemical properties that are usually described with different descriptors as molecular surface, isoelectric point, H-bond (donors/acceptors), rotatable bonds, hydrophobicity (logP),... For our analysis we will focus in the electric dipole moment of the antibiotic and its orientation with respect to the principal axis of inertia of the molecule.

In the first example we chose two cephalosporins: cefepime and cefotaxime (fig.24a,d), and we set up two translocation experiments in OmpF from *E.coli*. Using metadynamics 4.2.1 we calculated the corresponding free energy surfaces (FES) shown in figure 24b,e. For each set-up the main minima found in the free energy surface (FES) were analysed by extracting from the dynamics the corresponding conformations. For each of the antibiotic's conformation the electric dipole moment was calculated respect to the molecule's principal axis of inertia. The projection onto the the transversal plane of the average dipole moment of the antibiotic in each minima is depicted in fig.24c,f.

For clarity in figure 25 the OmpF data is reprinted from the original work[1]. By comparing the projections of the transversal dipole moment of the antibiotic (fig. 24c,f) and the corresponding total averaged dipole moment for water inside OmpF (fig. 25b) it is clear that the antibiotic follows the same 'choreography' as water inside the protein.

The selected molecules, cefepime and cefotaxime, have similar size but very different charge distribution, the former being zwitterionic at the considered pH and the latter negatively charged. Both have similar averaged electric dipole moment, 20.5 ± 1.3 Debye and 25.8 ± 2.2 Debye, respectively, but the orientation of the dipole moment with respect to the principal axis of inertia of the molecule is very different, as it is shown in figure 24a,d. Regardless their differences, both cefepime and cefotaxime experienced the highest energy barrier in the central region of the channel. More precisely, when approaching the CR from the EV, both antibiotics are accompanied by a rather low energetic cost. The highest energy barrier was found to exit the CR, that is, where the water analysis has revealed the unique abrupt change in the direction of the waters net dipole moment (Figure 25b,) with a reorientation of almost 60° upon emerging from the CR to the PV. Because such reorientation occurs in the constricted region of the lumen, this might lead to an increase of the translocation free energy barrier. In this case the ability of the molecule to reorient and fit in the constricted region will determine the penalty. This issue is further discussed in the second work presented as part of this dissertation in which the averaged electric dipole moment of two carbapenems: imipenem and

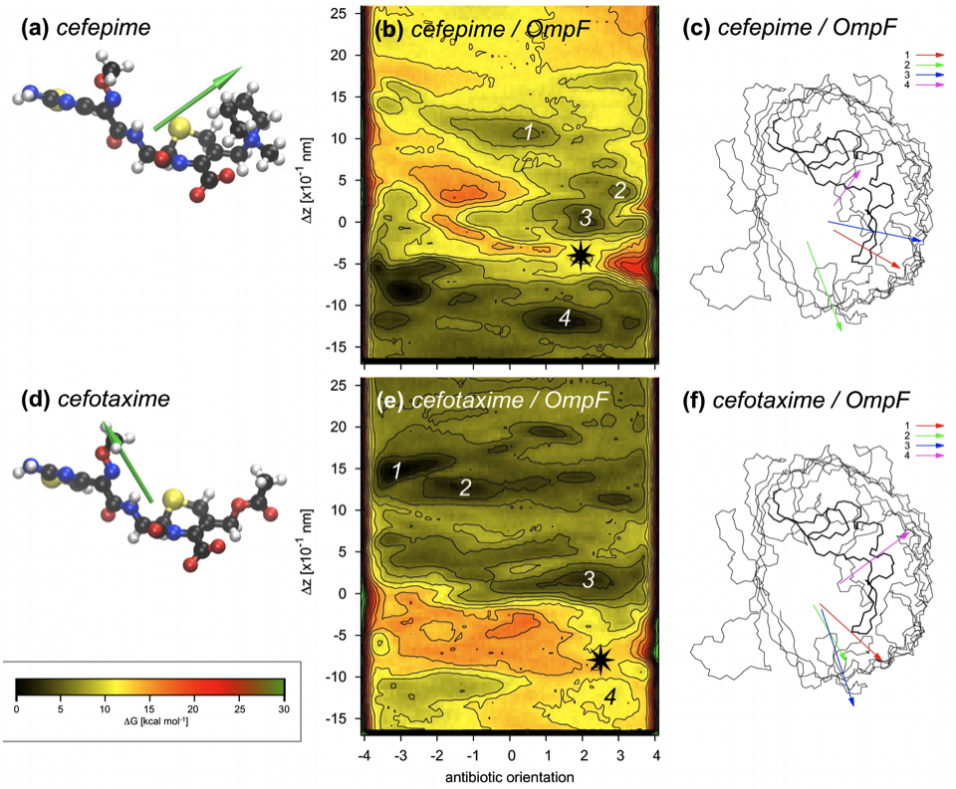

Figure 24: Cefepime (a) and cefotaxime (d) are shown together with the corresponding electric dipole (green arrow). Chemical elements are color coded as follows: C, black; H, white; N, blue; O, red; S, yellow. The FES for translocation through OmpF are shown in (b, e), where the main minima are labelled with consecutive numbers. The highest barrier is marked by an asterisk. Antibiotic orientation is defined as the difference of the z coordinate between the lactam carbonyl C and the S-bonded C. For each of the labelled minima, the molecular electric dipole was calculated and the average vector is reported in (c, f) together with the channel backbone trace. The loop L3 is bolded. Reprinted from JPCL

meropenem, was analyzed while traslocating trough OmpF, OmpC, OmpC20 and OmpC33. This analysis shows the importance of the capability of drugs to properly align their electric dipole to the internal electric field in the restricted region of the pore as discussed in this section for cefepime and cefotaxime. The extension of the analysis to the whole series (OmpF, OmpC, OmpC20 and OmpC33) using two different carbapenems (imipenem and meropenem) revealed the differences in filtering imposed by the different internal electrostatics in the extracellular vestibule and its consequences in the drug's translocation.

In this case the free-energy surface for the translocation of the same molecule in different channels was found to be very different[144]. An al-

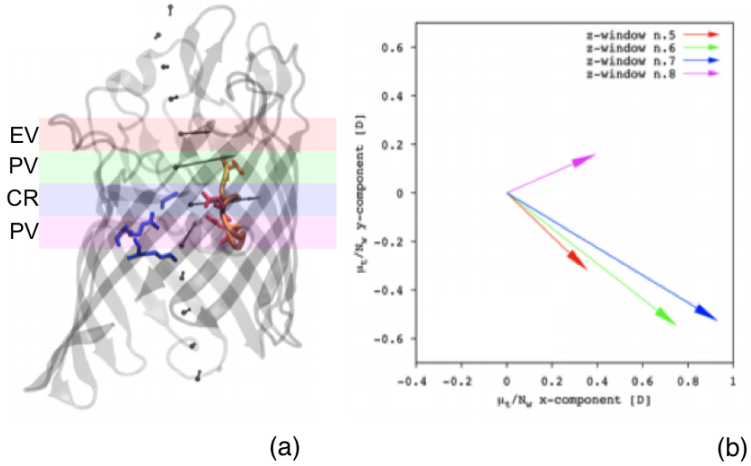

Figure 25: (a) Dipole water orientation in OmpF, from *E. coli*. A cartoon of the first monomer is shown together with the positively and negatively charged residues of the "basic ladder" and loop L3 (orange), respectively. The former are reported in blue,the latter in red. Vectors represent the time average of the total dipole moment μ_t of the water molecules found in the corresponding protein section, normalized by the number of water molecules N_w.(b) the xy projections of the μ_t/N_w vectors pertaining to the central z regions of OmpF are depicted.

tered number of hydrogen bonding or charged groups in the CR could not be invoked to explain the differences observed in the translocation free energy of each of the two carbapenems, since no amino acid mutations are present in the CR (fig.18). All four porins have a comparable size[94], but exhibit different electrostatic patterns. In order to prove that the ultimate factor determining the difference in translocation is the different electrostatics along the lumen of the pore an extensive analysis of the electric dipole moment of the translocating molecules was performed for each case. The optimal orientation of the antibiotic electric dipole moment inside the CR is the one directed from the positive basic ladder toward the negative loop L3 (fig. 25a, CR). In OmpF this orientation was already adopted before entering the CR when the antibiotic was still in the pre-orientation zone (fig. 25a, PR). Correspondingly a relatively easy accessibility was observed for the two antibiotics when approaching the CR from the extracellular vestibule. In OmpC the almost ineffective pre-orientation (fig.21a) caused the drug to be not properly oriented before entering the CR. Indeed, the free energy barrier for translocation was observed to start before the actual CR. In OmpC20 the pre-orientation was strong and pointing $\sim 180°$ away from the optimal direction to descend into the

CR (fig.20a) inducing a huge reorientation in the molecule in a narrow space (less than 2nm) along the translocation path. Finally, in OmpC33 the adverse pre-orientation persist till a very short distance from the CR. Correspondingly, the free energy barrier was extremely wide and this is reflected by the fact that the antibiotic never reaches the proper orientation inside the CR. In order to effectively compensate the entropic cost due to desolvation and drug confinement inside the CR, the alignment of the antibiotic's electric dipole to the porin's internal electrostatics seems to be crucial. In figure 26 we show the different conformations of the electric dipole moment with respect to the principal axis of inertia of the molecule extracted from the conformational analysis of known antibiotics (www.dsf.unica.it/translocation/db). Almost all known antibiotics pertain to one of this categories.

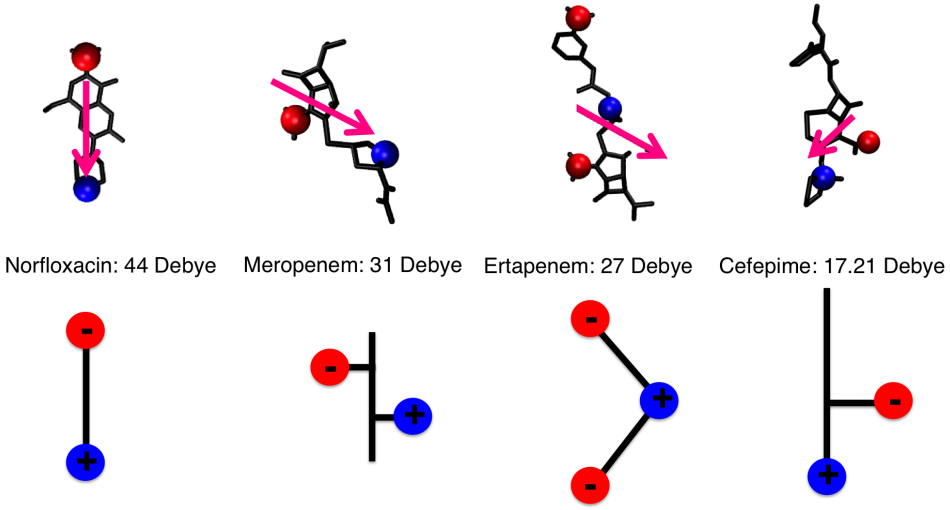

Figure 26: Dipoles and shapes

The carbapenems study suggested that the molecule with the best permeation properties might be the one aligned with its long axis of inertia to the axis of diffusion, z, and at the same time having its electric dipole aligned to the internal electric field. For instance, we expect that a molecule with the electric dipole directed along its main axis of inertia is not a good permeant, like norfloxacin in figure 26, because it would be forced by the porin's electrostatics to adopt a transverse orientation inside the CR, thus, maximizing the steric hindrance. Diverse realization of dipoles are depicted in figure 26.

As it is shown in figure 27 during translocation the number of conformations for the antibiotic to fit inside the CR is restricted by different conditions, especially the eyelet size that generates the main barrier depicted in black in figure 27. The alignment of the molecule's electric dipole to the internal electrostatics could eventually decreased these

barrier (enthalpic compensation) depicted in orange in figure 27. Nevertheless, the alignment is constraint by the correct orientation of the H-bonding groups and of course the size of the antibiotic and the eyelet. The molecules with the best permeation performance are predicted be the ones endowed with enough flexibility to change the direction of their electric dipole with "low-cost" dihedral torsions of specific groups, without the need for more "expensive" molecular reorientations. The concepts presented here can contribute to provide the basis for future in-silico screening aimed at identifying molecules with enhanced permeation properties. A further energetic analysis of the entropic and enthalpic contributions of the translocation problem are discussed in the final chapter 7 where an ultra-coarse-grained model for the free-energy along the diffusion pathway is discussed.

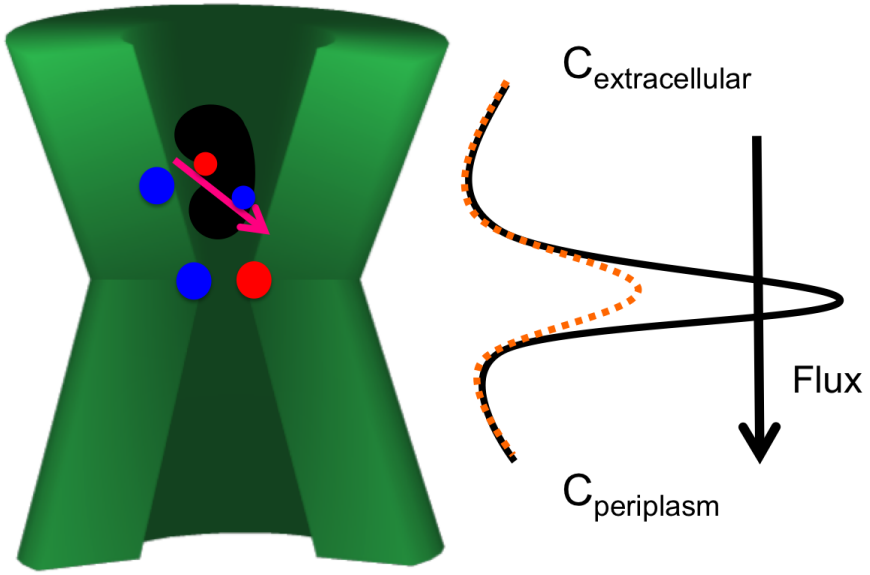

Figure 27: Electric field filtering mechanism. The steric barrier in the constriction region, (black solid line in (c)) is reduced (dashed orange line in (c)) by the interaction of the electric dipole moment of the molecule (b) with the internal electric field of the pore (a)

6

QUANTIFYING THE MACROSCOPIC INTRINSIC ELECTRIC FIELD

Contents

6.1 Summary 67
6.2 Electrostatic problem 68
6.3 Response Function 72
6.4 The method 73
6.5 Electrostatic Characterization of porins 75
6.6 Changes in the Macroscopic electric field due to pH, media osmolarity 77

6.1 SUMMARY

We present in this chapter a computational all-atom approach for the calculation of the macroscopic electric field inside water-filled channels using water as a probe. The method allows to compare not only different systems but also the same system under different conditions, i.e. pH and ion concentration. It provides a detailed picture of electrostatics in biological nanopores shedding more light on how the charged residues of proteins determine the electric field inside, and also how medium can tune it. Moreover, in the case of MOMP from Campylobacter jejuni the calculation of the internal electric field might explain the selectivity change induced by the presence of a metallic ion in its constriction region.

We showed in the previous chapter how using water as a probe we were able to map the electrostatics of the channel and track qualitatively the effect of mutations in the channel electrostatics. Moreover, we showed how antibiotics follow a similar choreography, constraint by its size, flexibility and electric dipole moment orientation with respect to their inertia axis. The big qualitative picture point to a compensation of the entropic barrier (due to size reduction) with favourable electrostatic interactions between the molecule and the channel along the diffusion path.

In order to quantify the electrostatic interaction of the permeating molecule with the channel we need to quantify the macroscopic electric field inside the pore. We need to quantify the average electric field that the permeating molecule feels along the diffusion pathway.

6.2 ELECTROSTATIC PROBLEM

The straightforward approach to the problem is to solve the macroscopic Maxwell equations,

$$\nabla \cdot \mathbf{D} = 4\pi\rho_{free}(\mathbf{r}); \nabla \times \mathbf{E} = 0; \tag{43}$$

where $\mathbf{D}$ is the electric displacement, ρ_{free} the free charges distribution and $\mathbf{E}$ the desire electric field. The electric field and the electric displacement vector are related to each other through the polarization density of the media, $\mathbf{P}(\mathbf{r})$, $\mathbf{D}(\mathbf{r}) = \mathbf{E}(\mathbf{r}) + 4\pi\mathbf{P}(\mathbf{r})$. Knowing the free charges distribution and the dielectric response function of the media, $\mathbf{P}(\mathbf{E}, \mathbf{r})$, the electric field can be easily calculated by solving the macroscopic Maxwell equations with the correct boundary conditions.

In the standard linear-isotropic approximation the dielectric response of the media is enclosed in the local dielectric constant of the media, $\varepsilon(\mathbf{r})$, hence, $\mathbf{D}(\mathbf{r}) = \varepsilon(\mathbf{r})\mathbf{E}$. In this approximation the Maxwell equations are reduced to the Poisson equation,

$$\nabla \cdot \varepsilon(\mathbf{r})\nabla\varphi = -4\pi\rho_{free}(\mathbf{r}) \tag{44}$$

for the electrostatic potential and, hence, the electric field, $\mathbf{E} = -\nabla\varphi$. In complex systems like biological ones, the selection of the dielectric constant for the different constituents of the system is not straightforward. A usual approach is to choose a constant function model for $\varepsilon(\mathbf{r})$, and assign different values for different constituents of the system, in other words, to use a multi-dielectric model for the system like in the pioneer work of Karshikoff *et.al*[79]. In the case of solvated membrane channels, different dielectric constants are used for the protein ($\varepsilon_p = 4$), the membrane ($\varepsilon_{mborders} = 40, \varepsilon_{mcore} = 4$) and solvent, in this case water ($\varepsilon_s = 80$).

The dielectric constant of water in the lumen of the channel is decisive in this case for calculating the macroscopic field along the diffusion pathway. The non-linear response of water to an applied electric field is widely recognized[4,6,20,155] and such nonlinearity of water polarization is reflected by the decrease of the dielectric constant with increasing applied electric field, the so-called water dielectric saturation effect. In the case of the lumen of protein channels one faces two problems: the non-linearity and non-uniformity of the media, remarkably complicating the selection of an appropriate dielectric constant.[171]

Different solutions have been taken for the dielectric response of water when solving the Poisson equation for protein channels to deal with dielectric saturation under applied electrics fields. One solution is to consider an effective (smaller) dielectric constant for the regions

were a strong electric field is present[140]. Another solution is to approximate the non-linear dielectric function of water, $\varepsilon_s(\mathbf{E})$ with a Langevin-type function parametrized for bulk solvent response[97]. In this case, the spatial dependence of the dielectric constant of the solvent arises from the non-linear response and the spatially varying electric field, $\varepsilon_s(\mathbf{r}) = \varepsilon_s(E(\mathbf{r}))$. Then the Poisson equation is solved by assuming a free charge density, $\rho_{free}(\mathbf{r})$, composed of the fixed charges of the groups in the protein and mobile ions. Ion densities at equilibrium can be treated by assuming Boltzmann statistics using the Poisson-Boltzmann method[79] or a linear version, for example the Debye-Hückel method for low ion concentration. In case ions are not in equilibrium the diffusion-drift (Nerst-Planck) theory or more general Brownian dynamics methods should be employed[67] and coupled to the Poisson equation for calculating the ion density and the electrostatic potential together.

There exist different continuum electrostatic methods for calculating the electrostatic potential of macroscopic systems like membrane protein channels and they are widely used by the community. Most of them are based on the solution of the Poisson-Boltzmann equation with continuum electrostatic models[8]. As explained before they all require quite strong assumptions about the dielectric response of an inhomogeneous medium and the free ions distribution. Nevertheless, the visualization of the electrostatic potential distribution in and around macromolecules can give valuable insight on its function and stability.

We propose to calculate the macroscopic electric field along a path using water polarization from MD simulations. Water is a fascinating polar dielectric media, water molecules have a permanent electric dipole moment of 2.95 Debye in condensed phase at 300K. In the absence of an electric field the individual dipoles point to random directions and the total dipole moment is zero. When an electric field is applied two things can happen: (i) there is an induced dipole moment, electronic polarizability; (ii) the electric field tends to order water to produce a net dipole moment per volume unit. At ordinary temperatures the alignment is not perfect due to thermal fluctuations, but there is some net alignment and hence, the polarization density can be computed from the molecular dynamics trajectory of water as,

$$\mathbf{P} = \frac{\langle \boldsymbol{\mu} \rangle}{N_w v_w} \tag{45}$$

For bulk solvents, the polarization density produced by an external electric field is completely determined by its thermodynamic parameters: density (ρ), temperature (T), and the macroscopic electric field ($\mathbf{E}$) that generated the latter, $\mathbf{P} = \mathbf{P}(\rho, T, \mathbf{E})$. As polarization density

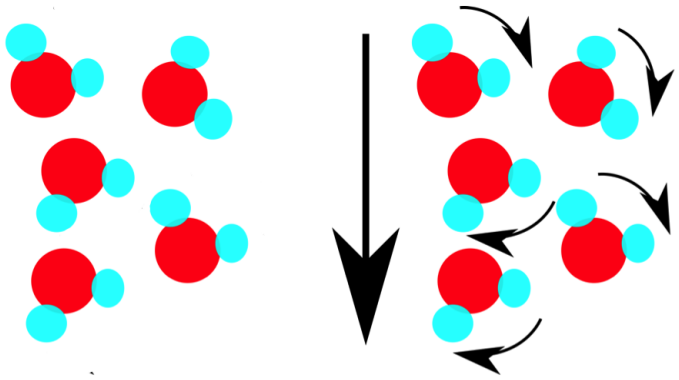

Figure 28: Cartoon representation of water re-ordering under an external electric field.

is pretty easy to obtain from molecular dynamics Eq. 45 we propose to use a response function and calculate the macroscopic electric field inside the channel from the polarization density of water. In this case we are assuming that the local dielectric response in the inhomogeneous regions of the system is the same as for bulk. However, this assumption is also made in the Poisson equation based methods[8,79,97??]. If we consider the local or microscopic Maxwell equations,

$$\nabla \cdot \mathbf{e} = \frac{1}{\varepsilon_0}\eta; \nabla \times \mathbf{e} = 0 \tag{46}$$

where $\mathbf{e}$ is the local electric field and η the microscopic or local charge. In order to obtain macroscopic observables like polarization $\mathbf{P}$ or current density $\mathbf{J}$, we need to perform a spatial average of the microscopic observables. Spatial averaging will cancel out microscopic fluctuations. The standard spatial average of a function $F(\mathbf{x}, t)$ with respect to a test function $f(\mathbf{x})$, reads,

$$\langle F(\mathbf{x}, t)\rangle = \int d^3x' f(\mathbf{x}')F(\mathbf{x} - \mathbf{x}', t) \tag{47}$$

where $f(\mathbf{x})$ is real, nonzero in some neighbourhood of $\mathbf{x} = 0$, and normalize to unity over space. In order to avoid biasing directional characteristics of the averaged physical properties, $f(\mathbf{x})$ must be taken isotropic. Two usual examples of averaging probe are the sphere and the gaussian.

The spherical probe has a discontinuity at r=R that leads to fast fluctuations in the macroscopic quantities when a molecule or group exits or enter the volume. On the other hand, the gaussian probe or any other smooth probe function eliminates that problem but introduces

higher orders in the Taylor series expansion. The only requirements for a probe function are continuity and smoothness so that the Taylor series expansion over distances of atomic dimension converges rapidly. Hence, by spatially averaging Eq. 46,

$$\varepsilon_0 \nabla \mathbf{E} = \varepsilon_0 \nabla \langle \mathbf{e} \rangle = \langle \eta(\mathbf{x}, t) \rangle ; \langle \nabla \times \mathbf{e} \rangle = 0 \tag{48}$$

As it can be followed in any Classical Electrodynamics book[70]. Polarization comes from the spatial averaging of the microscopic charge and depending on the selected probe the Taylor series expansion will depend on charge and dipole moment in the case of the sphere or higher electric-moments for non constant probes. We selected the spherical probe in order to recover $\mathbf{D} = \varepsilon_0 \mathbf{E} + \mathbf{P}$.

Within this approximation water alignment is assumed to come from the local averaged electric field in the spherical probe. Surface effects, like the response of molecules on the boundary of the probe or hydrogen bonds of molecules with the surface of the protein are not taken into account. The probe is assumed to be small enough to be homogeneous, and hence the inhomogeneity in the response can be also neglected. Of course, the number N of water molecules on the probe should be large enough as the surface effects scale as N^2 while the main volume effects scale as N^3. In order to test inhomogeneity and surface effects, different radii were used (Fig. 29) to calculate the macroscopic electric field. For $R = 4$Å the number of water molecules inside the probe is not enough and leads to big fluctuations of the averaged observables. For $R = 7$Å the profile is too smooth. We chose $R = 5$Å as optimum radius for the probe. It is important to note that the probe radius optimization is system dependent. Different approaches to calculation of the macro-

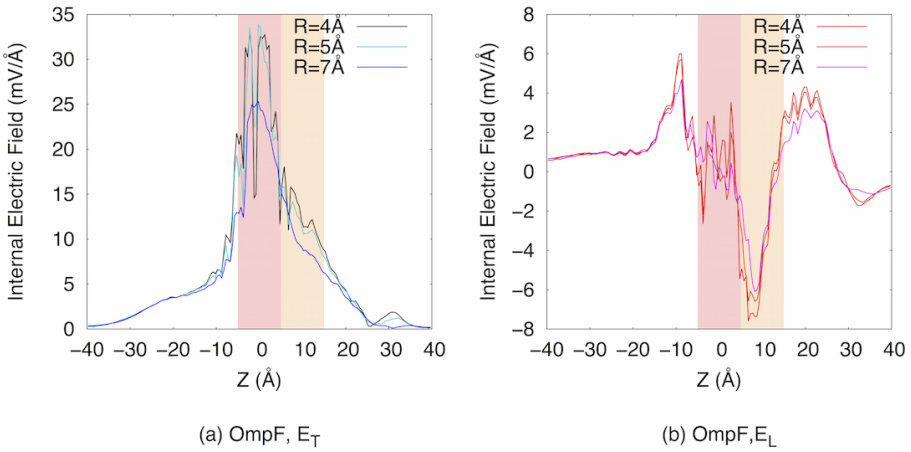

Figure 29: Macroscopic electric field calculated inside OmpF from *E.coli* for different spherical probes.

scopic electrostatic potential and charge distribution[2], use a gaussian coarse-graining function and in this case in the inhomogeneous regions, the averaged electrostatic field does not correspond to the standard continuum Maxwell equations but those containing the quadrupole an higher-order electric moments.

6.3 RESPONSE FUNCTION

In order to calculate the response function of the (bulk) solvent by using MD simulations of an NPT ensemble in an external electric field, one considers a water box under the same pressure and temperature as in the simulation of the channels. All solvent molecules (we used the TIP3P model for water) feel the same additional external and constant electric field $\mathbf{E}_{ext}$. Thus, the total Maxwell field should be the sum of $\mathbf{E}_{ext}$ and the averaged electric field $\mathbf{E}_{ind}$ generated by the aligned molecules, $\mathbf{E} = \mathbf{E}_{ind} + \mathbf{E}_{ext}$. The corresponding electrostatic potentials, φ, φ_{ind}, and φ_{ext}, obey the Laplace equation as there are no 'free' charges in the system. The treatment of the electrostatic interactions within the Particle Mesh Ewald method[39,49] assumes the periodic (constant) boundary conditions for electrostatic potential Ψ_{ind}, but not for the external one, $\varphi_{ext} = -(\mathbf{r} \cdot \mathbf{E}_{ext})$. The Laplace equation with the periodic (constant) boundary conditions has only constant solution. Thus, the electric field, $\mathbf{E}_{ind}$, generated by the molecules in the box equals zero even if the net polarization density $\mathbf{P}$ of the box is not null. The total macroscopic field $\mathbf{E}$ then equals the external applied electric field, $\mathbf{E} = \mathbf{E}_{ext}$, which generates the polarization density $\mathbf{P}$.

This result may also be interpreted from the viewpoint of macroscopic electrostatic theory. Indeed, the constant potential on the boundary corresponds to the conducting (or tin-foil) boundary conditions, explained in 4.1, where the dielectric boundary conditions are discussed. The conducting boundary generates the reaction field which exactly cancels out the field generated by polarized solvent molecules, $\mathbf{E}_{ind}$. The remaining macroscopic field is equal to the external applied one. Finally, the dielectric response function can be calculated from a MD trajectory for a given macroscopic field $\mathbf{E} = \mathbf{E}_{ext}$ by using Eq. 45, where $\langle \boldsymbol{\mu} \rangle (\mathbf{E}_{ext})$ is the average dipole moment of molecules in the spherical probe.

The calculated response function of water, Fig.30, is in excellent agreement with the Booth model for water dielectric saturation[20],

$$P_{Booth}(E) = \frac{(n^2-1)}{4\pi} E + \frac{\alpha(n^2+2)\mu}{4v_w} L\left(\frac{\beta(n^2+2)\mu E}{k_B T}\right) \qquad (49)$$

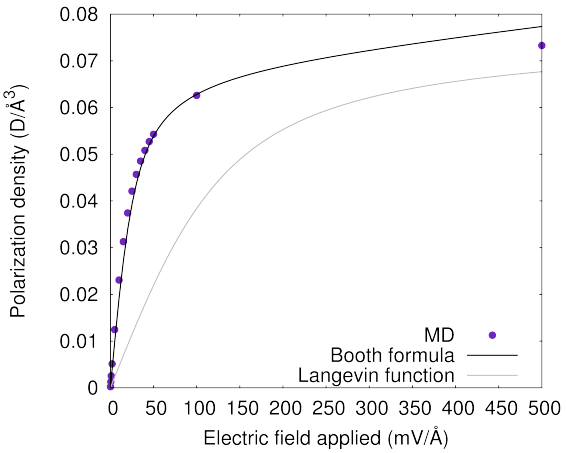

Figure 30: The dielectric response function of (bulk) water. The solid line corresponds to the Booth function[20] and the dashed line to the Langevin function with parameters from[158].

where $\alpha = \frac{28}{3\sqrt{73}}; \beta = \frac{\sqrt{73}}{6}; n = 1.33$ is the experimental optical refraction index of water; T is the absolute temperature; k_b the Boltzmann constant; v_w the volume of a water molecule; and $L(x) = coth(x - \frac{1}{x})$ is the Langevin function.

6.4 THE METHOD

The coordinates of the waters solvating the protein are extracted from an NVT equilibrium trajectory of at least $300ns$. In the particular problem of porins this corresponds to the extraction of waters within a cylinder of 80Å height and 17Å radius centered in the center of mass of the channel. For each cylinder every 0.5Å along the diffusion axis we calculate the geometrical center of the oxygen distribution in the corresponding plane or slice. Then, spherical water probes along the previously calculated water path, are extracted from the same MD trajectory. For each probe at each time step the polarization density is calculated as $P_{i\alpha} = \frac{1}{N_i v_w} \sum_{i=1}^{N_i} \mu_\alpha$; $\alpha = x, y, z$, where i is the number of planes along the diffusion axis and $v_w = 29.9\text{Å}^3$ is the volume of a single water molecule. Then, the polarization density of each spherical probe is averaged over the whole trajectory. Finally, because the protein channels under investigation are trimeric, trajectory averages were also averaged over the three equivalent monomers which can be considered statistically independent systems in this context. As schematize in Fig.31, once we know the response function calculated by applying a training set of external electric fields to a water box (fig.31a). The polarization inside the channel, generated by the intrinsic electric field

of the channel (fig.31b-c), is used to calculated the macroscopic electric field via the response function.

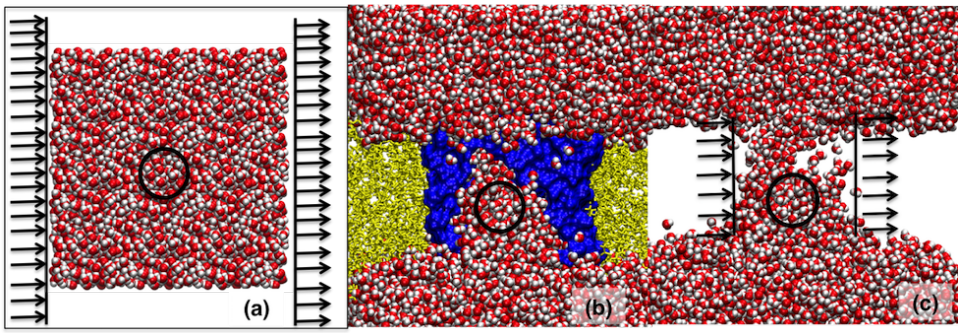

Figure 31: Schematic representation of the proposed method for the calculation of the Macroscopic electric field inside porins.

6.5 ELECTROSTATIC CHARACTERIZATION OF PORINS

Using the above described method the macroscopic internal electric field was first calculated for the porin series from *E.coli* OmpF, OmpC, OmpC20 and OmpC33 used in the previous chapter 5. As it can be observed in Fig.32 the polarization density along the diffusion pathway captures the differences in electrostatics inside the porins. As it was qualitatively describe in chapter 5 the intensity of the transversal component of the polarization density along the path decreases along the series, being the highest transversal polarization density $\sim 0.05 Debye/\text{Å}^3$ for OmpF and the lowest $0.03 Debye/\text{Å}^3$ for OmpC33.

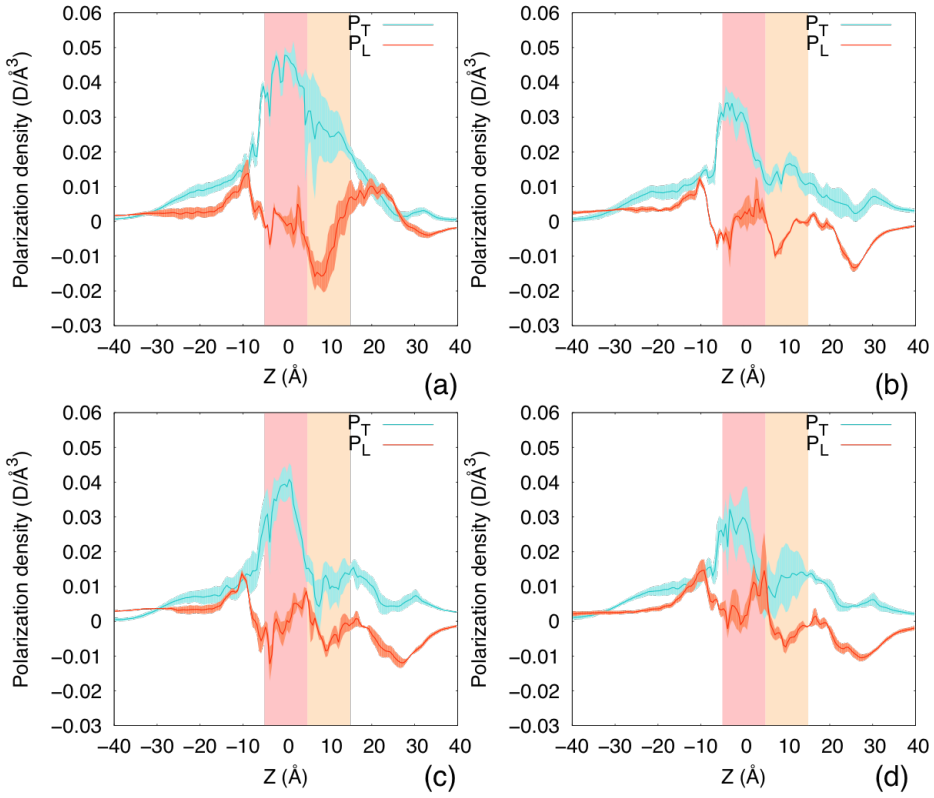

Figure 32: Polarization density. Transversal (cyan) and longitudinal (orange) components depicted for OmpF (a), OmpC (b), OmpC20 (c), OmpC33 (d)

Profiles are conserved when passing from the polarization density to the macroscopic electric field. In Fig.33 we observed how the highest intensity that corresponds to the transversal electric field of OmpF in the constriction region (CR) is $\sim 36 mV/\text{Å}$. In the case of OmpC the transversal component is reduced to $\sim 20 mV/\text{Å}$. The transversal component of OmpC20 is sharper than the one of OmpC and in the mu-

tated OmpC33, the electrostatics is almost destroyed, the transversal component is $\sim 12mV/\text{Å}$.

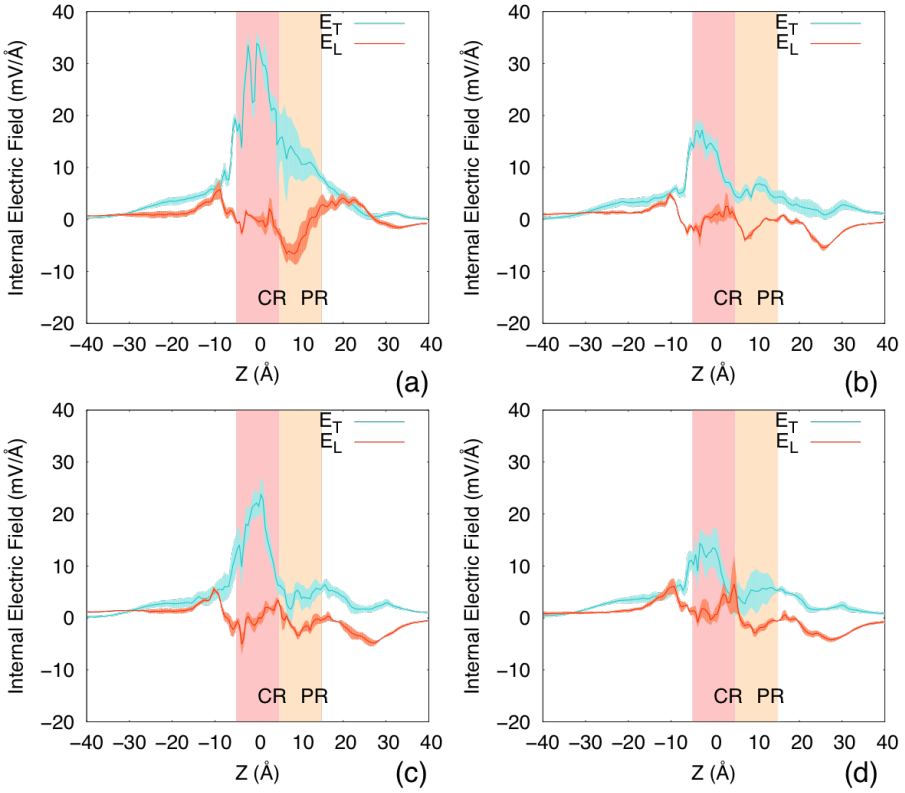

Figure 33: Macroscopic intrinsic electric field. Transversal (cyan) and longitudinal (orange) components depicted for OmpF (a), OmpC (b), OmpC20 (c), OmpC33 (d)

It is interesting to note that all four channels share the same profile for the transversal component of the macroscopic electric field with a central peak in the constricted area. But, while OmpF in the 'pre-orientation' region (PR) has a transversal electric field of $\sim 10mV/\text{Å}$ in the other channels this component is almost zero. The component of the macroscopic electric field parallel to the axis of diffusion on the molecule is low in all four cases in the range of $[0-10]mV/\text{Å}$. In the case of OmpF this component is almost always negative in the central region of the pore, meaning that it will attract positive charges. But it is almost zero in the constriction region (CR) where the transversal component is higher. In OmpC, the trend is conserved but the magnitude is very low and the same happens for OmpC20 and OmpC33.

Although the insertions along the series where mainly found in the extracellular vestibules of the pores we see how pin-point mutations of key charged residues, in this case in the 'pre-orientation' region of the

channel, gradually destroy the electrostatic profile, hence, changing the rules for filtering polar molecules along the series.

6.6 CHANGES IN THE MACROSCOPIC ELECTRIC FIELD DUE TO PH, MEDIA OSMOLARITY

In the previous section we showed how point mutations of key charged residues can modulate and eventually almost destroy the macroscopic electrostatic field inside porins. Environmental factors as pH, media osmolarity or the presence of more metallic ions can also modulate the internal electrostatics of the pore changing the electrostatic rules for filtering polar molecules. In the case of pH the protonation of one or more acidic residues can change the electrostatics of the channel. For OmpF at pH=5 two of the negatively charged residues (E117,D121) in the CR must be protonated as shown in Fig, 35 according to the pKa values evaluated using the PROPKA code.[118,149]

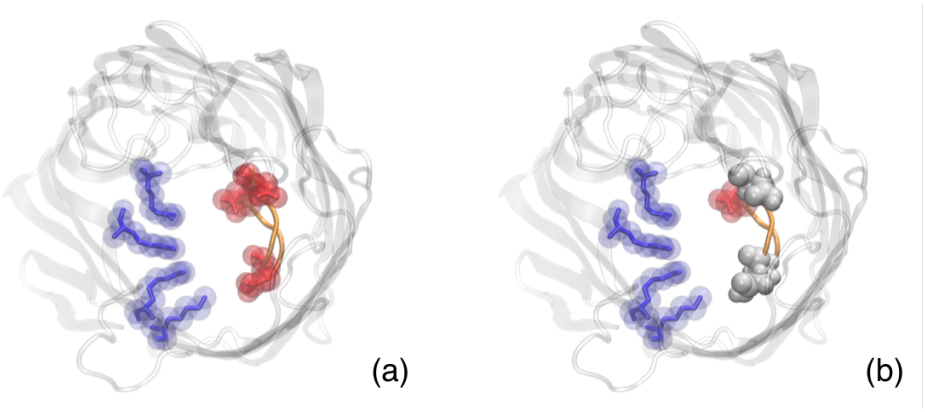

Figure 34: Top view of the constriction region of OmpF (a) at pH=7, (b) at pH=5, were two acidic residues have been protonated.

The macroscopic electric field for OmpF at two different pH values, 5 and 7, is displayed in Fig. 35. As it can be observed in panel (a) the transversal component is smaller at pH=5 than at pH=7. There is a reduction of almost $10mV/\text{Å}$ in the constriction region, where the two acidic residues have been protonated, but the protonation of D121 also affects the electric field in the 'pre-orientation' region (PR) completely destroying the transversal field in this area. The longitudinal component is also highly affected, the negative component in the PR disappears resembling the OmpC electric field longitudinal component. Hence, at pH=5 OmpF turns into OmpC in terms of internal electric field.

Media osmolarity affects the expression of OmpF and OmpC favouring the expression of OmpC in high osmolarity media[104], as it was

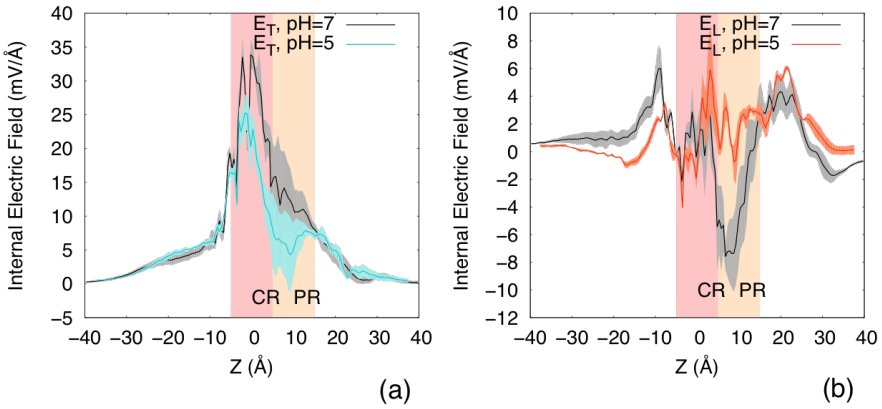

Figure 35: Electric field of OmpF for pH = 7 in grey/black, and pH = 5, (a) in cyan for the transversal, (b) in orange for the longitudinal components.

discussed in the previous sections. In figure 36 the internal electric field is displayed for OmpF in three different ion concentrations: 0.2M KCl (Fig. 36a-b), 0.4M KCl (Fig. 36c-d), and 1M KCl (Fig. 36e-f). For each concentration the transversal and longitudinal components of the electric field are compared with the corresponding component when only counterions are present.

The overall result is the destruction of the transversal component of the electric field with increasing concentration while the longitudinal , differently from pH effects, is very little affected. As well as an increase of the fluctuations due to ion-dynamics. At low salt contration ,0.2MKCl, the reduction is within the fluctuations but at 0.4MKCl the main peak is decreased by almost $10mV/\text{Å}$ and the 'pre-orienation' region disappears. This screening is even more dramatic at 1MKCl in which the transversal component is reduced to half its magnitude with respect to the counterions situation. At 1MKCl also the longitudinal component is slightly affected passing from $\sim -8mV/\text{Å}$ to $\sim -4mV/\text{Å}$ in the PR.

On the contrary, in figure 37 the internal transversal component of the electric field of OmpC is little affected by increasing ion concentration, as well as the longitudinal component, showing overall changes of $\sim 2mV/\text{Å}$. Although changes are in the range of a few $mV/\text{Å}$, it is striking how the 'pre-orientation' region is switched on with increasing ion concentration, becoming similar to OmpF.

As already mentioned OmpF is expressed in rich media, in this type of media a sharp molecular filter is needed to guarantee the uptake of nutrients and avoid noxious species[84]. However, most common antibiotics are characterized by a significant dipole moment[102]. In this case an engineered filter for polar molecules is easy to overcome for

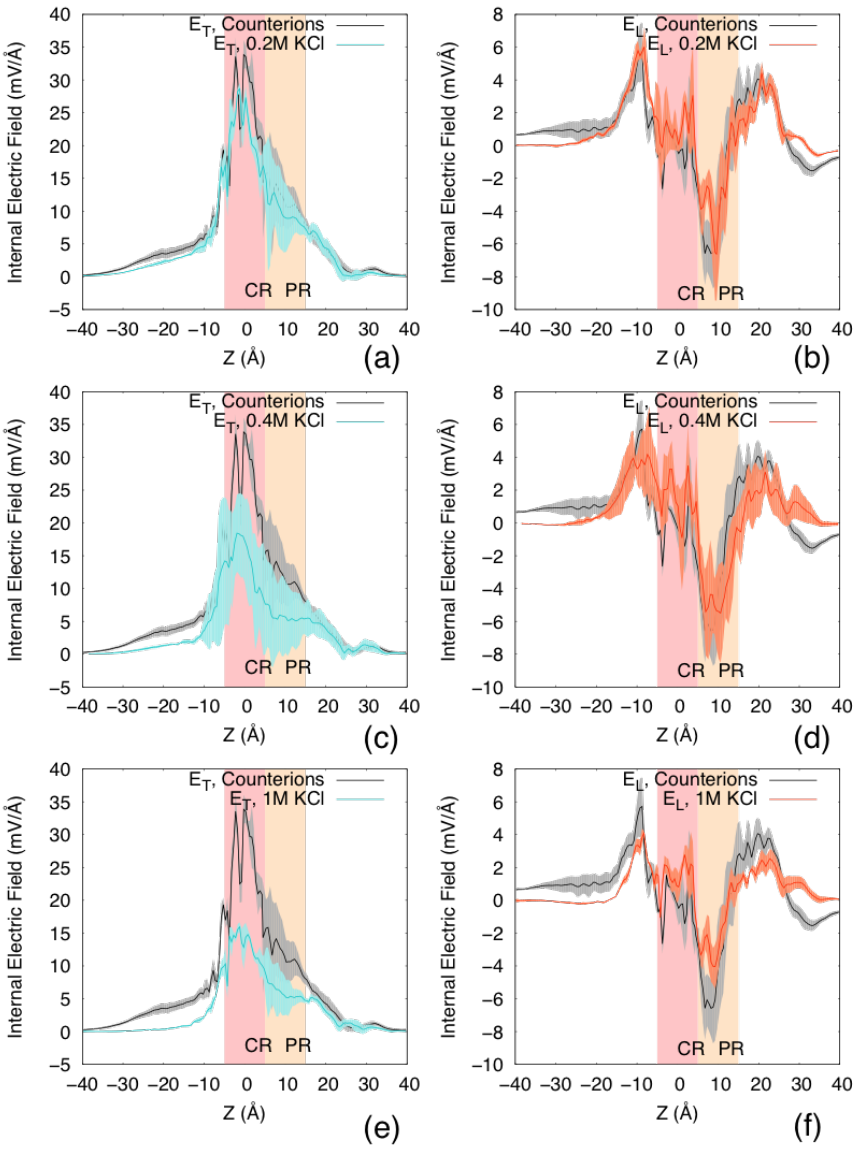

Figure 36: Macroscopic intrinsic electric field compared in different pH media. Transversal (cyan) and longitudinal (orange) components depicted for OmpF (a), OmpC (b), OmpC20 (c), OmpC33 (d)

antibiotics. On the contrary, when bacteria expresses OmpC instead of OmpF it becomes less susceptible to antibiotics. Probably the OmpF-like electrostatic profile is too selective for a poor media, and an overall decreased of the electrostatic filter is needed to guarantee nutrients uptake. Moreover, it has been found that at 0.4MKCl, OmpF and OmpC permeability is similar[84]. According to our results at that concentration both channel's electrostatics are comparable. OmpF is less sharp and OmpC has a higher 'pre-orientation' region, meaning that this

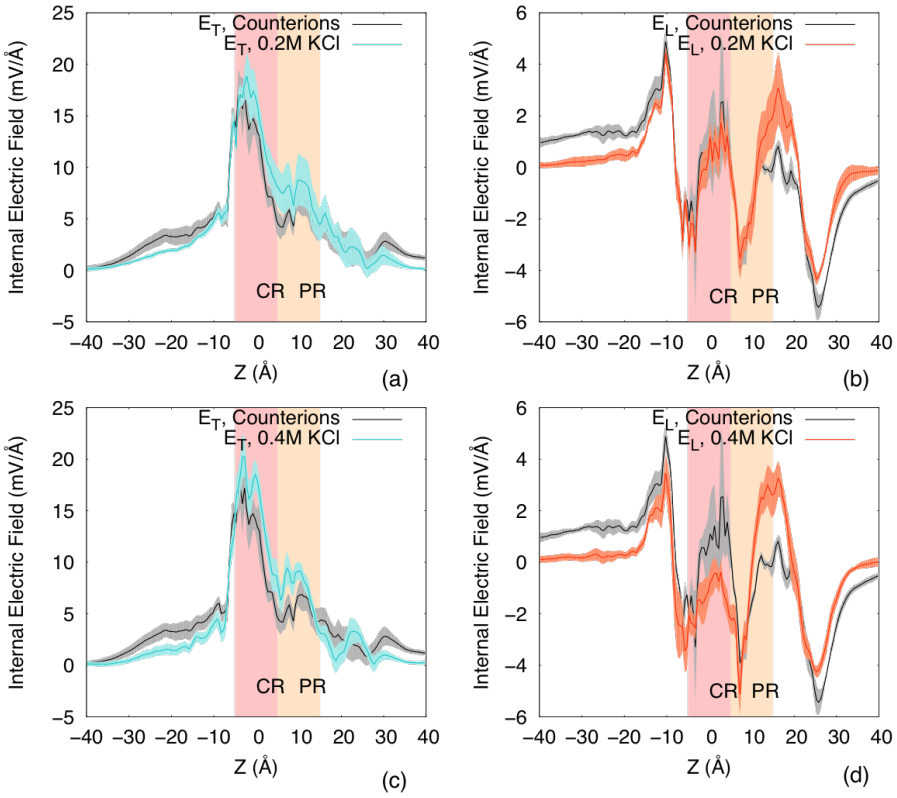

Figure 37: Macroscopic intrinsic electric field compared in different pH media. Transversal (cyan) and longitudinal (orange) components depicted for OmpF (a), OmpC (b), OmpC20 (c), OmpC33 (d)

region might be fundamental for the permeation of polar molecules. Further analysis must be done in this direction.

Finally we present how the presence of metallic ions inside the pore can change the overall electrostatics and hence, the pore selectivity. We analysed the structure of the Major Outer Membrane Porin (MOMP) from *Campylobacter jejuni* in the absence and presence of a metallic ion Ca^{2+} in its central region. The Ca^{2+} ion was present in the X-ray structure, but a further study of the structure in both scenario was needed in order to understand its functionality. As first approach the analysis of the putative pathway of water revealed different paths for each scenario, Fig.38. Even though in the absence of Ca^{2+} a counterion (Na^{+}) sits in the Ca^{2+} coordination position, there is a shift in the putative path that water was predicted to diffuse along. Water seems to avoid passing near the cluster of negative residues that bind the divalent ion located in the region (Fig. 38, purple path). On the contrary, when calcium was present the water pathway was shifted toward the ion position (Fig. 38, ice-blue path). This shift is also induced by the

conformational changes in the loops involved in the Ca^{2+} as seen in fig.38.

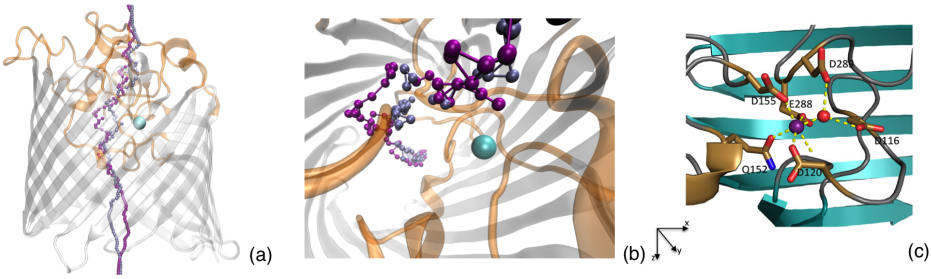

Figure 38: (a) The putative pathway for water diffusion shifts toward the calcium ion when it is present (ice blue), while in the structure without calcium ion (purple), it avoids the cluster of negative residues that coordinate Ca2+. MOMP monomer is shown in cartoon representation.(b) Zoom of the Ca^{2+} binding region. (c) Coordination of the Ca^{2+} ion, in purple, reprinted from the original article.

In the absence of the calcium ion (Fig. 39a) the transverse internal electric field is in the range of $\sim 18mV/Å$, comparable with the OmpC electric field ($\sim 20mV/Å$) but lower than the OmpF one ($\sim 36mV/Å$). When calcium is present the internal electric field is reduced to almost a third of its value due to charge screening, reducing the transversal electric field in the constriction region to $\sim 7mV/Å$ while increasing in the 'pre-orientation' region (PR) almost to $\sim 10mV/Å$. The divalent ion induced a rotation of the transversal electric field. The longitudinal component is also affected mainly in the PR where its magnitude is reduced to a third from $\sim 10mV/Å$ to $\sim 3mV/Å$.

In order to understand the effects of the presence of the cation in the permeation of polar antibiotics we calculated the free energy profiles for ciprofloxacin translocation for both calcium-bound and calcium-free channels. The free energy maps show that the main barrier to translocation was, as expected, located at the constriction zone (Fig. 40). Both free energy maps share common features but differ at the calcium-binding site. In the absence of calcium ciprofloxacin approaches the protein constriction region by entering with its positive group which is attracted toward the negatively charged calcium binding site (Fig.40). This is similar to what happens in OmpF from E. coli, where the negative patch on L3 modulated the translocation of antibiotics and traps a divalent cation[135]. In the presence of calcium ion (Fig.40) ciprofloxacin entered with the opposite orientation, pointing its carboxylic group toward the ion. The translocation of ciprofloxacin starting from the "cis" side required us to apply a voltage above +100 mV to achieve this

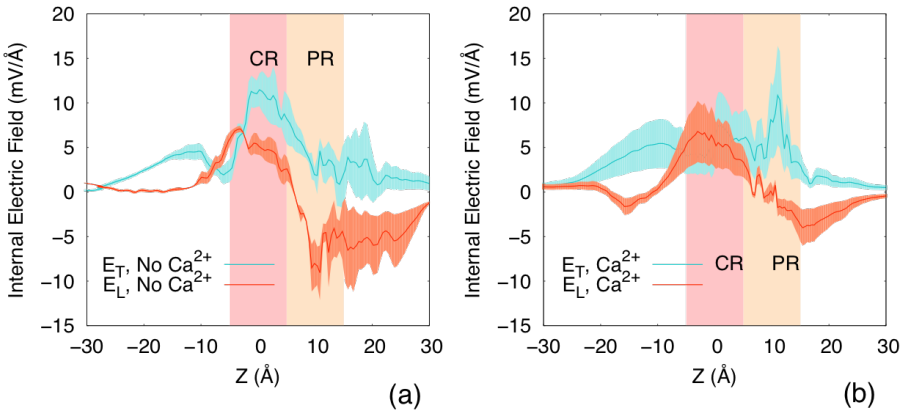

Figure 39: Macroscopic intrinsic electric field inside MOMP from *Campylobacter jejuni*, transversal (cyan) and longitudinal (orange) components are depicted for both scenarios: (a) without Ca^{2+}, (b) with Ca^{2+}

favourable orientation. Critically, molecular dynamics (MD) predicts that the antibiotic follows a different path and has a higher barrier to translocation in the presence of bound Ca^{2+} ion. This change in selectivity might be correlated to the decreased of the longitudinal component of the internal electric field in the 'pre-orientation' region.

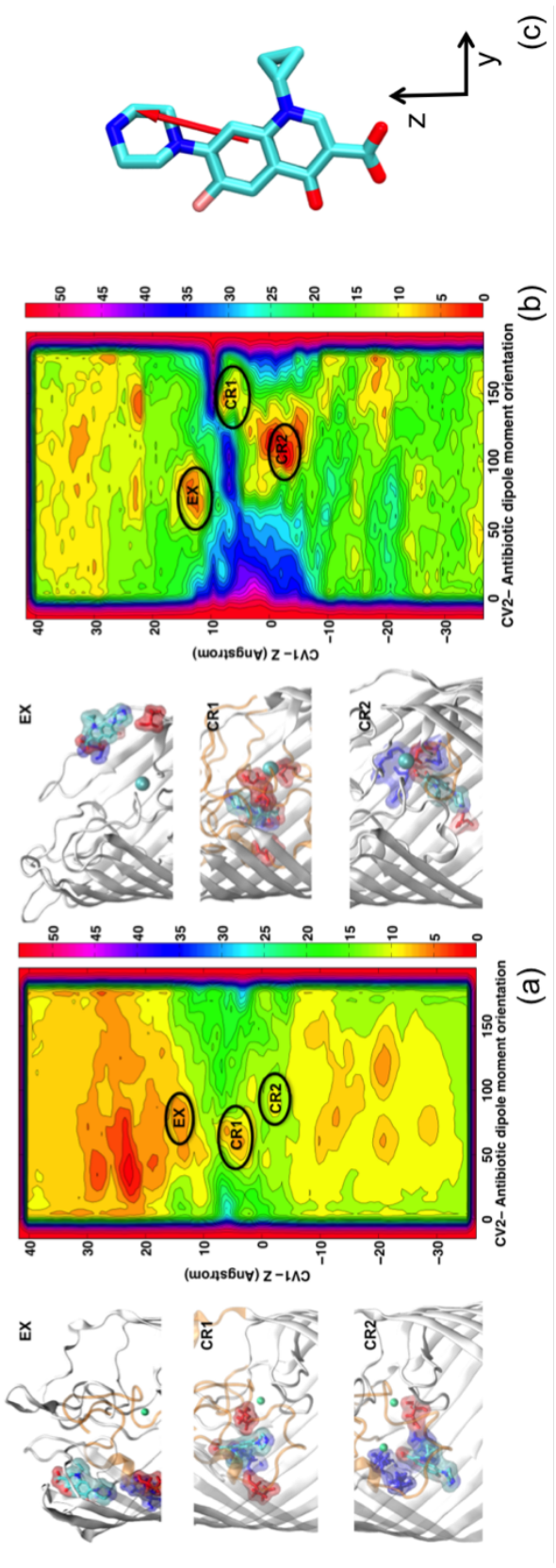

Figure 40: Free energy surface for the translocation of ciprofloxacin through MOMP without (a) and with calcium(b). (c)Antibiotic dipole moment orientation is depicted onto a licorice representation of ciprofloxacin in red. Each isocontour corresponds to a free energy difference of 2 kcal molâĹŠ1. Free energy values were rescaled for each surface in order to have the absolute minimum equal to zero. The most relevant minima for ciprofloxacin translocation have been labeled for both scenarios: one in the extracellular region (EX) and two inside the constriction region (CR_1, CR_2). For each case the most relevant minima are depicted on the left side of the FES.

7

ULTRA-COARSE-GRAINED MODEL FOR THE FREE-ENERGY OF POLAR COMPOUNDS TRANSLOCATION THROUGH PORINS.

Contents

7.1 Summary 85
7.2 Diffusion model 86
7.3 Docking of penicillins 89
7.4 Metadynamics: Translocation of penicillins 90
7.5 The free-energy model 94

Water is the driving force of all nature.

— Leonardo Da Vinci

7.1 SUMMARY

At equilibrium the flux of molecules through a finite channel depends on the concentration of the latter, its diffusion constant and its free-energy along the axis of diffusion. In this chapter we present an ultra-coarse-grained model for the calculation of the free-energy of permeating molecules. We selected a set of penicillins: ampicillin, benzylpenicillin and carbenicillin, for which a co-crystal structure with OmpF is published. In the case of benzylpenicllin we compare it with the crystal structure of a molecule with the same charge. The free-energy surface of the three molecules was calculated with metadynamics and compared with the ultra-coarse-grained model. Although the results are still preliminary, the model captures remarkably well the main barrier for permeation and in the case of the zwitterionic molecule the global minimum conformation of the free-energy for both the model and metadynamics was found to be the co-crystallized structure.

In order to design new antibiotics with enhanced permeability molecular descriptors for permeability are needed. Although enhanced molecular dynamics techniques have proven to be extremely useful for calculating the free energy of antibiotic translocation through porins, the reconstruction of a converged free energy surface is computationally demanding. This problem might be alleviated by new techniques like either the 'Bias Exchange' metadynamics or the 'Variational approach

to enhanced sampling', the latter described in 4.2.2. This elegant mathematical implementation leads to the exact free energy of the system by simply minimizing a functional of the potential and in addition allows to work with many collective variables. As part of this three years of PhD, the 'Variational approach to enhanced sampling' has been set up for the permeability problem discussed in this thesis dissertation, but research is still ongoing and about to deliver results.

As described in the introductory section 1 two general models have been traditionally discussed for permeability through porins: the general diffusion model and the two-barriers-one-binding-site model. Both models differ in the treatment of the particle-channel interaction during diffusion. The co-crystallization of different antibiotics with the OmpF porin from *E.coli*[175] showed that there's not a unique binding site for polar molecules inside OmpF: ampicillin, carbenicillin and ertapenem showed unexpectedly different binding sites. This three antibiotics exhibit different charge properties at pH=7, ampicllin is zwitterionic, while ertapenem is negatively charged and carbenicillin is charged -2. In this thesis we decided to substitute ertapenem, that is not completely solved in the co-complex, with benzylpenicillin as they have the same charge and benzylpenicillin is more similar structurally to the other two antibiotics.

We confirmed these binding sites using docking techniques **??**, preliminary results are shown in 7.3, and with metadynamics 7.4. Nevertheless, in order to put forward the physico-chemical parameters controlling permeability the static results obtained from docking are not enough and a dynamical picture is needed.

7.2 DIFFUSION MODEL

Aiming to model diffusion along one-dimension, in this case the diffusion axis of the channel, z, one might start by solving the equation governing the process, the diffusion equation in 1D,

$$\frac{\partial \phi(z,t)}{\partial t} = \frac{\partial}{\partial z} D(z) \Big(\frac{\partial \phi(z,t)}{\partial z} + \frac{\phi(z,t)}{k_B T} \frac{\partial U(z)}{\partial z} \Big) \tag{50}$$

where $\phi(z,t)$ is the molecule probability density, $D(z)$ its local diffusion coefficient, $U(z)$ the free energy of the molecule inside the pore, k_B the Boltzmann constant and T the system temperature. The flux, or number of molecules per second that permeate the channel is,

$$J(z,t) = -D(z) \Big(\frac{\partial \phi(z,t)}{\partial z} + \frac{\phi(z,t)}{k_B T} \frac{\partial U(z)}{\partial z} \Big) \tag{51}$$

so that the continuity equation is satisfied,

$$\frac{\partial \phi(z,t)}{\partial t} + \frac{\partial}{\partial z} J(z,t) = 0 \tag{52}$$

If we consider a quasi-stationary state in which the molecule probability density does not depend on time (quasi-stationary equilibrium), then according to the continuity equation the flux is constant, J_0, and hence, we obtain the time-independent diffusion equation,

$$J_0 = -D(z)\Big(\frac{\partial \phi(z)}{\partial z} + \frac{\phi(z)}{k_B T}\frac{\partial U(z)}{\partial z}\Big) \tag{53}$$

assuming a Boltzmann distribution for the molecules probability density, $\phi(z) = \varphi(z)e^{(-U(z)/k_B T)}$, in the time-independent diffusion equation 53,

$$\frac{\partial \varphi(z)}{\partial z} = -J_0 \frac{e^{\frac{U(z)}{k_B T}}}{D(z)} \tag{54}$$

which solution is,

$$\varphi(z) = \varphi_0 - J_0 \int_0^z \frac{e^{\frac{U(z')}{k_B T}}}{D(z')} dz' \tag{55}$$

so that the probability density is,

$$\phi(z) = \varphi_0 e^{-\frac{U(z)}{k_B T}} - J_0 e^{-\frac{U(z)}{k_B T}} \int_0^z \frac{e^{\frac{U(z')}{k_B T}}}{D(z')} dz' \tag{56}$$

The boundary conditions of the problem in this case are: the length of the channel: z=L, and the concentration at both ends of the channel. For small concentrations, the single-probability density is equal to the concentration,

$$\phi(z=0) = c_{z=0} = c_0; \phi(z=L) = c(z=L) = c_L \tag{57}$$

Finally the probability density for the selected boundary conditions reads,

$$\phi(z) = e^{-\frac{U(z)-U(0)}{k_B T}} \Big(c_0 - J_0 \int_0^z \frac{e^{\frac{U(z')-U(0)}{k_B T}}}{D(z')} dz'\Big) \tag{58}$$

where the integration constants are;

$$\varphi_0 = c_0 e^{\frac{U(0)}{k_B T}} \tag{59}$$

$$J_0 = \frac{c_0 e^{\frac{U(0)}{k_B T}} - c_L e^{\frac{U(L)}{k_B T}}}{\int_0^L \frac{e^{\frac{U(z)}{k_B T}}}{D(z)} dz} \tag{60}$$

In equilibrium when the diffusion current is zero, the probability density to find a molecule inside the channel is,

$$\phi(z) = c_0 e^{-\frac{U(z)-U(0)}{k_B T}} \tag{61}$$

only depending on the initial concentration and the free energy inside the channel. Hence, the total flux (eq. 51) in equilibrium only depends on both the molecule diffusion constant and the free energy inside the channel, respectively $D(z)$, and $U(z)$.

In the previous chapters, especially in 5, we conclude that the translocation free energy comes from the interplay between the entropic barrier imposed by the channel size reduction and the electrostatic interaction between the molecule and the channel. The entropic or steric barrier [1] of the channel can be obtained from the cross-section area of the channel and the dimension of the molecule as,

$$U_{steric}(z) = k_B T ln\Big(\frac{S(z) - S_{molecule}}{S(0) - S_{molecule}}\Big) \tag{62}$$

and the electrostatic interaction reads:

$$U_{electrostatic}(z) = Q_{molecule} V(z) + \langle \vec{E} \cdot \vec{D}_{molecule} \rangle \tag{63}$$

where $V(z)$ is the integral of the macroscopic electric field $\vec{E}$ along the axis of diffusion of the pore.

1 The derivation of the steric barrier is beyond the scope of this thesis derivation, as it is part of another member of the group work. Nevertheless, the final result is necessary for the free-energy model presented in this dissertation.

7.3 DOCKING OF PENICILLINS

Three antibiotics have been recently co-crystallized with OmpF from *E.coli*, namely ampicillin, carbenicillin and ertapenem (PDB-ids: 4GCP,4GCS,4GCQ). The reported crystals[175] have a resolution of less than 2Å but in the case of ertapenem the molecule is not fully resolved. In figure 41 the main interactions between the ligand and the protein are reported in a two-dimensional map.

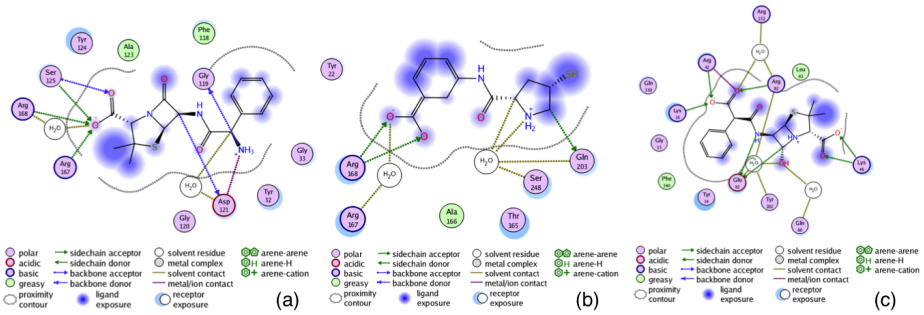

Figure 41: Ligand interaction diagrams of the co-crystal structures (PDB-ids: 4GCP,4GCS,4GCQ) of: (a) ampicillin, (b) benzylpenicillin and (c) ertapenem fragment, reported in[175]. The main interactions between the protein and the ligand are depicted using MOE[33].

We used a genetic algorithm based flexible docking software[73] to reproduce the co-crystals in figure **??**. Among the different score functions available, we selected CHEMSCORE as it ranked as first conformation the ampicillin co-crystal structure. In the case of ertapenem the docking results are poor as the small fragment presented in the x-ray structure is not enough to select well the docking region and more extensive analysis is needed. In the case of ampicillin and carbenicillin we performed 50 docking runs in a 15Å sphere centered in the center of mass of the minimized molecule crystal. The top ranked structures for ampicillin and carbenicillin are depicted in figure 42. For ampicillin the first ranked structure has a root-mean-square (rmsd) value of 1.84Å and the second ranked structure of 4.34Å. For carbenicillin the first ranked structure has an rmsd of 1.15Å and the second of 1.38Å.

Although the docking results are pretty good, as it is not clear the role of the binding site in the permeability of the problem molecules designed to have a high affinity for one of presented binding sites may not imply good permeation, as it was pointed out before[175]. A further analysis extending the docking searching region to the whole lumen is needed in order to understand better the affinity of the different identified regions towards certain molecules, but it is out of the scope of this thesis dissertation.

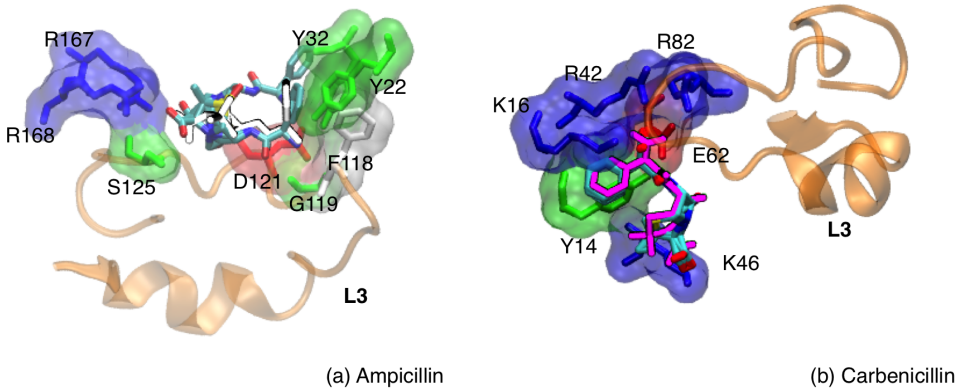

Figure 42: Best ranked structures superimposed to the crystal structure of: (a) ampicillin and (b) carbenicillin. The OmpF residues involved in the in the protein-ligand interaction have been highlighted in licorice with its van der waals surface in transparent material and coloured according to the residue type. The loop L3 is depicted as cartoon in orange as reference.

7.4 METADYNAMICS: TRANSLOCATION OF PENICILLINS

We reported in Fig.43 the three free energy surfaces corresponding to the translocation of ampicillin (fig.43d), benzylpenicillin (fig.43e) and carbenicillin (fig.43f). The antibiotic position with respect to the main axis of diffusion (Cv1) is reported in the y-axis, while the x-axis corresponds to the orientation of the beta-lactam ring for each of the antibiotics (CV2). The vector chosen for representing the beta-lactam ring orientation is plotted as a red arrow on the chemical structure of each of the considered antibiotics in figure 43a,b,c. For ampicillin and carbenicillin in figure 43 cyan ovals are placed to highlight the region were they were co-crystallized with the OmpF protein (PDB-ids: 4GCP, 4GCQ respectively)[175]. In the case of carbenicillin the selected region, with the carboxilic group pointing to the periplasmic vestibule in the FES it is not a deep minima, but the one with the carboxilic group pointing to the extracellular region. Though the ertapenem crystal structure in the co-complex (PDB-id: 4GCS) is not complete, only a fragment is reported, its position inside OmpF, highlighted with a cyan oval, corresponds to a minimum for benzylpenicillin in figure 43e.

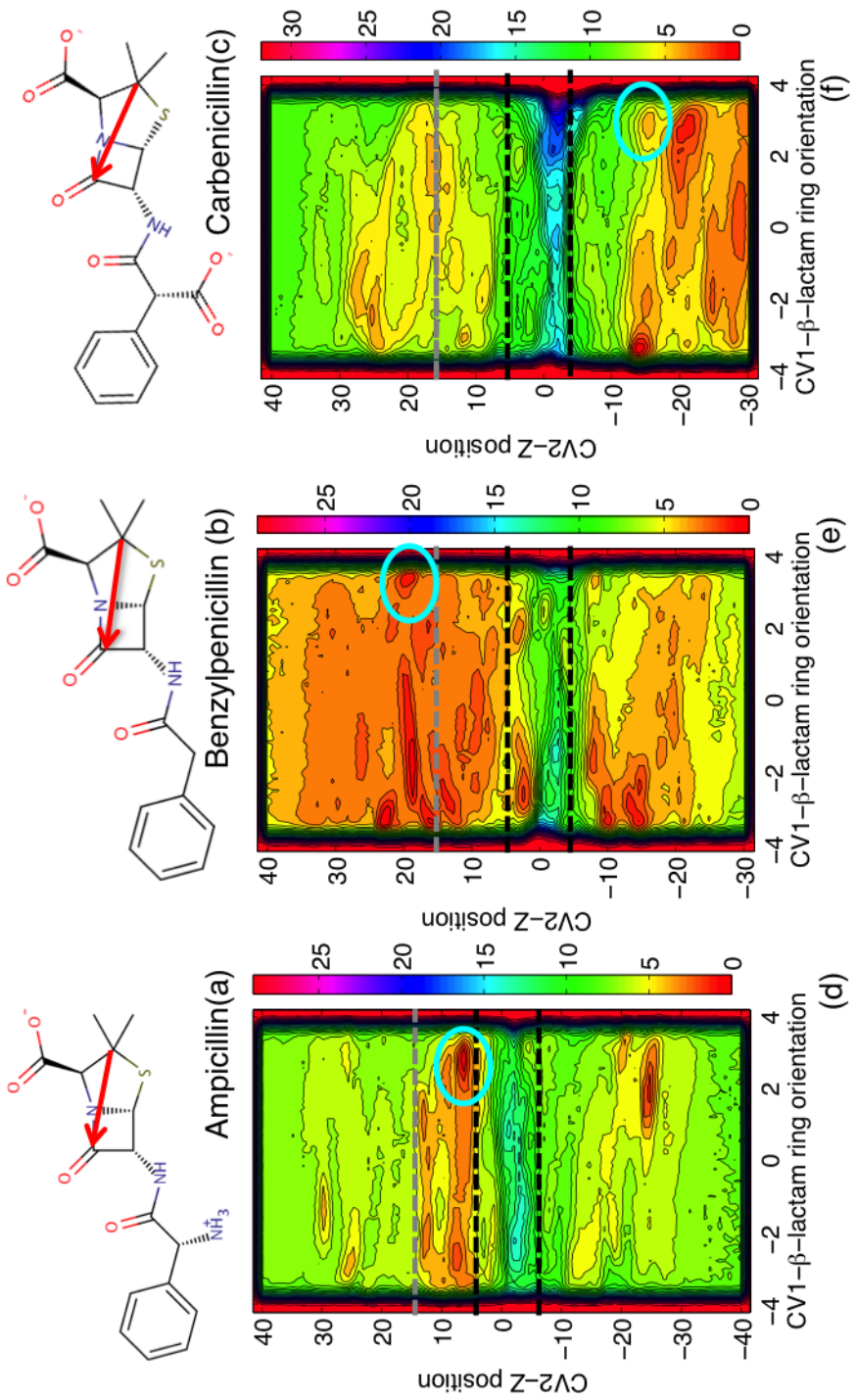

Figure 43: The chemical structure for the two penicillins considered is displayed in together with the free energy surface of the translocation for (a-d) Ampicillin, (b-e) benzylpenicillin and (c-f) carbenicillin. Y-axis corresponds to z coordinate (along the axis of diffusion) of the antibiotic and x-axis to the orientation of the beta-lactam ring. Each line corresponds to a difference of 1 Kcal/mol. Constriction region is delimited with dashed black lines between −5.0Å and 5.0Å along the axis of diffusion (z) and the 'pre-orientation' region (PR) is delimited at from 15Å with gray dashed lines. The region were the antibiotic-protein co-crystal was found is highlighted with a magenta oval.

In figure 44 the most relevant conformation for each of the minima highlighted in figure 43 are depicted. It is interesting to note how the neutral zwitterionic molecule (ampicillin) binds in the 'pre-orientation' region (PR) of the pore, the negatively charged (ertapenenm/benzylpenicillin) in the extracellular vestibule (EV) and the double-negatively charged (carbenicillin) binds in the exit of the constriction region (CR). Moreover, in the zwitterionic case (fig 43d) the 'pre-orientation' region is the more energetically favourable region inside the pore, as the minimum at $z \sim -25$Å corresponds to the bottom border of the barrel, while the CR and its exit are less favourable. In the CR the available space for the molecule to be aligned to the transversal electric field calculated in chapter 6 is reduced, but the alignment in the PR of the dipole moment of the molecule with the internal electric field calculated before, is perfect (fig.44a). In the case of the negatively charged molecule (fig. 43e), there are minima spread in all the regions, even in the CR, probably due to the fact that the charge-charge interaction is stronger than the dipole-electric field one. But the barrier to cross the constriction region is higher than in the zwitterionic case, as the decorated eyelet, especially the negative residues of the loop L3, tune the channel selectivity towards positive charges. In the case of the double negatively charged molecule (fig.43f), the barrier to cross the CR is even higher, and minima are only found near the basic ladder of the pore.

A closer look to the pore-antibiotic conformation extracted from the minima highlighted in the free-energy surfaces is given in figure 45. For the zwitterionic molecule (fig.43a) the reported crystal resolution is 1.98Å, the rmsd of the metadynamics conformation with respect to the crystal structure is $\sim$ 2.8Å which is not a bad agreement taking into account that the metadynamics CV's are absolutely general. The conformation is rotated in figure 45a, so that the electric dipole moment of ampicillin looks perpendicular to the axis of diffusion, but the original situation can be observed in figure 44a. The carboxilic group of ampicillin is in contact with the two arginines R167 and R168 while its amino group faces the acidic D121 from the constricting loop L3.

For the negative molecule case the resolution reported for the ertapenem co-crystal is 2.2Å. But, as already noticed the molecule is not complete. However, we can observe how the carboxilic group of benzylpenicillin and ertapenem are close contact with the same arginines found in the ampicillin co-complex, while the phenyl-group is accommodated in the hydrophobic residues of the external loops. In the carbenicillin case the reported resolution for the co-crystal is 1.87Å, and he rmsd of the metadynamics conformation with respect to the co-crystal structure is $\sim$ 3.42Å which is a bit high but not bad. In this case the

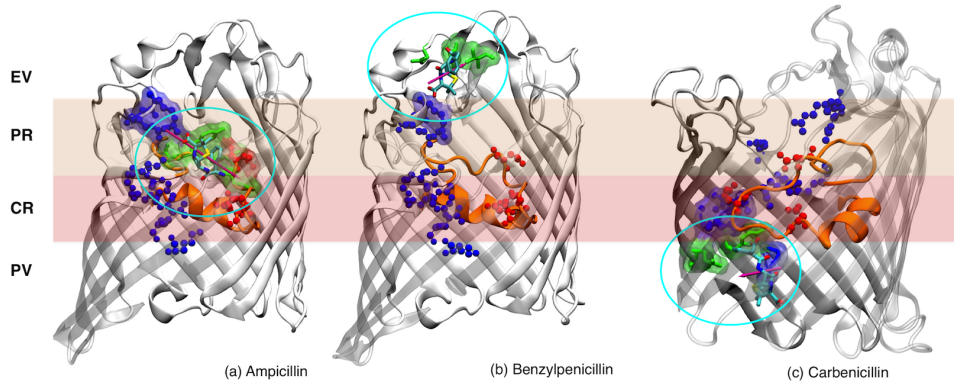

Figure 44: Most relevant conformations from the selected free energy minima. The antibiotic conformation is depicted in licorice, with its electric dipole moment in magenta for (a) ampicillin, (b) benzylpenicllin and (c) carbenicillin. The OmpF pore is represented as a white cartoon with the constricting loop (L3) in orange. The most relevant charged residues are highlighted in cpk representation and coloured accordantly to its charge. The residues within a sphere of radius 4Å centered in the antibiotic are depicted as licorice, with its van der waals surface in transparent material, and coloured accordingly to its type. In the case of carbenicillin the view is rotated by 90°. The different regions of the pore are labelled, the 'pre-oreintation' region (PR) and the constriction region (CR) are highlighted following the color scheme of chapter 6, orange and red respectively.

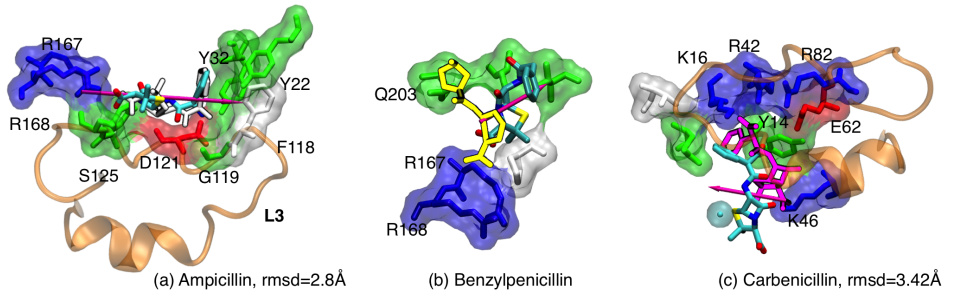

Figure 45: The antibiotic conformation is depicted in licorice with its dipole moment as a magenta arrow.The residues within a sphere of radius 4Å centered in the antibiotic are depicted as licorice, with its van der waals surface in transparent material, coloured accordingly to its type and labelled. The loop L3 is also depicted in orange as reference. The crystal structure of (a)ampicillin (white) and (c) carbenicillin (magenta) are superimposed to the conformation obtained from metadynamics, and the rmsd is reported. In the case of benzylpenicillin (b), the ertapenem fragment is reported as reference.

co-crystal structure is not the minimum conformation in metadynamics but the one with the carboxilic-group interacting with the basic-ladder, probably more specific CV's are needed in order to get the co-crystal structure as a minimum.

7.5 THE FREE-ENERGY MODEL

As introduced in section 7.2 after solving the diffusion equation with the suitable boundary conditions for the diffusion of a molecule through a finite channel the flux of molecules at equilibrium only depends on the diffusion constant of the molecule and its free-energy along the diffusion axis. In figure 46 we present the preliminary results of an ultra-coarse-grained model for the calculation of the molecule free-energy along the diffusion pathway applied to the three penicillins studied in the previous section.

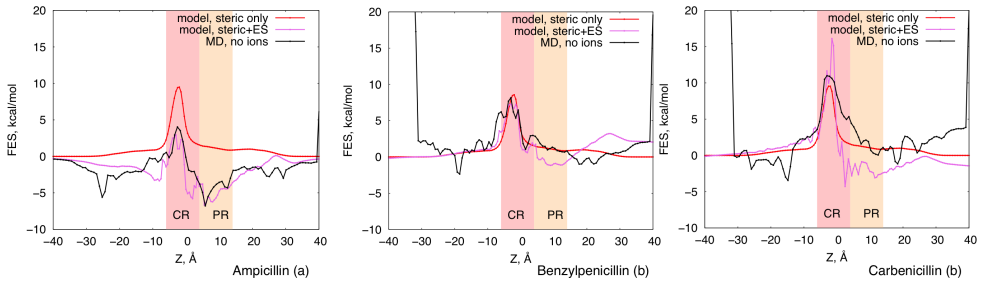

Figure 46: For the three studied penicillins: ampicllin(a), benzylpenicillin (b) and carbenicillin (c), the projection of the free-energy surface, obtained with metadynamics, along the diffusion axis is plotted in black, the steric-entropic contribution to the free-energy is plotted in red and the free-energy model : steric (entropy) + electrostatic interaction (enthalpy) is plotted in violet. The 'pre-orientation' region is highlighted in orange and the constriction region (CR) in red.

The main barrier for translocation comes from the size reduction of the pore and the size of the molecule, steric barrier, plotted in red for the three cases. As the three molecules have a similar size, minimal projection area of $\sim 50\text{Å}^2$ (ampicillin: 50.47Å^2, benzylpenicillin: 46.67Å^2 and carbenicillin: 50.00Å^2)[102], the steric contribution is very similar for ampicillin and carbenicillin $\sim 9.5 kcal/mol$ and little less for benzylpenicillin $\sim 8.5 kcal/mol$. However, the free-barriers barriers calculated with metadynamics are different for the three molecules: $\sim 5 kcal/mol$ for ampicillin, $\sim 8.5 kcal/mol$ for benzylpenicillin and $\sim 10 kcal/mol$ for carbenicillin. In the case of ampicillin (fig. 7a) the electrostatic interaction of its electric dipole moment with the inter-

nal electric field reduces the steric barrier by $\sim 3kcal/mol$, and interestingly the deepest minimum along the one-dimensional free-energy coincides for both the model and metadynamics at the co-crystal conformation, where the alignment of the dipole moment of ampicillin to the internal electric field of OmpF is perfect. In the case of benzylpenicillin the dipole/electric field reduction of the barrier is compensated with the repulsive charge/electrostatic potential additional interaction and the free energy barrier is almost equal to the steric contribution. This gets worse in the double-charged carbenicillin, where as anticipated the repulsive charge/electrostatic potential interaction in the CR is high and the resulting free-energy in both metadynamics and the model is higher than the steric barrier. Although the peripheral regions of the channel are not well described with our model the bottleneck for translocation is remarkably well-described with this simple theoretical model in which our channel is a simple charge decorated hourglass object.

The ultra-coarse-grained model can be set-up for the channel by calculating its cross-section area, the electric field and the electrostatic potential along the axis of diffusion. Once these three descriptors are defined it is possible to estimate the whole free energy along the channel for a molecule represented by its size, charge and electric dipole moment in a few seconds. This model would allow to virtually screen libraries of molecules searching for hits with enhanced permeability. Although the current model is based on few fundamental energetic terms, it can be easily extended in the future to account for specific interactions like hydrogen bonds or hydrophobic interactions.

8

CONCLUSIONS

In this thesis dissertation we have employed different computational techniques to shed some light into the mechanism and physical rules behind the permeability of antibiotics in Gram-negative bacteria through membrane channels or porins.

We have shown how porins can be modelled as hourglass shaped nanopores decorated with charged motifs which work as 'molecular sieves' allowing the diffusion of polar molecules. The qualitatively electrostatic pattern calculated for water, or water 'choreography' along the diffusion pathway, revealed striking differences among different pores with different susceptibility to antibiotics. Interestingly the narrower and charged region of the protein was always conserved along the series, as it may play a crucial role in the permeability barrier. The four channels analysed only differ in the internal electrostatics outside the constricted region of the protein. However, as it was shown through the analysis of antibiotic's 'choreography' along the translocation pathway, the same molecule follows a different path in each channel highlighting the importance of the whole pore electrostatics in the permeation process. Moreover, the ability of the molecule to reorient its electric dipole moment in order to align to the channel's electrostatic and at the same time fit in the eyelet region seems to be of great importance for permeation.

The quantification of the macroscopic electric field along the channel axis allows to quantify the differences revealed by water 'choreography' but also to understand better the influence of environmental changes as pH, osmolarity or metallic ions in the electrostatic along the diffusion pathway. Further, we shed some light in the OmpF/OmpC different susceptibility despite its great similarity and moreover, its comparable permeability at high salt concentrations. Furthermore, the quantification of the macroscopic field and the electrostatic potential, along the diffusion pathway, allowed as to put forward an ultra-coarse-grained model for the diffusion problem. In this model the free-energy of a small diffusing molecule is governed by the interplay between the entropic barrier, due to the size-exclusion criteria, and the enthalpic compensation arising from the electrostatic interaction with the internal electrostatic of the pore.

We tested the ultra-coarse-grained model with a set of penicillins with different electrostatic properties: zwitterionic, negatively charged

and double-negatively-charged. The three fundamental energetic terms of our model are enough to reproduce quite satisfactory the one-dimension free-energy obtained with metadynamics. In particular, we reproduce remarkably well the central barrier and the position of the main minima for the zwitterionic molecule. It is worth to mention that the position of the antibiotics in the recently solved co-complexes correspond to minima in the free-energy surface calculated with metadynamics, that we further used as reference to set our model.

Part III

COMPENDIUM

Filtering with the Electric Field: The case of *E. Coli porins*

THE JOURNAL OF PHYSICAL CHEMISTRY Letters

Letter

pubs.acs.org/JPCL

Filtering with Electric Field: The Case of *E. coli* Porins

Silvia Acosta-Gutierrez,[†,§] Mariano Andrea Scorciapino,[‡,§] Igor Bodrenko,[†] and Matteo Ceccarelli*[,†]

[†]Department of Physics, University of Cagliari, Cittadella Universitaria di Monserrato, S.P.8−km 0.700, 09042 Monserrato, Cagliari, Italy

[‡]Department of Biomedical Sciences, Biochemistry Unit, University of Cagliari, Cittadella Universitaria di Monserrato, S.P.8−km 0.700, 09042 Monserrato, Cagliari, Italy

Supporting Information

ABSTRACT: Although the role of general bacterial porins is well established as main pathway for polar antibiotics, the molecular details of their mode-of-action are still under debate. Using molecular dynamics simulations and water as a probe, we demonstrated the strong ordering of water molecules, differently tuned along the axis of diffusion in the transversal direction. Preserved features and important differences were characterized for different channels, allowing to put forward a general model for molecular filtering. The intrinsic electric field, responsible for water ordering, (i) filters those dipolar molecules that can compensate the entropy decrease by dipole alignment in the restricted region and (ii) might create an additional barrier by changing direction when escaping from the restricted region. We tested this model using two antibiotics, cefepime and cefotaxime, through metadynamics free energy calculations. A rational drug design should take this into account for screening molecules with improved permeation properties.

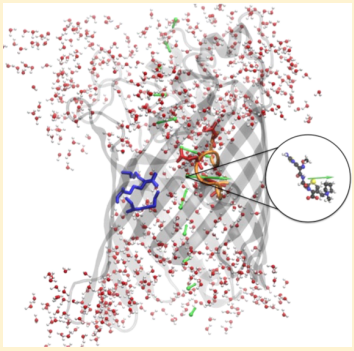

Since X-ray structures of protein channels became available, much attention has been devoted to small specific channels, such as ion and aquaporin channels,[1−3] and to generic channels large enough to allow the passage of DNA.[4] The interest in those unspecific channels allowing the passive transport of medium-size molecules has recently arisen, for instance, toward eukaryotic VDAC, which is expressed in the mitochondrial outer membrane,[5] or the prokaryotic OmpF/OmpC family, expressed in the outer membrane of all *Enterobacteriaceae*.[6] However, function and mechanism of these β-barrel channels are still under debate.[7−9] Their classification as water-filled channels makes characterization of the interaction with water necessary. For this reason, water has been conveniently used here as a molecular probe to sense the internal electric field of OmpF/OmpC channels. These trimeric proteins serve as a general pathway for the passive exchange of hydrophilic molecules up to 600 Da across the bacterial outer membrane.[10] The internally folded loop L3 determines the overall hourglass-shaped structure of each monomer, with a central constriction region (CR) characterized by a rather small size (3 Å radius compared to 17 Å at the mouths).[11] The observation that growth conditions characterized by high level of nutrients, such as in the mammal intestine, favor the expression of the smaller OmpC over OmpF,[10] led to the conclusion that pore size was probably the most important feature in modulating channel permeability.[11] However, numerous computational and experimental evidence are being gathered, pointing to the internal electrostatics.[12,13] The CR, indeed, is characterized by the negatively charged loop L3 that faces a positive "basic ladder". Recent experiments have shown that modulation of electrostatics by the medium osmolarity can account for the apparent difference in the permeability of OmpF and OmpC,[13] thus bolstering the opinion that electrostatics might play a key role in filtering. Understanding the key features responsible for permeability and selectivity of these Omp channels is fundamental, as they represent the main access to the bacterial cell for hydrophilic antibiotics from different classes, like β-lactams.[10] One of the pathogen strategies for drug resistance is to limit the uptake by modifying the porins or their relative expression.[14] It is now widely recognized that our inability to come up with novel effective antibiotics for Gram-negative pathogens mostly relies upon the insufficient comprehension of the molecular basis behind penetration through the outer membrane.[15] Studies have mostly focused on the CR of porins but a consistent picture is still missing.[8,9,16−18] Finding the translocation "golden rules" appears chimeric. Despite the unspecific character of this channel family, the available results suggest that permeation rates depend on quite general antibiotic physicochemical properties such as size, charge, hydrophobicity, and flexibility, without any evident correlation.

Some theoretical investigations are already reported in the literature, aimed at characterizing the electrostatics of water inside channels[19] and of OmpF in detail. On the basis of a macroscopic multidielectric model, Karshikoff et.al[20] calculated a transverse electric field up to a maximum value of 36 mV Å^{-1} at the CR. A full atomistic description of ion flow through the OmpF trimer with molecular dynamics (MD) simulations revealed a distinct pathway for anions and cations.[21] Full-atom, though rather short, MD simulations[22] of the transport of small

Received: March 23, 2015
Accepted: April 28, 2015
Published: April 28, 2015

DOI: 10.1021/acs.jpclett.5b00612
J. Phys. Chem. Lett. 2015, 6, 1807−1812

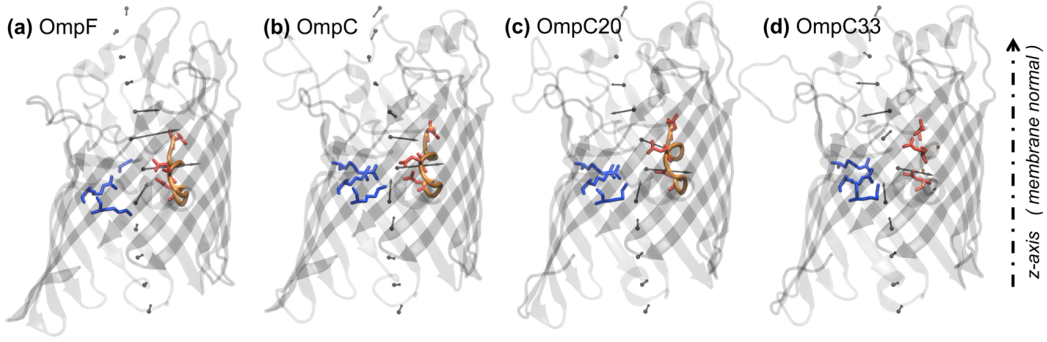

Figure 1. Dipole water orientation in (a) OmpF, (b) OmpC, (c) OmpC20 and (d) OmpC33 from *E. coli*. A cartoon of the first monomer is shown together with the positively and negatively charged residues of the "basic ladder" and loop L3 (orange), respectively. The former are reported in blue, the latter in red. Vectors represent the time average of the total dipole moment $\boldsymbol{\mu}_t$ of the water molecules found in the corresponding protein section, normalized by the number of water molecules N_w.

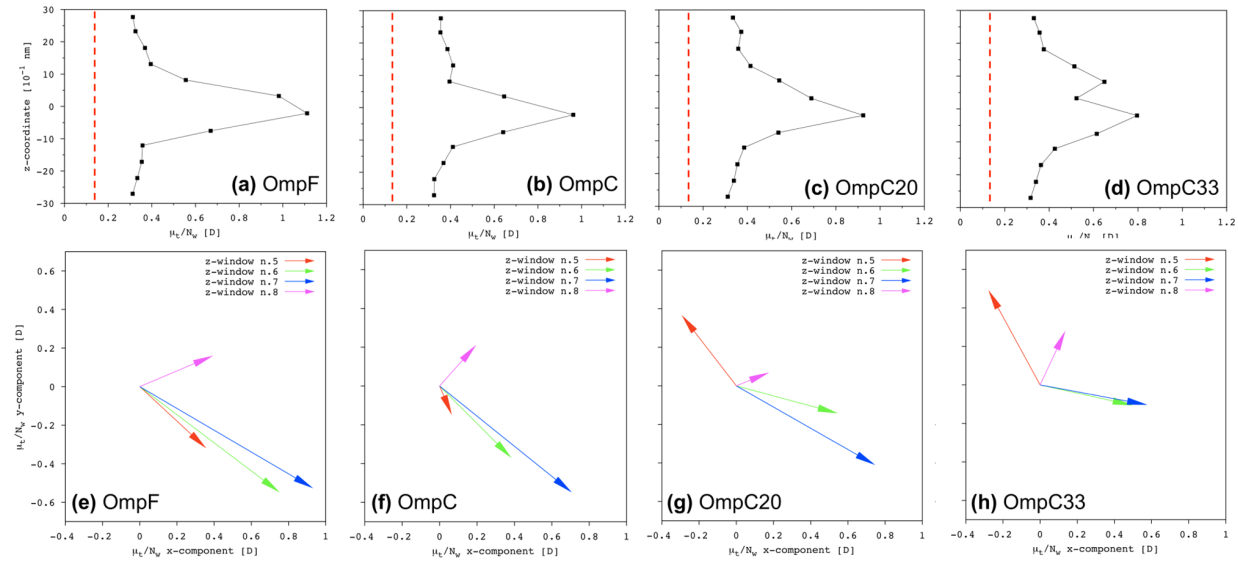

Figure 2. (a–d) The $\boldsymbol{\mu}_t/N_w$ module profile is shown along the channel axis. The red dashed line represents the value obtained for bulk water (0.12 D). In (e–h) the *xy* projections of the μ_t/N_w vectors pertaining to the central *z* windows of the protein channel are reported.

polar molecules have emphasized the existence of a strong transverse electric field halfway through the porin. In the present work, MD simulations in the microsecond time-range of the whole trimer embedded in a lipid membrane are presented, aimed at analyzing the internal electrostatics of different porins in detail, namely, OmpF, OmpC, and the two mutants OmpC20 and OmpC33, the first and the last one of a clinical series,[6] respectively. Interestingly, the structures of the OmpC mutants showed essentially an unchanged size,[6] offering a rare opportunity to investigate possible modulations of the internal electrostatics in correlation with the measured altered antibiotics permeability. Because water completely fills these channels and possesses a large dipole moment though its small size, it represents the natural probe for channels' internal electrostatics and the electric field experienced by diffusing molecules. Without restricting the attention to the CR but looking at the entire lumen, we could reveal a remarkable water "choreography" across the channel, with striking differences among the four porins investigated, particularly at the interface between the extracellular vestibule (EV) and the CR.

The multiple-structure alignment of the four porins under investigation (Supporting Information Figure S1) shows some interesting features: (i) insertions resulted only in extracellular loops of different length, (ii) the majority of charged residues mutations are observed in the extracellular loops, and (iii) at the CR, both the loop L3 and the "basic ladder" are highly conserved. This clearly suggests that CR electrostatics is comparable in OmpF and OmpC and it is not significantly altered throughout the series of OmpC mutants, isolated from increasingly resistant *E. coli* clinical strains.[6] This feature appears the fundamental structural determinant for correct filtering of nutrients and hard to be significantly mutated. Specific mutations consequently are due in other regions of the channel, allowing for filtering out noxious species but allowing the passage of desired nutrients at the same time. In order to analyze the net charge distribution, channels were positioned (their center of mass) in the center of the reference system with the diffusion axis oriented along *z*, and then split into three sections, namely, the EV ($z > +10$ Å), the CR ($+10$ Å $\leq z \leq -10$ Å) and the periplasmic vestibule (PV; $z < -10$ Å). All the investigated porins have a net negative charge (Supporting Information Figure S2), which increases from OmpF to OmpC and is even larger in the two mutants OmpC20 and OmpC33. As already mentioned, CR was found to be conserved. This is

DOI: 10.1021/acs.jpclett.5b00612
J. Phys. Chem. Lett. 2015, 6, 1807–1812

the more negative section of all the four porins and its net charge appears hard to be altered. Only a −1 difference was found in OmpC33, the last one of the clinical mutants series.[6] Quite surprisingly, the largest differences pertain to the EV, which is more negative in OmpC than in OmpF, and whose net negative charge is further increased in the clinical mutants. The same trend was found for the PV, despite the differences being less pronounced. It is also interesting to note that the PV is more negatively charged than the EV in the two wild-type porins, while, in the two clinical mutants, residues mutations led to the same net charge for both the vestibules.

In order to characterize and quantify such an altered electrostatics inside the lumen and to examine the effect of the porin's intrinsic electric field, the electric dipole $\boldsymbol{\mu}$ of the water molecules has been used as order parameter along the MD trajectory. To this aim, the protein channel was divided into 12 adjacent sections of identical thickness along the main axis of the pore (z windows). For each z window the total $\boldsymbol{\mu}_t$ due to all the water molecules N_w present in that z window, was computed. Then, the normalized electric dipole $\boldsymbol{\mu}_t/\boldsymbol{N}_w$ in each z window was obtained for each of the 6000 MD simulation frames (corresponding to 300 ns) and its time average was calculated. Bulk waters are characterized by a rather short correlation-time for reorientation, such that the corresponding autocorrelation function decays to zero rapidly. Conversely, ordering of water molecules by the internal electric field of the porin resulted to be time-correlated. The autocorrelation function of $\mu_t(t)/N_W$ did not decay to zero but asymptotically tended to a constant value, which depended upon the specific z window considered.

Figure 1 shows a cartoon representation of the first monomer of each of the four porins, together with the vectors corresponding to the time averaged $\boldsymbol{\mu}_t/\boldsymbol{N}_w$. It is immediately evident how, in all the cases, the maximum water ordering is reached halfway through the channel (z window 7, from the top of Figure 1), with the dipole pointing the loop L3 from the "basic ladder". This dipole corresponds to a transverse electric field as it has been already shown for OmpF.[20,21]

To better appreciate and quantify differences and similarities among the four porins, in Figure 2a−d we plotted the dipole strength μ_t/N_w in each z window, and in Figure 2e−h its projection on a plane perpendicular to the diffusion axis for the z windows close to and at the CR, that is, from z window 5 to 8. In the z window 6 the water dipole has almost the same direction as in the z window 7, but moving from OmpF to OmpC and then to the OmpC mutants, intensity decreases and a progressive difference in the xy component is observed.

Although all the porins are characterized by a conserved significant variation of the waters net dipole upon emerging from the CR to the PV (~90°; z window 7 to 8), the differences found at the level of the z window 5 are absolutely remarkable. In OmpF, the μ_t/N_w vector has almost the same direction as in the z windows 6 and 7. The same direction is preserved also in OmpC but water dipole strength is dramatically reduced. Astonishingly, water dipole direction is almost inverted in OmpC20 and the same was found in OmpC33 with an even higher strength. These profiles clearly show that the transverse electric field, as evaluated using the dipole moment of water molecules, is maximum at the CR in all the investigated porins. The observation that this particular feature was not modified in the drug resistant clinical strains[6] points once more to the importance of the electrostatics for the correct porin function as a filter for nutrients uptake.[13] However, although only a slight difference was observed in the maximum value of μ_t/N_w (Figure 2a-2d) in OmpF (1.11 D), OmpC (0.96 D), and OmpC20 (0.92 D), it is interesting to note that in the last clinical mutant, OmpC33, the water's net dipole significantly decreased (0.80 D) and became much more disordered in the CR (Figure 1d), as it was already put forward to explain the apparent decreased susceptibility to antibiotics.[6] However, the most striking difference among the investigated porins pertains to the transit from the EV to the CR. The ordering of water dipoles in each channel is determined by the specific distribution of the positively and negatively charged residues inside the lumen,[5,13,21] as is clearly shown by the detailed analysis reported in the Supporting Information. The overall emerging picture is that specific mutations have been introduced to tune the transversal electric field right at the entrance of the CR (z window 5) while leaving the CR almost unaffected. Upon entering the CR, the translocating molecule experiences a remarkable decrease of the conformational entropy, due to the significant pore size reduction. This is the most significant term controlling permeation. The resulting increase of the free energy would be compensated by a favorable preorientation of the molecular electric dipole with respect to the channel transverse electric field, as already claimed for the transport of urea in a specific urea channel.[23] Thus, the effect of a weak field just above the CR (e.g., in OmpC) or, even worse, of an electric field pointing in the opposite direction (e.g., in the two OmpC mutants) is expected to impose an adverse "preorientation" to the translocating molecule, exactly where steric hindrance to molecular reorientations starts to be severe. The same can be applied to the conserved water's order deviation observed upon emerging from the CR to the PV. From a general point of view, it is absolutely plausible that the internal electric field of the channel forces a dipolar molecule to align its moment accordingly while translocating. A higher free energy barrier for escaping the CR, thus, is expected for those molecules that cannot reorient easily inside this small region of the pore.

Because of the usually high negative net charge of the CR of bacterial general porins, like those investigated in the present work (Supporting Information Figure S2), permeation is widely believed to be easier for zwitterionic than for negatively charged antibiotics. This is absolutely reasonable because the presence of a net positive charged group on the translocating molecule should help approaching and then entering the CR. Both experimental and computational evidence have been provided in the literature[8,9] but, for the sake of completeness, it has to be mentioned that other authors have found only low correlation between electrophysiology measurements and antibiotics net charge.[16,24] The present investigation has shown a rather complex water "choreography" across the channel and suggests the electric dipole moment as a more general molecular feature to be looked at when comparing different antibiotics. Quite naively, zwitterionic molecules might be preferred for a rational drug design because a clear segregation between a positive and a negative charge would ensure a well-defined electric dipole.[18] However, regardless of whether the specific molecule is actually zwitterionic, but provided it has a comparable electric dipole, our simulations predict a general translocation mechanism. In order to preliminarily check this hypothesis, two cephalosporins were selected, namely, cefepime and cefotaxime, and the free energy surface (FES) for translocation through OmpF was reconstructed using metadynamics (details in the Supporting Information). These two molecules were chosen due to their

DOI: 10.1021/acs.jpclett.5b00612
J. Phys. Chem. Lett. 2015, 6, 1807−1812

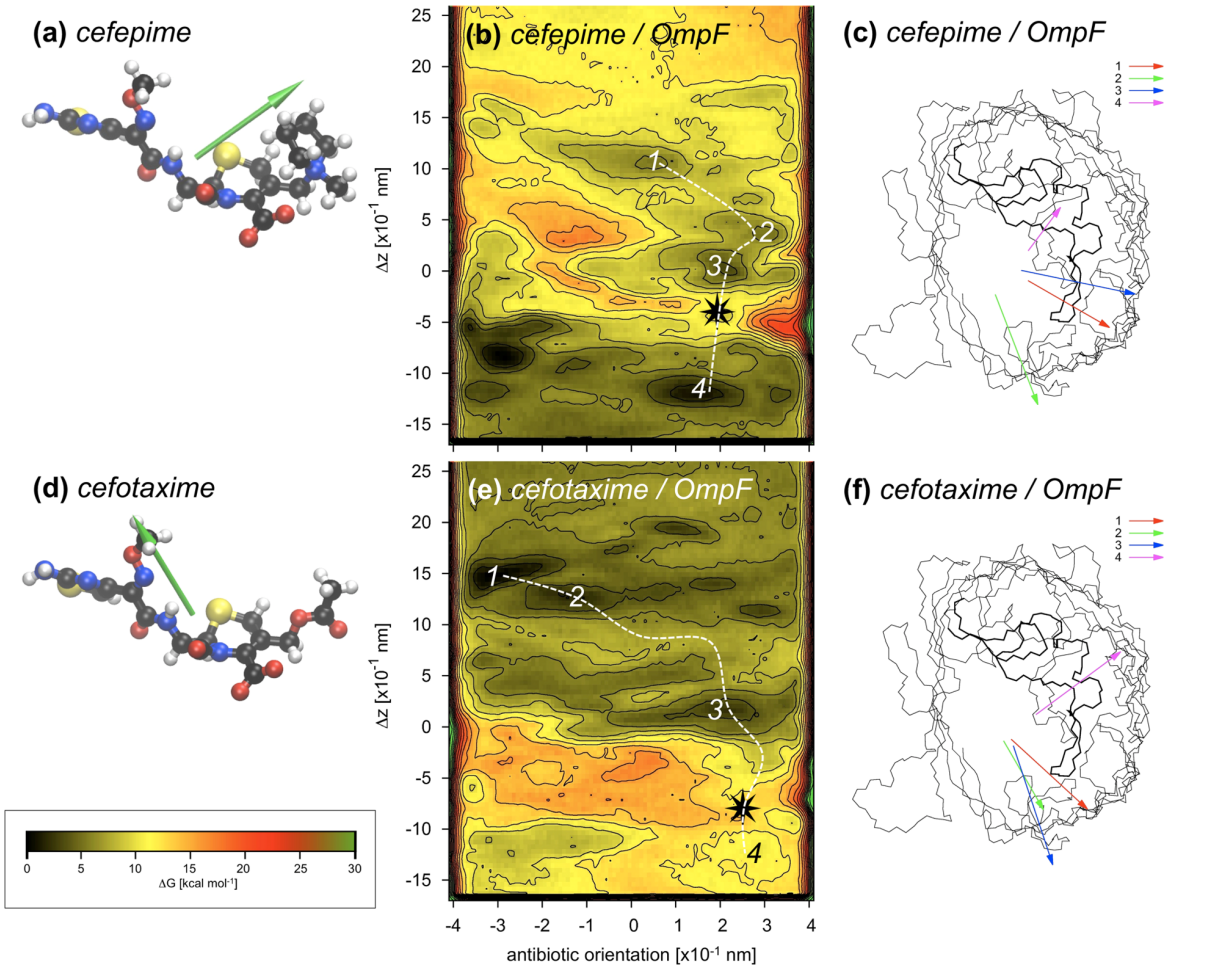

Figure 3. Cefepime (a) and cefotaxime (d) are shown together with the corresponding electric dipole (green arrow). Chemical elements are color coded as follows: C, black; H, white; N, blue; O, red; S, yellow. The FES for translocation through OmpF are shown in (b, e), where the main minima are labeled with consecutive numbers. The highest barrier is marked by an asterisk. Antibiotic orientation is defined as the difference of the z coordinate between the lactam carbonyl C and the S-bonded C. For each of the labeled minima, the molecular electric dipole was calculated and the average vector is reported in (c, f) together with the channel backbone trace. The loop L3 is bolded.

similar size (they differ only by one side chain) but the extremely different charge distribution, the former being zwitterionic at neutral pH, the latter being negatively charged with no positively charged groups. They are both characterized by a remarkable and similar electric dipole, 20.5 ± 1.3 D and 25.8 ± 2.2 D for cefepime and cefotaxime, respectively (calculated in their center of mass and averaged over the conformations sampled in the MD trajectories). Using the strength of the electric field as evaluated in ref 20, around 40 mV/Å, with a dipole moment of 20 D we obtain an energy of 3.8 kcal/mol for a perfect alignment between the molecule's dipole and the electric field. On the other hand, the strong alignment to a given direction can be accompanied by an additional reduction of configurational entropy. We calculated it for ampicillin,[25] another zwitterionic antibiotic (dipole ∼40 D), obtaining a value that does not exceed 2 kcal/mol, with a net compensation of a few kilocalories per mole on the steric barrier due to the pore size reduction.

The most interesting difference between the two antibiotics is the presence of a net positive group in cefepime. The presence of a methylpyrrole moiety changes certainly the dipole orientation with respect to the longest axis of the molecule (Figure 3a and d).

Figure 3b and e show the FES for the two antibiotics inside OmpF. Regardless their differences, both cefepime and cefotaxime experienced the highest energy barrier in the central region of the channel. More precisely, when approaching the CR from the EV, both antibiotics are accompanied by a rather low energetic cost, up to the z windows 6 and 7. The highest energy barrier was found between the z windows 7 and 8, that is, where the water analysis has revealed the unique abrupt change in the direction of the waters net dipole moment (Figure 2e) upon emerging from the CR to the PV. Figure 3c and f show the average antibiotic dipole corresponding to the various free energy states labeled on the FES. Before entering the CR, both antibiotics are preoriented by the electric field at the level of the EV such that, in the case of OmpF, the molecular electric dipole has an orientation favorable to get into the CR. However, upon emerging to the PV, the direction of the channel field is significantly different and the antibiotic should reorient to properly align its electric dipole. Because such reorientation occurs in the constricted region of the

DOI: 10.1021/acs.jpclett.5b00612
J. Phys. Chem. Lett. 2015, 6, 1807−1812

lumen, this might lead to an increase of the translocation free energy barrier.

In both human aquaporin-1 AQP1 and the *E. coli* aquaglyceroporin GlpF,[2,3] the intrinsic electric field of the transmembrane pore was found to be absolutely essential for both channel specificity and functionality. Water molecules and not protons permeate the channel by following a specifically designed "choreography", referred to as "global orientational tuning",[2,3] by aligning their dipole moment to the porin's electric field that changes orientation from the extracellular to intracellular side. In the completely different context of bacterial outer-membrane general porins, which are larger than aquaporins and not selective channels, the effect of the channel electric field is shown in this work, as highlighted by the waters "choreography" in Figure 1. When compared to the case of AQP1 and GlpF, where the direction of the water dipole mostly changes along the channel axis,[2,3] in the present case of general porins, the transverse reorientation appears to be predominant and represents the most striking difference among the examined channels, especially in the two porins extracted from clinical strains, for which a lower permeability was measured. The presented results have important implications for the formulation of a general model for antibiotics translocation. On the one hand, a common bottleneck was identified for all the investigated porins, the molecular reorientation due to a variation of the electric field upon escaping from the CR to the PV. On the other hand, the CR mouth on the extracellular side has emerged as the most critical area, susceptible to mutations and differentiating the inspected *E. coli* channels. Molecules can be unfavorably preoriented before entering the small CR. Then, when forced to reorient inside the constricted region, steric hindrance to such reorientations might contribute to increase the free-energy barrier to escape toward the PV. Moving from the concept that zwitterionic molecules should be favored[18] to the more informative suggestion that the molecule's electric dipole moment strength and orientation do determine permeability, a rational drug design should take this into account. Looking at the electric dipole moment of molecules rather than to their mere zwitterionic character, the ability to reorient and modulate the intensity of the electric dipole without the need of sterically hindered rotations is suggested as a promising route.

■ ASSOCIATED CONTENT

Supporting Information

Computational methods. Figure S1: multiple structure alignment. Figure S2: Net charge distribution. Figure S3−S5: Charged residues distribution for different protein sections is compared with the total dipole moment of the water molecules. Figure S6: The important amino acid mutations responsible for the different orientation of the water dipole moment at the extracellular mouth of the constriction region. The Supporting Information is available free of charge on the ACS Publications website at DOI: 10.1021/acs.jpclett.5b00612.

■ AUTHOR INFORMATION

Corresponding Author

*E-mail: matteo.ceccarelli@dsf.unica.it.

Author Contributions

[§](S.A.G., M.A.S.) These authors have equally contributed to the work.

Notes

The authors declare no competing financial interest.

■ ACKNOWLEDGMENTS

The research leading to these results was conducted as part of the "Translocation" consortium (www.translocation.com) and has received support from the Innovative Medicines Initiatives Joint Undertaking under Grant Agreement no. 115525, resources that are composed of financial contribution from the European Union's seventh framework programme (FP7/2007-2013) and EFPIA companies in kind contribution. S.A.G. is a Marie Skłodowska-Curie fellow within the "Translocation" Network, project no. 607694

■ REFERENCES

(1) Roux, B.; MacKinnon, R. The Cavity and Pore Helices in the KcsA K^+ Channel: Electrostatic Stabilization of Monovalent Cations. *Science* **1999**, *285*, 100−102.

(2) de Groot, B. L.; Grubmüller, H. Water Permeation Across Biological Membranes: Mechanism and Dynamics of Aquaporin-1 and GlpF. *Science* **2001**, *294*, 2353−2357.

(3) Tajkhorshid, E.; Nollert, P.; Jensen, M. Ø.; Miercke, L. J. W.; O'Connell, J.; Stroud, R. M.; Schulten, K. Control of the Selectivity of the Aquaporin Water Channel Family by Global Orientational Tuning. *Science* **2002**, *296*, 525−530.

(4) Mathé, J.; Aksimentiev, A.; Nelson, D.; Schulten, K.; Meller, A. Orientation Discrimination of Single-Stranded DNA Inside the A-Hemolysin Membrane Channel. *Proc. Natl. Acad. Sci. U.S.A.* **2005**, *102*, 12377−12382.

(5) Amodeo, G. F.; Scorciapino, M. A.; Messina, A.; De Pinto, V.; Ceccarelli, M. Charged Residues Distribution Modulates Selectivity of the Open State of Human Isoforms of the Voltage Dependent Anion-Selective Channel. *PLoS One* **2014**, *9*, e103879.

(6) Lou, H.; Chen, M.; Black, S. S.; Bushell, S. R.; Ceccarelli, M.; Mach, T.; Beis, K.; Low, A. S.; Bamford, V. A.; Booth, I. R.; et al. Altered Antibiotic Transport in OmpC Mutants Isolated From a Series of Clinical Strains of Multi-Drug Resistant *E. coli*. *PLoS One* **2011**, *6*, e25825.

(7) Hajjar, E.; Bessonov, A.; Molitor, A.; Kumar, A.; Mahendran, K. R.; Winterhalter, M.; Pagès, J.-M.; Ruggerone, P.; Ceccarelli, M. Toward Screening for Antibiotics with Enhanced Permeation Properties Through Bacterial Porins. *Biochemistry* **2010**, *49*, 6928−6935.

(8) Kojima, S.; Nikaido, H. Permeation Rates of Penicillins Indicate That *Escherichia coli* Porins Function Principally as Nonspecific Channels. *Proc. Natl. Acad. Sci. U.S.A.* **2013**, *110*, E2629−E2634.

(9) Ziervogel, B. K.; Roux, B. The Binding of Antibiotics in OmpF Porin. *Structure (London, U. K.)* **2012**, 1−12.

(10) Masi, M.; Pagès, J.-M. Structure, Function and Regulation of Outer Membrane Proteins Involved in Drug Transport in Enterobactericeae: the OmpF/C - TolC Case. *Open Microbiol. J.* **2013**, *7*, 22−33.

(11) Kumar, A.; Hajjar, E.; Ruggerone, P.; Ceccarelli, M. Structural and Dynamical Properties of the Porins OmpF and OmpC: Insights From Molecular Simulations. *J. Phys.: Condens. Matter* **2010**, *22*, 454125.

(12) Raj Singh, P.; Ceccarelli, M.; Lovelle, M.; Winterhalter, M.; Mahendran, K. R. Antibiotic Permeation Across the OmpF Channel: Modulation of the Affinity Site in the Presence of Magnesium. *J. Phys. Chem. B* **2012**, *116*, 4433−4438.

(13) Kojima, S.; Nikaido, H. High Salt Concentrations Increase Permeability Through OmpC Channels of *Escherichia coli*. *J. Biol. Chem.* **2014**, *289*, 26464−26473.

(14) Pagès, J.-M.; James, C. E.; Winterhalter, M. The Porin and the Permeating Antibiotic: a Selective Diffusion Barrier in Gram-Negative Bacteria. *Nat. Rev. Microbiol.* **2008**, *6*, 893−903.

DOI: 10.1021/acs.jpclett.5b00612
J. Phys. Chem. Lett. 2015, 6, 1807−1812

(15) Lewis, K. Platforms for Antibiotic Discovery. *Nat. Rev. Drug Discovery* **2013**, *12*, 371−387.
(16) Tran, Q.-T. Structure-Kinetic Relationship of Carbapenem Antibacterials Permeating Through *E. coli* OmpC Porin. *Proteins* **2014**, 1−40.
(17) Nestorovich, E. M.; Danelon, C.; Winterhalter, M.; Bezrukov, S. M. Designed to Penetrate: Time-Resolved Interaction of Single Antibiotic Molecules with Bacterial Pores. *Proc. Natl. Acad. Sci. U.S.A.* **2002**, *99*, 9789−9794.
(18) Danelon, C.; Nestorovich, E. M.; Winterhalter, M.; Ceccarelli, M.; Bezrukov, S. M. Interaction of Zwitterionic Penicillins with the OmpF Channel Facilitates Their Translocation. *Biophys. J.* **2006**, *90*, 1617−1627.
(19) Breed, J.; Sankararamakrishnan, R.; Kerr, I. D.; Sansom, M. S. Molecular Dynamics Simulations of Water Within Models of Ion Channels. *Biophys. J.* **1996**, *70*, 1643−1661.
(20) KARSHIKOFF, A.; SPASSOV, V.; Cowan, S. W.; LADENSTEIN, R.; Schirmer, T. Electrostatic Properties of 2 Porin Channels From *Escherichia coli*. *J. Mol. Biol.* **1994**, *240*, 372−384.
(21) Im, W.; Seefeld, S.; Roux, B. A Grand Canonical Monte Carlo-Brownian Dynamics Algorithm for Simulating Ion Channels. *Biophys. J.* **2000**, *79*, 788−801.
(22) Tieleman, D. P.; Berendsen, H. J. A Molecular Dynamics Study of the Pores Formed by *Escherichia coli* OmpF Porin in a Fully Hydrated Palmitoyloleoylphosphatidylcholine Bilayer. *Biophys. J.* **1998**, *74*, 2786−2801.
(23) McNulty, R.; Ulmschneider, J. P.; Luecke, H.; Ulmschneider, M. B. Mechanisms of Molecular Transport Through the Urea Channel of Helicobacter Pylori. *Nat. Commun.* **2013**, *4*, 2900.
(24) Mahendran, K. R.; Kreir, M.; Weingart, H.; Fertig, N.; Winterhalter, M. Permeation of Antibiotics Through *Escherichia coli* OmpF and OmpC Porins: Screening for Influx on a Single-Molecule Level. *J. Biomol. Screen* **2010**, *15*, 302−307.
(25) Kumar, A.; Hajjar, E.; Ruggerone, P.; Ceccarelli, M. Molecular Simulations Reveal the Mechanism and the Determinants for Ampicillin Translocation Through OmpF. *J. Phys. Chem. B* **2010**, *114*, 9608−9616.

DOI: 10.1021/acs.jpclett.5b00612
J. Phys. Chem. Lett. 2015, 6, 1807−1812

Exploiting the porin pathway for polar compound delivery into Gram-negative bacteria

"Reprinted with permission from M.A. Scorciapino, T. D'Agostino, **S. Acosta-Gutiérrez**, G. Malloci, I. Bodrenko, M. Ceccarelli, Exploiting the porin pathway for polar compounds delivery into Gram-negative bacteria, *Future Medicinal Chemistry* ,**8**,1047-1062 (2016)"

Research Article

For reprint orders, please contact reprints@future-science.com

Future Medicinal Chemistry

Exploiting the porin pathway for polar compound delivery into Gram-negative bacteria

Background: In Gram-negative bacteria, the outer-membrane represents an additional barrier for antibiotics to permeate inside pathogens. Our inability to come up with novel effective antibiotics mostly relies upon insufficient understanding of the molecular basis behind outer-membrane penetration. **Results:** Polar antibiotics can permeate through water-filled porins, such as OmpF and OmpC from *Escherichia Coli*. Through molecular modeling, permeation of imipenem and meropenem was found to be strongly dependent upon capability of drugs to properly align their electric dipole to the internal electric field in the restricted region of the pore. Electrostatics differences between OmpF and OmpC, and modifications along a series of OmpC mutants from *E. coli*-resistant clinical strains identify a 'preorientation' region, which dramatically affects antibiotic pathway. **Conclusion:** A novel perspective is presented, suggesting new molecular properties to be included in drug design.

First draft submitted: 13 February 2016; Accepted for publication: 18 April 2016; Published online: 15 June 2016

Keywords: antimicrobial drugs • drug design • computational chemistry and molecular modelling

Mariano Andrea Scorciapino[†,1], Tommaso D'Agostino[†,2], Silvia Acosta-Gutierrez[2], Giuliano Malloci[2], Igor Bodrenko[2] & Matteo Ceccarelli*[,2]

[1]Department of Biomedical Sciences, University of Cagliari, S.P. 8 km 0.700, I-09042 Monserrato, CA, Italy

[2]Department of Physics, University of Cagliari, S.P. 8 km 0.700, I-09042 Monserrato, CA, Italy

*Author for correspondence:
Tel.: +39 070 6754933
Fax: +39 070 6753191
matteo.ceccarelli@dsf.unica.it

[†]Authors contributed equally

Antimicrobial resistance is a natural phenomenon in micro-organisms. By a multitude of complex mechanisms, micro-organisms develop resistance to the commonly employed antimicrobial drugs, meaning that they acquire the capability to grow and proliferate in the presence of chemicals that were previously able to limit their growth or even to kill them. Antimicrobial resistance is accelerated by the selective pressure exerted by use and misuse of antimicrobial agents in humans and animals.

The lack of new classes of antimicrobials replacing those that have become ineffective, represents an additional problem. This issue is particularly urgent for Gram-negative pathogens [1–3]. A recent report published by the WHO reads: "The pipeline for the development of new antibacterial drugs is now virtually empty, particularly for the treatment of Gram-negative enteric bacteria, and research on treatments to replace antibacterial drugs is still in the early stages. (…) This means that progress in modern medicine, which relies on the availability of effective antibacterial drugs, is now at risk" [4].

In Gram-negative bacteria, the presence of an outer membrane (OM) represents an additional challenge, as the antibiotic has to overcome this barrier to permeate inside the pathogen. Besides the degradative action of devoted enzymes and the expulsion process operated by efflux pump systems, the accumulation of sufficient antibiotic inside the bacterial cell is of primary importance to have a significant effect [5,6]. Our inability to come up with novel effective antibiotics for Gram-negative pathogens mostly relies upon the insufficient understanding of the molecular basis behind penetration through the OM [7–10].

The latter consists of a lipopolysaccharide/phospholipid bilayer where water-filled

FUTURE SCIENCE part of fsg

protein channels are embedded and serve to regulate nutrient uptake. More specifically, in the Enterobacteriaceae (e.g., *Escherichia coli*), such a role is devolved to a family of trimeric nonspecific channels called porins, through which metabolites and ions cross the OM by passive diffusion [6,9,11,12]. These outer membrane porins (Omp) represent also the main access to the periplasmic space of the bacterial cell for hydrophilic antibiotics from different classes, like β-lactams. One of the strategies used by pathogens to increase their resistance to drugs is to limit their uptake by modifying, indeed, the expression or the structure of porins [6,13].

E. coli is one of the most studied and well known Gram-negative bacteria and is usually taken as prototype. The two main porins of *E. coli* are not surprisingly among the first Omps whose 3D structure was solved at high resolution, namely, OmpF [14] and OmpC [15]. They show very high sequence identity (~60%) and virtually identical topology. Three identical subunits are arranged to form a homotrimer. Each monomer is folded as a 16-strands β-barrel pore, where the longest loop L3 folds back and reduces water accessible area halfway through the channel. Thus, the lumen of each porin's monomer results in an hourglass shape, where the so-called constriction region generates the main steric barrier to the diffusion of molecules and ions.

For quite a long time, the reduced size and corresponding lower permeability of OmpC with respect to OmpF has led to the convincing idea that pore size was the primary feature determining drugs permeability [6,11,16]. This concept was also corroborated by evidence of different level of expression for OmpF and OmpC depending on the environment and by the observation that mutant strains lacking OmpF and expressing OmpC showed decreased antibiotic susceptibility. Changes in medium osmolarity affect the relative expression of OmpC and OmpF, preferentially expressed in high and low osmolarity, respectively. Environments where nutrient levels are high, such as the mammal intestine, favor OmpC expression, when limitation of the influx of large and charged molecules such as bile salts and antibiotics is required; conversely, OmpF is the major porin under conditions of nutritional deficiency, when less stringent filtering is preferable [6].

Despite the efforts spent during the last two decades [11,16–26], both experimental and theoretical rules for the design of novel drugs remain chimeric. Quite obviously, the focus of the studies has been typically the porin's constriction region. Different kinds of porin/antibiotic interactions have been invoked to explain permeability ranking, such as H-bonds, hydrophobic contacts and salt bridges. In some instances, the idea of a sort of binding or affinity site inside the channel has even loomed in the literature, in the search for a possible simple model to describe a clearly complex and multivariate process. The available results strongly suggest that permeation depends on general antibiotic physicochemical properties such as size, net charge, charge distribution, conformational plasticity and hydrophobicity, to name a few. Nevertheless, no evident strong correlation between the rates of permeation and any of these characteristics has been found so far, also for the lack of a robust method to measure permeability [27]. For the sake of completeness, it has to be mentioned that possible roles played by lipopolysaccharides (LPS) in the outer leaflet of the OM have been often underrated, if not completely neglected. The recent efforts spent in obtaining a reliable atomistic model for LPS simulations has revealed its nonpassive role, with membrane thinning and direct interaction with the extracellular loops of the OM protein being just two examples of how the exact composition and flexibility of the OM itself can actually affect the behavior of the embedded protein [28–33].

More recently, the idea of strong direct interactions between the diffusing antibiotic and the channel residues has been questioned [11], and the electrostatics of the lumen, more than its size, has been indicated to be of primary importance in regulating permeability [16,21]. By using water molecules as inherent natural probes, the authors have characterized the internal electrostatics of OmpF, OmpC and some of its mutants [34,35] identified in clinically resistant strains [21]. The latter, isolated along 2 years of treatment of a patient suffering from a chronic *E. coli* infection, showed progressively greater resistance to the β-lactam antibiotics used for treatment, including cefotaxime, ceftazidime, ciprofloxacine, imipenem and meropenem [36]. Interestingly, while the structures of the OmpC mutants showed essentially an unchanged size [21], remarkable differences were found in the internal electric field of OmpF, OmpC and the mutants [35]. All these porins share a constriction region with net segregation of oppositely charged residues. The loop L3 possesses several negatively charged residues, while the opposite side of the barrel wall is characterized by the presence of positively charged residues comprising the so-called 'basic ladder'. As expected, the internal electric field was found to be at the maximum in the constriction region, and this feature was absolutely invariant along the porin series investigated [34]. Conversely, major differences were found at the mouth of the constriction region on the extracellular side, and the existence of a 'preorientation region' has been put forward. Depending on

the channel being considered, the dipolar antibiotic might or may not be effectively oriented in the pre-orientation region, resulting in a facilitated access to the constriction region [34].

A clear and systematic analysis of the role played by the channel in the translocation of antimicrobials, based on the knowledge of the dynamics of the translocating drugs themselves, is still missing [27]. There are no experimental methods available to probe the translocation directly. Computer simulations appear particularly suitable, if not necessary. After having characterized the internal electrostatics of the above mentioned series of porins in-depth, we have focused on the dynamics of antibiotics in the present work. By taking the unique opportunity of having the 3D structure of porins from progressively more and more resistant *E. coli* strains [21], we have selected two carbapenems to which resistance was assessed, namely, imipenem and meropenem. Recently, some of the authors have published a joint experimental and computational study where these two carbapenems have been compared [37]. A general decrease in the association rate through electrophysiology experiments, as well as a reduced permeability through liposome swelling assays, was observed for these two antibiotics along the series of OmpC mutants, thus, correlating with the decreased susceptibility observed in the clinical strains [37]. In the present work, we have extended the computational investigation and the analysis extent in order to characterize in much more details the new model for translocation we had put forward. In addition, some antibiotic-specific differences were shown but not fully understood [37]. The free-energy profile of imipenem and meropenem translocation through OmpF, OmpC, OmpC20 and OmpC33 (the first and the last one of the clinical series, respectively) was reconstructed through metadynamics simulations. The analysis of the trajectories shows how the antibiotic actually tries to align its electric dipole with the channel's electrostatics along its translocation path, and how even subtle differences between the channels can deeply affect the translocation process. In addition, the presented results clearly show that beside the channel-specific 'background', the drug-specific properties do play a non-negligible role in determining the dynamics of the translocation process.

Methods

We performed molecular dynamics simulations at an all-atom level on the four porins embedded in a POPC symmetric bilayer and solvated with water, as described in [34], starting from their high-resolution x-ray structures (PDB Ids: 2OMF; 2J1N; 2XE2; 2XE3). The equilibrations were performed with the NAMD program. As interaction parameters we employed the Amber99SB-ILDN force field [38] for the protein and lipids, and TIP3P [39] for waters. All the amino acid residues were simulated in the ionization state at neutral pH except for the E296, which was protonated (net charge 0) as suggested for OmpF by Varma *et al.* [40].

We simulated the transport of antibiotics using an enhanced sampling technique, the well-tempered metadynamics algorithm [41], implemented in the ACEMD/PLUMED packages [42,43]. GAFF force-field parameters [44] were used to describe imipenem and meropenem, as described in details elsewhere [45]. Starting from the final configuration of the equilibrated porin simulation, the antibiotic was placed in the middle of the extracellular vestibule of the first monomer in a random orientation.

Two collective variables were biased, namely, the antibiotic position (z) and orientation inside the porin (Supplementary Figure 1), until the first translocation through the porin constriction region (0.0Å > z > -5.0Å) was observed. Then, four configurations were randomly selected, two with the antibiotic located in the extracellular vestibule, two in the periplasmic vestibule. Correspondingly, four multiple-walkers [46] were set to extend the metadynamics exploration of the free-energy surface (FES), reaching a total simulation time of 1.7–2.0 μs for each of the investigated cases. During the metadynamics stage, energy biases were added every 2.0 ps to each collective variable (the height of a single hill was 0.2 kcal mol^{-1}; the width was equal to 0.3 and 0.05 Å for position and orientation, respectively). For a well-tempered scheme, we used an initial height of the hills equal to 1.2 kcal mol^{-1}, modulated with a secondary temperature equal to 3000 K. These biases discouraged the system from visiting conformations that had already been explored, thus enhancing the exploration of other states accessible to the system [41].

Results & discussion

Free energy of antibiotic translocation: serial differences do not focus on the channel constriction zone

The FES obtained for imipenem and meropenem while translocating through OmpF, OmpC, OmpC20 and OmpC33 are shown in Figure 1. Antibiotic's depth inside the protein channel 'z' is reported on the y-axis: the constriction region encompasses the range between 0 and -5 Å. Antibiotic's orientation is reported on the x-axis: the closer to 0 the more perpendicular to the channel axis. The sign simply defines the two possible parallel orientations: a positive value corresponds

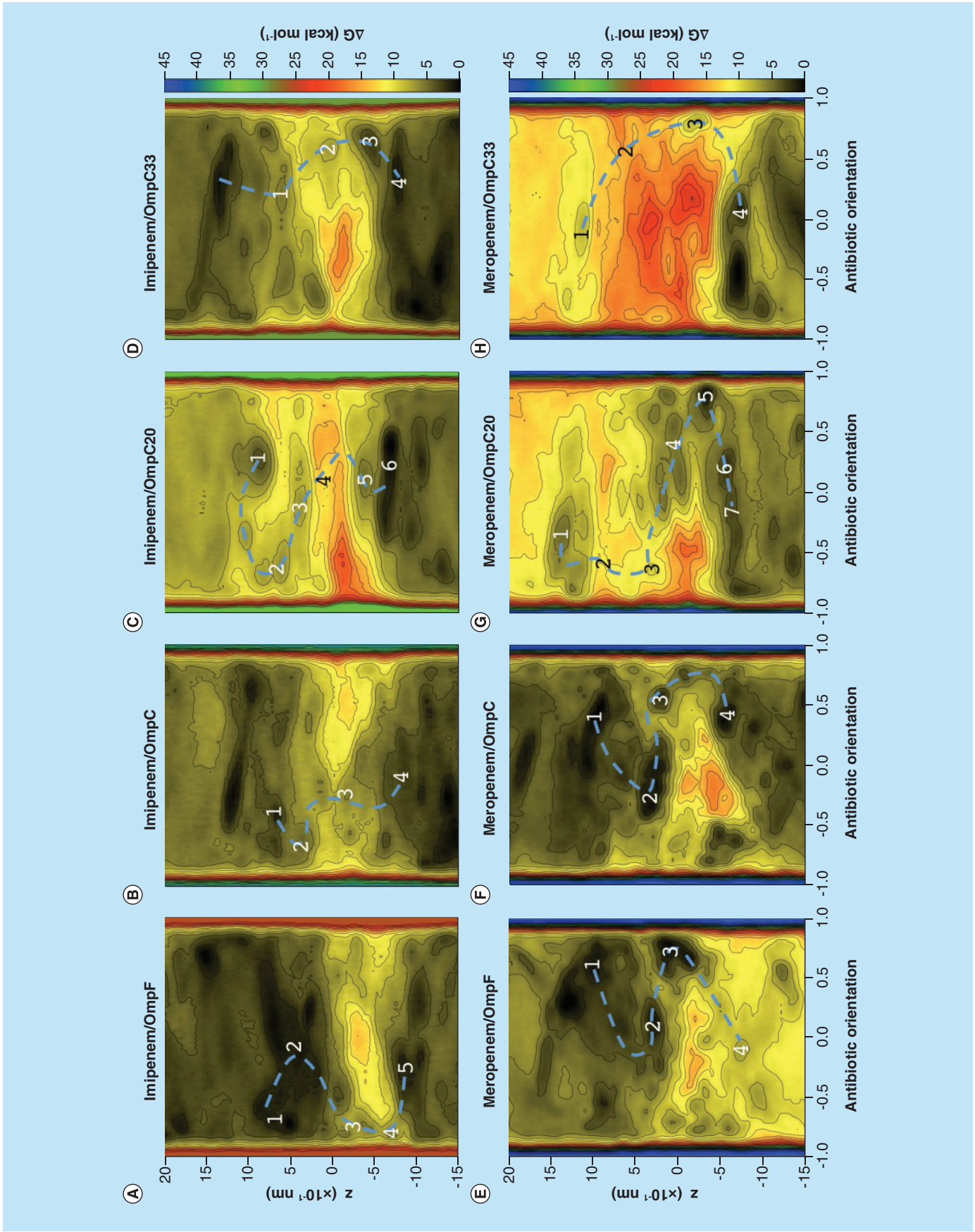
A
Imipenem/OmpF
B
Imipenem/OmpC
C
Imipenem/OmpC20
D
Imipenem/OmpC33
E
Meropenem/OmpF
F
Meropenem/OmpC
G
Meropenem/OmpC20
H
Meropenem/OmpC33
z (×10-1 nm)
ΔG (kcal mol-1)
Antibiotic orientation

Figure 1. Free energy surfaces for the translocation of imipenem and meropenem in outer membrane proteins from *Escherichia coli* (see facing page). Free energy surface of the translocation of imipenem **(A–D)** and meropenem **(E–H)** through four different outer membrane porins from *E. coli*. The wild-type OmpF **(A,E)** and OmpC **(B,F)** together with mutants OmpC20 **(C,G)** and OmpC33 **(D,H)** from clinical strains have been investigated. Antibiotic orientation is defined as the normalized difference of the z coordinate between the lactam carbonyl carbon and the S-bonded carbon. Each isocontour corresponds to a free energy difference of 2 kcal mol^{-1}. Free energy values were rescaled for each surface in order to have the absolute minimum equal to zero. Numerical labels are used to indicate specific regions analyzed in detail along the minimum energy path across the constriction region (0Å < z < -5Å).

to the antibiotic's positive part downward, in other words, closer to the periplasmic side. Thus, a change in the x-value on the FES represents the antibiotic undertaking some more or less extended reorientation inside the channel.

Along the minimum free energy path, different regions have been selected and analyzed in detail (see below), in order to sample different portions of the channel in the range +10Å > z > -10Å. These regions are labeled with consecutive numbers in Figure 1: moving from the extracellular to the periplasmic vestibule, the FES region's label increases. The highest free energy values are observed in the restricted central region in all the cases, in agreement with similar investigations reported in the literature [21,23,24]. However, the available space inside these four channels is known to be comparable [21], such that the differences observed in Figure 1 cannot be explained with large variations of the steric hindrance to the antibiotic translocation.

A first analysis can be performed by comparing the FES relative to imipenem (Figure 1A–D). Constriction region accessibility from the periplasmic side is comparable in the four porins. On the other hand, constriction region accessibility from the extracellular side shows significant differences, when the average free energy level in the extracellular vestibule is compared with that at the constriction region in the same porin. In OmpF, the average ΔG is rather low all over the extracellular vestibule and starts to increase significantly from z = 0 Å, which is exactly where the constriction region starts. In OmpC, the main free energy barrier for translocation is broader, with ΔG significantly increasing already at z ≈ +5 Å, meaning that accessibility to the core of the channel is less favorable than in OmpF [23]. In OmpC20, the main barrier is even more pronounced and broad, with rather high free energy values starting from z ≈ +10 Å, in other words, well outside the constriction region. Finally, in OmpC33, despite constriction region accessibility from the extracellular side looks ameliorated when compared with OmpC20, the main barrier to antibiotic diffusion is very broad and extends all the way from +10 to -5 Å.

The case of meropenem follows the same trend (Figure 1E–H). Similarly to imipenem, the results for OmpF and OmpC are comparable to each other, with constriction region accessibility being slightly less favorable in OmpC. In OmpC20, the main barrier for translocation is encountered well above the constriction region, clearly showing that in some circumstances the main difficulty might be approaching, more than crossing, the constriction region itself. In OmpC33, again, the central barrier is extremely broad, even more than observed for imipenem.

It is very interesting to note how the serial modifications observed along the channels series for both antibiotics pertain mostly to the area immediately above the constriction region (on the extracellular side) and not to the constriction region itself [34,37]. As already mentioned, all the four porins are comparable in size. In addition, the mutations differentiating them are not located in the constriction region [21], so that, similarly, an altered number of hydrogen bond donors/acceptors or charged groups in the constriction region cannot be invoked to explain the differences observed in the translocation FESs of each of the two carbapenems.

Porin's electrostatics sets the scene: role of the preorientation region

We have recently characterized the subtle modifications of the charge distribution inside these protein channels [34]. Using water molecules as intrinsic and natural molecular probes for the electrostatics, the results suggested that the channel electrostatics might force dipolar molecules to adopt a pore-dependent preferential orientation while permeating through the channel. In addition, such a preferential orientation was found to vary along the channel, as if the channel directed a sort of choreography for molecules passing through it. The choreography is different for each porin in the series examined here, and ultimately depends upon the serial amino acid mutations evolved in the corresponding antibiotic-resistant clinical strains [34,37].

It is thus plausible that antibiotics endowed with a significant electric dipole are forced to some extent to adopt a suitable orientation while translocating, in order to match the channel's electrostatics. As far as the latter is concerned, it has to be remarked that the most striking differences among the porins under investigation were found right at the mouth of the constriction region, on the extracellular side, which is exactly the same zone where the above described serial differences between the FESs have been found (Figure 1).

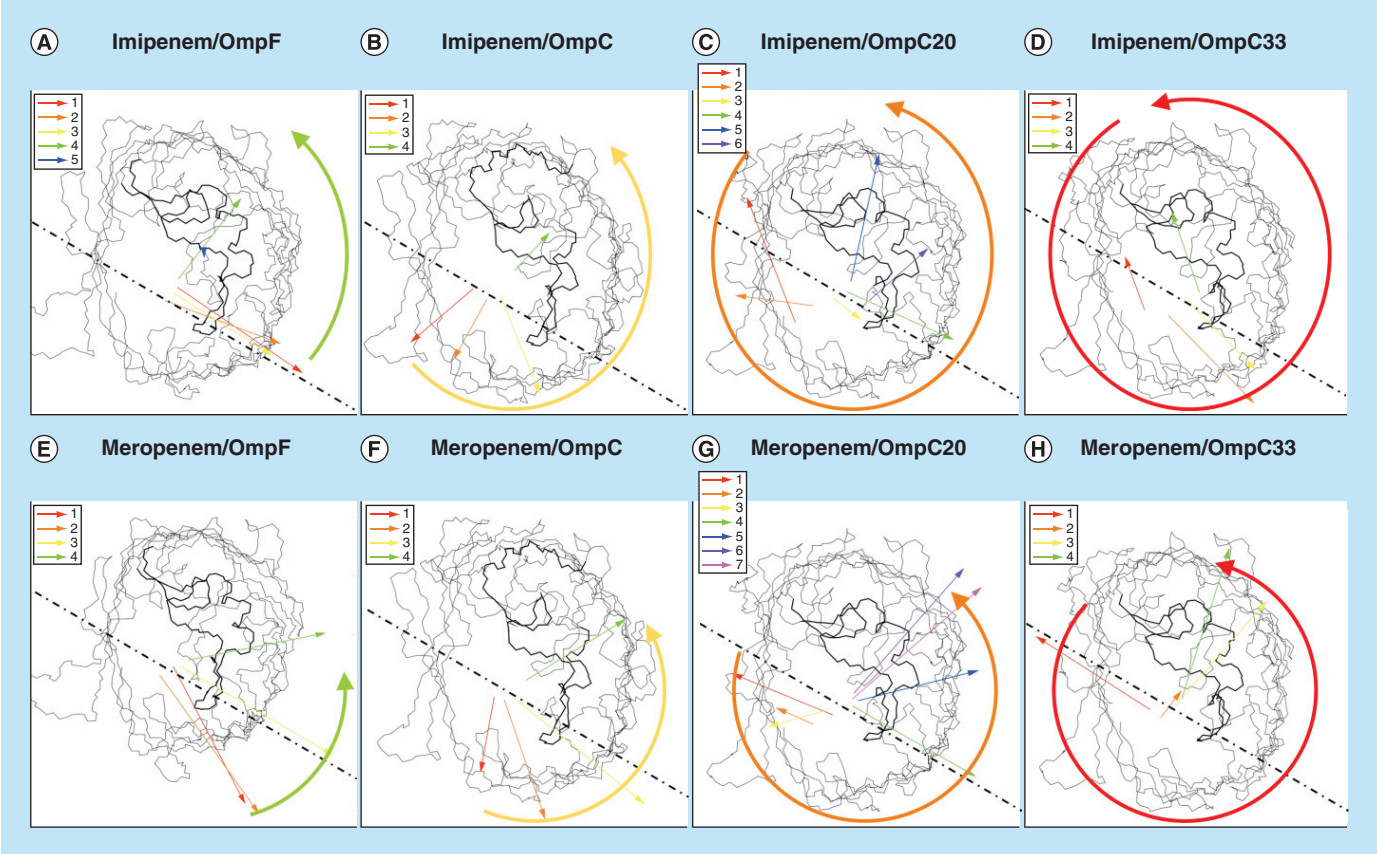

Figure 2. Reorientation of the dipole moment of imipenem and meropenem during translocation. Backbone xy-projection of the first monomer of the four different outer membrane porins from *E. coli*, namely, the wild-type OmpF **(A,E)** and OmpC **(B,F)** together with mutants OmpC20 **(C,G)** and OmpC33 **(D,H)** from clinical strains. The loop L3 is bolded to provide a visual reference. The dashed line is used to indicate the optimal direction for molecular dipoles inside the constriction region [34]. The average electric dipole of imipenem **(A–D)** and meropenem **(E–H)** in each of the labeled regions of the corresponding FES in Figure 1, are reported with different colors.

This specific region corresponds to z values in the range from +10 to +5 Å in the systems discussed here and, by analogy with our previous report [34] it will be referred to as the 'preorientation region'. This name was due to the differences observed between the four protein channels under investigation. It was shown that, in OmpF, waters' preferential orientation was almost the same as in the constriction region. The same direction was preserved also in OmpC but waters' ordering was lower, reflecting an attenuated (i.e., more balanced) electrostatics of the preorientation region. In OmpC20, water's orientation in the preorientation region was inverted with respect to the constriction region. The same applied to OmpC33 to an even higher extent.

Figure 2 shows the xy-projection of the backbone of the porins' first monomer. For each of the labeled regions in Figure 1, all the antibiotic conformers were extracted from MD trajectories and analyzed by calculating the average electric dipole, which is reported in Figure 2. In OmpF, imipenem does not change the orientation of its electric dipole while crossing the constriction region (Figure 2A). The dipole is oriented from the basic ladder, which is positively charged, toward the loop L3, which is negatively charged, and this specific orientation was already adopted before entering the constriction region, when the antibiotic was still in the preorientation zone. Finally, upon emerging from the constriction region on the periplasmic side, the average orientation of the electric dipole changes by approximately 90°, as it was previously observed for waters [34].

In OmpC, the situation is rather different (Figure 2B). Before entering into the constriction region, the electric dipole is not properly preoriented. Imipenem has to correct such a misalignment between its electric dipole and the channel electrostatics while crossing the constriction region. However, the change of dipole orientation is rather smooth, with approximately 90° variation covered along the path from region n.1 to n.3, while descending along the channel axis. Thus, finally, imipenem adopted the correct orientation in the constriction region. Afterwards, an additional approximately 90° variation upon emerging to the periplasmic vestibule is observed, similarly to the case of OmpF.

In OmpC20, the adverse preorientation above the constriction region is absolutely clear (Figure 2C). Imipenem has to rotate its dipole while descending along the channel in less than 1 nm (from region n.1 to n.3) in order to reach the correct alignment before getting into the most restricted zone. Finally, in OmpC33, the changes in the orientation of the dipole appear even sharper than in the case of OmpC20 (Figure 2D). Dipole orientation abruptly changes by approximately 180° both getting in and out of the constriction region, and it is not properly oriented even inside the constriction region.

The case of meropenem follows the same trend, bolstering the primary role played by channel electrostatics as a background for the antibiotic's translocation choreography. The analysis of the FES' selected

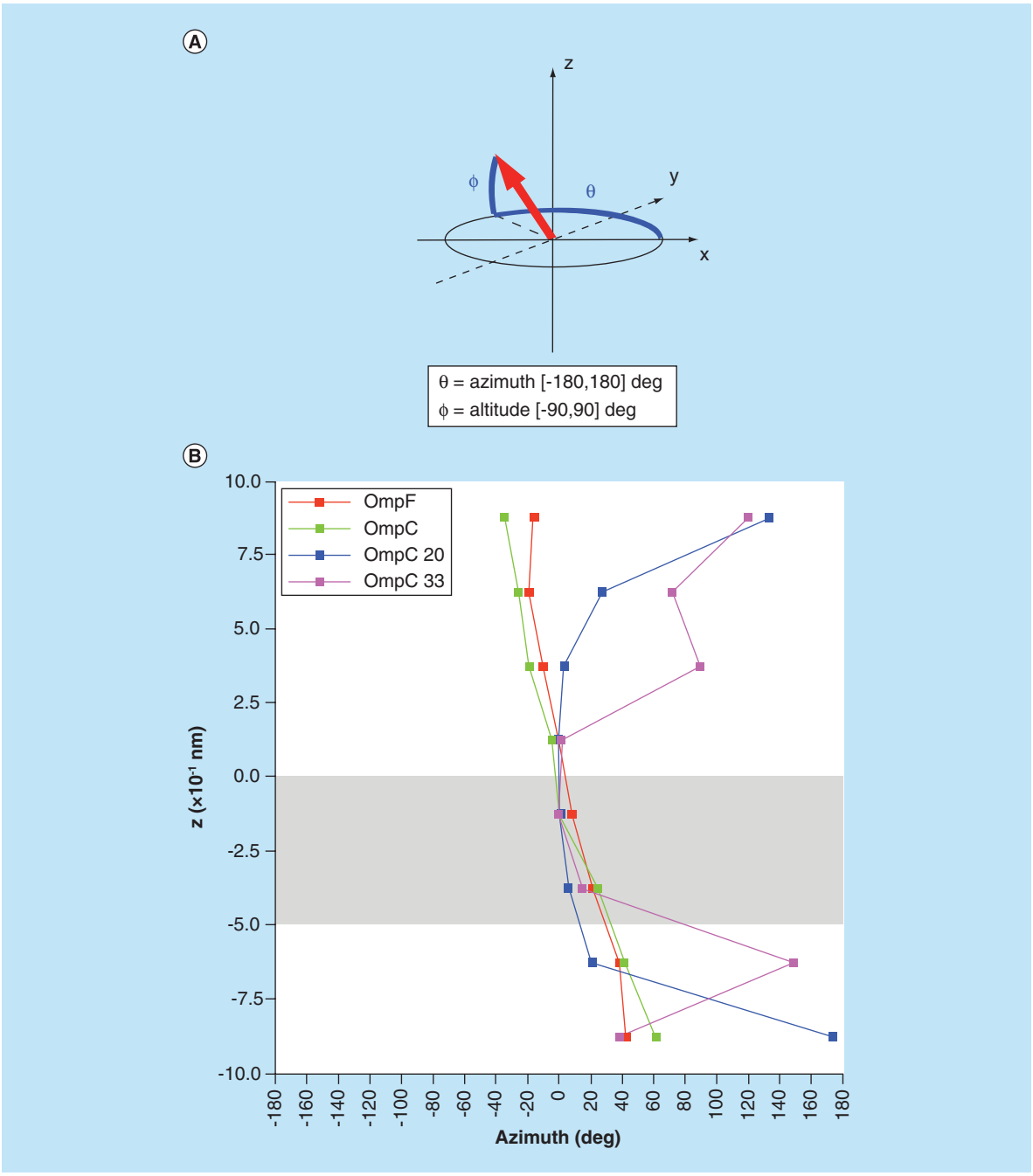

Figure 3. Reorientation of the dipole moment of water during translocation. Electric dipoles orientation was analyzed in terms of polar coordinates as defined in **(A)**. In **(B)**, the results of the azimuth angle of the waters' net dipole in the absence of antibiotic are reported for successive 2.5 Å cross-sections along the channel axis of the four porins under investigation. The shaded area indicates the constriction region.

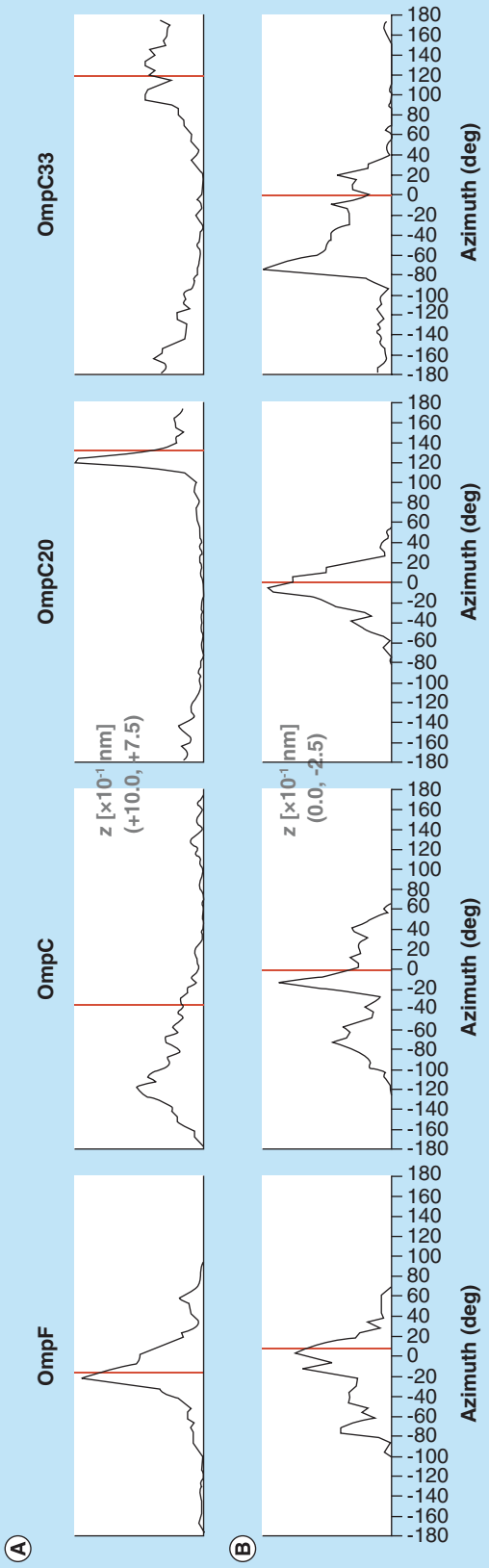
OmpC33
OmpC20
OmpC
OmpF
z [×10⁻¹ nm]
(+10.0, +7.5)
z [×10⁻¹ nm]
(0.0, -2.5)
Azimuth (deg)
180
160
140
120
100
80
60
40
20
0
-20
-40
-60
-80
-100
-120
-140
-160
-180
A
B

Figure 4. Distribution of the azimuth angles assumed by the dipole moment of imipenem in the preorientation and in the constriction zone (see facing page). The distribution of the azimuth angle of imipenem's electric dipole is shown for two selected 2.5 Å cross-sections along the channel axis of the four outer membrane porins under investigation. The first cross-section (+10.0 Å < z < +7.5 Å) is in the preorientation region, the second one (0.0 Å < z < -2.5 Å) is in the constriction region of the pore. The red lines are used as a reference for the azimuth of the waters' net dipole in the same channel cross-section, calculated in the absence of antibiotic.

regions along the minimum energy path shows that, in OmpF, the preorientation exerted by the electrostatics at the extracellular mouth of the constriction region is such that meropenem can enter the constriction region with just a slight change of orientation (Figure 2E). In OmpC, the change of orientation is larger but rather smooth while traversing the channel (Figure 2F). In OmpC20, the preorientation is strong and points approximately 180° away from the optimal direction to get into the constriction region (Figure 2G). An inversion of the molecular dipole orientation is needed while descending only 1–2 nm along the translocation path. Finally, in OmpC33, the adverse preorientation is clear and, in addition, the antibiotic seems to never reach the proper orientation inside the constriction region (Figure 2H).

From this qualitative analysis it is clear that both carbapenems, being highly dipolar molecules (14 and 31 D respectively for imipenem and meropenem [45]), are forced to adopt specific orientations along their way through the porin, in perfect agreement with our previous water analysis [34]. The drug possessing a dipole is effectively preoriented in OmpF at the level of the extracellular vestibule, that is, before entering the constriction region. This results in a very good accessibility of the constriction region from the extracellular side. In OmpC, preorientation is not effective, so that the dipolar drug has to find the proper orientation without any 'guide' from the channel electrostatics. In the case of the two clinical mutants, OmpC20 and OmpC33, the preorientation acts in the opposite direction with respect to the electrostatics in the constriction region, dramatically reducing the probability for the antibiotic to access the latter properly, in other words, with the optimal orientation of its electric dipole.

Zooming in for a close-up of antibiotic reorientations

The curved lines in Figure 2 show qualitatively the progressive variation of the dipole orientation inside the pore, correlated to the reorientation of the dipolar drug, moving from OmpF to OmpC and then for the two pores extracted from clinical strains. In order to get a more detailed and quantitative description of the reorientations executed by the two carbapenems inside the four channels, we performed a statistical analysis of the polar coordinates of the electric dipole. By taking into account all the MD frames pertaining to adjacent cross-sections of the channels with 2.5 Å width, we computed the distribution of the azimuth and altitude angles, as defined in Figure 3A. Figure 3B shows the azimuth of waters' net dipole, in the absence of any antibiotic, as a reference (the azimuth found in the cross-section with the highest waters order was used as angular reference and thus placed to zero; data pertaining to the other cross-sections, both in the presence and absence of the antibiotic, were phased accordingly). OmpF and OmpC are absolutely comparable from this point of view, the only difference is the magnitude of the xy-component of the waters' net dipole (not shown), which is strong in OmpF whereas almost absent in OmpC [34]. In OmpC20, the preorientation is opposite to the waters' order observed in the constriction region, but follows a smooth variation along the channel axis. In OmpC33, the adverse preorientation is retained deeper inside the channel and the dipole orientation is forced to change when the antibiotic is closer to the constriction region, in other words, where the available space is reduced.

As far as the two carbapenems' choreography is concerned, the altitude was never found to follow any specific and informative trend, which is absolutely reasonable given the rather small z-component of waters' net dipole when compared with the xy-component. On the other hand, the azimuth was found to be a clear descriptor for the differences in the behavior of the same antibiotic into the various porins. In Figure 4, the results for imipenem are shown for two selected cross-sections, one in the preorientation and one in the constriction region, respectively (Supplementary Figure 2). In OmpF, imipenem descends from the preorientation to the constriction region with the electric dipole pointing toward the same direction. The main fraction of conformers populates the portion of the azimuth domain closest to the reference waters' net dipole in the same cross-section. When imipenem enters the region of the channel with the lowest accessible area, molecular reorientations are hindered. The azimuth distribution reflects the reduced interchangeability between different orientations by a broader and more complex profile. Figure 5 shows, for instance, the centroid of three different clusters of molecular conformers, sampled from the azimuth distribution in the constriction region.

In OmpC, where preorientation is not effective, the azimuth distributions are broader than observed in OmpF, for every cross-section between the preorientation and the constriction region

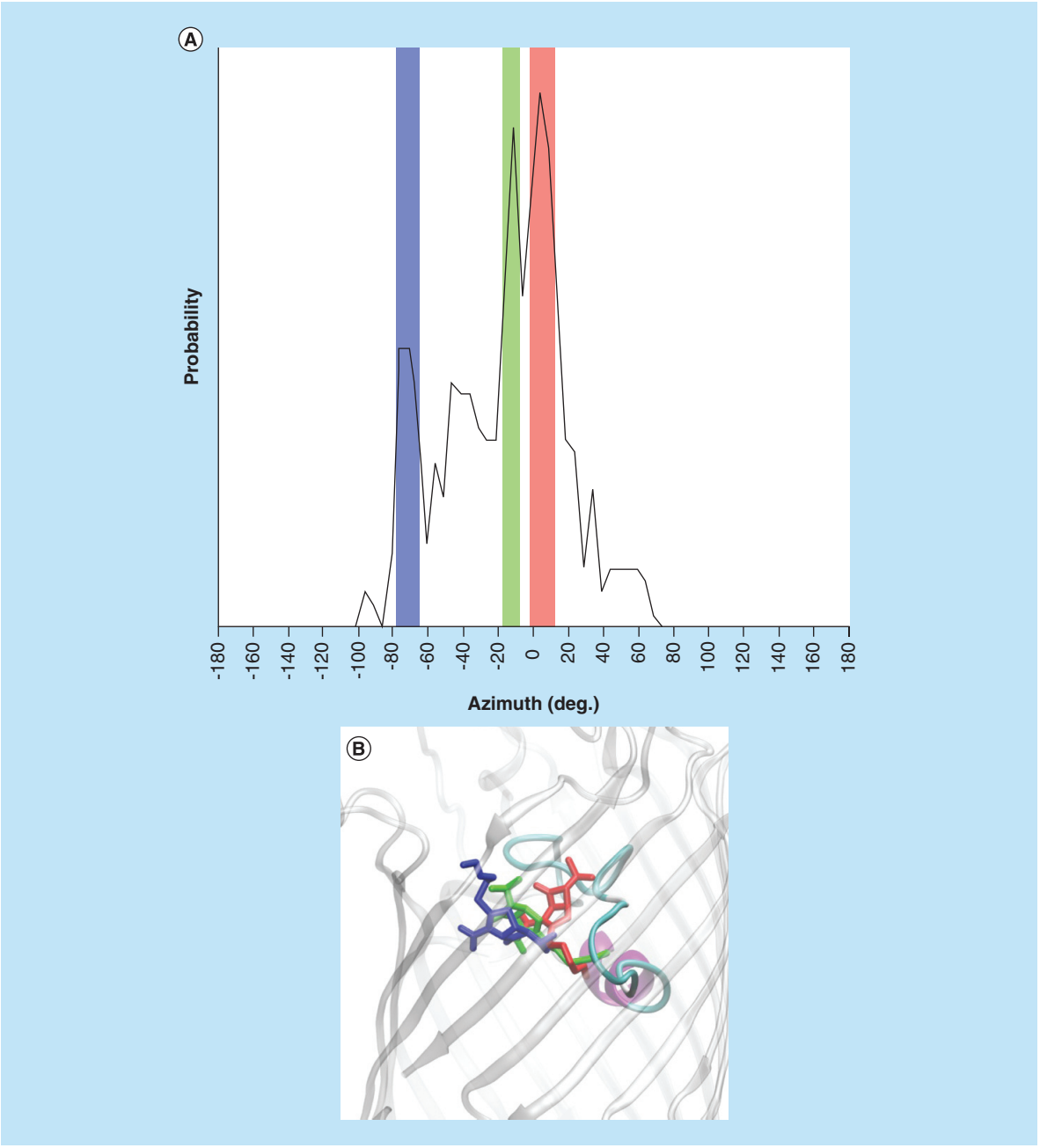

Figure 5. Comparison between the conformations relative to different values of the azimuth angle assumed by the dipole moment of imipenem. The distribution of the azimuth angle of imipenem's electric dipole at the constriction region of OmpF is shown **(A)**. The three shaded regions highlight the corresponding populations sampled (red, closest to the waters' net dipole; green, acceptable alignment; blue, severely misaligned). In **(B)**, the centroid of the three corresponding antibiotic clusters are color coded in agreement to **(A)**, and are shown inside the cartoon of the 3D structure of the porin's monomer, where only loop L3 is colored to provide a reference.

(Figure 4 & Supplementary Figure 2). There is not one clear main fraction of conformers properly aligned to the channel electrostatics, showing that imipenem is not driven to adopt any specific orientation along its way toward the constriction region.

The case of OmpC20 might be misleading at a first sight. The azimuth distributions clearly show that the electrostatics at the preorientation region is absolutely effective. By virtue of the large variation of directionality in the following cross-sections, imipenem is not able to properly follow the electrostatics variations while descending toward the constriction region. Nevertheless, quite surprisingly, the azimuth distribution in the constriction region results very well centered around the 'correct' orientation (Figure 4 & Supplementary Figure 2).

In order to discern this apparent discrepancy, it has to be noted that the azimuth distributions do not take the magnitude of the dipole xy-projection into any account. It is important to focus on the entropic nature of the main barrier for antibiotic translocation through the general porins under investigation [17,19,23,25,26,47,48]. The unfavorable entropic cost coming from desolvation and confinement of the drug inside the constriction region can be (partially) compensated by favorable drug-porin interactions, like H-bonds and salt bridges. In this scenario, where entropy–enthalpy balance is crucial, the optimal alignment of the antibiotic's electric dipole to the channel electrostatics comes into play.

Figure 6 shows different conformers, which were all extracted from the main population of the azimuth distribution of imipenem's dipole in the constriction region of OmpC20, as representative structures for different conformational clusters actually pertaining to the same azimuth population. The optimal molecular orientation was sometimes observed (Figure 6B), where the magnitude of the xy-component of the dipole is close to the maximum value achievable; however, imipenem was often found either to be extended but mostly oriented along the channel axis (Figure 6C & D), or to assume a compact scorpion-like conformation with a reduced electric dipole (Figure 6E & F). All of these conformers are characterized by a significantly lower xy-component of the dipole moment than the one depicted in Figure 6B, meaning that the energy gain coming from dipole alignment to the channel electrostatics is proportionally lower.

A comprehensive picture was obtained by calculating the cross-correlation between the azimuth distribution and the xy-magnitude of the electric dipole. Results are shown in Supplementary Figure 3. The agreement between these results and the qualitative argumentation on the constriction region accessibility discussed above (Figure 1) is remarkable. In OmpF, the highest probability is found for a good azimuthal alignment of the drug's dipole (around 0 degree) and rather high values of the xy-magnitude (>20 D). In OmpC, the ineffective preorientation translates into an increased disorder of

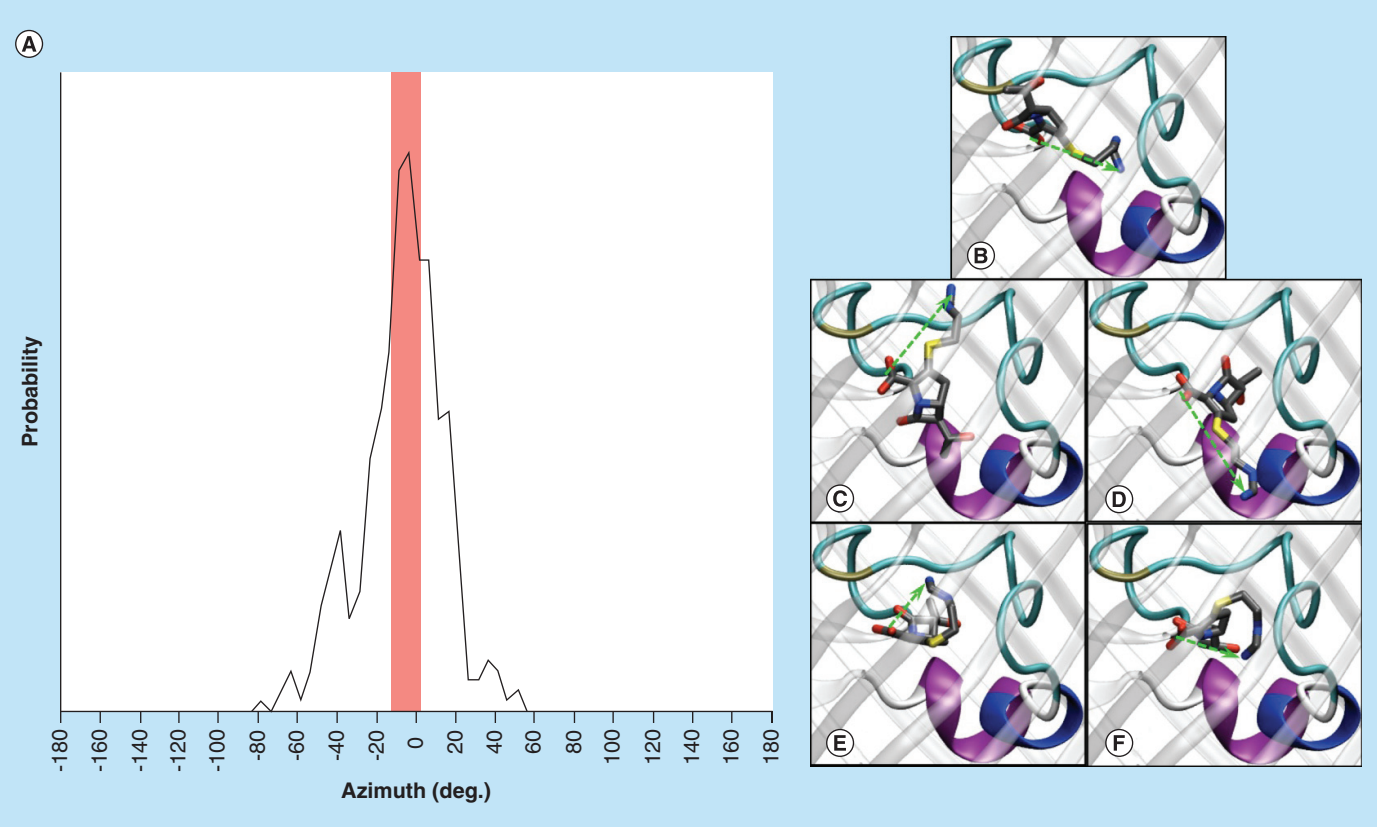

Figure 6. Comparison between different conformations relative to the same value of the azimuth angle assumed by the dipole moment of imipenem. The distribution of the azimuth angle of imipenem's electric dipole in the constriction region of OmpC20 is shown **(A)**. The red shaded region highlights the corresponding population sampled (the main one and closest to the waters' net dipole). In **(B–F)**, different conformers of imipenem are shown, chosen as being representative for different conformational clusters pertaining to the same azimuth population highlighted in **(A)**. These are shown inside the cartoon of the 3D structure of the porin's monomer, where only loop L3 is colored to provide a reference. The green dashed arrows are used to indicate the dipole's orientation.

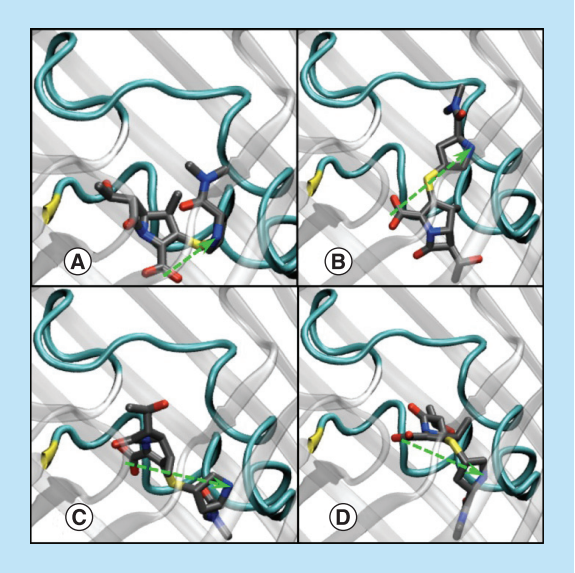

Figure 7. Comparison between different conformations assumed by meropenem and corresponding direction of the dipole moment. Different conformers of meropenem are shown, chosen as being representative for different conformational clusters in the constriction region of OmpC20. They are shown inside the cartoon of the 3D structure of the porin's monomer, where only loop L3 is colored to provide a reference. The green dashed arrows are used to indicate the dipole's orientation.

the antibiotics' dipole orientation inside the constriction region. In Supplementary Figure 3, a broader distribution with a significant probability for wrong orientations can be clearly seen for this protein. In OmpC20, despite the distribution of the azimuth is as narrow as in OmpF, the distribution of the xy-magnitude is broader, reaching values as low as approximately 10 D with a rather high probability. In the extracellular vestibule, the antibiotic is preoriented in the opposite direction to the one needed to get into the constriction region and should reorient while translocating by just approximately 1 nm. As a result, it often assumes nonoptimal conformations when entering the constriction region (Figure 6), thus loosing the benefits from an optimal alignment of the electric dipole to the pore's electrostatics. Finally, in OmpC33, the combination of an effective adverse preorientation and the fact that such preorientation is kept deeper into the channel (Figure 3), leads to a dramatic increase of the probability to obtain a misalignment of the dipole inside the constriction region (Supplementary Figure 3).

In Supplementary Figure 4, meropenem choreography in the four protein channels is compared. The overall trends and the differences are absolutely comparable to the case of imipenem. These results clearly point to the major role played by the electrostatics of the channel in driving the reorientations and, thus, the translocation path of dipolar antibiotics like the two carbapenems investigated in this work. In Supplementary Figure 5, the cross-correlation between the azimuth and xy-magnitude of the electric dipole is shown for meropenem in the constriction region of the four porins, providing a more comprehensive picture than the one offered by simple azimuth distributions.

In OmpF, the highest probability is found for good azimuthal alignment (around 0 degree) and high values of the xy-projection (around 30 Debye). In OmpC, the highest probability is similarly found for good azimuthal alignment but at a significantly lower xy-magnitude. In addition, the 2D probability distribution is more asymmetric than observed for OmpF in both dimensions. Along the xy-magnitude, the tail on the high values side has almost completely disappeared moving from OmpF to OmpC. Along the azimuth angle, the probability for negative deviations from the reference value obtained from water ordering has significantly increased. In the case of OmpC20, the deviation from the optimal alignment is clear. Finally, in OmpC33, similarly to the case of imipenem, the combination of an effective adverse preorientation, and the fact that this is kept deeper into the channel, leads to a dramatic increase of the probability for dipole misalignment from channel electrostatics inside the constriction region.

Antibiotic-specific features come into play on the porin's choreography

Besides the porin-dependent 'background', a deeper inspection of our results suggests important antibiotic-specific differences playing their role. The shorter and more flexible imipenem actually appears more sensitive to the preorientation. A generally more disordered population of conformers was found, indeed, when moving from one porin to the next along the series presented in this work. On the other hand, the longer and more rigid meropenem does not follow preorientation with the same accuracy as that of imipenem, since its reorientations are hindered already in the extracellular vestibule due to the larger size of this antibiotic. In addition, the positively charged group of meropenem is not located at the end of a flexible side chain like in imipenem, but on a rigid ring separated by only two rotatable bonds from the carboxyl group. The combination of these molecular features is reflected by a generally less disordered distribution of the electric dipole orientation inside the constriction region. Indeed, despite meropenem adopts different conformations, the azimuth and the xy-magnitude of its electric dipole are far less dependent from side chain fluctuations than they are in the case of imipenem. For instance, Figure 7 shows different conformers of meropenem in the constriction region of

OmpC20. All of these are representative structures of different conformational clusters.

Finally, aiming at capturing all of these molecular features in a unique parameter, Figure 8 compares the distributions of the dipole module and the angle between the dipole itself and the main molecular axis of inertia, obtained for all the investigated cases when the antibiotic is located inside the constriction region. The corresponding results obtained in bulk water (*ad hoc* MD simulations were performed with just the antibiotic in a water box) are also shown for the sake of comparison. No significant variation of the module of the electric dipole is observed in the different porins and when compared with the distribution in bulk water. Meropenem, on average, shows higher values than imipenem. On the other hand, more interesting differences are observed when the angle between the dipole and the main molecular axis is compared. In agreement with all of the results and comparisons shown above, OmpF (Figure 8F) does not impose the two antibiotics to populate conformations that are not inherently populated in bulk water (Figure 8J). As far as the electric dipole deviation from the main molecular axis is concerned, imipenem and meropenem appear fairly comparable in this case. However, looking at OmpC and its mutants, in the case of meropenem, such molecular feature is scarcely influenced by the specific porin being crossed, and the obtained distributions are comparable to each other and to the one in bulk water. Conversely, imipenem results deeply affected by the porin, as it populates conformations characterized by a larger dipole–main axis deviation, whose probability increases along the series OmpC, OmpC20 and OmpC33.

Conclusion

The similarities observed in the behavior of the two carbapenems investigated here show the major role played by the specific porins under consideration. The characteristic hourglass shape of these general unspecific channels dictates the presence of a main barrier for the translocation of metabolites and drugs, which is basically entropic. Differences in the electrostatics of the four channels result in impressive changes of the orientations assumed by dipolar molecules during the passage, as shown in the present work by comparing the translocation path of the same carbapenems through different porins. The effects of the electrostatics appear so large that in some cases it is more difficult for the drug to approach, rather than enter the channel's constric-

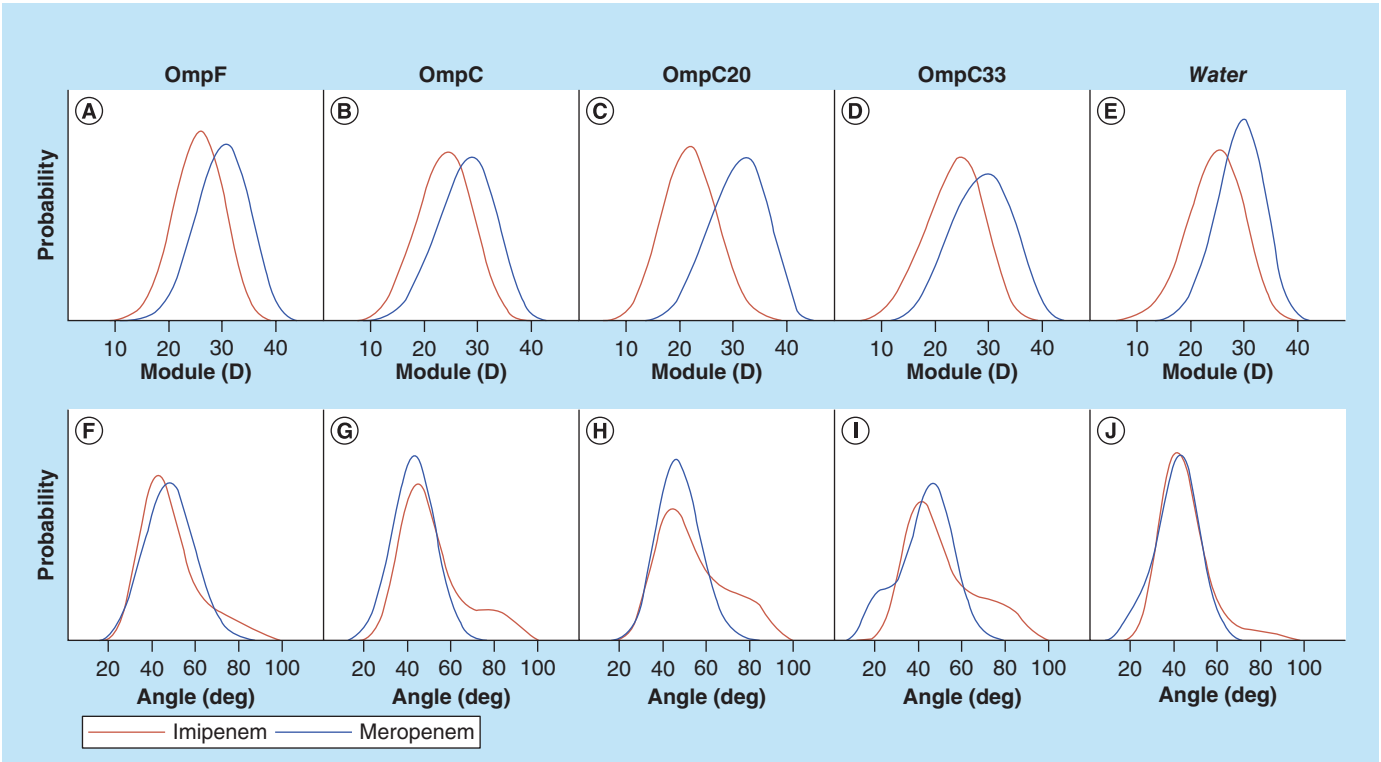

Figure 8. Distribution of the dipole model and angle between the dipole itself and the main axis of inertia for imipenem and meropenem in the study. The distribution of the dipole module **(A–E)** is shown together with the distribution of the plain angle between the electric dipole itself and the main axis of inertia **(F–J)** for imipenem (red) and meropenem (blue) inside the constriction region of the four porins under investigation, as well as in bulk water for the sake of comparison.

tion region, as observed for the two OmpC mutants from *E. coli* resistant strains.

Nevertheless, a deeper inspection and careful comparison of the results we have shown, suggested that important antibiotic-specific differences apply on the porin-dependent 'background'. The shorter and more flexible imipenem appeared more sensitive to the effects of a different preorientation. On the other hand, the longer and more rigid meropenem did not follow preorientation with the same accuracy as that of imipenem.

Interestingly, as a concluding remark, a closer look at the distributions obtained in bulk water reveals that an inherently different propensity toward large deviations between the direction of the electric dipole and the main molecular axis of inertia actually exists among these two carbapenems. In our opinion, the latter represents an intrinsic antibiotic-specific feature deserving particular attention in the future for a more rational drug design. By taking multiple molecular 'classic' parameters into account, being probably more important than the simple size, net charge, conformational plasticity and so on, it appears fundamental in determining the overall permeability through the target porin.

A concluding remark has also to be devoted to the membrane model employed here. Although certainly useful to compare our theoretical results to a variety of experimental setups, the overall permeability of dipolar molecules through OM porins is not only due the phenomena described in the present work. For instance, MD simulations of the TonB-dependent transporter FecA both within symmetric phospholipid bilayer and asymmetric phospholipid/LPS bilayer have shown how the extracellular loops of the embedded protein channel can interact with the LPS [49]. These interactions might result in significant differences of both local fluctuations as well as larger conformational motions of the protein loops, ultimately affecting permeability and transport properties [49]. Thus, the aspects investigated in the present work, focused on the dynamics of the crossing drug in response to the internal electrostatics of the channel, are hardly affected by the plasticity of the extracellular loops, but the latter may be among the main determinant for the overall permeability and surely deserves detailed investigations toward a comprehensive picture of the dipolar antibiotics' translocation across the OM.

Future perspective

To understand how porins located in the outer membrane of Gram-negative bacteria are able to filter noxious molecules is extremely important to design/optimize new antibacterials with better permeation. In this context, the availability of high-resolution crystal structures is fundamental to unveil the molecular mechanism of filtering in bacterial porins. The level of sophistication of modern molecular modeling algorithms together with the employment of new computer hardware makes it possible to simulate these complex processes at the molecular level of detail. Our recent efforts have shown that a synergistic combination of structural data, *in vitro* assays and computer simulations is capable to come to a real identification and description of the physical and chemical properties of molecules that can cross the outer membrane barrier. Once the 'golden rules' of permeation will be fully understood, the application of virtual screening techniques will help to search for new scaffolds with enhanced permeation, with molecular modeling being extremely helpful for compounds optimization.

Financial & competing interests disclosure

The research leading to these results was conducted as part of the 'Translocation' consortium (www.translocation.com) and has received support from the Innovative Medicine Initiatives Joint Undertaking under Grant Agreement no. 115525, resources that are composed of financial contribution from the European Union's seventh framework program (FP7/2007-2013) and EFPIA companies in kind contribution. S Acosta-Gutierrez is a Marie Skłodowska-Curie fellow within the 'Translocation' Network, project no. 607694. The authors also want to thank the financial support of MIUR (PRIN 2010CSJX4F). The authors have no other relevant affiliations or financial involvement with any organization or entity with a financial interest in or financial conflict with the subject matter or materials discussed in the manuscript apart from those disclosed.

No writing assistance was utilized in the production of this manuscript.

Supplementary data

To view the supplementary data that accompany this paper, please visit the journal website at: www.future-science.com/doi/full/10.4155/fmc-2016-0038

Executive summary

- The analysis of molecular dynamics trajectories revealed how dipolar antibiotics reorient inside bacterial porins to match the channel's electrostatics.
- The analysis of a series of clinical resistant mutants showed modifications in the so-called preorientation region as fundamentally altering the antibiotic translocation path.
- The importance of proper alignment of the molecular dipole during the translocation has been highlighted and the deviation of dipole direction from the main molecular axis of inertia has been put forward as a parameter for drug design.

References

Papers of special note have been highlighted as:
• of interest; •• of considerable interest

1 Brown ED, Wright GD. Antibacterial drug discovery in the resistance era. *Nature* 529(7586), 336–343 (2016).

• **Very recent review and perspective on antibiotics and resistance.**

2 Tommasi R, Brown DG, Walkup GK, Manchester JI, Miller AA. ESKAPEing the labyrinth of antibacterial discovery. *Nat. Rev. Drug Discov.* 14(8), 529–542 (2015).

3 When the drugs don't work. *Nat. Microbiol.* 1(2), 16003 (2016).

4 Antimicrobial resistance: global report on surveillance. www.who.int/drugresistance/documents/surveillancereport

5 Wright GD. The antibiotic resistome: the nexus of chemical and genetic diversity. *Nat. Rev. Microbiol.* 5(3), 175–186 (2007).

6 Masi M, Pagès J-M. Structure, function and regulation of outer membrane proteins involved in drug transport in enterobactericeae: the OmpF/C – TolC case. *Open Microbiol. J.* 7, 22–33 (2013).

7 Lewis K. Platforms for antibiotic discovery. *Nat. Rev. Drug Discov.* 12(5), 371–387 (2013).

8 Isabella VM, Campbell AJ, Manchester J *et al.* Toward the rational design of carbapenem uptake in *Pseudomonas aeruginosa*. *Chem. Biol.* 22(4), 535–547 (2015).

•• **They proved for the first time a direct correlation of MIC with decreased permeability of antibiotics modulated by small chemical modifications that increased target affinity.**

9 Delcour AH. Outer membrane permeability and antibiotic resistance. *Biochim. Biophys. Acta BBA* 1794(5), 808–816 (2009).

10 Samanta S, Scorciapino MA, Ceccarelli M. Molecular basis of substrate translocation through the outer membrane channel OprD of *Pseudomonas aeruginosa*. *Phys. Chem. Chem. Phys.* 17(37), 23867–23876 (2015).

11 Kojima S, Nikaido H. Permeation rates of penicillins indicate that *Escherichia coli* porins function principally as nonspecific channels. *Proc. Natl Acad. Sci. USA* 110(28), E2629–E2634 (2013).

12 Fairman JW, Noinaj N, Buchanan SK. The structural biology of β-barrel membrane proteins: a summary of recent reports. *Curr. Opin. Struct. Biol.* 21(4), 523–531 (2011).

13 Pagès J-M, James CE, Winterhalter M. The porin and the permeating antibiotic: a selective diffusion barrier in Gram-negative bacteria. *Nat. Rev. Microbiol.* 6(12), 893–903 (2008).

14 Cowan S, Schirmer T, Rummel G *et al.* Crystal-structures explain functional-properties of 2 *Escherichia-coli* porins. *Nature* 358(6389), 727–733 (1992).

15 Baslé A, Rummel G, Storici P, Rosenbusch JP, Schirmer T. Crystal structure of osmoporin OmpC from *E. coli* at 2.0 Å. *J. Mol. Biol.* 362(5), 933–942 (2006).

16 Kojima S, Nikaido H. High salt concentrations increase permeability through OmpC channels of *Escherichia coli*. *J. Biol. Chem.* 289(38), 26464–26473 (2014).

17 Tran Q-T, Williams S, Farid R, Erdemli G, Pearlstein R. The translocation kinetics of antibiotics through porin OmpC: insights from structure-based solvation mapping using WaterMap. *Proteins Struct. Funct. Bioinforma.* 81(2), 291–299 (2013).

18 Brown DG, May-Dracka TL, Gagnon MM, Tommasi R. Trends and exceptions of physical properties on antibacterial activity for Gram-positive and Gram-negative pathogens. *J. Med. Chem.* 57(23), 10144–10161 (2014).

19 Ziervogel BK, Roux B. The binding of antibiotics in OmpF porin. *Structure* 21(1), 76–87 (2013).

• **First porin-antibiotic co-complex solved at high resolution.**

20 Raj Singh P, Ceccarelli M, Lovelle M, Winterhalter M, Mahendran KR. Antibiotic permeation across the OmpF channel: modulation of the affinity site in the presence of magnesium. *J. Phys. Chem. B.* 116(15), 4433–4438 (2012).

21 Lou H, Chen M, Black SS *et al.* Altered antibiotic transport in OmpC mutants isolated from a series of clinical strains of multi-drug resistant *E. coli*. *PLoS ONE* 6(10), e25825 (2011).

•• **They resolved at high resolution a series of porins from clinical strains having the same internal size but different permeability due to electrostatic modifications.**

22 O'Shea R, Moser HE. Physicochemical properties of antibacterial compounds: implications for drug discovery. *J. Med. Chem.* 51(10), 2871–2878 (2008).

23 Kumar A, Hajjar E, Ruggerone P, Ceccarelli M. Molecular simulations reveal the mechanism and the determinants for ampicillin translocation through OmpF. *J. Phys. Chem. B.* 114(29), 9608–9616 (2010).

24 Mahendran KR, Hajjar E, Mach T *et al.* Molecular basis of enrofloxacin translocation through OmpF, an outer membrane channel of *Escherichia coli* – when binding does not imply translocation. *J. Phys. Chem. B.* 114(15), 5170–5179 (2010).

25 Danelon C, Nestorovich EM, Winterhalter M, Ceccarelli M, Bezrukov SM. Interaction of zwitterionic penicillins with the OmpF channel facilitates their translocation. *Biophys. J.* 90(5), 1617–1627 (2006).

26 Hajjar E, Bessonov A, Molitor A *et al.* Toward screening for antibiotics with enhanced permeation properties through bacterial porins. *Biochemistry (Mosc.).* 49(32), 6928–6935 (2010).

27 Winterhalter M, Ceccarelli M. Physical methods to quantify small antibiotic molecules uptake into Gram-negative bacteria. *Eur. J. Pharm. Biopharm.* 95, 63–67 (2015).

28 Patel DS, Re S, Wu EL *et al.* Dynamics and interactions of OmpF and LPS: influence on pore accessibility and ion permeability. *Biophys. J.* 110(4), 930–938 (2016).

29 Parkin J, Chavent M, Khalid S. Molecular simulations of Gram-negative bacterial membranes: a vignette of some recent successes. *Biophys. J.* 109(3), 461–468 (2015).

30 Berglund NA, Piggot TJ, Jefferies D, Sessions RB, Bond PJ, Khalid S. Interaction of the antimicrobial peptide polymyxin B1 with both membranes of *E. coli*: a molecular dynamics study. *PLoS Comput. Biol.* 11(4), e1004180 (2015).

31 Khalid S, Berglund NA, Holdbrook DA, Leung YM, Parkin J. The membranes of Gram-negative bacteria: progress

in molecular modelling and simulation. *Biochem. Soc. Trans.* 43(2), 162–167 (2015).

32 Wu EL, Fleming PJ, Yeom MS *et al. E. coli* outer membrane and interactions with OmpLA. *Biophys. J.* 106(11), 2493–2502 (2014).

33 Wu EL, Engström O, Jo S *et al.* Molecular dynamics and NMR spectroscopy studies of *E. coli* lipopolysaccharide structure and dynamics. *Biophys. J.* 105(6), 1444–1455 (2013).

34 Acosta-Gutierrez S, Scorciapino MA, Bodrenko I, Ceccarelli M. Filtering with electric field: the case of *E. coli* porins. *J. Phys. Chem. Lett.* 6(10), 1807–1812 (2015).

•• **They proposed a model for molecular filtering in general channels.**

35 Acosta-Gutiérrez S, Bodrenko I, Scorciapino MA, Ceccarelli M. Macroscopic electric field inside water-filled biological nanopores. *Phys. Chem. Chem. Phys.* 18(13), 8855–8864 (2016).

• **They proposed a way to quantify the macroscopic electric field using water as a probe.**

36 Low AS, MacKenzie FM, Gould IM, Booth IR. Protected environments allow parallel evolution of a bacterial pathogen in a patient subjected to long-term antibiotic therapy. *Mol. Microbiol.* 42(3), 619–630 (2001).

37 Bajaj H, Scorciapino MA, Moynié L *et al.* Molecular basis of filtering carbapenems by porins from β-lactam-resistant clinical strains of *Escherichia coli*. *J. Biol. Chem.* 291(6), 2837–2847 (2016).

• **They measured the effect of modified internal electrostatic of porins on the permeation of antibiotics.**

38 Lindorff-Larsen K, Piana S, Palmo K *et al.* Improved side-chain torsion potentials for the Amber ff99SB protein force field. *Proteins* 78, 1950–1958 (2010).

39 Jorgensen W, Chandrasekhar J, Madura J, Impey R, Klein M. Comparison of simple potential functions for simulating liquid water. *J. Chem. Phys.* 79, 926–936 (1983).

40 Varma S, Chiu S-W, Jakobsson E. The influence of amino acid protonation states on molecular dynamics simulations of the bacterial porin OmpF. *Biophys. J.* 90(1), 112–123 (2006).

41 Barducci A, Bussi G, Parrinello M. Well-tempered metadynamics: a smoothly converging and tunable free-energy method. *Phys. Rev. Lett.* 100(2), 020603 (2008).

42 Harvey M, Giupponi G, De Fabritiis G. ACEMD: accelerating biomolecular dynamics in the microsecond time scale. *J. Chem. Theory Comput.* 5, 1632–1639 (2009).

43 Tribello GA, Bonomi M, Branduardi D, Camilloni C, Bussi G. PLUMED 2: new feathers for an old bird. *Comput. Phys. Commun.* 185(2), 604–613 (2014).

44 Wang J, Wolf RM, Caldwell JW, Kollman PA, Case DA. Development and testing of a general amber force field. *J. Comput. Chem.* 25(9), 1157–1174 (2004).

45 Malloci G, Vargiu AV, Serra G, Bosin A, Ruggerone P, Ceccarelli M. A database of force-field parameters, dynamics, and properties of antimicrobial compounds. *Mol. Basel Switz.* 20(8), 13997–14021 (2015).

• **A structural and dynamical database on antibiotics.**

46 Raiteri P, Laio A, Gervasio FL, Micheletti C, Parrinello M. Efficient reconstruction of complex free energy landscapes by multiple walkers metadynamics. *J. Phys. Chem. B.* 110(8), 3533–3539 (2006).

47 Ceccarelli M, Vargiu AV, Ruggerone P. A kinetic Monte Carlo approach to investigate antibiotic translocation through bacterial porins. *J. Phys. Condens. Matter.* 24(10), 104012 (2012).

48 D'Agostino T, Salis S, Ceccarelli M. A kinetic model for molecular diffusion through pores. *Biochim. Biophys. Acta* doi:10.1016/j.bbamem.2016.01.004. (2016) (Epub ahead of print).

49 Piggot TJ, Holdbrook DA, Khalid S. Conformational dynamics and membrane interactions of the *E. coli* outer membrane protein FecA: a molecular dynamics simulation study. *Biochim. Biophys. Acta* 1828(2), 284–293 (2013).

Macroscopic Electric Field inside water-filled biological nanopores

PCCP

PAPER

View Article Online
View Journal | View Issue

Cite this: *Phys. Chem. Chem. Phys.*, 2016, **18**, 8855

Macroscopic electric field inside water-filled biological nanopores

Silvia Acosta Gutiérrez,[a] Igor Bodrenko,[a] Mariano Andrea Scorciapino[b] and Matteo Ceccarelli*[a]

Received 22nd December 2015,
Accepted 17th February 2016

DOI: 10.1039/c5cp07902k

www.rsc.org/pccp

Multi-drug resistance bacteria are a challenging problem of contemporary medicine. This is particularly critical for Gram-negative bacteria, where antibiotics are hindered by the outer membrane to reach internal targets. Here more polar antibiotics make use of nanometric water-filled channels to permeate inside. We present in this work a computational all-atom approach, using water as a probe, for the calculation of the macroscopic electric field inside water-filled channels. The method allows one to compare not only different systems but also the same system under different conditions, such as pH and ion concentration. This provides a detailed picture of electrostatics in biological nanopores shedding more light on how the charged residues of proteins determine the electric field inside, and also how medium can tune it. These details are central to unveil the filtering mechanism behind the permeation of small polar molecules through nanometric water-filled channels.

Introduction

Multi-drug resistance bacteria are a challenging problem of contemporary medicine.[1] New synergies and a molecular-based framework are necessary for identifying and developing the next generation anti-infectives.[2,3] This is particularly critical for Gram-negative bacteria where the presence of the additional outer membrane (OM) hinders any antibiotics to access internal targets.[4] In the OM, general diffusion porins are expressed to facilitate the entry of small polar molecules (less than 1000 Da), and today porins are considered to be the main pathway for polar antibiotics for overcoming the OM barrier.[5,6] Bacteria can develop resistance by reducing the OM permeability, either by modulating the expression of porins, or by selecting key residue mutations that alter the permeability of the porins themselves.[7] Further, no direct and robust methods to measure the permeation/accumulation of drugs are available at present,[8] neither *in vitro* nor *in vivo*. This technological gap reduced enormously the research and investment in the field,[1,2] leaving the pipeline empty. Therefore, the discovery of new effective antibiotics for Gram-negative bacteria passes through the determination of the mechanism controlling their permeation through porins.[9] The internal electrostatics of porins seem to play a major role[10] and simulations seem to have the potentiality to unravel such molecular mechanisms.[11,12]

Since the determination of their high-resolution X-ray structures, porin channels showed an hourglass shape and interesting electrostatic properties. Both OmpF and OmpC, the major porins expressed in *Escherichia coli*, show a well-separated distribution of charged residues in the nanometric eyelet region (7×11 Å).[13] Cell-free electrophysiology experiments at the single molecule level pointed out the key role of electrostatics in the interaction of polar molecules with these protein channels.[14,15] Despite being similar in size,[7] their expression level is usually not the same but profoundly affected by osmolarity, pH and growth conditions.[16] In particular, while OmpF is prevalent in low osmolarity media, OmpC is the most expressed outer membrane porin in high osmolarity.

Several theoretical attempts at characterizing the electrostatics inside porins have been reported,[17–20] starting from the pioneering work of Karshikoff,[17] which employed the Poisson–Boltzmann equation, till the valuable work reported by Im and Roux,[18] which, by using molecular dynamics (MD) simulations, described a screw-like electrostatics for OmpF, although at a rather high ion concentration (1 M). In the present work we propose a strategy to quantify the macroscopic electric field inside these nanometric water-filled channels from all-atom MD simulations. In order to show the detail level achievable, we selected four porins of the same family, namely, OmpF, OmpC and two mutants from *E. coli* clinical strains, OmpC20 and OmpC33, with assessable differences in susceptibility to polar molecules, in spite of the comparable pore size.[7] The same series was recently employed by our group to show the diverse filtering of

[a] *Department of Physics, University of Cagliari, Cittadella universitaria di Monserrato, S.P.8 – km 0.700, 09042 Monserrato (CA), Italy. E-mail: matteo.ceccarelli@dsf.unica.it*
[b] *Department of Biomedical Sciences, Biochemistry Unit, University of Cagliari, Cittadella universitaria di Monserrato, S.P.8 – km 0.700, 09042 Monserrato (CA), Italy*

carbapenem antibiotics[21] and the modulation of water ordering[10] upon charged residue mutations.

The ordering of water molecules is a raising question in many membrane proteins controlling key processes in the cell, such as aquaporins[22,23] and GPCR systems.[24] Here we have taken a step forward by quantifying the internal electric field, not just probing its effects on the water/ions as already done. We have made use of water molecules, since, naturally filling the selected porins, they can be considered an optimal and intrinsic probe. In addition, the small size of water is reflected by a rather low rotational correlation time,[25] whereas its relatively large electric dipole ensures sensitivity to the channel's electrostatics. The dielectric constant of water inside the channel is decisive in the calculation of the internal electric field. The non-linear response of water to an applied electric field is widely recognized[26–28] and such nonlinearity of water polarization is reflected by the decrease of the dielectric constant with increasing applied electric field, the so-called water dielectric saturation effect. In the case of the lumen of protein channels, one faces two problems, the non-linearity and non-uniformity of the media, remarkably complicating the selection of an appropriate dielectric constant.[29]

In the present study, the local macroscopic electric field is directly calculated from all-atom MD simulations by using the transfer function that contains the response of the media to the applied electric field. Importantly, the approach is applied without any initial guess of the dielectric constant inside the pore. This allowed us to characterize the electrostatics of the selected porins in detail by calculating the local intrinsic electric field along the channel axis. Subtle differences due to very few amino acid mutations have been identified and highlighted and, with the same level of details, it was possible to investigate the influence of physiologically important modifications of the media, such as the ion concentration and pH. The method is not only relevant to protein or water-filled channels in general, but can be easily extended to solvated proteins for the calculation of the electric field along the external surface or at a water-filled cavity. The only prerequisite is the presence of enough water molecules to be used as probes.

Methods

Theoretical background

Complex bio-molecular systems like protein channels are strongly inhomogeneous, as they are embedded into a lipid membrane and solvated. Therefore, the macroscopic (Maxwell) electrostatic field, $\boldsymbol{E}(\boldsymbol{r})$, must be considered locally. According to the standard paradigm of continuum classical electrostatic theory, the microscopic electric field, $\boldsymbol{e}$, must be statistically averaged over a small space (*e.g.*, a sphere) around the point $\boldsymbol{r}$, where one wants to calculate it, $\boldsymbol{E}(\boldsymbol{r}) = \langle \boldsymbol{e} \rangle_{\boldsymbol{r}}$. One should also determine the local polarization density, $\boldsymbol{P}(\boldsymbol{r})$, *i.e.*, the average dipole moment of the sphere per unit volume, the local electric displacement vector, $\boldsymbol{D}(\boldsymbol{r}) = \boldsymbol{E}(\boldsymbol{r}) + 4\pi\boldsymbol{P}(\boldsymbol{r})$, and the density, $\rho_f(\boldsymbol{r})$, of 'free' charges (unbound or uncompensated, which do not contribute to $\boldsymbol{P}$). All of these quantities are related to each other through the Maxwell equations: $\nabla\cdot\boldsymbol{D} = 4\pi\rho_f(\boldsymbol{r})$; $\nabla \times \boldsymbol{E} = 0$. If one knows $\rho_f(\boldsymbol{r})$ as well as the dielectric response function, $\boldsymbol{P}(\boldsymbol{E},\boldsymbol{r})$, the electric field may be obtained by solving the Maxwell equations with specified boundary conditions.

It is not trivial, however, to determine (both experimentally and theoretically) the local dielectric response for a strongly inhomogeneous system: in general, $\boldsymbol{P}(\boldsymbol{E},\boldsymbol{r})$ is anisotropic (vectors $\boldsymbol{P}$ and $\boldsymbol{E}$ are not parallel) and non-linear; moreover, the response may be non-local, *i.e.*, $\boldsymbol{P}$, is a non-local functional of $\boldsymbol{E}(\boldsymbol{r})$.

In the widely used local, linear and isotropic approximation, one defines the local dielectric constant, $\varepsilon(\boldsymbol{r})$, so that $\boldsymbol{D} = \varepsilon(\boldsymbol{r})\boldsymbol{E}$. Then, the Maxwell equations are reduced to the Poisson equation, $\boldsymbol{\nabla}\cdot\varepsilon(\boldsymbol{r})\boldsymbol{\nabla}\varphi = -4\pi\rho_f(\boldsymbol{r})$, for the electrostatic potential, $\varphi(\boldsymbol{r})$, and the electric field reads, $\boldsymbol{E} = -\boldsymbol{\nabla}\varphi$. One usually uses a piecewise constant function model for $\varepsilon(\boldsymbol{r})$. Thus, in the case of solvated membrane proteins, *e.g.* in ref. 17, $\varepsilon_p = 4$ is used for the protein part, $\varepsilon_s = 80$ for the solvent (water), *etc.* The non-linear electric field effects on the solvent due to the saturation of the dielectric response in a strong field was considered by taking an effective (smaller) dielectric constant for the regions of strong field.[30] In another study,[31] the non-linear dielectric function, $\varepsilon_s(E)$, was approximated by a Langevin-type function with the parameters adjusted to the bulk solvent response and then the non-linear Poisson equation was solved. There, the spatial dependence of the dielectric constant of the solvent comes from the non-linear response and the spatially varying electric field, $\varepsilon_s(\boldsymbol{r}) = \varepsilon_s(E(\boldsymbol{r}))$. The free charge density, $\rho_f(\boldsymbol{r})$, is composed of the fixed charged groups in proteins and mobile ions. The ion density at equilibrium is treated by assuming the Boltzmann statistics (the Poisson–Boltzmann method[17] or its linearized version, *i.e.* the Debye–Hückel method for low ion concentration). If the ion density is not at equilibrium, the diffusion-drift (Nernst–Planck) theory or a more general Brownian dynamics method should be employed,[18] coupled with the Poisson equation to calculate the ion density and the electrostatic potential simultaneously.

All the continuum electrostatics methods briefly presented hereinbefore require strong assumptions about the dielectric response of the inhomogeneous medium as well as about the free ion distribution. Differently, it is important to stress here that within the approach presented in this work, the macroscopic electrostatic field is calculated by using all-atom MD simulations with minimal assumptions (besides the standard ones that are fundamentals to the classical MD). In the following, we will consider the electric field in the regions of the system occupied by the solvent (water, in our case).

For the bulk (homogeneous) solvent, the polarization density is completely determined by the thermodynamic parameters: the density (ρ), the temperature (T), and the electric (macroscopic) field ($\boldsymbol{E}$), $\boldsymbol{P} = \boldsymbol{P}(\rho,T,\boldsymbol{E})$. Then, we suggest that the local dielectric response over the averaging space in the inhomogeneous regions of the system is the same as for the bulk. This assumption is also accepted and argued in the Poisson equation based applications mentioned above.[17,18,30,31] This is the only approximation we do as the ions, the solvent, the protein, the membrane, *etc.*,

are treated at the all-atom level. Within this approximation, the ordering (alignment) of water molecules in the nanopore is assumed to come from the local average electric field in the probe. The surface effects, like the different response of the molecules on the boundary of the probe or the hydrogen bonds of some water molecules with protein residues are formally not taken into account. However, the local macroscopic electric field is defined within a coarse-grained model that neglects any inhomogeneity within the probe, so that the inhomogeneity in the response should also be neglected. Of course, the number N of water molecules on the probe should be large enough as the surface effects scale as N^2 while the main volume effects scale as N^3. One may estimate the simultaneous effect of all kinds of inhomogeneity, including the surface effects, by calculating the local macroscopic field with various radii of the probe.

The approach we propose is the following. First, the polarization density of the solvent has to be calculated in a localized spherical probe along the MD trajectory,

$$\boldsymbol{P} = \frac{\langle \boldsymbol{\mu} \rangle}{N_w v_w}, \quad (1)$$

where $\langle \boldsymbol{\mu} \rangle$ is the average dipole moment of the water molecules within the spherical probe, N_w is the average number of water molecules in the probe, and $\nu_w(\rho)$ is the average volume per solvent molecule at the given water density. Then, the electric field may be estimated by using the bulk response function that relates water polarization to the local Maxwell field $\boldsymbol{E}$ that has generated it, $\boldsymbol{P}(\rho,T,\boldsymbol{E})$, which is calculated within the same MD model. The shape of the probe is important for an inhomogeneous medium as the surface properties may contribute to the electrostatics through the standard boundary conditions for the normal and the tangential components of the electric field. This results in the dependence of the direction of the polarization vector of the probe on the shape of the latter, *e.g.*, the polarization vector in the cylindrical or ellipsoidal probe may be non-parallel with the electric field. For that reason, the sphere seems to be the best choice, as the induced dipole moment is collinear with the electric field, assuming a local isotropic response.

In order to calculate the response function of the (bulk) solvent by using MD simulations of an *NPT* ensemble in an external electric field, one considers a water box under the same pressure and temperature as in the simulation of the channels. All solvent molecules (we used the TIP3P model for water) feel the same additional external and constant electric field $\boldsymbol{E}_{ext}$. Thus, the total Maxwell field should be the sum of $\boldsymbol{E}_{ext}$ and the averaged electric field $\boldsymbol{E}_{ind}$ generated by the aligned molecules, $\boldsymbol{E} = \boldsymbol{E}_{ind} + \boldsymbol{E}_{ext}$. The corresponding electrostatic potentials, φ, φ_{ind}, and φ_{ext}, obey the Laplace equation as there are no 'free' charges in the system. The treatment of the electrostatic interactions within the Particle Mesh Ewald method[32,33] assumes the periodic (constant) boundary conditions for electrostatic potential φ_{ind}, but not for the external one, $\varphi_{ext} = -(\boldsymbol{r}\cdot\boldsymbol{E}_{ext})$. The Laplace equation with the periodic (constant) boundary conditions has only constant solution. Thus, the electric field, $\boldsymbol{E}_{ind}$, generated by the molecules in the box equals zero even if the net polarization density $\boldsymbol{P}$ of the box is not null. The total macroscopic field E then equals the external applied electric field, $\boldsymbol{E} = \boldsymbol{E}_{ext}$, which generates the polarization density $\boldsymbol{P}$.

This result may also be interpreted from the viewpoint of macroscopic electrostatic theory. Indeed, the constant potential on the boundary corresponds to the conducting (or *tin-foil*) boundary conditions.[34] The conducting boundary generates the reaction field which exactly cancels out the field generated by polarized solvent molecules, $\boldsymbol{E}_{ind}$. The remaining macroscopic field is equal to the external applied one.

Finally, the dielectric response function can be calculated from a MD trajectory for a given macroscopic field $\boldsymbol{E} = \boldsymbol{E}_{ext}$ by using eqn (1), where $\langle \boldsymbol{\mu} \rangle(\boldsymbol{E}_{ext})$ is the average dipole moment of molecules in the spherical probe.

For an inhomogeneous medium, the profile of the probe (the coarse-graining function) affects the statistical averaging of the microscopic charge density and of the microscopic field. In other words, the macroscopic charge density and the macroscopic polarization density depend on the coarse-graining function. Moreover, there are also additional terms in the statistically averaged Maxwell equations depending on the quadrupole and higher-order electrical moment densities.[35] The additional non-dipole terms vanish for the homogeneous fluids.[36] Also, for an inhomogeneous fluid, the quadrupole contribution to the macroscopic Maxwell equation disappears for the specific choice of the coarse-graining function – the one constant within the probe and equal zero out of its boundary.[36] Thus, the use of a constant coarse-graining function in our analysis is justified as the obtained macroscopic electric field obeys the standard Maxwell equations of continuum electrostatics with common boundary conditions, additivity of the polarization density, *etc.*

We should also mention a different approach to average the microscopic electrostatic field presented in ref. 37 and implemented in VMD.[38] The authors use gaussians to smooth atomic charges, solve the Poisson equation to obtain the corresponding electrostatic potential at each frame of the MD trajectory and then average the potential along the trajectory. This approach corresponds to a gaussian coarse-graining function. In the homogeneous regions (*e.g.*, in the bulk solvent far outside the membrane) the averaged electrostatic field obtained using this method is the same as that calculated using the constant coarse-graining function in our approach. In the inhomogeneous regions (like those inside the channel), in general, the averaged electrostatic field does not obey the standard continuum Maxwell equations but those containing the quadrupole and the higher-order electric moments.

Computational details

Production run in the *NVT* ensemble was performed through starting from the systems equilibrated in ref. 10, after the *NVT* run, a suitable number of water molecules in the OmpF and OmpC systems were replaced with ions to have the desired KCl concentration. In the case of OmpF in order to improve statistics four simulations of 100 ns each were launched with different seeds and 1 microsecond was run after adding ions. For OmpC only 800 ns were run with ions. In the case of pH5

simulations, residues 117 and 121 in loop L3 were protonated according to the pK_a values evaluated using the PROPKA code.[39,40] All simulations were performed in the *NVT* ensemble using the ACEMD code[41] compiled for GPUs, by rescaling hydrogen mass to 4 au and increasing the time-step up to 4.0 fs.[42] The Langevin thermostat was used with 1 ps damping time. SPME was used to treat the electrostatics as for the equilibration stage. The Amber99SB-ILDN force field[43] was used for the protein and lipids, and the TIP3P[44] for waters.

Water analysis was performed separately for each protein monomer. Water molecules within a cylinder of 80 Å height and 17 Å radius, centered in the center of mass of the monomer, were extracted from MD trajectories. Each cylinder was divided in 0.5 Å slices along the channel axis (*z*-axis) and the distribution of oxygen atoms along the MD trajectory was calculated for each slice, 160 in total. A sphere was then centered at the average position of oxygen over time for each slice, and the water molecules within such spherical probe were extracted for each trajectory frame. Spherical probes of three different sizes were used (radius, R = 4 Å, 5 Å and 7 Å). The polarization density of each sphere was calculated to be $P_{i\alpha} = \frac{1}{N_i v_w} \sum_{j=1}^{N_i} \mu_\alpha \alpha = x, y, z$, where i goes from 1 to 160 and v_w = 29.9 Å^3 is the volume of a single water molecule. Then, the polarization density of each sphere was averaged over the whole trajectory. Finally, because the protein channels under investigation are trimeric, trajectory averages were also averaged over the three equivalent monomers, which can be considered statistically independent systems in this context.

Results and discussion

Dielectric response of bulk water

In order to calculate the dielectric response function of water, we performed different MD simulations in the *NVT* ensemble as described in the Methods section, with 17 different values of the applied electric field, from 0.1 to 500 mV Å^{-1} (20 ns for each production run). Polarization density was calculated in three different ways in order to test possible artifacts: (i) polarization density of the entire box, (ii) spheres of different sizes centered in the simulation box, and (iii) by using a set of spheres along the *z* axis. No significant differences were found. The results are shown in Fig. 1.

At electric field values above 30–40 mV Å^{-1}, the calculated dielectric response of water becomes non-linear and starts to saturate at field strengths above 100 mV Å^{-1}. This behavior is in excellent agreement with Booth's model[45]

$$P_B(E) = \frac{(n^2-1)}{4\pi} E + \frac{\alpha(n^2+2)\mu}{4v_w} L\left(\frac{\beta(n^2+2)\mu E}{kT}\right) \quad (2)$$

where $\alpha = \frac{28}{3\sqrt{73}}$; $\beta = \frac{\sqrt{73}}{6}$; n = 1.33 is the experimental optical refraction index of water; T is the absolute temperature; k is Boltzmann's constant; v_w – volume per water molecule; and $L(x) = \coth x - \frac{1}{x}$ is the Langevin function.

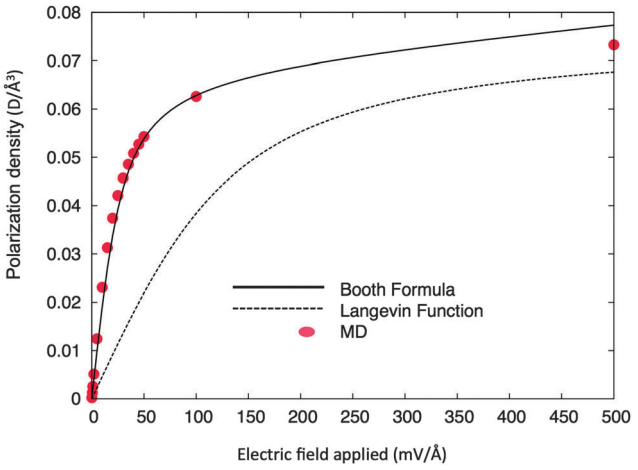

Fig. 1 The dielectric response function of (bulk) water. The solid line corresponds to the Booth function[45] and the dashed line to the Langevin function with parameters from ref. 46.

The dipole moment of water molecule, μ, is the only adjustable parameter of the model used by the author[45] to reproduce the experimental dielectric constant of water in the low-field limit. Although the obtained value, μ = 2.1 D, is larger than in a vacuum (1.86 D), it is still in reasonable agreement (*e.g.*, in the SPC water model the dipole model is 2.27 D, in TIP3P it is 2.35 D). The dielectric response within the Booth model, by assuming that T = 300 K and v_w = 29.9 Å, is shown in Fig. 1 with a solid curve. At field strengths below 100 mV Å^{-1}, the agreement between the MD results and the Booth model is excellent, in accordance with previous studies.[29] The slight deviation at higher electric fields may be due to several factors. First, the field induced structural reordering of water takes place leading to the phase transition at $E > 1$ V Å^{-1},[27] while Booth assumed the field independent model for near order of liquid water. Second, the water model used in current MD simulations is rigid, so that reorientation of molecules is the only mechanism of polarization, while the effects of electronic polarization and molecular bond/angle modification, which might become important at higher fields, are neglected. The Booth model actually takes molecular flexibility and the electronic polarization implicitly into account, by introducing the high-field limit constant from the experimental optical refraction index of water, $\varepsilon_{E\to\infty} = n^2$.

We will not go further into the details of the water dielectric response at high electric fields, as the field strength pertaining to the protein channels investigated here is well below 100 mV Å^{-1}. The important conclusion is that, at the electric field strength we will consider, the dielectric response of water is non-linear but absolutely consistent with the analytic microscopic model that assumes the independence of the local structure of liquid water (including the water density) of the applied electric field.

The dielectric response of water at $E < 100$ mV Å^{-1} can also be fitted by using the simple Langevin function,

$$P_L(E) = \frac{\mu}{v_w} L\left(\frac{\mu E}{kT}\right) \quad (3)$$

In this case, however, the fitting parameters, μ and ν_w, will not have physically meaningful values.[27,30] The dielectric response function given by eqn (3) calculated using physical values of the parameters[46] (μ = 2.27 D, V_w = 29.9 Å^3, T = 300 K) is plotted with the dashed line in Fig. 1. The polarization density is strongly underestimated and the saturation is shifted to higher electric field strength. This may lead, in turn, to a significant overestimation of the electric field based on the calculated values of the average dipole moment. We will return to this point with an example in the following paragraph.

Electric field in OmpF: effects of the probe radius and of the non-linear response

The local polarization density of water within the spherical probes of radius of 5 Å centered along the axes of the monomers was calculated for the OmpF porin by following the procedure discussed in the Computational details section. The Cartesian components of the polarization density vector *vs.* the position along channel's axis (the z coordinate) are shown in Fig. 2a (y-axis points *versus* the projection of loop L3 in the CR of the channel into the transversal plain). Corresponding electric field's components are shown in Fig. 2b. The parametric plot of the transversal electric field along the axis of the channel is shown in Fig. 3.

First, we note that there is a strong transversal component of the electric field, which has the greatest strength in the constriction region (Z around 0 Å), where it points out of the positive basic ladder towards the negative loop L3 (Y direction), as it should be expected. The presented approach to the calculation of the electric field by the way allows identifying finest details of the channel's electrostatics, which is hard to be unveiled with other methods. First, it has to be emphasized that the only 'active' component of the electric field in the CR is the Y. Both the X and, most importantly, the Z are absolutely negligible. Before the CR, on the extracellular side of the channel (Z in the range of +5– to +10 Å), the Y component is already significant and the Z is actually not negligible and negative. This means that the electric field lines already point down to the CR and towards loop L3 well before the actual CR. This specific region of the channel has been previously given the name 'preorientation region' in one recent authors' report,[10] and

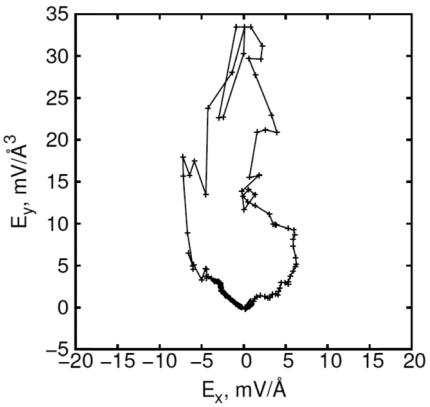

Fig. 3 The parametric plot, $\{E_x(z), E_y(z)\}$, of the transversal electric field shown in Fig. 2b.

the more accurate analysis presented here bolsters that concept. Also, upon emerging from the CR on the periplasmic side of the channel (negative Z), the transversal component of the electric field changes the direction quite sharply (the Y decreases while the X increases) but the Z is still negligible. The transversal electric field is characterized by a screw-like form and flips by 180° while passing through the pore (Fig. 3). These qualitative details of the OmpF electrostatics were known from previous studies,[17,18] the present analysis has confirmed them and provided a quantitative description.

The profile of the electric field in the CR (Fig. 2b) is sharper than that of the polarization density. This effect is due to the nonlinear response of water to the strong electric field in the constriction region.[30,31,46]

The values of the z-component of the polarization density along the channel axis (Fig. 2a) are in good agreement with previous MD simulations[46] (the average dipole per water molecule presented in Fig. 12 of ref. 46 should be divided by ν_w = 29.9 Å^3 to obtain the polarization density). However, as discussed above, the simple Langevin response function, with the physically chosen parameters used in ref. 46 significantly underestimate the polarization density at any given strength of the electric field (see Fig. 1 and discussion around). That is why the values of the electric field strength in the

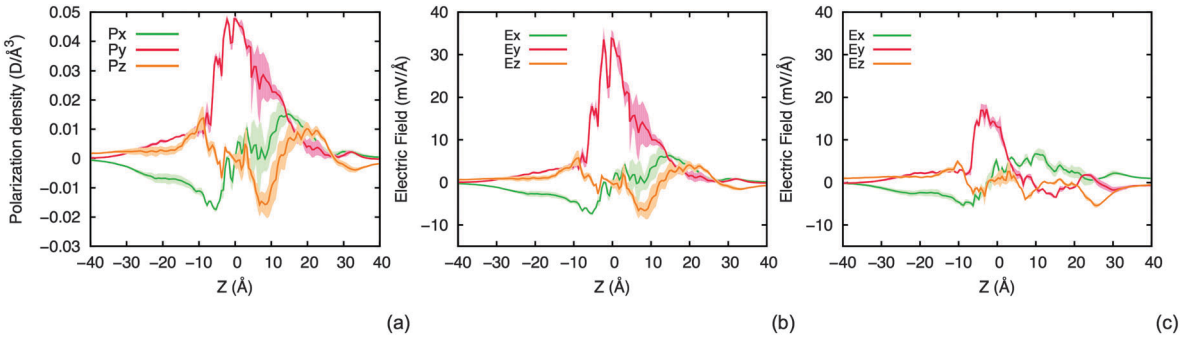

Fig. 2 (a) The components of the water polarization density vector averaged over spherical probes with a radius of 5 Å, located along OmpF's axis and (b) the corresponding components of the local macroscopic electric field. (c) Macroscopic electric field for OmpC. The standard deviation is shown with the shaded area around the curves.

CR reported in ref. 46 are about 2–3 times larger than the present results. The continuum Poisson–Boltzmann models[17,31] with a fixed bulk dielectric constant for water in the pore (ε_w = 78–80) and a fixed effective dielectric constant for the protein (ε_p = 4–20), result in a strength of the electric field in the CR equal to 30–40 mV Å^{-1}, which is in good agreement with our calculations (Fig. 2b). On the other hand, the Poisson–Boltzmann model[31] with the nonlinear response (Booth) function and a fixed effective dielectric constant for protein (ε_p = 10) result in the electric field approaching 80 mV Å^{-1}, *i.e.* 2–2.5 times larger than the present estimation.

Fig. 4 shows the results of the electrostatic field inside OmpF using different probe sizes. The latter clearly influences the fine structure of the curve because of the non-uniformity of the medium. We selected R = 5 Å for further analysis, as the field profile is substantially too smooth at R = 7 Å. At R = 4 Å on the other hand, the average number of water molecules in the probe is smaller than 10, leading to the large fluctuations of the averaged values of polarization and, consequently, of the electric field.

There are two kinds of statistical uncertainties in the calculated electric field, the inherent equilibrium thermodynamic fluctuations, and the statistical uncertainty of average values due to the finite time-length of MD trajectories. Thermodynamic fluctuations (at equilibrium) depend on the size of the probe, the ion density and other equilibrium thermodynamic variables of the system. In Fig. 2, for instance, we plot the standard deviation of thermodynamic fluctuations.

The average value itself has a statistical uncertainty due to the possible insufficient sampling provided by MD trajectories. This error of the average is reduced with the trajectory duration T. The simulation time, T, should be larger than the characteristic time of all relaxation processes in the system. We estimated the error of the average by dividing the whole trajectory into three pieces and by calculating the variance of the average electric field obtained for each piece. This calculation was also performed separately on each of the three protein monomers. The statistical error on the average values of the electric field was always smaller than its inherent thermodynamic (equilibrium) fluctuations.

Comparison of the two main general channels of *E. coli*, OmpF and OmpC

In Fig. 2, the electric field calculated along the channel axis is displayed for OmpF (2.b) and OmpC (2.c). These two proteins have been widely studied,[16] and it is still not clear why OmpF is much more permeable than OmpC despite the similar size.[47] In a recent work,[10] we showed how the polarization density of water molecules inside the channel is able to qualitatively capture the main electrostatic differences among the two channels, suggesting very important implications for rational drug design.

The electric field has the maximum value in the CR for both channels. They are also similar in having the most intense component of the electric field on the y-axis, *i.e.* pointing from the positive basic ladder towards the negative loop L3. However, while OmpF shows a field strength of ~36 mV Å^{-1} in the CR, a significant reduction to ~20 mV Å^{-1} is observed in OmpC. In addition, dramatic differences are observed in the so-called 'preorientation region',[10] which is between +5 and +10 Å along the z-axis in the present case.

Although OmpC has a higher net negative charge, it is not localized in the CR but in the extracellular vestibule.[10] The effect of this additional negative charge (due to specific amino acid mutations[10]) in OmpC, is the almost complete disruption of the opposite charge segregation that characterizes, instead, the OmpF preorientation zone. In turn, all of the three electric field components are negligible (Fig. 2c), meaning that in OmpC there is no effective electric field at the mouth of the CR, driving dipolar molecules to adopt any specific orientation before they get into the CR. Conversely, OmpF and OmpC are rather similar, as far as the electric field is concerned upon emerging from the CR on the periplasmic side of the channel (negative Z).

OmpF and OmpC, effects of the ionic strength

It is known how the relative expression of OmpF and OmpC is strictly dependent upon several environmental parameters, such as the ionic strength of the medium, the pH, the temperature and the level of nutrients.[16] The earlier observations that OmpF is predominant in low osmolarity media, while OmpC is more expressed at high osmolarity, led to the conclusion that the latter had a reduced size to act as a more selective filter in environments rich in nutrients but also in potentially noxious species. On the other hand, OmpF was concluded to be less stringent, which is required when bacteria are grown under nutritional deficiency.

It has been more recently experimentally shown that although the pore size is comparable among OmpF and OmpC,

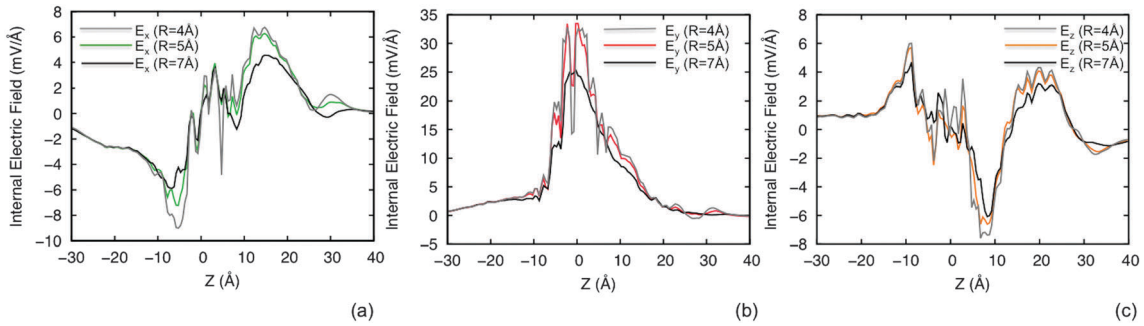

Fig. 4 Electric field inside OmpF for different radii of the probe, R = 4 Å, R = 5 Å, and R = 7 Å.

the internal electrostatics might be the major determinant for permeability differences.[48] In order to investigate the electrostatics of these two protein channels in a more physiologically relevant scenario, we performed additional (~5 μs) MD simulations in the presence of different KCl concentrations, namely, 200 and 400 mM. In the case of OmpF, MD was performed also at 1 M KCl. The results of electric field calculations are reported in Fig. 5 and 6 for OmpF and OmpC, respectively.

OmpF is very sensitive to the electrolyte concentration (Fig. 5). The *y*-component of the electrostatic field is dramatically reduced already at 200 mM KCl, down to values comparable to the OmpC in the absence of electrolytes (Fig. 2c). On the other hand, both the *x* and *z* components change only slightly, meaning that the overall 'choreography' is maintained, even at 1 M KCl. However, not only the CR electrostatics appear to be affected by increased ion concentration, also the preorientation region is perturbed, so that the *y*-component is significantly reduced there also, whereas the *z* one is not (Fig. 5).

Conversely, when the same conditions were applied to OmpC, no remarkable differences in the intrinsic electric field were found, up to 400 mM KCl (Fig. 6). However, in the preorientation zone, a closer inspection of the results reveals an increase of the *y*-component in the positive direction. This means that the perturbation of the electrostatic field of OmpC due to the presence of the physiological concentration of monovalent ions might be helpful to the passage of polar solutes, by creating a favorable preorientation field at the mouth of the CR, which was negligible in the absence of electrolytes.

It is quite astonishing how the present results fairly match the above mentioned general considerations about the OmpF and OmpC relative expression. Actually, these two porins look to be designed by evolution to work properly under different environmental conditions. The electrostatics of OmpF, devoted to low osmolarity, is profoundly affected by the presence of electrolytes in the medium. The OmpC, on the other hand, is almost insensitive to the ionic strength, preserving its inherent electrostatic profile in the presence of electrolytes at rather high concentrations.

Now, from the present results it can be speculated that an OmpF-like profile of the electric field (Fig. 2b), with a rather high field strength in the CR and a favorable preorientation zone may help the uptake of dipolar molecules. In an environment characterized by nutrient deficiency this should be a must for a general channel, in order to guarantee a sufficient influx of essential species.[16,48] However, most of the commonly employed antibiotics are characterized by a significant electric dipole[49] and should be, thus, similarly able to penetrate through OmpF possibly too easily, making bacteria expressing OmpF rather susceptible.

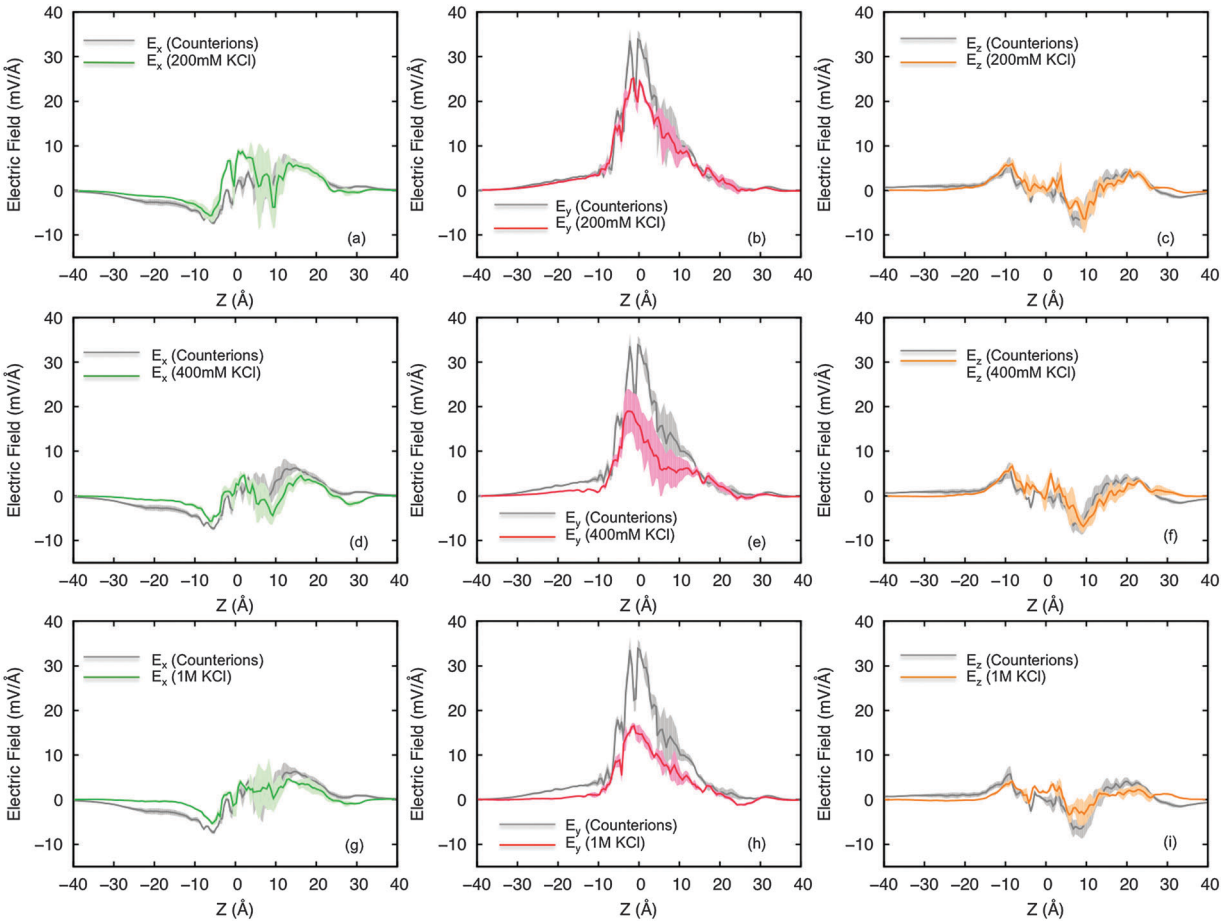

Fig. 5 Internal electric field in OmpF in the presence of different electrolyte concentrations, (a–c) 200 mM KCl, (d–f) 400 mM KCl, and (g–i) 1 M KCl.

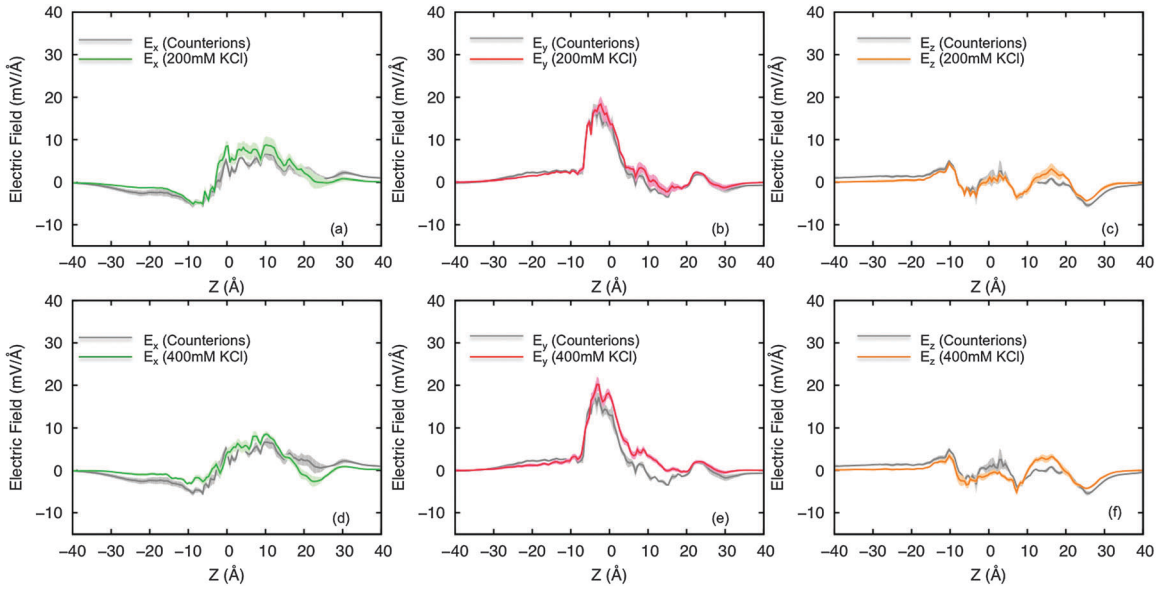

Fig. 6 Electric field in OmpC in the presence of different electrolyte concentrations, (a–c) 200 mM KCl and (d–f) 400 mM KCl.

Under the same conditions, OmpC expressing bacteria are known to be generally less susceptible, probably because of the lower field-strength in the CR and, most importantly, to the negligible preorientation (Fig. 2c).

When a high osmolarity environment is considered, a more stringent molecular filter is required, guaranteeing sufficient uptake of nutrients but avoiding penetration by noxious species to the maximum extent.[48] The OmpC-like profile of the electric field in the absence of electrolytes (Fig. 2c) is possibly too selective, but it is possible to suggest that its filtering behavior is finely tuned by the presence of electrolytes, leaving the CR almost unaffected and 'switching on' the preorientation zone (Fig. 6).

At the moment, these are mere speculations and explaining all the more recent experimental results is certainly beyond the aim of this work, but the major role of the electrostatics is clear and widely recognized. It is finally interesting to note how the present results are in agreement with recent experimental findings.[48] Overall permeability was shown to become comparable for OmpF and OmpC with increasing ionic strength of the medium. In our simulations, the electric field profiles do become comparable.

Despite the protein channel's electric field is certainly fundamental in defining permeability, other factors cannot be ignored, such as substrate flexibility and size, net charge and its distribution, H-bond donors/acceptors, desolvation of both protein residues and the substrate upon entering the CR, among others,[50] all of which potentially modulate the permeability in a substrate specific fashion, over a channel specific background.

Effects of the pH

As the protonation state of certain amino acid residues might change with pH, their net charge can be modified in turn. This should result, of course, in the modification of channel's electric field.

In Fig. 7, the results for OmpF at pH 5 are compared to the ones at pH 7. A dramatic change in the electric field can clearly be seen, pertaining both the CR and preorientation region. Similar to the effects shown above for increasing KCl concentration, also decreasing the pH, thus 'losing' some negative charges, reduces the y component of the electric field, leaving the x and z almost unaffected. In the case of pH reduction, however, the negative z component in the preorientation region is eliminated, while the electrolytes were not able to produce this alteration even at the highest concentration tested (Fig. 5).

Similar to the ionic strength, also the pH of the environment is known to impact the relative expression of OmpF and OmpC. In particular, acidic pH favors the expression of OmpC, while that of OmpF is repressed.[51] Coherently, the present work has shown how OmpF appears to be highly sensitive to the pH, as far as the internal electric field is concerned, bolstering the idea that evolution has finely designed these water filled channels to work under rather specific conditions. Going into further details is beyond the scope of this presentation, which is focused on the method, but the intriguing implications of these results certainly call for specifically targeted investigations.

Mutants from antibiotic resistant clinical isolates: OmpC20 and OmpC33

Quite recently, the crystal structure of a series of OmpC mutants has become available.[7] Seven *E. coli* strains were isolated during two years of antibiotics treatment of a patient suffering from the Caroli syndrome.[52] The antibiotics resistance of these clinical strains was progressively greater to the antibiotics used for treatment, including imipenem, meropenem, cefotaxime, ceftazidime and ciprofloxacin.[52]

As we pointed out in a recent work,[10] the electrostatic properties of the corresponding OmpC mutants showed a remarkable progressive variation directly related to the amino acid mutations inside the channels, while the size pore remained unchanged. In particular, we investigated the first and the last mutants of the series, OmpC20 and OmpC33, respectively,

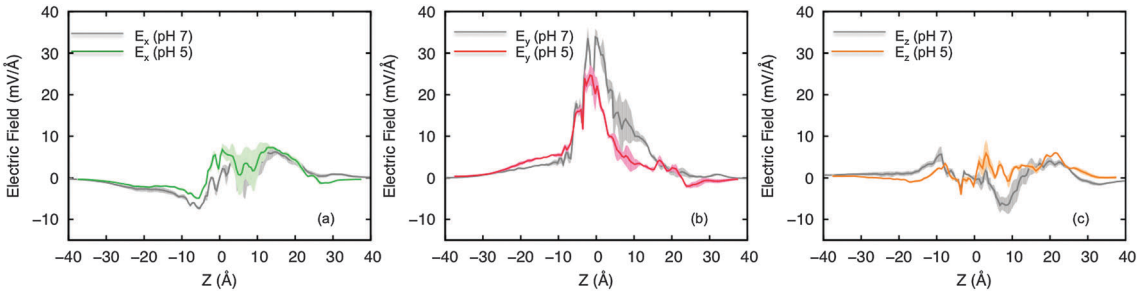

Fig. 7 Electric field of OmpF for pH = 7 in grey, and pH = 5, (a) in green for the *x*, (b) in red for *y*, and (c) in orange for the *z* component.

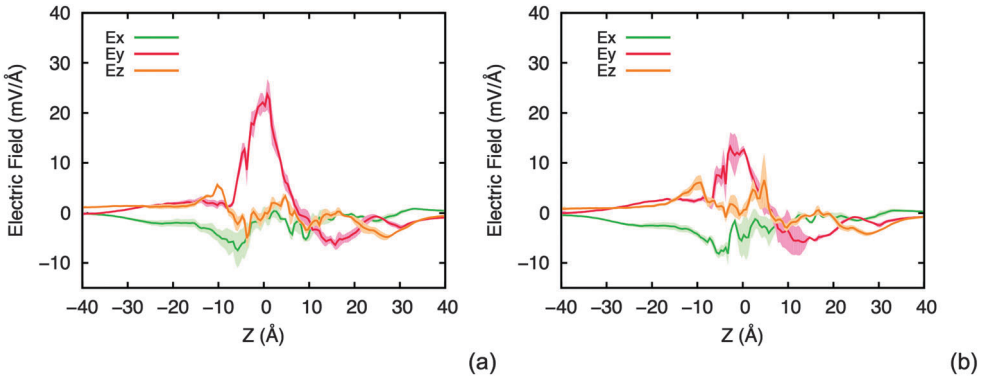

Fig. 8 Electric field in (a) OmpC20 and (b) OmpC33. The three components of the electric field are depicted, in green E_x, in red E_y and in orange E_z.

finding the more interesting differences in the preorientation, not in the CR region.

Starting from those results, we calculated their internal electric field. The results are shown in Fig. 8. In agreement with our previous study,[10] in what we called the preorientation region, just above the CR on the extracellular side of the channel, the *y*-component of the electric field is inverted with respect to OmpF (Fig. 5) and OmpC (Fig. 6), *i.e.* the *y* is negative in the reference system adopted here, while the other two components are comparable. The OmpC33, in addition, is characterized by a rather low field strength in the CR.

This electric field profile along the channel axis is expected to have a large influence on the permeability of polar species, which are preoriented in the extracellular vestibule with a direction opposite to the one imposed by the electrostatics of the CR. This means that the crossing molecule has to undertake sharp reorientations while traversing the channel, right at the mouth of the more restricted zone, where the steric hindrance is severe.

Conclusions

We have presented an all-atom simulation approach for the calculation of the macroscopic electric field inside nanometric water-filled channels under different environmental scenarios. Intrinsic water is taken as a natural probe, and its local polarization density is connected to the macroscopic field through the electrostatic response function. The method allows one to compare not only different systems but also the same system under different pH and ion concentration conditions.

Our method is accurate enough to be able to capture small differences upon subtle mutations of a few residues only, and for this reason it can be used as a way to characterize channels. This is a basic step to design new drugs with enhanced permeability but also such knowledge might be crucial for designing engineered biomimetic nanofilters. Indeed, the accurate quantification of the macroscopic electric field inside channels opens up the way to the definition of an electrostatic model to calculate the interaction energy of crossing polar molecules, which sense the internal macroscopic electric field by virtue of their charges/dipole.

Acknowledgements

The research leading to these results was conducted as part of the "Translocation" consortium (www.translocation.com) and has received support from the Innovative Medicines Initiatives Joint Undertaking under Grant Agreement no. 115525, resources that are composed of financial contribution from the European Union's seventh framework programme (FP7/2007–2013) and EFPIA companies in kind contribution. S. Acosta-Gutierrez is a Marie Skłodowska-Curie fellow within the "Translocation" Network, project no. 607694. We also want to thank MIUR (PRIN 2010CSJX4F) for financial support.

References

1 R. Tommasi, D. G. Brown, G. K. Walkup, J. I. Manchester and A. A. Miller, *Nat. Rev. Drug Discovery*, 2015, **14**, 529–542.

2 D. J. Payne, L. F. Miller, D. Findlay, J. Anderson and L. Marks, *Philos. Trans. R. Soc., B*, 2015, **370**, 20140086.
3 R. A. Stavenger and M. Winterhalter, *Sci. Transl. Med.*, 2014, **6**, 228ed7.
4 J.-M. Pagès, C. E. James and M. Winterhalter, *Nat. Rev. Microbiol.*, 2008, **6**, 893–903.
5 T. Mach, P. Neves, E. Spiga, H. Weingart, M. Winterhalter, P. Ruggerone, M. Ceccarelli and P. Gameiro, *J. Am. Chem. Soc.*, 2008, **130**, 13301–13309.
6 J. Cama, H. Bajaj, S. Pagliara, T. Maier, Y. Braun, M. Winterhalter and U. F. Keyser, *J. Am. Chem. Soc.*, 2015, **137**, 13836–13843.
7 H. Lou, M. Chen, S. S. Black, S. R. Bushell, M. Ceccarelli, T. Mach, K. Beis, A. S. Low, V. A. Bamford, I. R. Booth, H. Bayley and J. H. Naismith, *PLoS One*, 2011, **6**, e25825.
8 M. Winterhalter and M. Ceccarelli, *Eur. J. Pharm. Biopharm.*, 2015, **95**, 63–67.
9 V. M. Isabella, A. J. Campbell, J. Manchester, M. Sylvester, A. S. Nayar, K. E. Ferguson, R. Tommasi and A. A. Miller, *Chem. Biol.*, 2015, **22**, 535–547.
10 S. Acosta-Gutierrez, M. A. Scorciapino, I. Bodrenko and M. Ceccarelli, *J. Phys. Chem. Lett.*, 2015, **6**, 1807–1812.
11 A. Kumar, E. Hajjar, P. Ruggerone and M. Ceccarelli, *J. Phys. Chem. B*, 2010, **114**, 9608–9616.
12 S. Samanta, M. A. Scorciapino and M. Ceccarelli, *Phys. Chem. Chem. Phys.*, 2015, 1–10.
13 S. W. Cowan, T. Schirmer, G. Rummel, M. Steiert, R. Ghosh, R. A. Pauptit, J. N. Jansonius and J. P. Rosenbusch, *Nature*, 1992, **358**, 727–733.
14 E. M. Nestorovich, C. Danelon, M. Winterhalter and S. M. Bezrukov, *Proc. Natl. Acad. Sci. U. S. A.*, 2002, **99**, 9789–9794.
15 P. R. Singh, M. Ceccarelli, M. Lovelle, M. Winterhalter and K. R. Mahendran, *J. Phys. Chem. B*, 2012, **116**, 4433–4438.
16 M. Masi and J.-M. Pagès, *Open Microbiol. J.*, 2013, **7**, 22–33.
17 A. Karshikoff, V. Spassov, S. W. Cowan, R. Ladenstein and T. Schirmer, *J. Mol. Biol.*, 1994, **240**, 372–384.
18 W. Im and B. Roux, *J. Mol. Biol.*, 2002, **322**, 851–869.
19 M. Aguilella-Arzo, J. J. García-Celma, J. Cervera, A. Alcaraz and V. M. Aguilella, *Bioelectrochemistry*, 2007, **70**, 320–327.
20 A. Philippsen, W. Im, A. Engel, T. Schirmer, B. Roux and D. J. Müller, *Biophys. J.*, 2002, **82**, 1667–1676.
21 H. Bajaj, M. A. Scorciapino, L. Moynié, M. G. P. Page, J. H. Naismith, M. Ceccarelli and M. Winterhalter, *J. Biol. Chem.*, 2016, **291**, 2837–2847.
22 B. L. de Groot and H. Grubmüller, *Science*, 2001, **294**, 2353–2357.
23 E. Tajkhorshid, P. Nollert, M. Ø. Jensen, L. J. W. Miercke, J. O'Connell, R. M. Stroud and K. Schulten, *Science*, 2002, **296**, 525–530.
24 S. Yuan, H. Vogel and S. Filipek, *Angew. Chem., Int. Ed.*, 2013, **52**, 10112–10115.
25 M. Marchi, F. Sterpone and M. Ceccarelli, *J. Am. Chem. Soc.*, 2002, **124**, 6787–6791.
26 H. E. Alper and R. M. Levy, *J. Phys. Chem.*, 1990, **94**, 8401–8403.
27 G. Sutmann, *J. Electroanal. Chem.*, 1998, **450**, 289–302.
28 J. L. Aragones, L. G. MacDowell, J. I. Siepmann and C. Vega, *Phys. Rev. Lett.*, 2011, **107**, 155702.
29 I.-C. Yeh and M. L. Berkowitz, *J. Chem. Phys.*, 1999, **110**, 7935–7942.
30 M. S. Sansom, G. R. Smith, C. Adcock and P. C. Biggin, *Biophys. J.*, 1997, **73**, 2404–2415.
31 M. Aguilella-Arzo, A. Andrio, V. M. Aguilella and A. Alcaraz, *Phys. Chem. Chem. Phys.*, 2009, **11**, 358–365.
32 T. Darden, D. York and L. Pedersen, *J. Chem. Phys.*, 1993, **98**, 10089–10092.
33 L. Perera, U. Essmann and M. L. Berkowitz, *J. Chem. Phys.*, 1995, **102**, 450–456.
34 M. Neumann, *Mol. Phys.*, 2006, **50**, 841–858.
35 J. D. Jackson, *Classical Electrodynamics*, Wiley, New York, 3rd edn, 1999.
36 K. K. Mandadapu, J. A. Templeton and J. W. Lee, *J. Chem. Phys.*, 2013, **139**, 054115.
37 A. Aksimentiev and K. Schulten, *Biophys. J.*, 2005, **88**, 3745–3761.
38 W. Humphrey, A. Dalke and K. Schulten, *J. Mol. Graphics*, 1996, **14**, 33–38.
39 C. R. Søndergaard, M. H. M. Olsson, M. Rostkowski and J. H. Jensen, *J. Chem. Theory Comput.*, 2011, **7**, 2284–2295.
40 M. H. M. Olsson, C. R. Søndergaard, M. Rostkowski and J. H. Jensen, *J. Chem. Theory Comput.*, 2011, **7**, 525–537.
41 M. J. Harvey, G. Giupponi and G. De Fabritiis, *J. Chem. Theory Comput.*, 2009, **5**, 1632–1639.
42 I. Buch, T. Giorgino and G. De Fabritiis, *Proc. Natl. Acad. Sci. U. S. A.*, 2011, **108**, 10184–10189.
43 K. Lindorff-Larsen, S. Piana, K. Palmo, P. Maragakis, J. L. Klepeis, R. O. Dror and D. E. Shaw, *Proteins*, 2010, **78**, 1950–1958.
44 W. L. Jorgensen, J. Chandrasekhar, J. D. Madura, R. W. Impey and M. L. Klein, *J. Chem. Phys.*, 1983, **79**, 926.
45 F. Booth, *J. Chem. Phys.*, 1951, **19**, 391–394.
46 D. P. Tieleman and H. J. Berendsen, *Biophys. J.*, 1998, **74**, 2786–2801.
47 A. Kumar, E. Hajjar, P. Ruggerone and M. Ceccarelli, *J. Phys.: Condens. Matter*, 2010, **22**, 454125.
48 S. Kojima and H. Nikaido, *J. Biol. Chem.*, 2014, **289**, 26464–26473.
49 G. Malloci, A. Vargiu, G. Serra, A. Bosin, P. Ruggerone and M. Ceccarelli, *Molecules*, 2015, **20**, 13997–14021.
50 Q.-T. Tran, R. A. Pearlstein, S. Williams, J. Reilly, T. Krucker and G. Erdemli, *Proteins: Struct., Funct., Bioinf.*, 2014, **82**, 2998–3012.
51 M. Heyde and R. Portalier, *Mol. Gen. Genet.*, 1987, **208**, 511–517.
52 A. S. Low, F. M. MacKenzie, I. M. Gould and I. R. Booth, *Mol. Microbiol.*, 2001, **42**, 619–630.

MOMP from *Campylobacter jejuni* is a trimer of 18-stranded β-barrel monomers with a Ca^{2+} ion bound at the constriction zone

Luana G M Ferrara, Gregor D Wallat, Lucile MoyniÃľ, Naresh Niranjan Dhanasekar, Mathias Winterhalter, Jean-Michel Bolla, Soumeya Aliouane, Jean-Marie PagÃĺs, **Silvia Acosta-Gutiérrez**, Matteo Ceccarelli, James H Naismith, Crystal Structures of MOMP from Campylobacter jejuni,*Journal of Molecular BiologyAcepted* (2016)

MOMP from *Campylobacter jejuni* Is a Trimer of 18-Stranded β-Barrel Monomers with a Ca^{2+} Ion Bound at the Constriction Zone

Luana G M Ferrara[1,†], Gregor D Wallat[1,†], Lucile Moynié[1,†], Naresh N Dhanasekar[2,†], Soumeya Aliouane[3], Silvia Acosta-Gutiérrez[4], Jean-Marie Pagès[3], Jean-Michel Bolla[3], Mathias Winterhalter[2], Matteo Ceccarelli[4] and James H Naismith[1,5]

1 - Biomedical Sciences Research Complex, *University of St Andrews, 09042 St Andrews, UK*
2 - Department of Life Sciences and Chemistry, *Jacobs University Bremen, 28719 Bremen, Germany*
3 - Aix Marseille Univ, *IRBA, TMCD2, 13385 Marseille, France*
4 - Department of Physics, *University of Cagliari, Cittadella Universitaria Monserrato, S.P8-km 0.700, 09042 Monserrato, Cagliari (CA), Italy*
5 - State Key Laboratory of Biotherapy, *Sichuan University, Chengdu 610041, China*

Correspondence to James H Naismith: *State Key Laboratory of Biotherapy, Sichuan University, Chengdu 610041, China. naismith@st-andrews.ac.uk*
http://dx.doi.org/10.1016/j.jmb.2016.09.021
Edited by James Bowie

Abstract

The Gram-negative organism *Campylobacter jejuni* is the major cause of food poisoning. Unlike *Escherichia coli*, which has two major porins, OmpC and OmpF, *C. jejuni* has one, termed major outer membrane protein (MOMP) through which nutrients and antibiotics transit. We report the 2.1-Å crystal structure of *C. jejuni* MOMP expressed in *E. coli* and a lower resolution but otherwise identical structure purified directly from *C. jejuni.* The 2.1-Å resolution structure of recombinant MOMP showed that although the protein has timeric arrangement similar to OmpC, it is an 18-stranded, not 16-stranded, β-barrel. The structure has identified a Ca^{2+} bound at the constriction zone, which is functionally significant as suggested by molecular dynamics and single-channel experiments. The water-filled channel of MOMP has a narrow constriction zone, and single-molecule studies show a monomeric conductivity of 0.7 ± 0.2 nS and a trimeric conductance of 2.2 ± 0.2 nS. The ion neutralizes negative charges at the constriction zone, reducing the transverse electric field and reversing ion selectivity. Modeling of the transit of ciprofloxacin, an antibiotic of choice for treating *Campylobacter* infection, through the pore of MOMP reveals a trajectory that is dependent upon the presence metal ion.

Introduction

Campylobacter are Gram-negative bacteria belonging to the ε-proteobacteria, which are commensal in livestock, notably in poultry, and are thought to be the main natural reservoir. Human infection most commonly occurs via consumption of undercooked animal products or contaminated water and through contact with animals [1]. The pathogen *Campylobacter jejuni* is the major cause of human food poisoning and represents an economic burden [2]. In general, *C. jejuni* infection resolves without antibiotic treatment, but more serious cases (usually in infants) can be treated straightforwardly with antibiotics. Untreated campylobacteriosis can lead to a cycle of recurrent infections, and this in turn progresses to irritable bowel syndrome [3]. In rare but serious cases, infected individuals can develop non-trauma-related paralysis through Guillain–Barré syndrome [4].

In the recent years, multi-antibiotic-resistant *Campylobacter* species have emerged, and although not common, this trend has alarmed health care professionals [5]. Bacteria resist antibiotics by the expression of drug-modifying enzymes (e.g., β-lactamase), mutation of target (ribosome), drug efflux pumps (e.g., AcrAB-TolC in Enterobacteria,

Mex family in Pseudomonads, and CmeABC in Campylobacterales), and reduced uptake (e.g., decreased expression or mutations of porins in Gram-negative bacteria) [6,7]. Porins are responsible for the uptake of nutrients through the outer membrane of the Gram-negative bacteria by passive diffusion along the concentration gradients. Their substrate uptake can be specific or non-specific, depending on the nature of the protein [7].

Most antibiotics cannot pass through the outer membrane itself so instead must enter the cell via non-specific porins. In *Escherichia coli*, two outer membrane proteins, OmpC and OmpF, are predominant. A shift in expression profile from OmpF (higher conductance) to OmpC (lower conductance and less permeable to antibiotics) has been commonly observed in drug-resistant clinical isolates [8]. Combined structural, physical, and computational studies of a series of clinical OmpC mutations revealed a molecular basis for altered antibiotic uptake [9,10]. In contrast to *E. coli*, *C. jejuni* has only one major outer membrane protein (MOMP), which is thus far present in all isolates and is highly (but not absolutely) conserved in other Campylobacteria. MOMP is a 44-kDa protein, which has the sequence signature typical of β-barrel porin, and CD spectroscopy [11] confirmed the predominance of β-strand typical of porins. MOMP has been reported to be critical to the stability and integrity of the outer membrane of *C. jejuni* [12], while other studies have shown MOMP to have a role in adhesion to epithelial cells [13]. As might be expected, given its location in the bacterial cell, antibodies are frequently raised against it by the human immune system [14–16], and this has led to ideas for vaccine development [17]. Structural and biophysical data are thus highly desired for this protein.

Here, we report the successful recombinant expression, extraction, purification, and structure determination of *C. jejuni* 85H strain MOMP from an *E. coli* overexpression system. *Campylobacter* are ε-proteobacteria, while *E. coli* belongs to the γ-proteobacteria, meaning there are large differences in lipid composition in the outer membrane. To allay concerns about the "nativeness" of this recombinant structure arising from the difference in the lipid environment during expression, we also determined the structure of MOMP purified directly from *Campylobacter* and we found it to be essentially identical. Crystals, but no structure of MOMP from *C. jejuni*, have been previously reported [18]. The lower purity of the MOMP obtained directly from *Campylobacter* highlighted the key advantage of *E. coli* expression. MOMP exhibits conductivity similar to OmpC; however, its constriction zone has a number of important differences that may relate to antibiotic permeability. Using this structure, accurate models can be generated for MOMPs from other strains and other species of *Campylobacter*.

Results

Structure of MOMP

Codon-optimized MOMP-coding gene from strain 85H was cloned in pTAMAHisTEV vector, which inserts a tobacco etch virus and a cleavable hexa-histidine tag between the protein and the TamA signal peptide. After the overexpression in *E. coli* and purification, a final yield of 12 mg of MOMP per 50 g of *E. coli* cell paste was obtained. In a different approach, native MOMP was purified from *Campylobacter* as described previously [11] and yielded 1 mg protein per 3 g of *C. jejuni* cell paste. Both proteins gave crystals, although in different conditions with different crystal symmetry.

The structure of the overexpressed selenomethionine (SeMet) variant MOMP was solved using single-wavelength anomalous diffraction to provide initial phases, which were improved by density modification. This structure was then used to solve the high-resolution structure of MOMP purified from an *E. coli* overexpression system (rMOMP). The protein purified from *Campylobacter* (nMOMP) was solved via molecular replacement using the recombinant MOMP structure as a search model (Table 1). Beyond small differences due to crystal packing and resolution, we have not detected any meaningful structural difference between the two proteins (RMSD of 0.45 Å for 398 Cα position using SSM [19]; Supplementary Fig. 1). Our discussion focuses on the higher-resolution rMOMP structure (2.1 Å).

Table 1. Data collection, refinement, and validation statistic

	MOMP Native	MOMP Recombinant	Recombinant $MOMP^{SeMet}$
Space group	$P2_12_12_1$	$P6_3$	$P6_3$
Cell dimensions *a*, *b*, *c* (Å)	94.4, 99.4172.2	90.6, 90.6, 104.4	94.3, 94.3, 102.0
Cell dimensions α, β, γ (°)	90, 90, 90	90, 90, 120	90, 90, 120
Resolution (Å)	47.75–2.9 (3.06–2.9)	39.2–2.1 (2.17–2.1)	2.82
R_{merge}	0.14 (0.86)	0.06 (0.72)	0.076 (0.90)
Completeness	99.9 (99.8)	99.5 (99.5)	99.7 (99.7)
Multiplicity	7.3 (7.2)	13.5 (13.6)	14.6 (15.0)
$I/\sigma(I)$	12.9 (3.0)	29.89 (3.92)	23.1 (4.3)
Refinement			
R_{factor}/R_{free} (%)	23.9/27.1	19/22.27	
No. of unique reflections	36,693	28,313	
No. of residues	405	403	
Water	5	127	
Bonds length (Å)	0.01	0.01	
Bonds angles (°)	1.9	1.41	
MolProbity score	1.70	1.03	

Values in parentheses are for the highest-resolution shell.

We use rMOMP and nMOMP, where we discuss the evaluation of each preparation method (to establish they are essentially identical), and MOMP to refer to the generic protein.

MOMP is an 18-stranded antiparallel β-barrel porin with an elliptical shape common to other 18-stranded porins. The signal peptide of nMOMP from *C. jejuni* strain 85H (uniprot entry number: Q659I5) was predicted to cleave between Ala22 and Thr23. Henceforth, Thr23 being the first residue in the tertiary structure was defined as the first residue in our residue count and was renamed to Thr1. In rMOMP, however, due to cloning artifacts, we have three additional non-native residues after signal peptide cleavage (Gly-Ala-Met), followed by a single point mutation of Thr1 to Gly. Typical of porins, the axis of the strands is offset, relative to the membrane normal. The long axis of the ellipse is approximately 37 Å (the distance from Gly179 to Glu280) and the minor axis is 31 Å (Arg45 to Ala234). The vertical height of the barrel varies between 19 Å (distance between Val10 and Phe86) and 37 Å (distance between Thr221 and Val334, on the opposite side; Fig. 1a–b). The N terminus on the periplasmic face has a strand, followed by an N-terminal α-helix that points away from the barrel wall (Fig. 1c). In the protein purified from *Campylobacter,* the helix is also present and adopts the same organization but lacks the short strand seen in the overexpressed recombinant protein. In keeping with convention for porins, extracellular loops connecting the strands are numbered sequentially and prefixed by L, whereas periplasmic loop connections are prefixed by T (also numbered sequentially). Four extracellular loops L1, L3, L4, and L6 fold inside of the barrel, with L3, L4, and L6 forming the constriction zone. Loop 4 contains Phe173-Lys174, the site of the proteinase K cleavage [20]; the structure shows that the site to be exposed is consistent with its cleavage. MOMP from another strain (79AH) is not cleaved at this position as it lacks the protease site. We observed additional electron density adjacent to L3 and L4 that we identify as a Ca^{2+} (rather than Zn^{2+} or Mg^{2+}, or K^{+} or Na^{+}) based on electron density and coordination (distance and geometry). The proteins expressed in *E. coli* have not had any Ca^{2+} ion added and we conclude that the ion was bound during expression in *E. coli* and has remained attached in throughput purification. The ion has octahedral coordination, with one oxygen atom from the side chain of Asp120, Gln152, Asp155, and Glu288, and has the carbonyl of Asp120 with a water molecule filling the final sixth position. The water is in turn coordinated by the amino acid Asp116 and Asp289 (Fig. 1d–e). The metal ion creates a cross-link among L3, L4, and L6. Additionally, the difference electron density map showed a residual elongated density that was modeled as an ethylene glycol like the molecule [from polyethylene glycol (PEG) 400 or C8E4] in the rMOMP. This molecule sits below the constriction zone underneath L3. The protein purified from *Campylobacter* was crystallized in the presence of Ca^{2+} ions and has an ion in an identical position but also has a second ion located outside the barrel at the interface between subunits. This ion is coordinated by Asp145 (main chain and side chain), Asn180 (side chain), and the main of Gly72 from the neighboring subunit. The recombinant structure shows a different side-chain conformation, implying that in the recombinant protein, this site does not exist. It had been hypothesized, according to molecular modeling, that in the 79AH strain, there is a metal-ion-binding site at Ser81 and Asp82 (found as Glu82 and Lys83 in 85H) that is important for the trimerization of 79AH [20]. These residues are located within a regular strand (β4); consequently, the side chains point in opposite directions and we suggest that there is no such metal-ion-binding site.

Analysis of the molecular surface using the program CCP4MG [21] shows that the outside wall of the barrel is uncharged as expected for proteins embedded within a hydrophobic lipid membrane bilayer. The extracellular surface of MOMP has regions of both positive and negative charge with the funnel-shaped region leading to the constriction zone, termed the eyelet, which is strongly negatively charged. The periplasmic face of the protein, including the inside surface of the barrel below the constriction, is predominantly negatively charged (Fig. 2). The pore axis is slightly offset, relative to the membrane normal. When viewed from the extracellular face, L7 sits above the entrance. Analysis with MolAxis [22] reveals that the constriction zone narrows to a radius of 2.6 Å. The constriction zone, like the protein, has an elliptical, not circular, shape. On one surface of the constriction zone, Tyr304 sits among amino acids Asp116, Asp120, Asp155, Asp289, and Glu300, which form a strongly negatively charged region of the pore; significantly, these residues also coordinate the Ca^{2+} ion. On the opposite side of the constriction zone, the surface is formed by residues Arg17, Arg19, Arg45, and Arg398, which create a strongly positively charged region. This arrangement gives rise to a profound dipole across the short axis of the elliptical constriction zone, termed the transverse electric field. Lys43 and Lys404 are not in the constriction zone but point toward it from the extracellular and periplasmic sides, respectively. In addition to the metal ion, several contacts appear crucial to maintain the structure of the constriction zone; Arg362 makes salt bridges with Asp337 and Glu109; Arg45 with Asp65, Asp120, and Glu151.

Although only one monomer is present in the asymmetric unit, analysis of the crystal packing reveals a trimeric arrangement reminiscent of that seen in OmpC [23] and OmpF [24]. The identical trimeric arrangement is found in the protein purified from *Campylobacter*, in this case, the trimer is found in the crystallographic asymmetric unit. Analysis of the

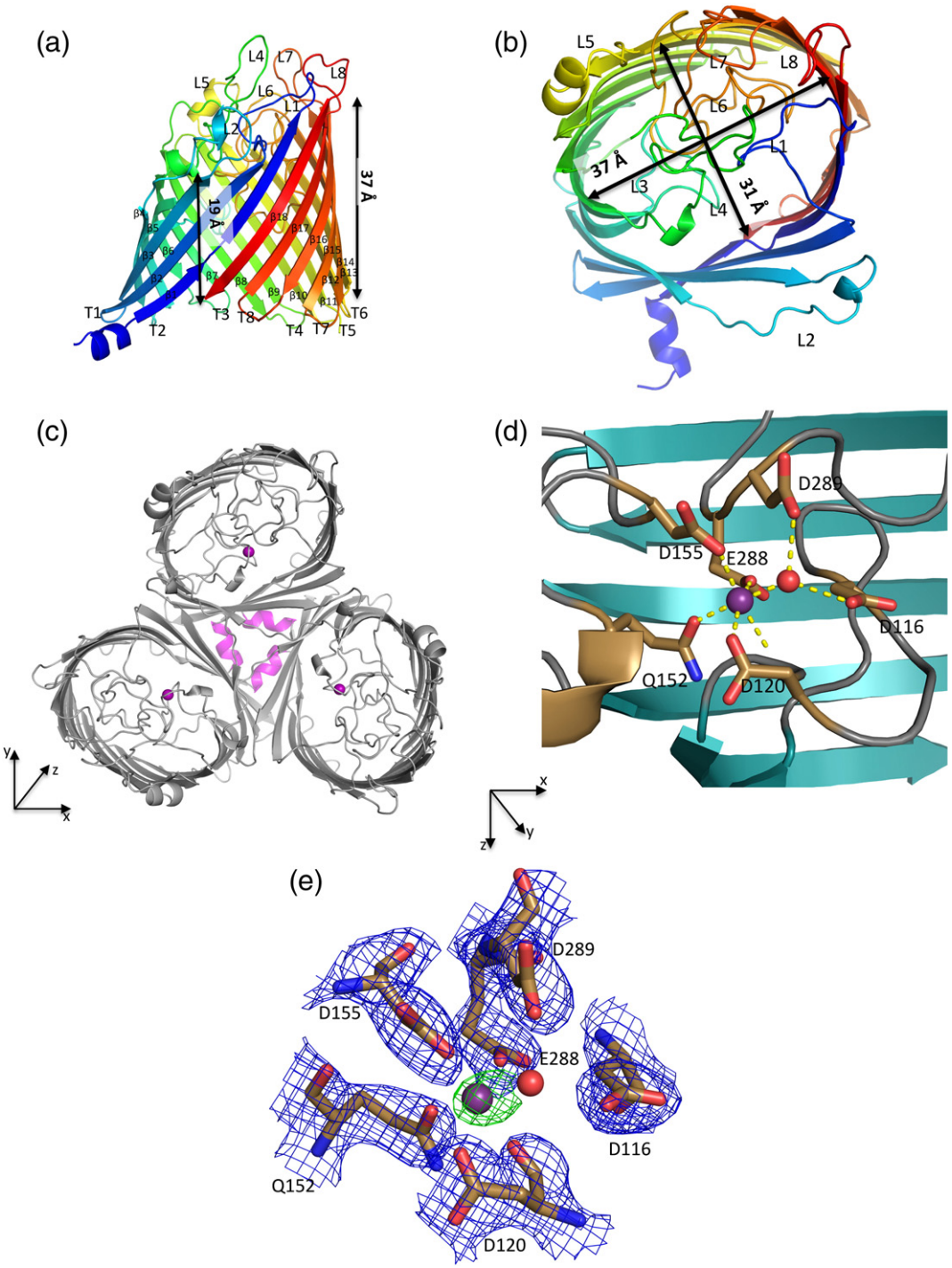

Fig. 1. The structure of the MOMP monomer. (a) Viewed from the side, parallel to the membrane. (b) The structure has been rotated 90° so that it is viewed from the outside of the cell (looking in), perpendicular to the membrane. (c) The trimer viewed as in (b), the periplasmic N-terminal α-helix is colored magenta and the calcium in purple. An XYZ axis is shown to orientation. (d) The calcium is depicted as a purple sphere and the water molecule as a red sphere. Residues involved in the calcium coordination are shown as sticks. An XYZ axis shows the view that has been rotated by 90° around the *X* axis when compared to (c). (e) A detailed view of the amino acids involved in calcium-binding site; same orientation as in (d). The F_o-F_c and $2F_o$-F_c electron density maps at 5σ and 2σ, respectively, have shown the final refined coordinates. The phases for the calculation of the map were based on a model that had never included the metal ion.

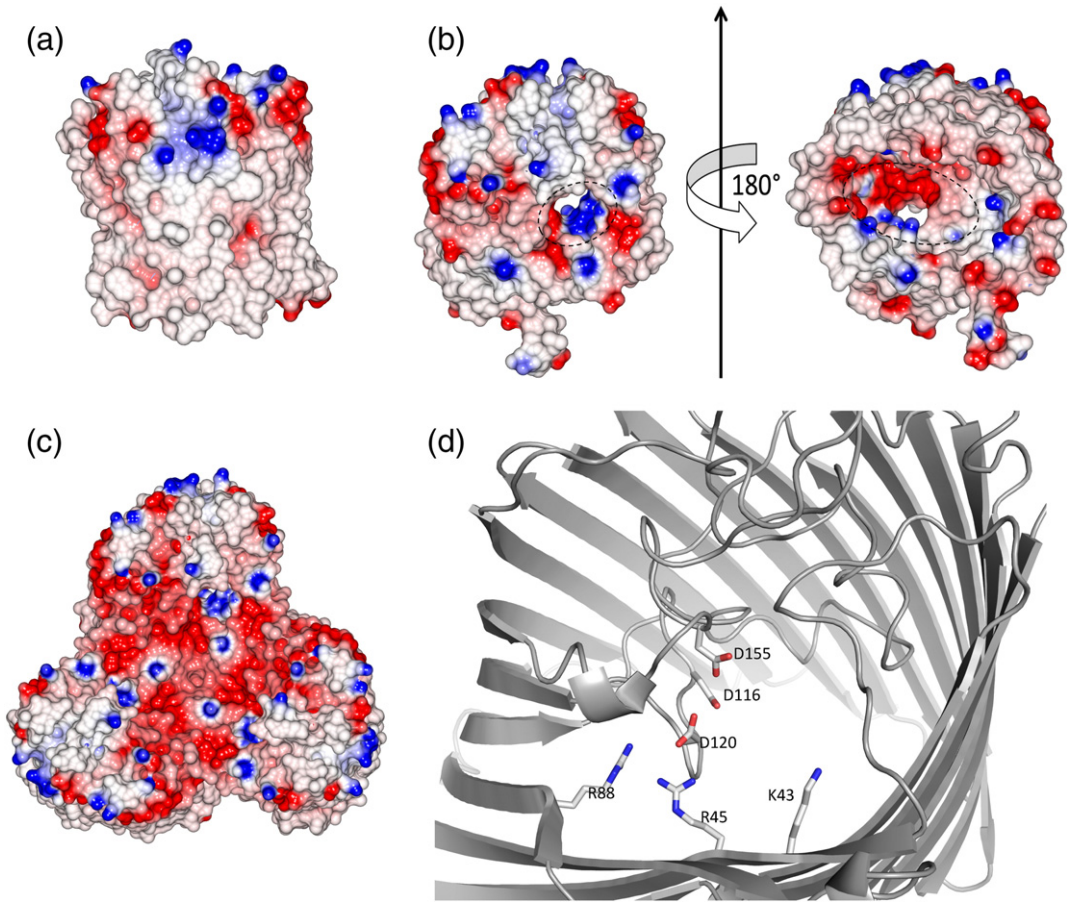

Fig. 2. The pore of MOMP. (a) The surface of MOMP is colored by electrostatic charge calculated in CCP4MG [21]. The structure has the same orientation as in Fig. 1a. (b) The structure is colored as in (a), with the constriction zone circled. The structure on the left is the same orientation as in Fig. 1b; the structure on the right has been rotated 180° (in effect, looking from the periplasm through the membrane to outside the cell). (c) MOMP trimer viewed from outside the cell; the structure has the same orientation as in Fig. 1c. (d) A detailed view of the charged amino acids at the constriction zone; the view is from outside the cell and the same as in Fig. 1b. The Ca^{2+} ion, which has been omitted for clarity, is bound to Glu155.

contacts between monomers using the PISA server [25] (which assesses the likely stability of multimers) identifies this trimer as the stable unit of MOMP. Gel-filtration data point to a trimeric arrangement consistent with electron microscopy of MOMP reconstituted into lipid bilayers [26]. The N-terminal Thr1 (Gly1 in recombinant MOMP) makes hydrogen bonds to strand 1 of the neighboring monomer; consequently, the three N-terminal helices in the trimer form a triangle. The main points of contact that stabilize the trimer arise from interactions with L2 from one monomer with L2, strand 5, strand 6, and L3 from the other monomer. Notably, residues Asn80 to Lys84 in this loop make main chain and, in some cases, side-chain hydrogen bonds across this interface. There is also a smaller area of contact on the periplasmic face between T8 (Lys370 to Phe376) on one monomer and T1 (Asp56 to Phe58) from the other. Each monomer–monomer interface buries over 2400 $Å^2$ of surface area; the trimer buries 11,600 $Å^2$ of surface area.

Single-channel conductance measurements

The pore-forming activities of both the rMOMP (Fig. 3) and nMOMP (Supplementary Fig. 3) were measured by single-channel ion-conductance measurements. Figure 3a and b shows the typical ion-current electrical signature of single monomeric and trimeric rMOMP, respectively. Figure 3a shows the monomers at negative (−100 mV) and at positive (+100 mV) applied transmembrane voltages. It is interesting to note that at positive voltages, we observe only downward but never upward spikes, suggesting the presence of a monomer channel as opposed to the partially blocked oligomers. At negative voltages, the MOMP monomer has upward spikes leading to the closure of the pore (Fig. 3a and Supplementary Fig. 3b). After the single-channel insertion, we flush the cuvette intensively with fresh buffer to avoid further insertion. Figure 3b shows the typical traces of trimers. At positive voltages, the trimeric channel gives a smooth response, whereas at

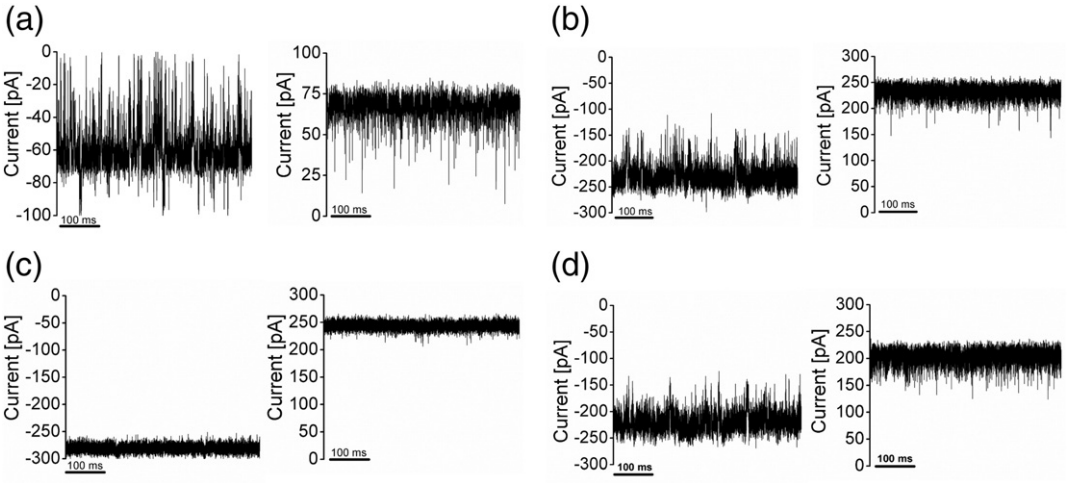

Fig. 3. Representative ion-current traces of rMOMP in 1 M KCl and 10 mM Mes (pH 6.0). (a) The ion-current corresponding to one open monomer at negative (top panel, left) and positive (top panel, right) transmembrane potential of 100 mV. (b) The ion-current corresponding to the trimer at negative (top panel, left) and positive (top panel, right) transmembrane potential of 100 mV. (c) The ion-current corresponding to a trimer following the addition of 10 mM $CaCl_2$ (1 M KCl at pH 6.0) at negative (bottom panel, left) and positive (bottom panel, right) transmembrane potential of 100 mV. (d) The ion-current corresponding to a trimer following the addition of 10 mM $MgCl_2$ (1 M KCl at pH 6.0) at negative (bottom panel, left) and positive (bottom panel, right) transmembrane potential of 100 mV. The monomer and the trimer were produced from different bilayer measurements.

negative voltages, flickering noise occurs. The analysis of repeated single rMOMP channel reconstitution in 1 M KCl revealed two main conductance levels, a lower level of 0.7 ± 0.2 and a higher level of 2.2 ± 0.2 nS, suggesting a monomeric and trimeric state. The same analysis for nMOMP yields 0.7 ± 0.2 and 2.3 ± 0.3 nS, respectively. Like other trimeric porins, both monomer and trimer follow an ohmic conductance pattern between ±200 mV (Supplementary Fig. 3a). No meaningful differences between the nMOMP and rMOMP proteins were observed. To investigate the homogeneity in the insertion of proteins, we followed multichannel measurements, and the distribution between monomers and trimers was random (Supplementary Fig. 3f). Control measurements with 1 M NaCl instead of KCl and 10 mM Mes (pH 6.0) revealed similar flickering at negative voltages (Supplementary Fig. 4a).

To elucidate the effect of divalent cation, we performed conductance measurements with 10 mM calcium chloride in the presence of 1 M KCl at pH 6.0. The presence of calcium chloride (Fig. 3c) eliminated the noise with a slight increase in conductance of 2.4 ± 0.2 nS at positive transmembrane potential of +100 mV and a somewhat higher conductance of 2.8 ± 0.2 nS at negative transmembrane potential of −100 mV. It is interesting to note that the measurements performed in either 10 mM $MgCl_2$ (Fig. 3d) or 10 mM $ZnCl_2$ (Supplementary Fig. 4b) caused flickering as observed in a calcium-free solution (Fig. 3a and b).

Conductance measurements were performed in the presence of the chelating agent EGTA. After the overnight incubation of the protein samples with 10 mM of EGTA, we observed in 1 M KCl, 10 mM Mes, and 10 mM EGTA at pH 6.0 a conductance of 2.4 ± 0.1 nS and, at negative potential, a conductance of 2.5 ± 0.1 nS (Supplementary Fig. 4c). As with native protein, noisy traces were observed with upward spikes seen at negative voltages. In a control measurement, we removed the EGTA by the addition of 10 mM $CaCl_2$ in 1 M KCl buffer and observed the previous $CaCl_2$ behavior (Supplementary Fig. 4d).

Ion selectivity

The ion selectivity was obtained from zero-current membrane potential measurements in the presence of up to 8-fold KCl concentration ratio (0.1 M KCl *versus* 0.8 M KCl). Approximately, 300–500 protein channels were reconstituted under a voltage of +20 mV. After the saturation of channel insertion, we measured the zero-current membrane potential under a wide range of concentration gradient ratios ranging from 1.5 to 7.5. At a concentration gradient of 500 mM (0.1 M *versus* 0.5 M), the zero-current membrane potential was 28 ± 4 mV at the diluted side, revealing the preference for cations. Goldman–Hodgkin–Katz equation [27] determines the ratio of cation to anion (P_{K+}/P_{Cl-}) to be 7 ± 2 for nMOMP and within the error identical for rMOMP (6 ± 1). Similarly, measurements were performed in the presence of 8-fold calcium chloride (0.1 M $CaCl_2$ *versus* 0.8 M $CaCl_2$) and no KCl. The zero-current membrane potential was measured as −19 ± 1 mV, which implies that the cationic selectivity exhibited by the

channel in monovalent cation (KCl) turns into anionic in the presence of divalent cation ($CaCl_2$). This is consistent with the structure that shows that the narrow region of the constriction zone is lined with five negatively charged amino acid residues, which would favor the transport of cationic molecules over anionic ones. However, in the presence of calcium chloride, Ca^{2+} binds to the negatively charged residues reversing the ion selectivity (Supplementary Fig. 3g).

Interaction of ciprofloxacin with MOMP

A single trimeric channel of MOMP was reconstituted into artificial lipid bilayers containing 1 M KCl (without $CaCl_2$). Addition of 1 mM ciprofloxacin to the *trans* side of the lipid bilayer decreased the conductance by 0.2 nS to 2.2 nS, along with an increase in the current noise (Supplementary Fig. 5a and b). The stronger flickering does not allow individual blocking events to be distinguished (Supplementary Fig. 5a). Increasing the concentration of ciprofloxacin to 2 mM reduces the conductance to ~2.1 nS at +150 mV (Supplementary Fig. 5a and c). In the presence 1 M KCl, 10 mM Mes, and 10 mM $CaCl_2$ addition of 0.5 mM ciprofloxacin to trimeric MOMP resulted in distinct blockages, which were concentration dependent (Fig. 4a and b). The blockage events were fitted into a kinetic binding model with an on rate, k_{on}, of υ/3[c] (υ = number of blockages per second; [c] is concentration) and an off rate, k_{off}, of 1/τ (τ = dwell time) [28]. The average dwell time did not depend on the concentration of the ciprofloxacin and was found to be in the range of 60 μs for the voltages applied between 125 and 199 mV (Supplementary Fig. 5d and e). The values of k_{on} and k_{off} obtained are shown in Table 2. Twofold increase in the blocking events on the addition of ciprofloxacin on the *trans* side when compared to the addition to the *cis* side was observed. This suggests that ciprofloxacin accessed the binding site more readily from the *trans* side. Addition of ciprofloxacin in the presence of magnesium chloride resulted in fast flickering events (Supplementary Fig. 6), consistent with a specific modulation in function by Ca^{2+}. In fact, in the presence of $CaCl_2$, we saw mainly a trimeric protein, suggesting that the MOMP trimer was itself stabilized by $CaCl_2$. The interaction of ciprofloxacin with MOMP trimers in the presence of calcium chloride resulted in clean blockage events. With monomeric protein, the blocking events were replaced with flickering.

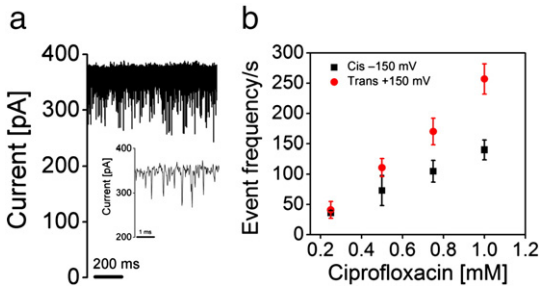

Fig. 4. Ciprofloxacin binds to and blocks channel conductance. (a) Transient blockages are observed in the ion-current trace of single trimeric rMOMP channel in the presence of 1 M KCl, 10 mM Mes, and 10 mM $CaCl_2$ (pH 6.0) when 0.5 mM ciprofloxacin is added to *trans* side. The applied transmembrane potential was +150 mV. (b) The number of binding events increases with the increase in the concentration of the ciprofloxacin from 0.25 to 1 mM measured at 150 mV.

In silico modeling

Two rMOMP structures, one with calcium and one without, were equilibrated in silico, and the RMSD and root mean square fluctuations (RMSF) of the protein's backbone were calculated. With calcium, the structure is considerably more stable (RMSD of 1.45 Å *versus* 1.75 Å and RMSF halved). The instability was focused on the loops involved in calcium coordination (Fig. 5a). Although the empty site was occupied transiently by one of the sodium ions used to neutralize the system, its presence was not sufficient for the stabilization of the structure. Figure 5b shows that the pore size slightly increased in the absence of Ca^{2+}.

In the absence of the calcium ion (Fig. 5c), the transverse internal electric field [29] of ~18 mV/Å was comparable to OmpC (~20 mV/Å) but lower than OmpF (36 mV/Å). When calcium was present, the internal electric field was reduced to almost a third of its value due to charge screening, which in turn reduced the transversal electric field in the constriction region to ~7 mV/Å. The divalent ion induced a rotation of the transversal electric field and a change in the conformation of the internal loops, which led to a shift in the putative path that water was predicted to diffuse along. When calcium was not present, water avoided passing near the cluster of negative residues that bind the divalent ion located in the region (Fig. 5d), whereas when calcium was present and the transversal electric field rotated, the water pathway was shifted toward the ion position.

In order to understand the effects of the presence of the cation in the permeation of polar antibiotics, the free energy profiles were calculated for ciprofloxacin translocation for both calcium-bound and calcium-free

Table 2. Kinetics of ciprofloxacin entry into MOMP channel

Rate constants	0.5 mM ciprofloxacin
$k_{on\ cis}$ ($\times 10^3$ M^{-1} s^{-1})	47 ± 10
$k_{on\ trans}$ ($\times 10^3$ M^{-1} s^{-1})	73 ± 7
k_{off} ($\times 10^3$ s^{-1})	16 ± 1

Experimental conditions: 1 M KCl, 10 mM Mes, 10 mM $CaCl_2$, and 0.5 mM ciprofloxacin (pH 6.0); T = 20 °C. The applied transmembrane voltage was 150 mV.

protein. The free energy maps show that the main barrier to translocation was, as expected, located at the constriction zone (Fig. 5e). Both free energy maps share common features but differed at the calcium-binding site. In the absence of calcium, ciprofloxacin approaches the protein constriction region by entering with its positive group, which is attracted toward the negatively charged calcium-binding site (Supplementary Fig. 7). This is similar to what happens in OmpF from *E. coli*, where the

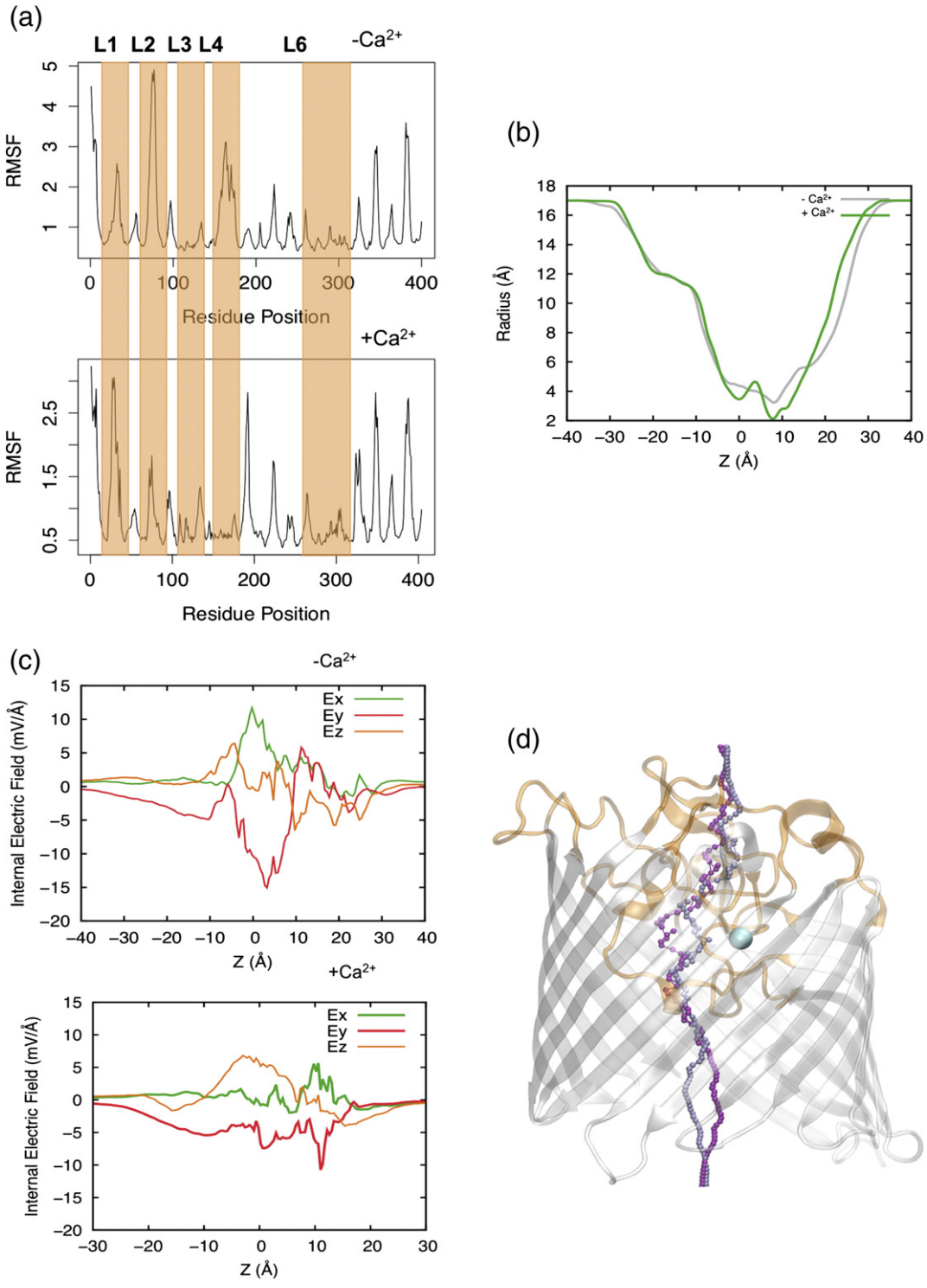

Fig. 5 (*legend on next page*)

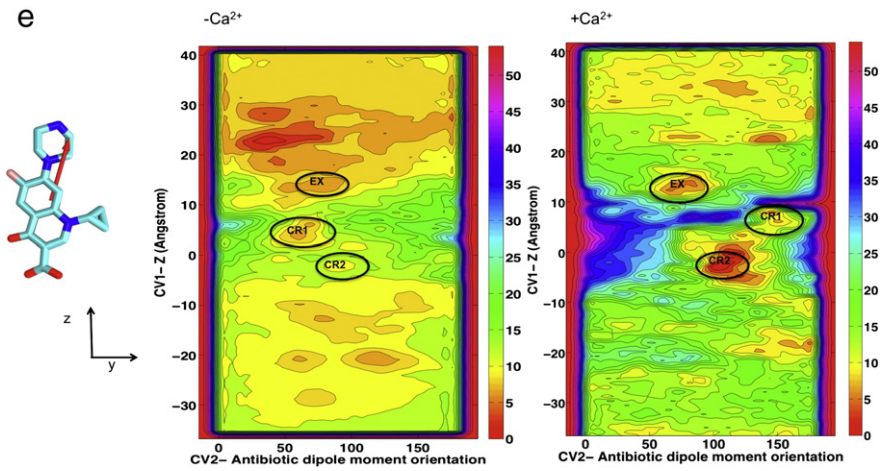

Fig. 5. MOMP permeability. (a) RMSF of protein backbone for the two simulated structures: not Ca^{2+} bound and Ca^{2+} bound. The loops presenting bigger changes in fluctuation values are highlighted in orange. (b) The pore radius of MOMP monomer moving from the extracellular side to the periplasm without bound calcium (gray) and with bound calcium (green). (c) The macroscopic intrinsic electric field of MOMP with and without calcium. A reduction of the transversal components from ~18 mV/Å in the structure without calcium to ~7 mV/Å when calcium is present. (d) The putative pathway for water diffusion shifts toward the calcium ion when it is present (ice blue), while in the structure without calcium ion (purple), it avoids the cluster of negative residues that coordinate Ca^{2+}. MOMP monomer is shown in cartoon representation. (e) Free energy surface for the translocation of ciprofloxacin through MOMP without and with calcium. Antibiotic dipole moment orientation is depicted onto a licorice representation of ciprofloxacin in red. Each isocontour corresponds to a free energy difference of 2 kcal mol^{-1}. Free energy values were rescaled for each surface in order to have the absolute minimum equal to zero. The most relevant minima for ciprofloxacin translocation have been labeled for both scenarios: one in the extracellular region (EX) and two inside the constriction region (CR1, CR2).

negative patch on L3 modulated the translocation of antibiotics and traps a divalent cation [30].

In the presence of calcium ion (Supplementary Fig. 7), ciprofloxacin entered with the opposite orientation, pointing its carboxylic group toward the ion. Translocation of ciprofloxacin starting from the "*cis*" side required us to apply a voltage above +100 mV to achieve this favorable orientation. Critically, molecular dynamics (MD) predicts that the antibiotic follows a different path and has a higher barrier to translocation in the presence of bound Ca^{2+} ion.

Discussion

We detected no difference in structure or function between the MOMP purified from *C. jejuni* and the MOMP heterologously expressed in *E. coli*. Unusually for an 18-stranded β-barrel, MOMP adopts the same trimeric arrangement as seen for OmpF and OmpC, which are 16-stranded β-barrels. Similar to these trimers, a loop from one monomer reaches across and partly into the central pore of another monomer. Whether the trimer has functional significance, other than stability, is unclear. A distinctive structural feature of MOMP is the α-helix at the N terminus. The other known outer membrane proteins with an N-terminal helix are OprB from *Pseudomonas aeruginosa* and the palmitoyl transferase PagP from *E. coli*; both proteins are monomers [31,32]. The trimeric sucrose-specific porin (ScrY) from *Salmonella typhimurium* comprises a coiled-coil domain at the N-terminal periplasmic domain [33]. Although the secondary structure of the N terminus was not determined from its crystal structure [33], spectroscopic and biophysical analyses suggested that it forms α-helical coiled-coil complexes that might be involved in the supramolecular stabilization and low-affinity sugar binding of ScrY [34]. The role of the N-terminal α-helix in MOMP has not been experimentally investigated, but structural analysis suggests that it favors trimerization. The most striking difference between MOMP and OmpF/OmpC from *E. coli* is the presence of a Ca^{2+}-binding site in the constriction zone of MOMP. The site clearly has a high affinity for calcium, since the overexpressed protein had selectively bound the ion from the culture and held onto it during purification. The ion is bound to a number of key loops that form the constriction zone, suggesting its structural role. Addition of EDTA to isolated protein, which would remove any calcium, has been previously shown to destabilize the protein [20]. We see that EGTA addition results in noisy conductance (Supplementary Fig. 4) comparable to native protein, whereas the addition of 10 mM $CaCl_2$ containing 1 M KCl gives stable conductance traces (Fig. 3c). Addition of Mg^{2+} (Fig. 3d) or Zn^{2+} (Supplementary Fig. 4b) did not

result in a stable ion-current, suggesting that this is a specific feature of Ca^{2+}. MD analysis showed that in the absence of calcium, the loops become unstable and disrupted the order of the constriction zone. We suggest that the binding of Ca^{2+} anchors the loops, thus ordering the eyelet, preventing them from "flopping" into the pore, and hence eliminating the spikes seen in ion-current in the absence of calcium (Fig. 3a and b).

Comparison of MOMP sequences (one each) from *C. jejuni*, *Campylobacter coli*, *Campylobacter fetus*, *Campylobacter lari*, and *Campylobacter upsaliensis* shows that three (Asp116, Glu288, and Asp289) of the five amino acids involved in metal binding are absolutely conserved. Asp120, which coordinates the metal ion in *C. jejuni* is conserved in *C. coli* and *C. upsaliensis*, but not in *C. fetus* or *C. lari* where there is a deletion of 4 aa. Gln152, which coordinates the metal ion with its side-chain oxygen, is fully conserved in *C. jejuni*, *C. coli*, and *C. upsaliensis* but is replaced by an asparagine in *C. fetus* and an aspartic acid in *C. lari* (Supplementary Fig. 2). MOMP, in the absence of Ca^{2+}, is a cation-selective intermediate between OmpC (most) and OmpF (least). The calculated radius at the narrowest point in the constriction zone of MOMP is 2.6 Å, somewhat larger than OmpC (2.2 Å) and smaller than OmpF (3.3 Å). Liposome swelling studies [35] have shown that MOMP is capable of transporting larger neutral molecules (such as arabinose, glucose, mannose, α-ketoglutarate, etc.) than OmpC, consistent with a pore that is larger than that of OmpC.

The single-channel conductance for rMOMP and nMOMP from the 85H strain of *C. jejuni* was 0.7 ± 0.2 for the monomeric and 2.2 ± 0.2 nS for the trimeric state in 1 M KCl. Previously, Dé and colleagues reported lower conductances for the monomer (0.51 ± 0.04 nS) and trimer (1.5 ± 0.06 nS) [36]. Given that the different buffer condition (here at pH 6.0, rather than pH 7.4, as reported by Dé *et al.*) may reflect differences in experimental conditions, both the rMOMP and nMOMP channels from *C. jejuni* exhibit two distinct channel conductance values related to the trimer and the monomer. We are unable to determine if the monomer species represents a trimer with two closed channels or a genuine monomer arising from dissociation of the trimer. The trimer exhibits a large single-channel conductance of 2.2 nS, similar to the conductance of cyanobacterium species *Synechocystis* sp. PCC 6714 [37] and comparable to the *E. coli* OmpC (2.5 nS) [38]. The conductance of the monomer is similar to the unitary conductance of cation-selective monomeric channel *P. aeruginosa* OccD3 (around 0.7 nS) [39] and *E. coli* OmpF (1 nS; all in 1 M KCl) [40,41]. The monomeric value is also comparable to the triton/EDTA-solubilized protein of *C. jejuni* UA580 strain [42] and *C. coli* UA30 [35], whose single-channel conductances are 0.82 and 0.53 nS, respectively. In KCl solution, the channel was selective for cations, but after the addition of $CaCl_2$, the channel switched its selectivity for anions. This inversion of selectivity mirrors that seen for OmpF in the presence of $MgCl_2$ [30].

The presence of Ca^{2+} (but once again not Mg^{2+}) also altered the behavior of MOMP with ciprofloxacin in single-channel experiments (Fig. 4). The antibiotic blocked the channel with frequent binding events of short residence time (60 μs). When Ca^{2+} ions were not present, ciprofloxacin reduced the current flow in a concentration-dependent manner (Supplementary Fig. 5a), but individual blocking events were not seen. We conclude that in the absence of the Ca^{2+}, antibiotic translocation occurs too rapidly to see individual events under our experimental conditions. Metal-ion-dependent blockages were observed with imipenem added to OmpPst1 channel from *Providencia stuartii* [28] in the presence of La^{3+} and with enrofloxacin added to OmpF channel in the presence of Mg^{2+} [30]. In both these cases, the ion does not co-purify with the protein or seem to have any role in stability.

The presence of a calcium ion at the constriction zone partly neutralizes the negative charges and thus in turn profoundly weakens the transverse electric field at the eyelet. The transverse field is known to play a key role in the translocation of polar molecules [43]. MD shows that the presence of the Ca^{2+} increased the barrier to transport compared to an artificial model without the ion; a prediction entirely consistent with the experimental single-channel data. A review of the antibiotic sensitivity of *C. jejuni* showed that the organism is less susceptible to singly or doubly anionic antibiotics and to larger, dipolar ionic molecules [35]. The increased resistance to the charged antibiotics is consistent with a reduced transverse field, which would increase the barrier to translocation.

Food poisoning by ingestion of *Campylobacter* is common and, as resistant strains have emerged, is causing concern. Unlike *E. coli*, *Campylobacter* have evolved to possess only one MOMP; thus, it cannot switch between OmpC and OmpF expression as *E. coli* does to alter antibiotic entry to the cell. In structural terms, MOMP is distinct from both OmpC and OmpF; however, in terms of pore size, it is intermediate. Uniquely, MOMP may rely on a permanently bound Ca^{2+} ion to modulate translocation across the outer membrane.

Materials and Methods

Molecular biology

A gene encoding MOMP from *C. jejuni* strain 85H (Uniprot entry number: Q659I5) was synthesized with codon optimization for *E. coli* by Eurofins MWG (Germany). The gene carried an NcoI enzymatic cleavage site at the 5′-end and a

stop codon followed by HindIII site at the 3′-end. The *momp* gene was cloned into a pTAMAHisTEV expression vector. The pTAMAHisTEV vector was created by placing a TamA signal peptide into the T7 promoter ampicillin resistance pHisTEV vector [44]. Consequently, the pTAMAHisTEV plasmid expressed a protein with a TAMA signal peptide at the N terminus, followed by a histidine tag, then the TEV recognition sequence ENLYFQG, and finally the N-terminus of the target protein (here MOMP).

Protein expression

The plasmid pTAMAHisTEV harboring the MOMP gene was transformed into C43(DE3) competent cells. A 250-ml LB startup culture containing 100 μg ml^{-1} ampicillin was incubated at 37 °C and at 200 RPM. Then, 20 ml of startup culture was transferred to 10 × 1 L LB containing the same amount of ampicillin and was grown at 37 °C until an OD_{600} of ~0.6. At this stage, cells were induced with 0.4 mM IPTG, the temperature was dropped to 25 °C, and growth continued for 16 h. Cells were harvested by centrifugation at 6200*g* (JLA8.1000 rotor, Beckman Coulter).

Cell pellets were resuspended in lysis buffer containing 20 mM Tris–HCl (pH 8.0), 300 mM NaCl, 10% glycerol, 20 μg ml^{-1} DNAse, 100 μg ml^{-1} lysozyme (both Sigma-Aldrich), and EDTA-free protease inhibitor cocktail (Roche). Cells were lysed by two passes through a chilled cell disruptor at 30 kpsi. Cellular debris was removed by centrifugation at 10,000*g* (JA 25.50 rotor, Beckman Coulter). The membrane fraction was retained by ultracentrifugation at 100,000*g* (50.2 Ti rotor, Beckman Coulter) at 4 °C for 1 h. A two-step process failed in our hands, in which the inner membrane was with *N*-lauroyl sarcosine and then discarded, followed by solubilization of the outer membrane with SB3.14, N,N-dimethyldodecylamine N-oxide (LDAO), *n*-octylpolyoxyethylene (Octyl--POE), or other detergents; the MOMP remained insoluble. Direct solubilization of total cell membrane with either 1% SB3.14 or 5% Elugent™ gave much improved extraction. As TEV protease was inactive in the presence of SB3.14, extraction was carried out in 20 mM Tris–HCl (pH 8.0), 150 mM NaCl, 5% (vol/vol) Elugent™ (Merck Millipore), and EDTA-free protease inhibitor cocktail using a tissue grinder and subsequent incubation at 4 °C overnight with gentle rotation. Insoluble material was removed by centrifugation (100,000*g* for 1 h). Elugent concentration was reduced by dilution to a final concentration of 1.25% (vol/vol). This protein solution was cycled over Ni-NTA column at 4 °C overnight using a peristaltic pump to ensure binding. The column was washed extensively with a buffer containing 20 mM Tris–HCl (pH 8.0), 30 mM imidazole, 150 mM NaCl, and 0.25% (vol/vol) Elugent™. MOMP was eluted with 2 column volume (CV) of buffer containing 250 mM imidazole. The eluent was supplemented with 1 mg His_6-tagged TEV protease and dialyzed in SnakeSkin tubing (Thermo Scientific) against a buffer containing 10 mM imidazole at room temperature overnight. The dialyzed sample was passed through a 0.45-μm syringe filter to remove insoluble particles before the sample was applied to 2-ml Ni-NTA resin. Cleaved MOMP was collected from the flow-through fraction. MOMP was further purified by gel filtration (16/60 Superdex 200 pg; GE Healthcare) on an Äkta Express purifier during which Elugent™ was exchanged for 0.45% (wt/vol) C_8E_4. MOMP was concentrated to 10 mg ml^{-1} for crystallization. Purity and integrity were monitored on SDS-PAGE (NuPAGE, Invitrogen) and mass spectrometry. SeMet-labeled MOMP was produced according to the metabolic inhibition method [45] using SeMet media from Molecular Dimensions and was purified as described above.

C. jejuni 85H strain [46] was grown according to Bolla *et al.* [11]. *C. jejuni* strain was spread onto a blood agar plate and incubated for 24 h at 42 °C. Bacteria were recovered with 1 ml of 2YT medium. Four Columbia agar plates supplemented with the appropriate amount of *Campylobacter* selective antibiotics supplement (Oxoid) were inoculated with 150 μl of the recovered bacteria solution and incubated for 48 h at 42 °C. 2YT medium was used to recover the bacteria, which were subsequently inoculated on 40 plates of Columbia agar and incubated for 48 h at 42 °C. Subsequently, each plate was rinsed with 5 ml of 10 mM Tris–EDTA buffer (pH 7.4) and agitated for 15 min at room temperature; then, bacterial suspension was recovered and the OD_{600} checked. From this point, all the following steps were performed at 4 °C. The bacteria were pelleted by centrifugation at 10,000*g* for 30 min. The pellet was resuspended in 200 ml of 200 mM Glycine–HCl (pH 2.2) and agitated for 15 min. Bacteria were harvested by centrifugation at 10,000*g* for 30 min and washed in 100 mM Tris–HCl (pH 7.4). Cells resuspended in Tris–HCl 10 mM (pH 7.4) were then lysed by using two passes at 30 Kpsi through a high-pressure cell disruption for micro volumes (Constant System Ltd). Unbroken cells were removed by spinning the cell lysate at 10,000*g* for 30 min. The supernatant was kept and spun down at 100,000*g* for 1 h. The pellet was then homogenized in 10 mM Tris–HCl (pH 7.4) and 0.1% (wt/vol) of sodium lauryl sarcosinate (Sigma) and was left rocking for 30 min. The outer membrane was recovered by ultracentrifugation at 100,000*g* for 1 h. The supernatant containing the inner membrane protein fraction was discarded, and the pellet was homogenized with 20 mM sodium phosphate buffer (pH 7.4) and 1% of Octyl-POE (Bachem AG) and was left rocking at 4 °C for 30 min. Solubilized proteins were recovered by ultracentrifugation at 100,000*g* for 1 h. Protein was loaded onto a MonoQ HR ion exchange column (GE Healthcare) and was equilibrated with 5 CV of buffer A (30 mM Na_2HPO_4, 10 mM NaCl, and 0.6% Octyl-POE). The bounded proteins were eluted stepwise with 5, 12, 20, 70, and 100% of buffer A supplemented with 1 M NaCl. The chromatography was performed on ÄKTA Explorer 10 system (GE Healthcare). Each fraction was examined with SDS-PAGE and Western blot with specific antibodies. Eluted fractions containing MOMP were collected and concentrated to 5 ml and injected onto a Superdex 200 16/60 GL (GE Healthcare) column equilibrated with 2 CV of 20 mM Tris–HCl (pH 8.0), 150 mM NaCl, and 0.45% (wt/vol) C_8E_4. Fractions containing MOMP were combined and concentrated to 10 mg ml^{-1}.

Crystallization

Recombinantly expressed MOMP crystallized in 50 mM sodium citrate (pH 4.25), 35% (vol/vol) PEG 400, and 70 mM KCl in a hanging-drop vapor-diffusion experiment at 20 °C with 500 μl reservoir solution and a crystallization droplet of 2 μl protein and 1 μl precipitant. SeMet MOMP crystallized under identical conditions. Crystals grew to full size after 1 week and were hexagonal in shape.

MOMP purified from *Campylobacter* crystallized in 0.05 M calcium chloride, 0.05 M barium chloride, 0.1 M Tris (pH 7.5), and 30% (vol/vol) PEG 400. Crystals were optimized using hanging-drop vapor-diffusion technique. Crystals appeared after 3 days in a drop made of 1 µl protein and 1 µl reservoir made of 0.05 M calcium chloride, 0.05 M barium chloride, 0.1 M Tris (pH 8), and 32% (vol/vol) PEG 400. In all cases, crystals were flash cooled before data collection, but no cryoprotectant was added.

Data collection, and structure determination and refinement

X-ray data of recombinant SeMet crystals were collected at beamline ID23-1 in ESRF, Grenoble, France and native data at Diamond. Data were processed with Xia2 [47]. Both belong to spacegroup $P6_3$ with one monomer per asymmetric unit. The SeMet structure was solved by single-wavelength anomalous dispersion to a 2.7-Å resolution with Autosolve program of Phenix [48]. Using this as search model, the 2.1-Å native structure was solved with the PHASER MR from Phenix [49]. The model was built using Arp/Warp [50]. X-ray data from a crystal of MOMP purified from *Campylobacter* crystals were collected in house using a Rigaku Micromax™-007HF Cu anode with VariMax optics and a Rigaku Saturn 944+ CCD detector and processed with Xia2 [47]. The structure was solved to a resolution of 2.9 Å by molecular replacement using the recombinant MOMP structure as a search model with the program Phaser [49]. Crystals belong to spacegroup $P2_12_12_1$ with three molecules per asymmetric unit and a Matthew's coefficient of 45%.

The three models were manually completed in Coot [51] and refined with REFMAC [52]. Structures were validated with Molprobity [53]. Data collection and refinement statistic are listed in Table 1. The webserver "Checkmy-Metal" validates the identification as calcium [54]. Additionally, the difference electron density map showed a residual elongated density that was modeled as an ethylene glycol like the molecule (from PEG 400 or C8E4) in the recombinant MOMP. This molecule sits below the constriction zone underneath loop 3.

Single-channel conductance measurements

A planar lipid bilayer was formed using solvent-free lipid bilayer technique [55]. In brief, the cuvettes used for our bilayer experiments consist of *cis* and *trans* chambers separated by a 25-µm thick teflon film (Goodfellow) carrying an aperture with a diameter of 40–70 µm. The spherical hole in the teflon film was made by a high-voltage cathode discharge (Electrotechnic Products). In order to form the lipid bilayer, the aperture is pre-painted with 1 µl of 1% hexadecane in hexane. Due to its high mechanical and chemical stability, 5% solution of diphytanoyl phosphatidylcholine (DPhPC, Avanti Polar Lipids) is commonly used [56]. The bilayer it forms allows for the insertion of transmembrane pores. The chambers are filled with electrolyte solution, which usually consist of 1 M KCl and 10 mM Mes (pH 6.0) with a total solution volume of 2.5 ml. MOMP was added to the *cis* side (which is the electrical ground or reference potential) of the chamber at a final concentration of 2 ng ml^{-1}, and the channel insertion was facilitated by the rapid mixing of the contents of the chamber while applying a transmembrane potential of −199 mV. Electrical recordings were made through a pair of Ag/AgCl electrodes (World Precision Instruments), attached to an Axon Instruments 200B amplifier (Axon Instruments Inc.) in the voltage clamp mode. Data were filtered by a low-pass Bessel filter at 10 kHz and directly saved into the computer memory with a sampling frequency of 50 kHz. Data analyses were performed using Clampfit 10.0 software (Axon Instruments Inc). As observed previously [35], multiple channel events for MOMP were non-homogeneous and hence were not analyzed further (Supplementary Fig. 3h).

Ion-selectivity measurements

The ion selectivity of ~44-kDa MOMP was carried out by measuring the zero-current membrane potential as described elsewhere [27]. The Teflon cuvettes consist of two chambers, with a pre-designed spherical hole having a diameter of 0.5–0.5 mm^2. In chloroform, 2% DPhPC serves as the pre-painting solution, and 1% solution of DPhPC in *n*-decane serves as the lipid for the formation of black lipid membranes. After the formation of a stable membrane, 50–100 ng/ml of MOMP protein was added to both sides of the Teflon chambers containing 0.1 M KCl solution. After the incorporation of 200–500 channels, a salt gradient was established by adding 3 M solution of KCl on one side of the membrane, and an equal volume of 0.1 M solution of KCl was added on the other side with uniform stirring of the contents. The resulting zero-current membrane potentials were measured using the high-impedance electrometer (Keithley 617).

MD

The high-resolution X-ray structure of trimeric MOMP was used as starting coordinates for MD simulations. Loop 2 from Ala77 to Glu81 was missing in the crystal structure and was modeled using MODELLER [57] that considered the optimal structure among 100 generated models. Amino acid residues were simulated in its ionization state at neutral pH. The entire trimer was embedded in a pre-equilibrated 1-palmitoyl-2-oleoyl-sn-glycero-3-phosphocholine bilayer of 471 lipids and the system was oriented in order to center the protein at the origin of the coordinate system and align the channel along the *z*-axis (positive z: extracellular side; negative z: periplasmic side). We added 53 sodium ions to neutralize the system total charge. The system was solvated with ~40,997 TIP3P water molecules (simulation box size: 13.72, 23.80, 10.71 nm; total number of atoms: ~204 k). Simulations were performed with and without the calcium ion to evaluate its effect on the structure and dynamics of loops.

After 1 ps of energy minimization (conjugate gradients), a slow heating from 10 to 300 K was carried out for 1 ns. During this stage, positional restraints were applied on the protein α-carbons (all three dimensions) and on the lipids' phosphorus atoms (along z only). After releasing the constraints on the 1-palmitoyl-2-oleoyl-sn-glycero-3-phosphocholine, an equilibration stage follows for 4 ns in the isothermal-isobaric (NPT) ensemble at 1.0 bar and 300 K. Finally, 0.9-µs MD simulations were performed in the canonical (NVT) ensemble after the elimination of the protein restraints.

The NPT equilibration was performed with the program NAMD [58], with 1.0 fs time step, and by treating long-range electrostatics with the soft particle mesh Ewald method (64

grid points and order 4 with direct cutoff at 1.0 nm and 1.0 Å grid size). Pressure control was applied using the Nose–Hoover method (extended Lagrangian) with isotropic cell, integrated with the Langevin Dynamics (200 fs and 100 fs of piston period and decay, respectively). The latter was also applied for temperature control with 200-fs thermostat damping time. Production run in the NVT ensemble was performed with the ACEMD code [59] compiled for graphic processing units (GPUs) by rescaling the hydrogen mass to 4 au and increasing the time step up to 4.0 fs [60]. The Langevin thermostat was used with 1-ps damping time. Soft particle mesh Ewald was used to treat the electrostatics as for the equilibration stage. The Amber99SB-ILDN force field [61] was used for the protein and lipids, and the TIP3P [62] for waters.

The GAFF force field parameters [63] were used to describe ciprofloxacin (DrugBank [64] n. DB00537). Partial atomic charges were evaluated according to the restrained electrostatic potential (RESP) approach [65]: the molecule was first optimized at the HF/6-31G(d) level, up to a convergence in energy of 10^{-5} au, using the Gaussian03 package [66]. Atomic RESP charges were derived from the electrostatic potential using the antechamber module of the AMBER package [67]. Parameters are freely available[†] [68].

Starting from the final configuration of the MOMP simulation without the calcium ion described above, the antibiotic was placed inside the lumen of the first monomer. The difference between the *z*-coordinate of the center of mass (com) of the antibiotic two-ring system and the *z*-coordinate of the com of the protein monomer was +32.9 Å. A thousand steps of energy minimization were performed. The equilibration stage followed for 1 ns in the NVT ensemble at 300 K as described hereinbefore. Well-tempered metadynamics simulation (500 ns) was performed with the ACEMD code, until the first effective translocation through the protein constriction region was observed [69,70]. Then, four configurations were randomly selected, two with the antibiotic located in the extracellular vestibule and two in the periplasmic vestibule. Correspondingly, four multiple walkers [71] were set to extend the metadynamics reconstruction of the free energy surface. Two biased collective variables were used, namely, the antibiotic position and the projection of the dipole moment of the antibiotic onto the *x*-axis of the channel. In practice, the "position" Δz was defined as the difference of the *z*-coordinate between the com of the antibiotic two-ring system and that of the porin first monomer. We run 4 × 1 μs, arriving to a total simulation time of 4.5 μs. During the metadynamics, energy biases were added every 1.25 ps to each collective variable (initial height: 1.0 kcal mol^{-1}; σ 0.3 kcal mol^{-1} and 5.0 degree for position and dipole moment orientation, respectively). Well-tempered ΔT was 5000 K.

Accession numbers

Coordinates and structure factors have been deposited in the Protein Data Bank with the ID codes 5ldt and 5ldv.

Acknowledgments

L.G.M.F. and S.A.-G. are funded by EU FP7-PEOPLE-2013-ITN Translocation network Nr. 607694. The research leading to these results was conducted as part of the Translocation consortium (www.translocation.com) and has received support from the Innovative Medicines Initiatives Joint Undertaking under Grant Agreement no.115525, resources of which are composed of financial contribution from the European Union's seventh framework programme (FP7/2007-2013) and of the EFPIA companies in kind contribution. J.H.N. is Royal Society Wolfson Merit Award holder, Senior Investigator Wellcome Trust (WT100209MA), and Chinese Academy of Science 1000 Talent Scholar. M.C. thanks the PRACE consortium for the use of the Research Infrastructure CURIE based in France at TGCC through the project Tier-0 nr. RA2699. The use of beamlines at both Diamond and ESRF is acknowledged.

Appendix A. Supplementary Data

Supplementary data to this article can be found online at http://dx.doi.org/10.1016/j.jmb.2016.09.021.

Received 5 July 2016;
Received in revised form 26 September 2016;
Accepted 26 September 2016
Available online 30 September 2016

Keywords:
Campylobacter;
outer membrane proteins;
antibiotic resistance;
β-barrel;
porins

†L.F., G.W., L.M., and N.D contributed equally to this work.

Abbreviations used:
MOMP, major outer membrane protein; SeMet, selenomethionine; rMOMP, high-resolution structure of MOMP purified from an *E. coli* overexpression system; nMOMP, high-resolution structure of MOMP purified from *Campylobacter*; PEG, polyethylene glycol; RMSF, root mean square fluctuations; MD, molecular dynamics; Octyl-POE, *n*-octylpolyoxyethylene; CV, column volume.

References

[1] N.O. Kaakoush, N. Castaño-Rodríguez, H.M. Mitchell, S.M. Man, Global epidemiology of *Campylobacter* infection, Clin. Microbiol. Rev. 28 (2015) 687–720.
[2] G.M. Ruiz-Palacios, The health burden of *Campylobacter* infection and the impact of antimicrobial resistance: playing chicken, Clin. Infect. Dis. 44 (2007) 701–703.
[3] L.D. Kalischuk, A.G. Buret, A role for *Campylobacter jejuni*-induced enteritis in inflammatory bowel disease? Am. J. Physiol. Gastrointest. Liver Physiol. 298 (2010) G1–G9.

[4] B.M. Allos, Association between *Campylobacter* infection and Guillain–Barré syndrome, J. Infect. Dis. 176 (1997) S125–S128.
[5] T. Luangtongkum, B. Jeon, J. Han, P. Plummer, C.M. Logue, Q. Zhang, Antibiotic resistance in *Campylobacter*: emergence, transmission and persistence, Future Microbiol 4 (2010) 189–200.
[6] X.-Z. Li, P. Plésiat, H. Nikaido, The challenge of efflux-mediated antibiotic resistance in Gram-negative bacteria, Clin. Microbiol. Rev. 28 (2015) 337–418.
[7] J.P. Lavigne, A. Sotto, M.H. Nicolas-Chanoine, N. Bouziges, J.M. Pagès, A. Davin-Regli, An adaptive response of *Enterobacter aerogenes* to imipenem: regulation of porin balance in clinical isolates, Int. J. Antimicrob. Agents 41 (2013) 130–136.
[8] L.A. Pratt, W. Hsing, K.E. Gibson, T.J. Silhavy, From acids to osmZ: multiple factors influence synthesis of the OmpF and OmpC porins in *Escherichia coli*, Mol. Microbiol. 20 (1996) 911–917.
[9] H. Lou, M. Chen, S.S. Black, S.R. Bushell, M. Ceccarelli, T. Mach, K. Beis, A.S. Low, V.A. Bamford, I.R. Booth, H. Bayley, J.H. Naismith, Altered antibiotic transport in OmpC mutants isolated from a series of clinical strains of multi-drug resistant *E. coli*, PLoS One 6 (2011), e25825.
[10] H. Bajaj, M.A. Scorciapino, L. Moynié, M.G.P. Page, J.H. Naismith, M. Ceccarelli, M. Winterhalter, Molecular basis of filtering carbapenems by porins from β-lactam-resistant clinical strains of *Escherichia coli*, J. Biol. Chem. 291 (2015) 2837–2847.
[11] J.M. Bolla, E. Loret, M. Zalewski, J.M. Pages, Conformational analysis of the *Campylobacter jejuni* porin, J. Bacteriol. 177 (1995) 4266–4271.
[12] K. Amako, S.N. Wai, A. Umeda, M. Shigematsu, A. Takade, Electron microscopy of the major outer membrane protein of *Campylobacter jejuni*, Microbiol. Immunol. 40 (1996) 749–754.
[13] I. Moser, W. Schroeder, J. Salnikow, Campylobacter jejuni major outer membrane protein and a 59-kDa protein are involved in binding to fibronectin and INT 407 cell membranes, FEMS Microbiol. Lett. 157 (1997) 233–238.
[14] D.G. Newell, H. McBride, A.D. Pearson, The identification of outer membrane proteins and flagella of *Campylobacter jejuni*, J. Gen. Microbiol. 130 (1984) 1201–1208.
[15] D.G. Newell, H. McBride, J.M. Dolby, Investigations on the role of flagella in the colonization of infant mice with *Campylobacter jejuni* and attachment of *Campylobacter jejuni* to human epithelial cell lines, J. Hyg. (Lond.) 95 (1985) 217–227.
[16] W.M. Wenman, J. Chai, T.J. Louie, C. Goudreau, H. Lior, D.G. Newell, A.D. Pearson, D.E. Taylor, Antigenic analysis of *Campylobacter* flagellar protein and other proteins, J. Clin. Microbiol. 21 (1985) 108–112.
[17] A. Islam, R. Raghupathy, M.J. Albert, Recombinant PorA, the major outer membrane protein of *Campylobacter jejuni*, provides heterologous protection in an adult mouse intestinal colonization model, Clin. Vaccine Immunol. 17 (2010) 1666–1671.
[18] J.M. Bolla, N. Saint, G. Labesse, J.M. Pagès, C. Dumas, Crystallization and preliminary crystallographic studies of MOMP (major outer membrane protein) from *Campylobacter jejuni*, Acta Crystallogr. Sect. D Biol. Crystallogr. 60 (2004) 2349–2351.
[19] E. Krissinel, K. Henrick, Secondary-structure matching (SSM), a new tool for fast protein structure alignment in three dimensions, Acta Crystallogr. Sect. D Biol. Crystallogr. 60 (2004) 2256–2268.
[20] G. Labesse, E. Garnotel, S. Bonnel, C. Dumas, J.M. Pages, J.M. Bolla, MOMP, a divergent porin from *Campylobacter*: cloning and primary structural characterization, Biochem. Biophys. Res. Commun. 280 (2001) 380–387.
[21] S. McNicholas, E. Potterton, K.S. Wilson, M.E.M. Noble, Presenting your structures: the CCP4mg molecular-graphics software, Acta Crystallogr. Sect. D Biol. Crystallogr. 67 (2011) 386–394.
[22] E. Yaffe, D. Fishelovitch, H.J. Wolfson, D. Halperin, R. Nussinov, MolAxis: a server for identification of channels in macromolecules, Nucleic Acids Res. 36 (2008) W210–W215.
[23] A. Baslé, G. Rummel, P. Storici, J.P. Rosenbusch, T. Schirmer, Crystal structure of osmoporin OmpC from *E. coli* at 2.0 Å, J. Mol. Biol. 362 (2006) 933–942.
[24] S. Cowan, R. Garavito, J. Jansonius, J. Jenkins, R. Karlsson, N. König, E. Pai, R. Pauptit, P. Rizkallah, J. Rosenbusch, G. Rummel, T. Schirmer, The structure of OmpF porin in a tetragonal crystal form, Structure 3 (1995) 1041–1050.
[25] E. Krissinel, K. Henrick, Detection of protein assemblies in crystals, Comput. Life Sci. 3695 (2005) 163–174.
[26] J. Zhuang, A. Engel, J.M. Pagés, J.M. Bolla, The *Campylobacter jejuni* porin trimers pack into different lattice types when reconstituted in the presence of lipid, Eur. J. Biochem. 244 (1997) 575–579.
[27] R. Benz, A. Schmid, R.E.W. Hancock, Ion selectivity of gram-negative bacterial porins, J. Bacteriol. 162 (1985) 722–727.
[28] H. Bajaj, Q.T. Tran, K.R. Mahendran, C. Nasrallah, J.P. Colletier, A. Davin-Regli, J.M. Bolla, J.M. Pagès, M. Winterhalter, Antibiotic uptake through membrane channels: role of *Providencia stuartii* OmpPst1 porin in carbapenem resistance, Biochemistry 51 (2014) 10,244–10,249.
[29] S.A. Gutiérrez, I. Bodrenko, M.A. Scorciapino, M. Ceccarelli, Macroscopic electric field inside water-filled biological nanopores, Phys. Chem. Chem. Phys. 18 (2016) 8855–8864.
[30] P. Raj Singh, M. Ceccarelli, M. Lovelle, M. Winterhalter, K.R. Mahendran, Antibiotic permeation across the OmpF channel: modulation of the affinity site in the presence of magnesium, J. Phys. Chem. B 116 (2012) 4433–4438.
[31] B. VaneDE Berg, Structural basis for outer membrane sugar uptake in pseudo monads, J. Biol. Chem. 287 (2012) 41,044–41,052.
[32] P.M. Hwang, W.-Y. Choy, E.I. Lo, L. Chen, J.D. Forman-Kay, C.R.H. Raetz, G.G. Privé, R.E. Bishop, L.E. Kay, Solution structure and dynamics of the outer membrane enzyme PagP by NMR, Proc. Natl. Acad. Sci. U. S. A. 99 (2002) 13,560–13,565.
[33] D. Forst, W. Welte, T. Wacker, K. Diederichs, Structure of the sucrose-specific porin ScrY from *Salmonella typhimurium* and its complex with sucrose, Nat. Struct. Biol. 5 (1998) 37–46.
[34] J. Michels, A. Geyer, V. Mocanu, W. Welte, A.L. Burlingame, M. Przybylski, Structure and functional characterization of the periplasmic N-terminal polypeptide domain of the sugar-specific ion channel protein (ScrY porin), Protein Sci. 11 (2002) 1565–1574.
[35] W.J. Page, G. Huyer, M. Huyer, E.A. Worobec, Characterization of the porins of *Campylobacter jejuni* and *Campylobacter coli* and implications for antibiotic susceptibility, Antimicrob. Agents Chemother. 33 (1989) 297–303.
[36] E. Dé, M. Jullien, G. Labesse, J.M. Pages, G. Molle, J.M. Bolla, MOMP (major outer membrane protein) of *Campylobacter jejuni*, a versatile pore-forming protein, FEBS Lett. 469 (2000) 93–97.
[37] U.J. Jürgens, R. Benz, Pore-forming activity of outer membrane extracts from the unicellular cyanobacterium

Synechocystis sp. PCC 6714, Z. Naturforsch. 44 (1989) 65–169.
[38] K.R. Mahendran, M. Kreir, H. Weingart, N. Fertig, M. Winterhalter, Permeation of antibiotics through *Escherichia coli* OmpF and OmpC porins: screening for influx on a single-molecule level, J. Biomol. Screen. Off. J. Soc. Biomol. Screen 15 (2010) 302–307.
[39] J. Liu, A.J. Wolfe, E. Eren, J. Vijayaraghavan, M. Indic, B. Van Den Berg, L. Movileanu, Cation selectivity is a conserved feature in the OccD subfamily of *Pseudomonas aeruginosa*, Biochim. Biophys. Acta Biomembr. 1818 (2012) 2908–2916.
[40] K.L. Lout, N. Saint, A. Prilipov, G. Rummel, S.A. Benson, J.P. Rosenbusch, T. Schirmer, Structural and functional characterization of OmpF porin mutants selected for larger pore size. I. Crystallographic analysis, J. Biol. Chem. 271 (1996) 20,669–20,675.
[41] C. Chimerel, L. Movileanu, S. Pezeshki, M. Winterhalter, U. Kleinekathöfer, Transport at the nanoscale: temperature dependence of ion conductance, Eur. Biophys. J. 38 (2008) 121–125.
[42] M. Huyer, T.R. Jr Parr, R.E.W. Hancock, W.J. Page, Outer membrane porin protein of *Campylobacter jejuni*, FEMS Microbiol. Lett. 37 (1986) 247–250.
[43] S. Acosta-Gutierrez, M.A. Scorciapino, I. Bodrenko, M. Ceccarelli, Filtering with electric field: the case of *E. coli* porins, J. Phys. Chem. Lett. 6 (2015) 1807–1812.
[44] H. Liu, J.H. Naismith, A simple and efficient expression and purification system using two newly constructed vectors, Protein Expr. Purif. 63 (2009) 102–111.
[45] G.D. Van Duyne, R.F. Standaert, P.A. Karplus, S.L. Schreiber, J. Clardy, Atomic structures of the human immunophilin FKBP-12 complexes with FK506 and rapamycin, J. Mol. Biol. 229 (1993) 105–124.
[46] M. Kervella, J.L. Fauchere, D. Fourel, J.M. Pages, Immunological cross-reactivity between outer-membrane pore proteins of C*ampylobacter jejuni* and *Escherichia coli*, FEMS Microbiol. Lett. 99 (1992) 281–285.
[47] G. Winter, Xia2: an expert system for macromolecular crystallography data reduction, J. Appl. Crystallogr. 43 (2010) 186–190.
[48] P.H. Zwart, P.V. Afonine, R.W. Grosse-Kunstleve, L.-W. Hung, T.R. Ioerger, A.J. McCoy, E. McKee, N.W. Moriarty, R.J. Read, J.C. Sacchettini, N.K. Sauter, L.C. Storoni, T.C. Terwilliger, P.D. Adams, Automated structure solution with the PHENIX suite, Methods Mol. Biol. 426 (2008) 419–435.
[49] T.C. Terwilliger, R.W. Grosse-Kunstleve, P.V. Afonine, N.W. Moriarty, P.H. Zwart, L.W. Hung, R.J. Read, P.D. Adams, Iterative model building, structure refinement and density modification with the PHENIX AutoBuild wizard, Acta Crystallogr. D Biol. Crystallogr. (2007) 61–69.
[50] A. Perrakis, M. Harkiolaki, K.S. Wilson, V.S. Lamzin, ARP/wARP and molecular replacement, Acta Crystallogr. D Biol. Crystallogr. 57 (2001) 1445–1450.
[51] P. Emsley, K. Cowtan, Coot: model-building tools for molecular graphics, Acta Crystallogr. D Biol. Crystallogr. 60 (2004) 2126–2132.
[52] G.N. Murshudov, A.A. Vagin, E.J. Dodson, Refinement of macromolecular structures by the maximum-likelihood method, Acta Crystallogr. D Biol. Crystallogr. 53 (1997) 240–255.
[53] I.W. Davis, L.W. Murray, J.S. Richardson, D.C. Richardson, MolProbity: structure validation and all-atom contact analysis for nucleic acids and their complexes, Nucleic Acids Res. 32 (2004) 615–619.
[54] H. Zheng, M.D. Chordia, D.R. Cooper, M. Chruszcz, P. Müller, G.M. Sheldrick, W. Minor, Validation of metal-binding sites in macromolecular structures with the CheckMyMetal web server, Nat. Protoc. 9 (2014) 156–170.
[55] M. Montal, P. Mueller, Formation of bimolecular membranes from lipid monolayers and a study of their electrical properties, Proc. Natl. Acad. Sci. U. S. A. 69 (1972) 3561–3566.
[56] U. Lamichhane, T. Islam, S. Prasad, H. Weingart, K.R. Mahendran, M. Winterhalter, Peptide translocation through the mesoscopic channel: binding kinetics at the single molecule level, Eur. Biophys. J. 42 (2013) 363–369.
[57] A. Sali, T.L. Blundell, Comparative protein modelling by satisfaction of spatial restraints, J. Mol. Biol. 234 (1993) 779–815.
[58] J.C. Phillips, R. Braun, W. Wang, J. Gumbart, E. Tajkhorshid, E. Villa, C. Chipot, R.D. Skeel, L. Kal, K. Schulten, Scalable molecular dynamics with NAMD, J. Comput. Chem. 26 (2005) 1781–1802.
[59] M.J. Harvey, G. Giupponi, G. De Fabritiis, ACEMD: accelerating biomolecular dynamics in the microsecond time scale, J. Chem. Theory Comput. 5 (2009) 1632–1639.
[60] I. Buch, T. Giorgino, G. De Fabritiis, Complete reconstruction of an enzyme-inhibitor binding process by molecular dynamics simulations, Proc. Natl. Acad. Sci. U. S. A. 108 (2011) 10,184–10,189.
[61] K. Lindorff-Larsen, S. Piana, K. Palmo, P. Maragakis, J.L. Klepeis, R.O. Dror, D.E. Shaw, Improved side-chain torsion potentials for the amber ff99SB protein force field, Proteins Struct. Funct. Bioinf. 78 (2010) 1950–1958.
[62] W.L. Jorgensen, J. Chandrasekhar, J.D. Madura, R.W. Impey, M.L. Klein, Comparison of simple potential functions for simulating liquid water, J. Chem. Phys. 79 (1983) 926.
[63] J. Wang, R.M. Wolf, J.W. Caldwell, P.A. Kollman, D.A. Case, Development and testing of a general amber force field, J. Comput. Chem. 25 (2004) 1157–1174.
[64] V. Law, C. Knox, Y. Djoumbou, T. Jewison, A.C. Guo, Y. Liu, A. Maclejewski, D. Arndt, M. Wilson, V. Neveu, A. Tang, G. Gabriel, C. Ly, S. Adamjee, Z.T. Dame, B. Han, Y. Zhou, D.S. Wishart, DrugBank 4.0: shedding new light on drug metabolism, Nucleic Acids Res. 42 (2014) 1091–1097.
[65] W.D. Cornell, P. Cieplak, C.I. Bayly, I.R. Gould, K.M. Merz, D.M. Ferguson, D.C. Spellmeyer, T. Fox, J.W. Caldwell, P.A. Kollman, A second generation force field for the simulation of proteins, nucleic acids, and organic molecules, J. Am. Chem. Soc. 117 (1995) 5179–5197.
[66] M.J. Frisch, G.W. Trucks, H.B. Schlegel, G.E. Scuseria, M.A. Robb, J.R. Cheeseman, G. Scalmani, V. Barone, B. Mennucci, G.A. Petersson, H. Nakatsuji, M. Caricato, X. Li, H.P. Hratchian, A.F. Izmaylov, J. Bloino, G. Zheng, J.L. Sonnenberg, M. Hada, M. Ehara, K. Toyota, R. Fukuda, J. Hasegawa, M. Ishida, T. Nakajima, Y. Honda, O. Kitao, H. Nakai, T. Vreven, J.A. Montgomery Jr., J.E. Peralta, F. Ogliaro, M. Bearpark, J.J. Heyd, E. Brothers, K.N. Kudin, V.N. Staroverov, R. Kobayashi, J. Normand, K. Raghavachari, A. Rendell, J.C. Burant, S.S. Iyengar, J. Tomasi, M. Cossi, N. Rega, J.M. Millam, M. Klene, J.E. Knox, J.B. Cross, V. Bakken, C. Adamo, J. Jaramillo, R. Gomperts, R.E. Stratmann, O. Yazyev, A.J. Austin, R. Cammi, C. Pomelli, J.W. Ochterski, R.L. Martin, K. Morokuma, V.G. Zakrzewski, G.A. Voth, P. Salvador, J.J. Dannenberg, S. Dapprich, A.D. Daniels, Ö. Farkas, J.B. Foresman, J.V. Ortiz, J. Cioslowski, D.J. Fox, Gaussian 09, Revision A.02, Gaussian Inc, Wallingford CT, 2009 34.
[67] J. Wang, W. Wang, D.A. Kollman, Case, automatic atom type and bond type perception in molecular mechanical calculations, J. Mol. Graph. Model. 25 (2006) 247–260.

[68] G. Malloci, A.V. Vargiu, G. Serra, A. Bosin, P. Ruggerone, M. Ceccarelli, A database of force-field parameters, dynamics, and properties of antimicrobial compounds, Molecules 20 (2015) 13,997–14,021.
[69] A. Barducci, G. Bussi, M. Parrinello, Well-tempered metadynamics: a smoothly converging and tunable free-energy method, Phys. Rev. Lett. 100 (2) (2008) 100.
[70] A. Laio, M. Parrinello, Escaping free-energy minima, Proc. Natl. Acad. Sci. U. S. A. 99 (2002) 12,562–12,566.
[71] P. Raiteri, A. Laio, F.L. Gervasio, C. Micheletti, M. Parrinello, Efficient reconstruction of complex free energy landscapes by multiple walkers metadynamics, J. Phys. Chem. B 110 (2006) 3533–3539.

Part IV

APPENDIX

A

COMPUTATIONAL METHODS

The computational details of chapter 5 and 7 are described in this section. For the rest of articles presented as part of this thesis dissertation the computational details can be found in the original article in the Compendium section.

A.1 FILTERING WITH THE ELECTRIC FIELD: THE CASE OF *e. coli porins*

The experimental X-ray structure of OmpF (PDB Id: 2OMF; 2.4Å resolution), OmpC (PDB Id: 2J1N; 2.0Å) and OmpC20 (PDB Id: 2XE2; 2.5Å) from E. coli were used as starting coordinates for molecular dynamics (MD) simulations. In the case of OmpC33, since only poor resolution data are available (3.55Å)[94], the X-ray coordinates of OmpC28 (PDB Id: 2XE3; 2.85Å) were used, after the substitution R124H. All the amino acid residues were simulated in the ionization state at neutral pH except for the E296, which was protonated (net charge 0) as suggested for OmpF by Varma et al.[165]. The entire trimer was embedded in a pre-equilibrated POPC (1- palmitoyl-2-oleoyl-sn-glycero-3-phosphocholine) bilayer of 259 lipids and the system was oriented in order to center the protein at the origin of the coordinate system and align the channel along the z-axis (positive z: extracellular side; negative z: periplasmic side). A suitable number of sodium ions were added to neutralize the system total charge. The system was solvated with $\sim$ 17000 water molecules (simulation box size: 11, 11, 9 nm; total number of atoms: $\sim$ 100k). After 1 ps of energy minimization (conjugate gradients), a slow heating from 10 to 300 K was carried out for 1 ns. During this stage, positional restraints were applied on the protein α-carbons (all three dimensions) as well as on the lipids phosphorus atoms (along z only). After releasing the constraints on the POPC, an equilibration stage follows for 4 ns in the NPT ensemble at 1.0 bar and 300 K. Finally, 400 ns MD simulations were performed in the NVT ensemble after the elimination of the protein restraints. Only the last 300 ns were used for the analysis.

The NPT equilibration was performed with the program NAMD[129], with 1.0 fs time-step, and treating long-range electrostatics with the soft particle mesh Ewald (SPME) method (64 grid points and order 4 with

direct cutoff at 1.0 nm and 1.0 Å grid-size). Pressure control was applied using the Nose-Hoover method (extended Lagrangian) with isotropic cell, integrated with the Langevin Dynamics (200 fs and 100 fs of piston period and decay, respectively). The latter was also applied for temperature control with 200 fs thermostat damping time. Production run in the NVT ensemble was performed through the ACEMD code[59] compiled for GPUs, by rescaling hydrogen mass to 4 au and increasing the time-step up to 4.0 fs[24]. The Langevin thermostat was used with 1 ps damping time. SPME was used to treat the electrostatics as for the equilibration stage. The Amber99SB-ILDN force field[92] was used for the protein and lipids, and the TIP3P[75] for waters. Structure alignment was performed within the software VMD[66,137]. Water analysis was performed by dividing the channel in 12 adjacent windows along the z-axis (z-windows). Each z-window has a height of 6 Å and overlapped the adjacent windows by 1 Å. For all the waters found inside each of the z-windows, the total electric dipole moment μ_t was calculated for each frame along the MD trajectory. The μ_t was then normalized by the number of waters N_w included in the z-window and then time averaged. The three protein monomers were separately analyzed and resulted to be absolutely comparable with each other. For the sake of brevity, only the results pertaining to the first monomer are shown. The GAFF force-field parameters[167] were used to describe cefepime (DrugBank[89] n. DB01413) and cefotaxime (DrugBank n. DB00493). Partial atomic charges were evaluated according to the RESP approach[12]: the molecule was first optimized at the HF/6-31G (d) level, up to a convergence in energy of 10-5 au, using the Gaussian03 package[53]. Atomic RESP charges were derived from the electrostatic potential using the antechamber module of the AMBER package[28].

Starting from the final configuration of the OmpF simulation described above, the antibiotic was placed inside the lumen of the first monomer. The difference between the z-coordinate of the center of mass (com) of the antibiotic two-ring system and the z-coordinate of the com of the protein monomer was +12.5Å. A thousand steps of energy minimization were performed. The equilibration stage followed for 1 ns in the NVT ensemble at 300 K as described herein-before. Well-tempered metadynamics[10,87] simulation (200-400 ns) was performed with the ACEMD code[?], until the first effective translocation through the protein constriction region (CR) was observed. Then, four configurations were randomly selected, two with the antibiotic located in the extracellular vestibule (EV), two in the periplasmic vestibule (PV). Correspondingly, four multiple-walkers[134] were set to extend the metadynamics reconstruction of the free-energy surface (FES). Two biased collective variables were used, namely, the antibiotic position and orientation

inside the channel. In practice, the 'position' Δ_z was defined as the difference of the z-coordinate between the com of the antibiotic two-ring system and that of the porin first monomer. The 'orientation' was defined on the basis of the orientation of the rigid two-ring system, as the difference of the z-coordinate between the lactam carbonyl carbon and the sulfur bonded carbon. 4x200 ns were run, arriving to a total simulation time of 1.0-1.1 μs. During the metadynamics, energy biases were added every 2.0 ps to each collective variable (height 0.2 au; σ 0.3 and 0.05 au for position and orientation, respectively). Well-tempered ΔT was 3000 K.

A.2 MODEL

The equilibrated structure in A.1 was used to perform metadynamics of three antibiotics: ampicillin, benzylpenicillin and carbenicillin, the parameters for the three molecules were obtained from the Antibiotics database of our group, the parametrization protocol is described in the database (http://www.dsf.unica.it/translocation/db/). For each antibiotic the difference between the z-coordinate of the center of mass (com) of the antibiotic two-ring system and the z-coordinate of the com of the protein monomer is reported in Table 1. A thousand steps of energy minimization were performed. The equilibration stage followed for 1 ns in the NVT ensemble at 300 K as described in A.1. Well-tempered metadynamics[10,87] simulation was performed with the ACEMD code[59], until the first effective translocation through the protein constriction region (CR) was observed (Table 1). Then, four configurations were randomly selected, two with the antibiotic located in the extracellular vestibule (EV), two in the periplasmic vestibule (PV). Correspondingly, four multiple-walkers[134] were set to extend the metadynamics reconstruction of the free-energy surface (FES). Two biased collective variables were used, namely, the antibiotic position and the orientation of beta-lactamic ring. In practice, the 'position' Δz was defined as the difference of the z-coordinate between the com of the antibiotic two-ring system and that of the porin first monomer. In Table 1 the simulation time for each Walker, as well as total simulation length are displayed. During the metadynamics, energy biases were added every 1.25 ps to each collective variable. Well-tempered ΔT was 3000K for all antibiotics but for ampicllin which was simulated at 5000K.

	Initial z coordinate (Å)	First effective translocation time (ns)	Simulation time per walker (ns)	Total simulation time (μ s)	Gaussian height (kcal/mol)	σ_{cv1}	σ_{cv2}
Ampicillin	12.73	300	500	2.3	0.2	0.08	0.3
Benzylpenicillin	10.78	300	600	2.7	1.0	0.08	0.25
Carbenicillin	17.07	400	600	2.8	1.0	0.08	0.25

Table 1: Initial coordinate, simulation time for first effective translocation, total simulation time and metadynamics gaussians specifications

BIBLIOGRAPHY

[1] Silvia Acosta-Gutierrez, Mariano Andrea Scorciapino, Igor Bodrenko, and Matteo Ceccarelli. Filtering with electric field: The case of e. coli porins. *The Journal of Physical Chemistry Letters*, 6:1807–1812, 2015. (Cited on page 61.)

[2] Aleksij Aksimentiev and Klaus Schulten. Imaging α-hemolysin with molecular dynamics: ionic conductance, osmotic permeability, and the electrostatic potential map. *Biophysical journal*, 88 (6):3745–3761, 2005. (Cited on page 72.)

[3] Mike P Allen and Dominic J Tildesley. *Computer simulation of liquids*. Oxford university press, 1989. (Cited on pages 29, 30, and 35.)

[4] H. E. Alper and R. M. Levy. Fluid strength dependence of dielectric saturation in liquid water. *The Journal of Physical Chemistry*, 94:8401–8403, 1990. (Cited on page 68.)

[5] Hans C Andersen. Molecular dynamics simulations at constant pressure and/or temperature. *The Journal of chemical physics*, 72(4):2384–2393, 1980. (Cited on page 30.)

[6] J. L. Aragones, L. G. MacDowell, J. I. Siepmann, and C. Vega. Phase diagram of water under an applied electric field. *Physical Review Letters*, 107:155702, 2011. (Cited on page 68.)

[7] F Bach, E Moulines, C Burges, L Bottou, M Welling, Z Ghahramani, and K Weinberger. Advances in neural information processing systems 26. *Burges, C., Bottou, L., Welling, M., Ghahramani, Z., Weinberger, K., Eds*, pages 773–781, 2013. (Cited on page 45.)

[8] Nathan A Baker, David Sept, Simpson Joseph, Michael J Holst, and J Andrew McCammon. Electrostatics of nanosystems: application to microtubules and the ribosome. *Proceedings of the National Academy of Sciences*, 98(18):10037–10041, 2001. (Cited on pages 69 and 70.)

[9] A. Barducci, M. Bonomi, and M. Parrinello. Linking well-tempered metadynamics simulations with experiments. *Biophysical Journal*, 98:L44–L46, 2010. (Cited on page 41.)

[10] Alessandro Barducci, Giovanni Bussi, and Michele Parrinello. Well-tempered metadynamics: A smoothly converging and tunable free-energy method. *Physical review letters*, 100(2):020603, 2008. (Cited on pages 40, 41, 160, and 161.)

[11] Arnaud Baslé, Gabriele Rummel, Paola Storici, Juerg P Rosenbusch, and Tilman Schirmer. Crystal structure of osmoporin ompc from e. coli at 2.0 . *Journal of molecular biology*, 362(5): 933–942, 2006. (Cited on page 18.)

[12] Christopher I Bayly, Piotr Cieplak, Wendy Cornell, and Peter A Kollman. A well-behaved electrostatic potential based method using charge restraints for deriving atomic charges: the resp model. *The Journal of Physical Chemistry*, 97(40):10269–10280, 1993. (Cited on page 160.)

[13] R. Benz. Structure and function of porins from gram-negative bacteria. *Annual Review of Microbiology*, 42:359–93, 1988. (Cited on pages 17, 25, and 53.)

[14] Roland Benz and RE Hancock. Mechanism of ion transport through the anion-selective channel of the pseudomonas aeruginosa outer membrane. *The Journal of general physiology*, 89(2): 275–295, 1987. (Cited on page 5.)

[15] Roland Benz, Angela Schmid, and Greetje H Vos-Scheperkeuter. Mechanism of sugar transport through the sugar-specific lamb channel ofescherichia coli outer membrane. *The Journal of membrane biology*, 100(1):21–29, 1987. (Cited on pages 5, 6, and 20.)

[16] E. Berkane, F. Orlik, A. Charbit, C. Danelon, D. Fournier, R. Benz, and M. Winterhalter. Nanopores: maltoporin channel as a sensor for maltodextrin and lambda-phage. *Journal of Nanobiotechnology*, 3(1):3, 2005. ISSN 1477-3155. doi: 10.1186/1477-3155-3-3. URL http://dx.doi.org/10.1186/1477-3155-3-3. (Cited on page 23.)

[17] Igor Bodrenko, Harsha Bajaj, Paolo Ruggerone, Mathias Winterhalter, and Matteo Ceccarelli. Analysis of fast channel blockage: revealing substrate binding in the microsecond range. *Analyst*, 2015. (Cited on page 23.)

[18] M Bonomi, A. Barducci, and M. Parrinello. Reconstructing the equilibrium boltzmann distribution from well-tempered metadynamics. *Journal of Computational Chemistry*, 30:1615–1621, 2009. (Cited on page 41.)

[19] Massimiliano Bonomi and Michele Parrinello. Enhanced sampling in the well-tempered ensemble. *Physical review letters*, 104 (19):190601, 2010. (Cited on pages 41 and 43.)

[20] F. Booth. The dielectric constant of water and the saturation effect. *The Journal of Chemical Physics*, 19:391–394, 1951. (Cited on pages 68, 72, and 73.)

[21] Jérôme Bredin, Nathalie Saint, Monique Malléa, Emmanuelle De, Gérard Molle, V Simonet, et al. Alteration of pore properties of escherichia coli ompf induced by mutation of key residues in antiloop 3 region. *Biochem. J*, 363:521–528, 2002. (Cited on page 26.)

[22] E. D. Brown and G. D. Wright. Antibacterial drug discovery in the resistance era. *Nature*, 529:336–43, 2016. (Cited on pages 3, 10, 11, and 25.)

[23] A. Bryskier. Antimicrobial agents: Antibacterials and antifungals. 2005. (Cited on page 25.)

[24] Ignasi Buch, Toni Giorgino, and Gianni De Fabritiis. Complete reconstruction of an enzyme-inhibitor binding process by molecular dynamics simulations. *Proceedings of the National Academy of Sciences*, 108(25):10184–10189, 2011. (Cited on page 160.)

[25] Giovanni Bussi, Francesco Luigi Gervasio, Alessandro Laio, and Michele Parrinello. Free-energy landscape for β hairpin folding from combined parallel tempering and metadynamics. *Journal of the American Chemical Society*, 128(41):13435–13441, 2006. (Cited on page 42.)

[26] Hongliang Cai, Kelly Rose, Lan-Hsin Liang, Steve Dunham, and Charles Stover. Development of a liquid chromatography/mass spectrometry-based drug accumulation assay in pseudomonas aeruginosa. *Analytical biochemistry*, 385(2):321–325, 2009. (Cited on page 22.)

[27] C. Camilloni, D. Provasi, Tiana G., and R.A. Broglia. Exploring the protein g helix free-energy surface by solute tempering metadynamics. *Proteins*, 71:1647–1654, 2008. (Cited on page 43.)

[28] David A Case, TA Darden, Thomas E Cheatham III, CL Simmerling, Junmei Wang, Robert E Duke, Ray Luo, Kenneth M Merz, David A Pearlman, Mike Crowley, et al. Amber 9. *University of California, San Francisco*, 45, 2006. (Cited on page 160.)

[29] Matteo Ceccarelli, Christophe Danelon, Alessandro Laio, and Michele Parrinello. Microscopic mechanism of antibiotics translocation through a porin. *Biophysical journal*, 87(1):58–64, 2004. (Cited on page 25.)

[30] Matteo Ceccarelli, Attilio V. Vargiu, and Paolo Ruggerone. A kinetic monte carlo approach to investigate antibiotic translocation through bacterial porins. *Journal of Physics: Condensed Matter*, 24(10):104012, 2012. (Cited on page 26.)

[31] Yu-Chian Chen. Beware of docking! *Trends in pharmacological sciences*, 36(2):78–95, 2015. (Cited on page 46.)

[32] Bakowies D Baron R BÃijrgi R Geerke DP Heinz TN Kastenholz MA KrÃď utler V Oostenbrink C et al. Christen M, HÃijnenberger PH. The gromos soft- ware for biomolecular simulation: Gromos05. *Journal of Computational Chemistry*, 26(16):1719–1751, 2005. (Cited on page 35.)

[33] Alex M Clark, Paul Labute, and Martin Santavy. 2d structure depiction. *Journal of chemical information and modeling*, 46(3): 1107–1123, 2006. (Cited on page 89.)

[34] Kim Cooper, Eric Jakobsson, and Peter Wolynes. The theory of ion transport through membrane channels. *Progress in Biophysics and Molecular Biology*, 46(1):51–96, 1985. (Cited on page 4.)

[35] Wendy D. Cornell, Piotr Cieplak, Christopher I. Bayly, Ian R. Gould, Kenneth M. Merz, David M. Ferguson, David C. Spellmeyer, Thomas Fox, James W. Caldwell, and Peter A. Kollman. A second generation force field for the simulation of proteins, nucleic acids, and organic molecules. *Journal of the American Chemical Society*, 117(19):5179–5197, 1995. (Cited on page 35.)

[36] S.W. Cowan, T. Schirmer, G. Rummel, M. Steiert, R. Ghosh, R.A. Pauptit, J.N. Jansonius, and J.P. Rosenbusch. Crystal structures explain functional properties of two e. coli porins. *Nature*, 358 (6389):727–733, 1992. (Cited on pages 3, 18, 24, and 51.)

[37] James F. Dama, Michele Parrinello, and Gregory A. Voth. Well-tempered metadynamics converges asymptotically. *Physical Review Letters*, 112(24), 2014. (Cited on page 41.)

[38] Christophe Danelon, Ekaterina M Nestorovich, Mathias Winterhalter, Matteo Ceccarelli, and Sergey M Bezrukov. Interaction

of zwitterionic penicillins with the ompf channel facilitates their translocation. *Biophysical journal*, 90(5):1617–1627, 2006. (Cited on pages 25 and 26.)

[39] Tom Darden, Darrin York, and Lee Pedersen. Particle mesh ewald: An nâŃĚ log (n) method for ewald sums in large systems. *The Journal of chemical physics*, 98(12):10089–10092, 1993. (Cited on page 72.)

[40] Tony D Davis, Christopher J Gerry, and Derek S Tan. General platform for systematic quantitative evaluation of small-molecule permeability in bacteria. *ACS chemical biology*, 9(11):2535–2544, 2014. (Cited on page 22.)

[41] B. L. de Groot and H. Grubmüller. Water permeation across biological membranes: Mechanism and dynamics of aquaporin-1 and glpf. (Cited on pages 53 and 60.)

[42] Simon W de Leeuw, John William Perram, and Edgar Roderick Smith. Simulation of electrostatic systems in periodic boundary conditions. i. lattice sums and dielectric constants. In *Proceedings of the Royal Society of London A: Mathematical, Physical and Engineering Sciences*, volume 373, pages 27–56. The Royal Society, 1980. (Cited on page 32.)

[43] Anne H. Delcour. Outer membrane permeability and antibiotic resistance. *Biochimica et Biophysica Acta (BBA)-Proteins and Proteomics*, 1794(5):808–816, 2009. (Cited on pages 17, 18, and 20.)

[44] C. Dellago and Geissler P.L. Bolhuis, P.G. Transition path sampling. *Advances in Chemical Physics*, 123, pages = 1-78, year = 2002,. (Cited on page 41.)

[45] Balasundaresan Dhakshnamoorthy, Brigitte K Ziervogel, Lydia Blachowicz, and Benoît Roux. A structural study of ion permeation in ompf porin from anomalous x-ray diffraction and molecular dynamics simulations. *Journal of the American Chemical Society*, 135(44):16561–16568, 2013. (Cited on page 4.)

[46] D. Donadio, P. Raiteri, and M. Parrinello. Topological defects and bulk melting of hexagonal ice. *Journal of Physical Chemistry B*, 109:5421–5424, 2005. (Cited on page 41.)

[47] G. M. Eliopoulos et al. *In vitro* and *in vivo* avtivity of ly 146032 a new cyclic lipopeptide antibiotic. *Antimicrobial Agents and Chemotherapy*, 30:532–535, 1986. (Cited on page 11.)

[48] Elif Eren, Jagamya Vijayaraghavan, Jiaming Liu, Belete R Cheneke, Debra S Touw, Bryan W Lepore, Mridhu Indic, Liviu Movileanu, and Bert Van den Berg. Substrate specificity within a family of outer membrane carboxylate channels. *PLoS Biol*, 10 (1):e1001242, 2012. (Cited on page 20.)

[49] Ulrich Essmann, Lalith Perera, Max L Berkowitz, Tom Darden, Hsing Lee, and Lee G Pedersen. A smooth particle mesh ewald method. *The Journal of chemical physics*, 103(19):8577–8593, 1995. (Cited on pages 31 and 72.)

[50] Paul Peter Ewald. Die berechnung optischer und elektrostatischer gitterpotentiale. *Annalen der Physik*, 369(3):253–287, 1921. (Cited on page 30.)

[51] Lucía Fernández and Robert EW Hancock. Adaptive and mutational resistance: role of porins and efflux pumps in drug resistance. *Clinical microbiology reviews*, 25(4):661–681, 2012. (Cited on page 17.)

[52] Daan Frenkel and Berend Smit. *Understanding molecular simulation: from algorithms to applications, volume 1*. Academic press, 2001. (Cited on page 28.)

[53] Æleen Frisch, Michael J Frisch, and Gary W Trucks. *Gaussian 03 user's reference*. Gaussian, Incorporated, 2003. (Cited on page 160.)

[54] Tiana G. Estimation of microscopic averages from metadynamics. *The European Physical Journal B*, 63:235–238, 2008. (Cited on page 41.)

[55] J. Tirado-Rives G. A. Kaminski, R. A. Friesner and W. L. Jorgensen. Evaluation and reparametrization of the opls-aa force field for proteins via comparison with accurate quantum chemical calculations on peptides. *The JOurnal of Physical Chemistry B*, 105(28):6474–6487, 2001. (Cited on page 35.)

[56] Eric Hajjar, Andrey Bessonov, Alexander Molitor, Amit Kumar, Kozhinjampara R Mahendran, Mathias Winterhalter, Jean-Marie Pagès, Paolo Ruggerone, and Matteo Ceccarelli. Toward screening for antibiotics with enhanced permeation properties through bacterial porins. *Biochemistry*, 49(32):6928–6935, 2010. (Cited on pages 25 and 26.)

[57] Robert EW Hancock and Fiona SL Brinkman. Function of pseudomonas porins in uptake and efflux. *Annual Reviews in Microbiology*, 56(1):17–38, 2002. (Cited on page 20.)

[58] Ulrich H.E. Hansmann. Parallel tempering algorithm for conformational studies of biological molecules. *Chemical Physics Letters*, 281(1):140–150, 1997. (Cited on page 42.)

[59] Matt J Harvey, Giovanni Giupponi, and G De Fabritiis. Acemd: accelerating biomolecular dynamics in the microsecond time scale. *Journal of chemical theory and computation*, 5(6):1632–1639, 2009. (Cited on pages 160 and 161.)

[60] P.G. Higgins, C. Dammhayn, M. Hackel, and H. Seifert. Global spread of carbapenem-resistant *acinetobacter baumannii*. *Journal of Antimicrobial Chemotherapy*, 65:233–238, 2010. (Cited on page 10.)

[61] R Hockney and J Eastwood. Computer simulations using particles mcgraw-hill. *New York*, 1981. (Cited on page 31.)

[62] William G Hoover. Canonical dynamics: equilibrium phase-space distributions. *Physical Review A*, 31(3):1695, 1985. (Cited on page 30.)

[63] Sheng-You Huang and Xiaoqin Zou. Ensemble docking of multiple protein structures: considering protein structural variations in molecular docking. *Proteins: Structure, Function, and Bioinformatics*, 66(2):399–421, 2007. (Cited on page 46.)

[64] Sheng-You Huang, Sam Z Grinter, and Xiaoqin Zou. Scoring functions and their evaluation methods for protein–ligand docking: recent advances and future directions. *Physical Chemistry Chemical Physics*, 12(40):12899–12908, 2010. (Cited on page 47.)

[65] Thomas Huber, Andrew E. Torda, and Wilfred F. Gunsteren. Local elevation: a method for improving the searching properties of molecular dynamics simulation. *Journal of Computer-aided Molecular Design*, 8(6):695–708, 1994. (Cited on page 38.)

[66] William Humphrey, Andrew Dalke, and Klaus Schulten. Vmd: visual molecular dynamics. *Journal of molecular graphics*, 14(1): 33–38, 1996. (Cited on page 160.)

[67] Wonpil Im and B. Roux. Ion permeation and selectivity of ompf porin: a theoretical study based on molecular dynamics, brownian dynamics, and continuum electrodiffusion theory. *Journal of*

molecular biology, 322(4):851–869, 2002. (Cited on pages 25, 53, and 69.)

[68] Wonpil Im and B. Roux. Ions and counterions in a biological channel: a molecular dynamics simulation of ompf porin from escherichia coli in an explicit membrane with 1m kcl aqueous salt solution. *Journal of molecular biology*, 319(5):1177–1197, 2002. (Cited on pages 18, 25, and 53.)

[69] V. M. Isabella, A. J. Campbell, J. Manchester, M. Sylvester, A. S. Nayar, K. E. Ferguson, R. Tommasi, and A. A. Miller. Toward the rational design of carbapenem uptake in pseudomonas aeruginosa. *Chemistry & Biology*, 22(4):535âĂŞ547, 2015. (Cited on page 7.)

[70] J.D. Jackson. *Classical Electrodynamics, 3rd edition*. Wiley, New York, 1999. (Cited on page 71.)

[71] J.Cama, H. Bajaj, S. Pagliara, T.Maier, Y.Braun, M.Winterhalter, and U.F.Keyser. Quantification of fluoroquinolone uptake through the outer membrane channel ompf of escherichia coli. *Journal of the American Chemical Society*, 137 (43):13836âĂŞ13843, 2015. (Cited on page 3.)

[72] Ron O Dror John L Klepeis, Kresten Lindorff-Larsen and David E Shaw. Long-timescale molecular dynamics simulations of protein structure and function. *Current Opinion in Structural Biology*, 19(2):120–127„ 2009. (Cited on page 38.)

[73] Gareth Jones, Peter Willett, Robert C Glen, Andrew R Leach, and Robin Taylor. Development and validation of a genetic algorithm for flexible docking. *Journal of molecular biology*, 267(3): 727–748, 1997. (Cited on page 89.)

[74] William L Jorgensen. The many roles of computation in drug discovery. *Science*, 303(5665):1813–1818, 2004. (Cited on page 46.)

[75] William L. Jorgensen, Jayaraman Chandrasekhar, Jeffry D. Madura, Roger W. Impey, and Michael L. Klein. Comparison of simple potential functions for simulating liquid water. *The Journal of chemical physics*, 79(2):926–935, 1983. (Cited on page 160.)

[76] William L. Jorgensen, D. S. Maxwell, and J. Tirado-Rives. *Journal of American Chemical Society*, 118(45):11225–11236, 1996. (Cited on page 35.)

[77] Lewis K. Antibiotic: recover the lost art of drug discovery. *Nature*, 485:439–440, 2012. (Cited on page 12.)

[78] Lewis K. Platforms for antibiotic discovery. *Nature Reviews in Drug Discovery*, 12:371–87, 2013. (Cited on page 12.)

[79] A. Karshikoff, V. Spassov, S. W. Cowan, R. Ladenstein, and T. Schirmer. Electrostatic properties of 2 porin channels from escherichia coli. *The Journal of Molecular Biology*, 240:372–384, 1994. (Cited on pages 24, 68, 69, and 70.)

[80] Slávka Kaščáková, Laure Maigre, Jacqueline Chevalier, Matthieu Réfrégiers, and Jean-Marie Pagès. Antibiotic transport in resistant bacteria: synchrotron uv fluorescence microscopy to determine antibiotic accumulation with single cell resolution. *PLoS One*, 7(6):e38624, 2012. (Cited on page 21.)

[81] Locher K. P. & Van Gelder P. Koebnik, R. Structure and function of bacterial outer membrane proteins: barrels in a nutshell. *Molecular Microbiology*, 37:239–253, 2000. (Cited on pages 17 and 18.)

[82] M. A. Kohanski, D. J. Dwyer, B. Hayete, and J. J. Lawrence, C. A. & Collins. A common mechanism of cellular death induced by bactericidal antibiotics. *Cell*, 130:797–810, 2007. (Cited on page 25.)

[83] S. Kojima and H. Nikaido. Permeation rates of penicillins indicate that escherichia coli porins function principally as nonspecific channels. *Proceedings of the National Academy of Science*, 110:E2629âĹŠE2634, 2013. (Cited on pages 25 and 53.)

[84] S. Kojima and H. Nikaido. High salt concentrations increase permeability through ompc channels of escherichia coli. *The Journal of Biological Chemistry*, 289:26464–26473, 2014. (Cited on pages 4, 18, 25, 53, 78, and 79.)

[85] A. Kumar, E. Hajjar, P. Ruggerone, and M. Ceccarelli. Molecular simulations reveal the mechanism and the determinants for ampicillin translocation through ompf. *The Journal of Physical Chemistry B*, 114(29):9608âĂŞ9616, 2010. (Cited on page 26.)

[86] Amit Kumar, Eric Hajjar, Paolo Ruggerone, and Matteo Ceccarelli. Structural and dynamical properties of the porins ompf and ompc: insights from molecular simulations. *Journal of Physics: Condensed Matter*, 22(45):454125, 2010. (Cited on pages 18 and 25.)

[87] Alessandro Laio and Michele Parrinello. Escaping free-energy minima. *Proceedings of the National Academy of Sciences*, 99 (20):12562–12566, 2002. (Cited on pages 38, 160, and 161.)

[88] P Läuger. Ion transport through pores: a rate-theory analysis. *Biochimica et Biophysica Acta (BBA)-Biomembranes*, 311 (3):423–441, 1973. (Cited on page 4.)

[89] Vivian Law, Craig Knox, Yannick Djoumbou, Tim Jewison, An Chi Guo, Yifeng Liu, Adam Maciejewski, David Arndt, Michael Wilson, Vanessa Neveu, et al. Drugbank 4.0: shedding new light on drug metabolism. *Nucleic acids research*, 42(D1): D1091–D1097, 2014. (Cited on page 160.)

[90] V. Levadny, V. M. Aguilella, M. Aguilella-Arzo, and M Belaya. Interaction of a polar molecule with an ion channel. *Physical Review E*, 70(4):041912, 2004. (Cited on pages 4 and 26.)

[91] WR Lieb and WD Stein. Testing and characterizing the simple pore. *Biochimica et Biophysica Acta (BBA)-Biomembranes*, 373 (2):165–177, 1974. (Cited on page 4.)

[92] Kresten Lindorff-Larsen, Stefano Piana, Kim Palmo, Paul Maragakis, John L Klepeis, Ron O Dror, and David E Shaw. Improved side-chain torsion potentials for the amber ff99sb protein force field. *Proteins: Structure, Function, and Bioinformatics*, 78(8): 1950–1958, 2010. (Cited on page 160.)

[93] Kim B. Liu P, R.A. Friesner, and B.J. Berne. Replica exchange with solute tempering: a method for sampling biological systems in explicit water. *Proceedings of the National Academy of Science*, 102:13749âĂŞ13754, 2005. (Cited on page 43.)

[94] Hubing Lou, Min Chen, Susan S Black, Simon R Bushell, Matteo Ceccarelli, Tivadar Mach, Konstantinos Beis, Alison S Low, Victoria A Bamford, Ian R Booth, et al. Altered antibiotic transport in ompc mutants isolated from a series of clinical strains of multidrug resistant e. coli. *PLoS One*, 6(10):e25825, 2011. (Cited on pages 3, 25, 53, 54, 63, and 159.)

[95] Alison S. Low, Fiona M. MacKenzie, Ian M. Gould, and Ian R. Booth. Protected environments allow parallel evolution of a bacterial pathogen in a patient subjected to long-term antibiotic therapy. *Molecular microbiology*, 42(3):619–630, 2001. (Cited on page 53.)

[96] Mary Luckey and Hiroshi Nikaido. Diffusion of solutes through channels produced by phage lambda receptor protein of escherichiacoli: Inhibition by higher oligosaccharides of maltose series. *Biochemical and biophysical research communications*, 93 (1):166–171, 1980. (Cited on page 22.)

[97] V. M. Aguilella M. Aguilella-Arzo, A. Andrio and A. Alcaraz. Dielectric saturation of water in a membrane protein channel. *Physical Chemistry Chemical Physics*, 11:358–365, 2009. (Cited on pages 69 and 70.)

[98] T. Mach, P. Neves, E. Spiga, H. Weingart, M. Winterhalter, P. Ruggerone, M. Ceccarelli, and P. Gameiro. Facilitated permeation of antibiotics across membrane channels âĹŠ interaction of the quinolone moxifloxacin with the ompf channel. *Journal of American Chemical Society*, 130(40):13301âĂŞ13309, 2008. (Cited on page 3.)

[99] Jr. Bashford D. Bellott M. Dunbrack R. L. Evanseck J. D. Field M. J. Fischer S. Gao J. Guo H. Ha S. Joseph-McCarthy D. Kuchnir L. Kuczera K. Lau F. T. K. Mattos C. Michnick S. Ngo T. Nguyen D. T. Prodhom B. Reiher W. E. Roux B. Schlenkrich M. Smith J. C. Stote R. Straub J. Watanabe M. Wiorkiewicz-Kuczera J. Yin D. MacKerell, A. D. and M. Karplus. All-atom empirical potential for molecular modeling and dynamics studies of proteins. *The Journal of Physical Chemistry B*, 102:3586–3616, 1998. (Cited on page 35.)

[100] K. R. Mahendran, E. Hajjar, T. Mach, M. Lovelle, A. Kumar, Sousa I., E. Spiga, H. Weingart, P. Gameiro, M. Winterhalter, and M. Ceccarelli. Molecular basis of enorfloxacin translocation through ompf, an outer membrane channel of *escherichia coli*when binding does not imply translocation. *Journal of Physical Chemistry B*, 114:5170–9, 2010. (Cited on page 26.)

[101] K. R. Mahendran, M. Kreir, H. Weingart, N. Fertig, and M. Winterhalter. Permeation of antibiotics through escherichia coli ompf and ompc porins: Screening for influx on a single-molecule level. *Journal of Biomolecular Screening*, 15(25):302–307, 2010. (Cited on pages 23, 25, and 53.)

[102] Giuliano Malloci, Attilio Vittorio Vargiu, Giovanni Serra, Andrea Bosin, Paolo Ruggerone, and Matteo Ceccarelli. A database of force-field parameters, dynamics, and properties of antimicrobial compounds. *Molecules*, 20(8):13997–14021, 2015. (Cited on pages 78 and 94.)

[103] Fabrizio Marinelli, Fabio Pietrucci, Alessandro Laio, and Stefano Piana. A kinetic model of trp-cage folding from multiple biased molecular dynamics simulations. *PLoS Comput. Biol*, 5(8): e1000452, 2009. (Cited on page 41.)

[104] Muriel Masi and Jean-Marie Pagès. Structure, function and regulation of outer membrane proteins involved in drug transport in enterobactericeae: the ompf/c–tolc case. *The open microbiology journal*, 7:22, 2013. (Cited on pages 18, 25, 53, 54, and 77.)

[105] O Matsuoka, E Clementi, and M Yoshimine. Ci study of the water dimer potential surface. *The Journal of Chemical Physics*, 64(4):1351–1361, 1976. (Cited on page 35.)

[106] Reginald McNulty, Jakob P Ulmschneider, Hartmut Luecke, and Martin B Ulmschneider. Mechanisms of molecular transport through the urea channel of helicobacter pylori. *Nature communications*, 4, 2013. (Cited on page 60.)

[107] Milet A. Michel C, Laio A. Tracing the entropy along a reactive pathway: the energy as a generalized reaction coordinate. *Journal of Chemical Theory and Computation*, 5:2193–2196, 2009. (Cited on page 41.)

[108] Parrinello M. Micheletti C, Laio A. Reconstructing the density of states by history-dependent metadynamics. *Physical Review Letters*, 92:170601, 2004. (Cited on page 41.)

[109] Henk Miedema, Maarten Vrouenraets, Jenny Wierenga, Wim Meijberg, George Robillard, and Bob Eisenberg. A biological porin engineered into a molecular, nanofluidic diode. *Nano letters*, 7(9):2886–2891, 2007. (Cited on page 59.)

[110] Alexandre V Morozov, Tanja Kortemme, Kiril Tsemekhman, and David Baker. Close agreement between the orientation dependence of hydrogen bonds observed in protein structures and quantum mechanical calculations. *Proceedings of the National Academy of Sciences of the United States of America*, 101(18): 6946–6951, 2004. (Cited on page 36.)

[111] PGS Mortimer and LJV Piddock. A comparison of methods used for measuring the accumulation of quinolones by enterobacteriaceae, pseudomonas aeruginosa and staphylococcus aureus. *Journal of Antimicrobial Chemotherapy*, 28(5):639–653, 1991. (Cited on page 21.)

[112] Corinne Nardin, Sandra Thoeni, Jörg Widmer, Mathias Winterhalter, and Wolfgang Meier. Nanoreactors based on (polymerized) aba-triblock copolymer vesicles. *Chemical Communications*, (15): 1433–1434, 2000. (Cited on page 21.)

[113] Ekaterina M Nestorovich, Christophe Danelon, Mathias Winterhalter, and Sergey M Bezrukov. Designed to penetrate: time-resolved interaction of single antibiotic molecules with bacterial pores. *Proceedings of the National Academy of Sciences*, 99(15): 9789–9794, 2002. (Cited on pages 4, 6, and 26.)

[114] H Nikaido and Vaara M. Molecular basis of bacterial outer membrane permeability. *Microbiology Reviews*, 49:1–32, 1985. (Cited on pages 25 and 53.)

[115] Hiroshi Nikaido. Molecular basis of bacterial outer membrane permeability revisited. *Microbiology and molecular biology reviews*, 67(4):593–656, 2003. (Cited on pages 16, 17, and 18.)

[116] Hiroshi Nikaido and EMIKO Y Rosenberg. Porin channels in escherichia coli: studies with liposomes reconstituted from purified proteins. *Journal of Bacteriology*, 153(1):241–252, 1983. (Cited on pages 25 and 53.)

[117] Shuichi Nosé. A unified formulation of the constant temperature molecular dynamics methods. *The Journal of chemical physics*, 81(1):511–519, 1984. (Cited on page 30.)

[118] Mats HM Olsson, Chresten R Søndergaard, Michal Rostkowski, and Jan H Jensen. Propka3: consistent treatment of internal and surface residues in empirical p k a predictions. *Journal of Chemical Theory and Computation*, 7(2):525–537, 2011. (Cited on page 77.)

[119] World Health Organization. Antimicrobial resistance: global report on surveillance. 2014. (Cited on page 10.)

[120] R. O'Shea and H.E. Moser. Physiochemical properties of antibacterial compounds: Implications for drug discovery. *Journal of Medicinal Chemistry*, 51:2871–8, 2008. (Cited on page 25.)

[121] John C Owicki and Harold A Scheraga. Monte carlo calculations in the isothermal-isobaric ensemble. 1. liquid water. *Journal of the American Chemical Society*, 99(23):7403–7412, 1977. (Cited on page 35.)

[122] James Chloë E Pagès, Jean-Marie and Mathias Winterhalter. The porin and the permeating antibiotic: a selective diffusion barrier in gram-negative bacteria. *Nature Reviews Microbiology*, 6(12): 893–903, 2008. (Cited on pages 3, 17, and 22.)

[123] Jean-Marie Pagès. Role of bacterial porins in antibiotic susceptibility of gram-negative bacteria. *Bacterial and Eukaryotic Porins*, pages 41–59, 2004. (Cited on page 17.)

[124] Michele Parrinello and Aneesur Rahman. Polymorphic transitions in single crystals: A new molecular dynamics method. *Journal of Applied physics*, 52(12):7182–7190, 1981. (Cited on page 30.)

[125] Dhilon S Patel, Suyong Re, Emilia L Wu, Yifei Qi, Phillip E Klebba, Göran Widmalm, Min Sun Yeom, Yuji Sugita, and Wonpil Im. Dynamics and interactions of ompf and lps: Influence on pore accessibility and ion permeability. *Biophysical journal*, 110 (4):930–938, 2016. (Cited on page 53.)

[126] Gwynn M. N. Holmes D. J. Payne, D. J. and D. L. Pompliano. Drugs for bad bugs: confornting the challenges of antibacterial discovery. *Nature Reviews. Drug Discovery*, 6:29–40, 2007. (Cited on pages 3 and 11.)

[127] Prashant S Phale, Tilman Schirmer, Alexej Prilipov, Kuo-Long Lou, Ariane Hardmeyer, and Jurg P Rosenbusch. Voltage gating of escherichia coli porin channels: role of the constriction loop. *Proceedings of the National Academy of Sciences*, 94(13):6741–6745, 1997. (Cited on page 18.)

[128] P.S. Phale, Philippsen A., Widmer C., Phale V.P., J.P. Rosenbusch, and Schirmer T. Role of charged residues of the ompf porin channel constriction region probed by mutagenesis and simulations. *Biochemistry*, 40:6319–25, 2001. (Cited on page 26.)

[129] James C Phillips, Rosemary Braun, Wei Wang, James Gumbart, Emad Tajkhorshid, Elizabeth Villa, Christophe Chipot, Robert D Skeel, Laxmikant Kale, and Klaus Schulten. Scalable molecular dynamics with namd. *Journal of computational chemistry*, 26 (16):1781–1802, 2005. (Cited on page 159.)

[130] Stefano Piana and Alessandro Laio. A bias-exchange approach to protein folding. *The Journal of Physical Chemistry B*, 111(17): 4553–4559, 2007. (Cited on page 43.)

[131] EL Pollock and Jim Glosli. Comments on p 3 m, fmm, and the ewald method for large periodic coulombic systems. *Computer Physics Communications*, 95(2):93–110, 1996. (Cited on page 31.)

[132] W. H. Press. *Numerical recipes 3rd edition: The art of scientific computing*. Cambridge university press, 2007. (Cited on page 29.)

[133] Stavenger R.A. and Winterhalter M. 2014 translocation project: how to get good drugs into bad bugs. *Science Translational Medicine*, 6(228), 2014. (Cited on page 3.)

[134] Paolo Raiteri, Alessandro Laio, Francesco Luigi Gervasio, Cristian Micheletti, and Michele Parrinello. Efficient reconstruction of complex free energy landscapes by multiple walkers metadynamics. *The Journal of Physical Chemistry B*, 110(8):3533–3539, 2006. (Cited on pages 40, 160, and 161.)

[135] M.; Lovelle M.; Winterhalter M.; Mahendran K. R. Raj Singh, P.; Ceccarelli. Antibiotic permeation across the ompf channel: Modulation of the affinity site in the presence of magnesium. *The Journal of Physical Chemistry B*, 116:4433âĹŠ4438, 2012. (Cited on pages 18, 25, and 81.)

[136] Dennis C Rapaport. *The art of molecular dynamics simulation*. Cambridge university press, 2004. (Cited on page 28.)

[137] Elijah Roberts, John Eargle, Dan Wright, and Zaida Luthey-Schulten. Multiseq: unifying sequence and structure data for evolutionary analysis. *BMC bioinformatics*, 7(1):1, 2006. (Cited on page 160.)

[138] Kindal M Robertson and D.Peter Tieleman. Orientation and interactions of dipolar molecules during transport through ompf porin. *FEBS Letters*, 528(1-3):53–57, 2002. ISSN 1873-3468. doi: 10.1016/S0014-5793(02)03173-3. URL http://dx.doi.org/10.1016/S0014-5793(02)03173-3. (Cited on pages 4 and 25.)

[139] Celeste Sagui and Thomas Darden. Multigrid methods for classical molecular dynamics simulations of biomolecules. *The Journal of Chemical Physics*, 114(15):6578–6591, 2001. (Cited on page 31.)

[140] M. S. Sansom, G. R. Smith, C. Adcock, and P. C. Biggin. The dielectric properties of water within model transbilayer pores. *Biophysical Journal*, 73(5):2404âĂŞ2415, 1997. (Cited on pages 24 and 69.)

[141] Tilman Schirmer. General and specific porins from bacterial outer membranes. *Journal of structural biology*, 121(2):101–109, 1998. (Cited on page 18.)

[142] Tilman Schirmer, Thomas A Keller, Yan-Fei Wang, and Jurg P Rosenbusch. Structural basis for sugar translocation through maltoporin channels at 3.1 angstrom resolution. *Science*, 267(5197): 512, 1995. (Cited on page 20.)

[143] G. E. Schulz. The structure of bacterial outer membrane proteins. *Biochimica e Biophysica Acta*, 1565:308–317, 2002. (Cited on pages 17 and 18.)

[144] Mariano Andrea Scorciapino, Tommaso D'Agostino, Silvia Acosta-Gutierrez, Giuliano Malloci, Igor Bodrenko, and Matteo Ceccarelli. Exploiting the porin pathway for polar compound delivery into gram-negative bacteria. *Future Medicinal Chemistry*, 8(10):1047–1062, 2016. (Cited on page 62.)

[145] L. L. Silver. Challenges of antibaterial discovery. *Clinical microbiology reviews*, 24(1):71–109, 2011. (Cited on pages 11 and 12.)

[146] Pratik Raj Singh, Harsha Bajaj, Roland Benz, Mathias Winterhalter, and Kozhinjampara R Mahendran. Transport across the outer membrane porin of mycolic acid containing actinomycetales: Nocardia farcinica. *Biochimica et Biophysica Acta (BBA)-Biomembranes*, 1848(2):654–661, 2015. (Cited on page 23.)

[147] CM Soares, J Björkstén, and O Tapia. L3 loop-mediated mechanisms of pore closing in porin: a molecular dynamics perturbation approach. *Protein engineering*, 8(1):5–12, 1995. (Cited on page 18.)

[148] Kastenholz MA KrÃďutler V Lenz T Lins RD Oostenbrink C Soares T A, HÃijnenberger PH and van Gunsteren WF. An improved nucleic acid parameter set for the gromos force field. *Journal of Computational Chemistry*, 26(7):725–737, 2005. (Cited on page 35.)

[149] Chresten R Søndergaard, Mats HM Olsson, Michał Rostkowski, and Jan H Jensen. Improved treatment of ligands and coupling effects in empirical calculation and rationalization of p k a values. *Journal of Chemical Theory and Computation*, 7(7):2284–2295, 2011. (Cited on page 77.)

[150] Sergio Filipe Sousa, Pedro Alexandrino Fernandes, and Maria Joao Ramos. Protein–ligand docking: current status and

future challenges. *Proteins: Structure, Function, and Bioinformatics*, 65(1):15–26, 2006. (Cited on page 46.)

[151] David E Shaw Stefano Piana, John L Klepeis. Assessing the accuracy of physical models used in protein-folding simulations: quantitative evidence from long molecular dynamics simulations. *Current opinion in structural biology*, 24:98–105, 2014. (Cited on page 38.)

[152] Peter J Steinbach and Bernard R Brooks. New spherical-cutoff methods for long-range forces in macromolecular simulation. *Journal of computational chemistry*, 15(7):667–683, 1994. (Cited on page 30.)

[153] JB Stock, B Rauch, and S Roseman. Periplasmic space in salmonella typhimurium and escherichia coli. *Journal of Biological Chemistry*, 252(21):7850–7861, 1977. (Cited on page 21.)

[154] Okamoto Y. Sugita Y. Replica-exchange molecular dynamics method for protein folding. *Chemical Physics Letters*, 6314:141–151, 1999. (Cited on page 42.)

[155] G. Sutmann. Structure formation and dynamics of water in strong external electric fields. *Journal of Electroanalytical Chemistry*, 450:289–302, 1998. (Cited on page 68.)

[156] P.; Jensen M. ÃŸ.; Miercke L. J. W.; OâĂŹConnell J.; Stroud R. M.; Schulten K. Tajkhorshid, E.; Nollert. Control of the selectivity of the aquaporin water channel family by global orientational tuning. *Science*, 296:525–530, 2002. (Cited on pages 53 and 60.)

[157] Sandeep Tamber, Martina M Ochs, and Robert EW Hancock. Role of the novel oprd family of porins in nutrient uptake in pseudomonas aeruginosa. *Journal of bacteriology*, 188(1):45–54, 2006. (Cited on page 20.)

[158] H. J. Tieleman, D. P.; Berendsen. A molecular dynamics study of the pores formed by escherichia coli ompf porin in a fully hydrated palmitoyloleoylphosphatidylcholine bilayer. *Biophysical Journal*, 74:2786âĹŠ2801, 1998. (Cited on pages 18, 24, 53, 56, and 73.)

[159] Pratyush Tiwary and Michele Parrinello. A time-independent free energy estimator for metadynamics. *The Journal of Physical Chem- istry B*, 119(3):736–742, 2014. (Cited on page 41.)

[160] Walkup G. K. Manchester J. I. Tommasi R., Brown D. G. and Miller A. A. Eskapeing the labyrinth of antibacterial discovery.

Nature Reviews in Drug Discovery, 14:529–42, 2015. (Cited on pages 3, 10, and 11.)

[161] Glenn M Torrie and John P Valleau. Nonphysical sampling distributions in monte carlo free-energy estimation: Umbrella sampling. *Journal of Computational Physics*, 23(2):187–199, 1977. (Cited on page 38.)

[162] Maxim Totrov and Ruben Abagyan. Flexible ligand docking to multiple receptor conformations: a practical alternative. *Current opinion in structural biology*, 18(2):178–184, 2008. (Cited on page 46.)

[163] Que-Tien Tran, William S., Farid R., Erdemli G., and Pearlstein R. The translocation kinetics of antibiotics through porin ompc: Insights from structure-based solvation mapping using watermap. *Proteins. Structure. Function.Bioinformatics*, 81:291–9, 2013. (Cited on pages 25 and 26.)

[164] Omar Valsson and Michele Parrinello. Variational approach to enhanced sampling and free energy calculations. *Physical review letters*, 113(9):090601, 2014. (Cited on page 43.)

[165] Sameer Varma, See-Wing Chiu, and Eric Jakobsson. The influence of amino acid protonation states on molecular dynamics simulations of the bacterial porin ompf. *Biophysical journal*, 90 (1):112–123, 2006. (Cited on page 159.)

[166] Arthur F Voter. Hyperdynamics: Accelerated molecular dynamics of infrequent events. *Physical Review Letters*, 78(20):3908, 1997. (Cited on page 38.)

[167] Junmei Wang, Romain M Wolf, James W Caldwell, Peter A Kollman, and David A Case. Development and testing of a general amber force field. *Journal of computational chemistry*, 25(9): 1157–1174, 2004. (Cited on page 160.)

[168] Van Gunsteren WF and Berendsen HJC. Groningen molecular simulation (gromos). *Library manual, Biomos, Groningen, The Netherlands*, pages 1–221, 1987. (Cited on page 35.)

[169] M Winterhalter, C Hilty, SM Bezrukov, C Nardin, W Meier, and D Fournier. Controlling membrane permeability with bacterial porins: application to encapsulated enzymes. *Talanta*, 55(5):965–971, 2001. (Cited on page 21.)

[170] Mathias Winterhalter and Matteo Ceccarelli. Physical methods to quantify small antibiotic molecules uptake into gram-negative bacteria. *European Journal of Pharmaceutics and Biopharmaceutics*, 95:63–67, 2015. (Cited on pages 3 and 21.)

[171] I.-C. Yeh and M. L. Berkowitz. Dielectric constant of water at high electric fields: Molecular dynamics study. *The Journal of Chemical Physics*, 110(16):7935âĂŞ7942, 1999. (Cited on page 68.)

[172] Darrin York and Weitao Yang. The fast fourier poisson method for calculating ewald sums. *The Journal of Chemical Physics*, 101 (4):3298–3300, 1994. (Cited on page 31.)

[173] Darrin M York, Tom A Darden, and Lee G Pedersen. The effect of long-range electrostatic interactions in simulations of macromolecular crystals: A comparison of the ewald and truncated list methods. *The Journal of chemical physics*, 99(10):8345–8348, 1993. (Cited on page 31.)

[174] Ying Zhou, Camil Joubran, Lakshmi Miller-Vedam, Vincent Isabella, Asha Nayar, Sharon Tentarelli, and Alita Miller. Thinking outside the âĂIJbugâĂİ: a unique assay to measure intracellular drug penetration in gram-negative bacteria. *Analytical chemistry*, 87(7):3579–3584, 2015. (Cited on page 22.)

[175] Brigitte K Ziervogel and Benoît Roux. The binding of antibiotics in ompf porin. *Structure*, 21(1):76–87, 2013. (Cited on pages 6, 25, 26, 86, 89, and 90.)

[176] Willy Zimmermann and Armel Rosselet. Function of the outer membrane of escherichia coli as a permeability barrier to beta-lactam antibiotics. *Antimicrobial Agents and Chemotherapy*, 12 (3):368–372, 1977. (Cited on page 21.)